Edward G. W. GASSON

# The past relationship between temperature and sea level – from proxy records and ice sheet modelling

word count: 51,380

II

# Abstract

Due to current uncertainties about the response of the ice sheets to anthropogenic climate forcing, there has been a growing interest in what the palaeo-record can tell us about the past response of the ice sheets to natural climate forcings. Direct qualitative and quantitative inferences have been made based on the past relationships between climate and sea level (which parallels ice sheet changes). Here we attempt to define better the past relationship between temperature and sea level. We first review existing temperature and sea level records, with a discussion of uncertainty in each of these datasets. We then synthesise the sea level and temperature data and test plausible forms for the sea level versus temperature relationship over the past 50 million years. We suggest that a nonlinear form for this relationship is evident in the data, which can be explained by the different glacial thresholds for Northern Hemisphere and Southern Hemisphere glaciation and the ice sheet carrying capacity of the Antarctic continent.

We next perform ice sheet model simulations of the large ice sheets that either exist today (the East Antarctic ice sheet) or have existed in the past (the Northern Hemisphere ice sheets), focusing on past periods of large-scale change to these ice sheets. We use our simulations of the Northern Hemisphere ice sheets during the last glacial cycle to test and refine our modelling approach. We then investigate ice sheet hysteresis and the different thresholds for glaciation and deglaciation; this may limit the usefulness of using data from the Cenozoic, which is broadly a period of cooling, to make inferences about the future ice sheet response to ongoing warming. Finally we compare our model results with the earlier data synthesis and a recent study of the past relationship between atmospheric $CO_2$ and sea level on long timescales.

IV

# Acknowledgements

I would like to first thank my two main supervisors, Mark Siddall and Dan Lunt. Mark for his encouragement, friendship, always being very generous with his time and for putting up with me disagreeing. This thesis was also much easier to write thanks to regular editing sessions in the pub. Dan, for many interesting discussions and his shared enthusiasm for going off on tangents. I'd like to thank Dave Pollard and his family for their hospitality during the few months I spent at Penn State and also the World Universities Network for funding this visit. I'm also very grateful for the funding for this thesis from NERC and BAS. Thanks to the organisers and people I met during the Urbino and ACDC summer schools.

I'd like to thank Emma Stone, Owen Rackham and Lauren Gregoire for much technical support, in particular Emma for always being so helpful. Also, my third supervisor Richard Hindmarsh, Carrie Lear and Derek Vance for useful discussions. I thank my mother for proofreading and much support during my studies. I'd like to thank Pete and the whole of my year for a very enjoyable few years at Bristol. Finally I'd like to thank Kate for all of her support.

# Author's Declaration

I declare that the work in this dissertation was carried out in accordance with the requirements of the University's Regulations and Code of Practice for Research Degree Programmes and that it has not been submitted for any other academic award. Except where indicated by specific reference in the text, the work is the candidate's own work. Work done in collaboration with, or with the assistance of, others, is indicated as such. Any views expressed in the dissertation are those of the author.

SIGNED: ............................................................. DATE:...........................

# Contents

# List of Figures

XV

XVII

# List of Tables

# List of variables

| Symbol | Description | Units |
|:------:|:-----------:|:-----:|
| $\alpha$ | albedo feedback | - |
| $a$ | ablation | m yr$^{-1}$ |
| $\hat{a}_s$ | potential snowmelt | m yr$^{-1}$ |
| $A$ | temperature dependant flow law coefficient | - |
| $A_t$ | period of year | - |
| $b_0$ | refreezing capacity of snowpack | m yr$^{-1}$ |
| $B$ | surface mass balance | m yr$^{-1}$ |
| $B_{wat}$ | basal water depth | m |
| $D_p$ | PDD sum | days (d) |
| $s$ | elevation of bedrock | m |
| $H$ | ice thickness | m |
| $I$ | top of atmosphere insolation | w m$^{-2}$ |
| $O_l$ | local orography | m |
| $O_g$ | global orography | m |
| $P$ | precipitation | m yr$^{-1}$ |
| $\mathbf{R}$ | random fluctuation on PDD model | °C |
| $s$ | ice sheet elevation | m |
| $S$ | basal melt rate | m yr$^{-1}$ |
| $T_a$ | surface air temperature | °C |
| $t$ | time | yr |
| $u$ | ice velocity | m yr$^{-1}$ |
| $V$ | total ice volume in domain | km$^3$ |

# List of constants

| Symbol | Description | Default Value | Units |
|--------|-------------|---------------|-------|
| $\alpha_i$ | PDD factor for ice | 8.0 | mm d$^{-1}$ °C |
| $\alpha_s$ | PDD factor for snow | 3.0 | mm d$^{-1}$ °C |
| $B_s$ | basal sliding parameter | 0 | mm yr$^{-1}$ Pa$^{-1}$ |
| $c_i$ | specific heat capacity of ice | 2009 | J kg$^{-1}$ K$^{-1}$ |
| $f$ | flow enhancement factor | 3.0 | - |
| $\gamma$ | lapse rate | 7.0 | °C km$^{-1}$ |
| $g$ | acceleration due to gravity | 9.81 | m s$^{-2}$ |
| $G$ | geothermal heat flux | -50 | mW m$^{-2}$ |
| $k_i$ | thermal conductivity of ice | 2.1 | W m$^{-1}$ K$^{-1}$ |
| $L$ | specific latent heat of fusion | $335 \times 10^3$ | J kg$^{-1}$ |
| $n$ | flow law exponent | 3 | - |
| $\rho_i$ | density of ice | 910 | kg m$^{-3}$ |
| $\sigma_T$ | standard deviation of temperature fluctuations | 5.0 | °C |
| $w_{max}$ | fraction of snowfall that can refreeze | 0.6 | - |

# List of abbreviations

| | |
|---|---|
| ACC | Antarctic Circumpolar Current |
| AST | ASTronomical forcing method |
| BBC | British Broadcasting Corporation |
| BS | Basal Sliding method |
| CCD | Calcite Compensation Depth |
| CCSM | Community Climate System Model |
| CLIMBER | CLIMate and BiospheREe model |
| DSDP | Deep Sea Drilling Project |
| DST | Deep Sea Temperature |
| EAIS | East Antarctic Ice Sheet |
| ECMWF | European Centre for Medium range Weather Forecasts |
| EoMIP | Eocene Modelling Inter-comparison Project |
| EOT | Eocene Oligocene Transition |
| EPICA | European Project for Ice Coring in Antarctica |
| ERA-40 | 40 year ECMWF Re-Analysis project |
| FAMOUS | FAst Met Office / UK Universities Simulator |
| FB | albedo FeedBack method |
| GA | Genetic Algorithm |
| GCM | General Circulation Model |
| GDGT | Glycerol Dialkyl Glycerol Tetraethers |
| GENESIS | Global ENvironmental and Ecological Simulation of Interactive Systems |
| GHG | GreenHouse Gas |
| GISS | Goddard Institute for Space Studies |
| HadAM3 | Hadley centre Atmosphere Model 3 |
| HadCM3 | Hadley centre Coupled Model 3 |

| | |
|---|---|
| HMB | Height-Mass Balance |
| ICE-5G | global ice sheet reconstruction - 5th generation |
| IPCC | Intergovernmental Panel on Climate Change |
| IRD | Ice Rafted Debris |
| ISM | Ice Sheet Model |
| ka | kiloannum ($10^3$ years) |
| LGM | Last Glacial Maximum |
| LIG | Last InterGlaciation |
| Ma | Megaannum ($10^6$ years) |
| MAT | Mean surface Air Temperature |
| MECO | Middle Eocene Climatic Optimum |
| MMCO | Middle Miocene Climatic Optimum |
| MWP | MeltWater Pulse |
| NODC_WOA98 | National Oceanographic Data Centre - World Ocean Atlas 1998 |
| NJ | New Jersey |
| OAGCM | Ocean Atmosphere General Circulation Model |
| ODP | Ocean Drilling Programme |
| PDD | Positive Degree Day |
| PIC | Pre-Industrial atmospheric $CO_2$ Concentration |
| ppmv | parts per million by volume |
| RMSE | Root Mean Squared Error |
| SIA | Shallow Ice Approximation |
| SLE | Sea Level Equivalent |
| SPECMAP | SPECtral MApping Project |
| SST | Sea Surface Temperature |
| $TEX_{86}$ | TetraEther indeX of tetraethers consisting of 86 carbon atoms |
| TOA | Top Of Atmosphere |
| TOPO | bedrock TOPOgraphy |
| UNFCCC | |
| $U^{k'}_{37}$ | Alkenone unsaturation index |
| WAIS | West Antarctic Ice Sheet |

# Chapter 1

# Introduction

Part of this chapter was originally published in 2012, here it is modified from the first half of that paper, with an extended introduction: Gasson, E., Siddall, M., Lunt, D., Rackham, O. J. L., Lear, C. H., and Pollard, D. (2012). Exploring uncertainties in the relationship between temperature, ice volume, and sea level over the past 50 million years. *Reviews of Geophysics*, 50(RG1005):135. E. Gasson performed all analysis, created figures and wrote the paper, additional comments were provided by the co-authors, 4 reviewers and the editor, E. Rohling. For figures with a time series the axes are reversed so that time runs left to right, for consistency with all other figures in this thesis.

## 1.1 Background

Of the global human population, ~10 % currently live in low elevation coastal zones less than 10 m above present day sea level and over a third live within 100 km of the coastline (McGranahan et al., 2007; Camoin et al., 2009). The ice sheets are the largest potential contributor to sea level rise, but understanding and predicting glacier and ice sheet dynamics is notoriously difficult (Alley et al., 2005; Allison et al., 2009). Because of this limited understanding, in its fourth assessment report (AR4) the Intergovernmental Panel on Climate Change (IPCC) did not provide sea level projections that accounted for rapid dynamical changes in ice flow (Solomon et al., 2007). It should be noted that since AR4 there has been a substantial effort to improve observations and projections of the dynamic ice response to warming (e.g. Schoof, 2007; Holland et al., 2008; Joughin and Alley, 2011; Sundal et al., 2011; Pattyn et al., 2012; Cornford et al., 2013).

The observational record contains examples of nonlinear threshold type responses, such as the collapse of the Larsen B ice shelf and subsequent surging of glaciers (De Angelis and Skvarca, 2003; Rignot, 2004; Domack et al., 2005). However, the observational record does not help us to constrain large changes to the ice sheets. Although there is no known analogue to projected future warming in the palaeoclimate record (Crowley, 1990; Haywood et al., 2011), it does contain examples of large-scale changes to the ice sheets (DeConto and Pollard, 2003a; Miller et al., 2005a). The palaeoclimate record can therefore aid understanding of ice sheet behaviour and provide insight into the plausibility of large ice sheet changes in a warming world (Scherer, 1998; Pollard and DeConto, 2009). By looking to the palaeoclimate record we can also attempt to understand better the relationship between different climate parameters, such as temperature, atmospheric $CO_2$, ice volume, and sea level (Rohling et al., 2009; Foster and Rohling, 2013).

The palaeoclimate record is useful in illustrating how dynamic the Earth system has been in the past. A key problem of communicating the dangers of climate change, such as the oft-cited 2 °C limit for increased global mean temperature (e.g. Nordhaus, 1979; European Commission, 2007; UNFCCC, 2009; Schmidt and Archer, 2009), is that it is difficult to reconcile human experience of weather and climate with changes in the global mean temperature (Hulme, 2012). As an extreme example, the difference between the warmest (56.7 °C, Death Valley, USA, 10/07/1913) and coolest (-89.2 °C, Vostok Station, Antarctica, 21/07/1983) temperatures observed on Earth is 145.9 °C (El Fadli et al., 2012; WMO, 2012). Although most humans will never experience such weather extremes, the diurnal temperature range can exceed 35 °C
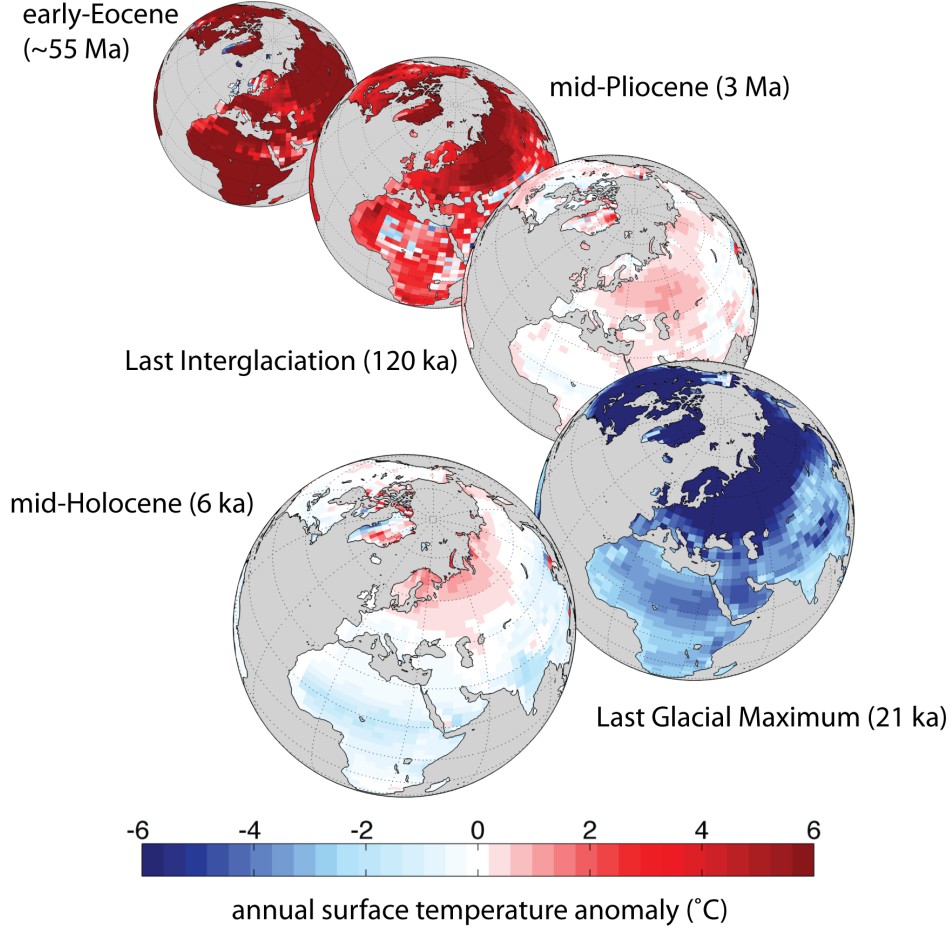
Figure 1.1: *HadCM3 / HadCM3L simulations of past climates, shown as annual temperature anomalies over land relative to a pre-industrial control simulation (Singarayer and Valdes, 2010; Lunt et al., 2010b,a). Note that the early Eocene (1120 ppmv $CO_2$) simulation has a different continental configuration, although it is shown here as an anomaly relative to the modern. Figure based on that of Hill et al. (2012).*

in parts of central USA (Sun et al., 2006). Consequently it is perhaps understandable that humans have difficulty comprehending a 2 °C increase in the global mean temperature above pre-industrial (1.2 °C above present) (Hulme, 2012). The palaeoclimate record can provide examples of periods when the global mean temperature is only a few degrees different from today (see Figure 1.1).

Over the past 50 Ma, eustatic sea level has varied between ~100 m above present in the early Eocene (~56 − 49 Ma), when there was little or no land ice on Earth and the ocean basin volume was less than present (Miller et al., 2005a; Kominz et al., 2008; Miller et al., 2009b), and 120 − 140 m below present (Fairbanks, 1989; Yokoyama et al., 2000) during the Last Glacial

Maximum (LGM; $23 - 19$ ka), when there were large ice sheets in Antarctica, North America, Asia, and Europe (Clark et al., 2009). On this timescale, large (greater than 10 m) eustatic sea level variations have been caused predominately by changes in the volume of land ice (Miller et al., 2005a). Broadly, there have been four ice sheet states, these being (1) largely unglaciated conditions, (2) a glaciated East Antarctic, (3) interglacial conditions with additional ice sheets in the West Antarctic and Greenland (i.e., present-day conditions), and (4) glacial conditions with the additional growth of large ice sheets in the Northern Hemisphere and a slight increase in volume of the Antarctic ice sheets (de Boer et al., 2010). The glaciation of the East Antarctic can also be further broken down into an intermediate state with ephemeral mountain ice caps and a fully glaciated state (DeConto and Pollard, 2003a; Langebroek et al., 2009).

The temperature range over the past 50 Ma is perhaps less well understood. Deep-sea palaeoclimate proxies are commonly used to interpret past climate changes because much of the regional and seasonal changes present in surface ocean and terrestrial records are reduced by the large volume and slow recycling of the deep ocean (Lear et al., 2000; Lear, 2007; Sosdian and Rosenthal, 2009). Deep-sea temperatures (DSTs) in the early Eocene (50 Ma) may have been $7 - 15\,^{\circ}\mathrm{C}$ warmer than present, with a best estimate of $\sim 12\,^{\circ}\mathrm{C}$ (Lear et al., 2000; Zachos et al., 2001a; Billups and Schrag, 2003; Lear, 2007). The deep sea was $\sim 1.5 - 2\,^{\circ}\mathrm{C}$ cooler than present during the LGM, with further cooling limited as temperatures approached the freezing point for seawater (Waelbroeck et al., 2002; Adkins et al., 2002; Elderfield et al., 2010; Siddall et al., 2010a).

Sea surface temperature (SST) proxies suggest that during the Eocene the high latitudes were significantly warmer than present, approaching or even exceeding temperatures seen in the modern tropics (Bijl et al., 2009; Hollis et al., 2009; Liu et al., 2009; Bijl et al., 2010). However, the lower latitudes were only a few degrees warmer than present in the Eocene (Sexton et al., 2006; Lear et al., 2008; Keating-Bitonti et al., 2011), suggesting that there was a much reduced latitudinal temperature gradient (Huber, 2008; Bijl et al., 2009). During glacial conditions the surface high latitudes show cooling (Jouzel et al., 2007), with this cooling also extending to low latitudes suggesting that there were additional feedbacks on the climate system, such as $CO_2$ feedbacks, in addition to astronomical driven forcing (Herbert et al., 2010; Rohling et al., 2012).

### 1.1.1   Temperature to sea level relationship

Surface temperature is broadly related to sea level through its control on the amount of ice stored on land and through thermal expansion. A frequently reproduced plot of temperature against sea level was created by Archer (2007) (see Figure 1.2, reproduced by: Jaeger et al., 2008; Gulledge et al., 2008; Archer and Brovkin, 2008; Grassl, 2011) and has featured in governmental reports on climate change (Schubert et al., 2006; Steffen et al., 2009). Archer (2007) suggest a linear relationship between temperature and sea level over the past 40 Ma. Although this figure is presented with the caveat that it represents the long-term sea level response in equilibrium with the climate, it has been used to suggest that for the warming projected by the end of the 21st century the long-term sea level rise will be up to 50 m above present (Archer, 2007; Gulledge et al., 2008). A plot of the relationship between atmospheric $CO_2$ and sea level on long timescales is shown by Alley et al. (2005), which is comparable to the plot shown in Figure 1.2 if the logarithmic relationship between atmospheric $CO_2$ and temperature is taken into account. However these plots use limited data covering a very long period of Earth's history. Perhaps the use of such figures in policy documents stems from their simplicity and because they are easy to understand. This does not mean that they should be over-simplified. Indeed, a recent in-depth synthesis of atmospheric $CO_2$ and sea level reconstructions showed a more complex relationship (Foster and Rohling, 2013).

In addition to the qualitative use of temperature versus sea level plots in illustrating the past dynamism of the Earth system, quantitative sea level projections for the 21st century have also been made using functions based on similar relationships. The semi-empirical method uses data for past temperature and sea level to project future sea level response to a temperature forcing (Rahmstorf, 2007). All of these projections have so far assumed a linear function for the relationship between the rate of sea level change and the temperature forcing (Rahmstorf, 2007; Grinsted et al., 2008; Vermeer and Rahmstorf, 2009). Although this linear form may be a reasonable approximation of recent sea level rise, which has been predominantly caused by thermal expansion and is of a relatively low magnitude, it may be less appropriate for large changes in temperature and sea level caused by changes in terrestrial ice volumes (Grinsted et al., 2008; Rahmstorf et al., 2011; Orlić and Pasarić, 2013). The data used for calibration of semi-empirical models has so far relied on the observational record (Rahmstorf, 2007; Vermeer and Rahmstorf, 2009) or has used palaeodata from the past 2 ka (Grinsted et al., 2008). This calibration range does not cover the full range of temperature estimates for the 21st century
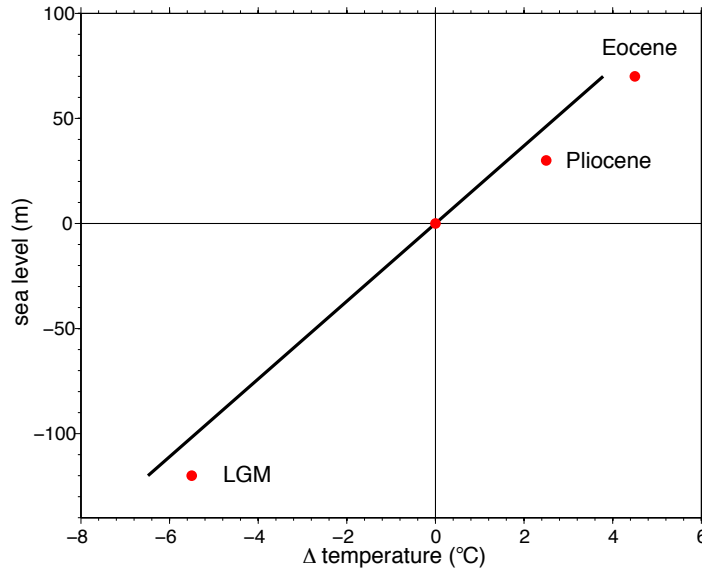
Figure 1.2: *Relationship between temperature and sea level on geological timescales, after Archer (2007). Data used are: LGM sea level 120 m below present (Fairbanks, 1989) and temperature 4-7 °C below present (Waelbroeck et al., 2002; Schneider von Deimling et al., 2006; Rahmstorf, 2007); Pliocene sea level 25-35 m above present and temperature 2-3 °C above present (Dowsett et al., 1994); Eocene sea level 70 m above present (i.e. ice-free conditions) (Miller et al., 2009b) and temperature 4-5 °C above present (Covey et al., 1996).*

and therefore future projections require extrapolation well outside of the range of calibration (Rahmstorf, 2007; Grinsted et al., 2008). There has so far been limited work on constraining the past form of the near-equilibrium temperature to sea level relationship for temperatures projected by the end of the 21st century (Rohling et al., 2009; Siddall et al., 2010a,b). The overall aim of this thesis is to explore the form of the past relationship between near-equilibrium temperature and sea level. Although we do not attempt to make any semi-empirical projections based on this relationship, due to large uncertainties in the presently available data and current lack of constraint on rates of sea level response, we do suggest plausible functional forms for this relationship.

Sea level response to temperature forcing over the past 0.5 Ma, a period predominantly cooler than present, has been studied in detail using proxy data from ice cores, ocean sediments, and fossil corals (Rohling et al., 2009; Siddall et al., 2010a,b). However, further back in time $(10^6 - 10^7$ years) which includes extended periods warmer than present, only modelled estimates

have been published (albeit constrained by deep-sea oxygen isotope data de Boer et al., 2010). In the first two chapters of this thesis, we will use existing proxy records from the past 50 Ma to investigate the relationship and uncertainties between temperature and sea level reconstructions during the transition to an 'ice-house' world.

### 1.1.2 Thesis aims and outline

The aim of the first two chapters of this thesis is to investigate what proxy data can tell us about the past relationship between temperature and sea level. We shall concentrate on the DST to sea level relationship for the past 50 Ma because the DST record is more complete than the surface temperature record. We will complement this analysis by investigating the surface temperature to sea level relationship over a key interval for sea level change, the Eocene-Oligocene transition (EOT; $\sim$34 Ma) which is generally considered the period when a continental-sized East Antarctic ice sheet first formed (e.g. Zachos et al., 2001a). We shall also investigate possible functions which can describe this relationship, which may have significance for future semi-empirical studies (e.g. Orlić and Pasarić, 2013).

The second aim of the thesis is to undertake new ice sheet model simulations of the large ice sheets which are present today or which have existed in the past (the East Antarctic, North American and Eurasian ice sheets); to compliment the data synthesis we will also present these results as temperature / sea level plots. In Chapter 3 we describe a method for performing long-duration ice sheet simulations. We then test this method by performing simulations of the Northern Hemisphere ice sheets which formed and then deglaciated during the relatively data-rich period of the last glacial cycle ($\sim$120 ka $-$ present).

To constrain the upper part (high temperatures and sea levels) of the temperature to sea level relationship we need to better understand the transition from ice-free conditions to partial glaciation. It is the aim of the the later chapters to investigate the formation of the East Antarctic ice sheet across the EOT and in particular whether small ice sheets could have existed in the warmth of the Eocene (which would have implications for the past temperature to sea level relationship towards higher temperatures). In Chapter 4 we perform an inter-model comparison investigating the atmospheric $CO_2$ thresholds for the onset of East Antarctic glaciation, with the aim of investigating the model dependancy of our results. In Chapter 5 we investigate ice sheet hysteresis and the different thresholds for glaciation and deglaciation. Ice sheet hysteresis may have implications for using temperature and sea level data from the Cenozoic, which over

long time-scales ($10^7$ years) represents a broad cooling (Lear et al., 2000), to make inferences about the future response of the ice sheets to a sustained warming (Pollard and DeConto, 2005). In Chapter 6 we aim to tie together our data synthesis with what we learn from ice sheet modelling. Finally in Chapter 7, we conclude with an overview of the main findings and suggest directions for future work. The remainder of this chapter and the next chapter was published in *Reviews of Geophysics* in 2012 (Gasson et al., 2012).

## 1.2 Proxy records

Long-duration ($10^7$ years) records of sea level, ice volume, and temperature over the past 50 Ma are limited to ocean sediment deposits. Although other proxy records exist (e.g., from isotope analysis of fossil tooth enamel (Zanazzi et al., 2007) or sediment records from an incised river valley (Peters et al., 2010)), these are of a too short duration for the purposes of this thesis. Long-term ($10^7$ years) records are presently limited to sequence stratigraphy records of sea level (Miller et al., 2005a), Mg/Ca proxy records of DST (Lear et al., 2000; Billups and Schrag, 2003), and records of oxygen isotopes ($\delta^{18}O$), which are a mixed climate signal (Zachos et al., 2001a). Other proxies, such as the tetraether index ($TEX_{86}$) and the alkenone unsaturation index ($U_{37}^{k'}$), have been used to create intermediate-duration ($10^6$ years) SST records (Bijl et al., 2009; Liu et al., 2009). We discuss each of these proxies in the following sections.

When looking at this long time period, the proxy record of surface temperature is limited in both duration and spatial coverage, although records are improving with the continued development of new and existing proxies (e.g. Lear et al., 2008; Liu et al., 2009). A limitation of using localised surface temperature proxies is that there are inherent uncertainties as to whether they actually represent regional and/or seasonal temperature fluctuations (Lear et al., 2000). These potential biases are reduced in the DST record, although the DST record has other significant limitations (Lear et al., 2000; Billups and Schrag, 2003). DST is coupled to SST at regions of deep-water formation, which for the present day are predominantly, although not exclusively (Gebbie and Huybers, 2011), the high latitudes (Zachos et al., 2001a). Therefore, DST proxies should not be seen as a pure record of past global temperature but should instead be viewed as analogous to past high-latitude surface temperature (Zachos et al., 2001a). The DST record is useful when investigating the sea level to temperature relationship, as it is best coupled to the surface at regions of ice formation. Over the past 50 Ma there have been major tectonic changes, such as the uplift of the Himalaya following the collision of India with Asia, the opening

of the Drake and Tasman passages, and the closing of the Panama seaway, which have all had an influence on the climate system (Zachos et al., 2001a).

### 1.2.1 Sequence stratigraphy: a sea level proxy

Sequence stratigraphy of passive continental margins can provide a record of regional sea level over the past 50 Ma and even longer timescales (Vail et al., 1977; Haq et al., 1987; Miller et al., 2005a; Kominz et al., 2008). Depositional sequences bounded by unconformities (periods of nondeposition and/or surfaces of erosion) show changes in regional sea level. By accurately dating sequences and inferring the past water depth during depositional phases from lithofacies and biofacies models, a quantitative estimate of sea level through time can be created (Miller et al., 1998, 2005a; Kominz et al., 2008; Browning et al., 2008).

Vail et al. (1977) developed a method for inferring global sea level by correlating sequences from multiple depositional basins. This work led to the production of the "Haq curve", which was claimed at the time to be a global eustatic record of sea level (Haq et al., 1987). Miall (1992) was critical of the approach used by Haq et al. (1987) as it assumes that the dating of sequences is accurate enough to allow for correlation across multiple depositional basins. However, the duration of some of the sequences is often less than the age error estimate. Miall (1992) demonstrated that sequences created using a random number generator with the same age errors could generate a good correlation with the Haq curve. It is unclear whether the sequences are the result of a global sea level signal or generated by regional processes, making correlation across multiple basins questionable (Christie-Blick et al., 1988). Other criticism has focused on the lack of availability of data that made up the Haq curve, meaning that independent verification of the record is not possible (Miall, 1992). Given these fundamental weaknesses, (Miall, 1992) suggested that the Haq curve in particular should be abandoned and efforts should be focused on independent well-dated records, such as those discussed in the following.

Within the last 15 years, multiple well-dated sediment cores from one region, the New Jersey (NJ) margin in the northeastern United States, have been used to create a sequence stratigraphy record of sea level over the past $100 - 10$ Ma (see Figure 1.3). Sea level for $9 - 0$ Ma in the study by Miller et al. (2005a) is estimated from a calibration of the $\delta^{18}$O record as the NJ sequence stratigraphy record is incomplete from $7 - 0$ Ma (Miller et al., 2005a; Kominz et al., 2008). By taking into account compaction, loading, and subsidence of the sediment core (the backstripping method), a regional sea level record was created (Browning et al., 2008). The

sequences are dated using a combination of biostratigraphy, magnetostratigraphy, and strontium isotope stratigraphy, providing age control better than $\pm 0.5$ Ma (Kominz et al., 2008), which is a significant improvement on the $\pm 3$ Ma age errors of the Haq curve (Miall, 1992).

When regional sea level drops below the level of the core hole site, there is a hiatus in the record, identified as an unconformity. This is a potential limitation of sequence stratigraphy because it means water depth information is restricted during lowstands. This is overcome in part by having multiple core hole locations from both onshore and offshore sites; however, there are still significant hiatuses in the composite record during lowstands. Although a quantitative record of water depth is limited during lowstands, it is likely that sea level was lower than surrounding highstands given the lack of sediment deposition. As shown in Figure 1.3, Kominz et al. (2008) provide conceptual lowstands, which highlight that sea level is lower during periods when there are no deposits; errors during these periods are significantly higher than during highstands. Here we assume generous errors of $\pm 50$ m during lowstands, based on the highest error estimate of Miller et al. (2005a). The highstand sea level estimate has an associated water depth error. The errors generally increase with increasing water depth; highstand errors for the NJ sea level record are typically $\pm 10 - 20$ m (Miller et al., 2005a).

As shown in Figure 1.3, the NJ record shows a long-term fall in sea level of $\sim 100$ m over the course of the past 50 Ma, which is greater than can be explained by the formation of the modern ice sheets (Kominz et al., 2008; Miller et al., 2009b). Estimates of the total amount of ice stored in the modern ice sheets, in terms of sea level equivalence (ice volume divided by the ocean area and accounting for the change in volume with change in state from ice to seawater), vary from $64 - 80$ m (Lythe and Vaughan, 2001; Bamber et al., 2001; Miller et al., 2005a; Lemke et al., 2007). However, this is not directly relatable to the NJ sea level record.

If this additional mass of water was added to the oceans, it has been suggested that it would have an isostatic effect (hydroisostasy), meaning that the sea level rise visible from NJ may be $\sim 33$ % less (Pekar et al., 2002; Miller et al., 2009b). This assumes that the added water weight would lead to a global subsidence of the crust into the mantle (based on a simple "Airy" loading based on the density of the mantle ($3.18$ g cm$^{-3}$) divided by the density of the mantle less the density of seawater (Kominz and Pekar, 2001)). It should be noted that this simple hydroisostatic correction is not universally accepted (e.g., Cramer et al., 2011) and that regional isostatic effects (discussed later) may be more important. Cramer et al. (2011) use the corrected and uncorrected NJ record as plausible end-members.
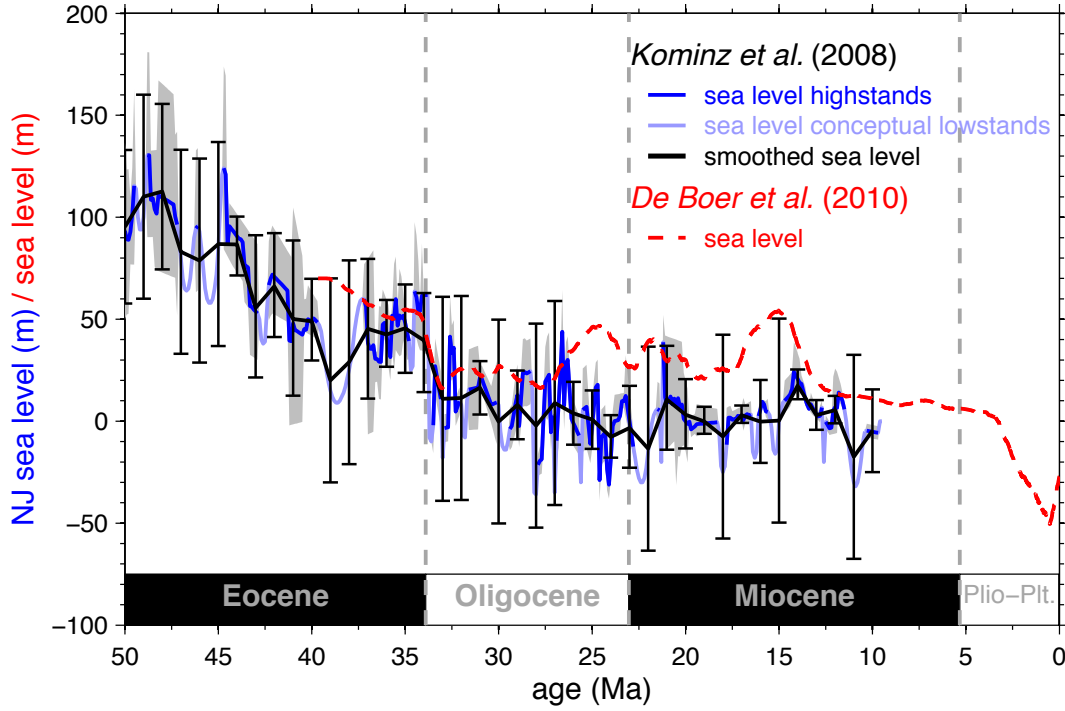
Figure 1.3: *Sea level time series from 50 to 0 Ma. Kominz et al. (2008) regional sequence stratigraphy sea level data from the New Jersey margin (50-10 Ma), showing highstand data and "conceptual" low-stands (blue lines). Smoothed sea level data using a center-weighted running mean with a window size of ±0.5 Ma and interpolated to a 1 Ma temporal resolution (black line). Highstand errors (gray band) are from Kominz et al. (2008); lowstand errors shown here are ±50 m, based on the highest error estimate of Miller et al. (2005a). de Boer et al. (2010) sea level (red dashed line) was modelled using observation-constrained forward modelling with benthic foraminifera $\delta^{18}O$ data as input (Zachos et al., 2008).*

If we do assume full hydorisostatic adjustment, only $\sim 43 - 54$ m of the long-term fall in the NJ record can be explained by the formation of the modern ice sheets (Pekar et al., 2002; Miller et al., 2005a). Assuming that DSTs have cooled by $\sim 12\,°C$ over the past 50 Ma (see 1.2.2; Lear et al., 2000; Zachos et al., 2001a), $\sim 12$ m can be explained by thermosteric sea level fall (Miller et al., 2009b). This leaves an additional sea level fall, which could reasonably be explained by an increase in ocean basin volume (Miller et al., 2009b).

Ocean crust production rates may have decreased since the early Cenozoic (Xu et al., 2006). Because seafloor becomes deeper as it ages, slower ocean crust production rate effectively increases ocean basin volume (Xu et al., 2006). This is not consistent with the results of Rowley (2002), which suggested ocean crust production rates, and therefore ocean basin volume, have not varied significantly over the past 180 Ma. Cramer et al. (2011) attempted to separate

the ice volume component of the NJ sea level record from the ocean basin volume component by assuming that all sea level change above the ice-free level (64 m, or 43 m if corrected for hydroisostatic effect; Pekar et al., 2002) is due to changes in ocean basin volume. They then removed the low frequency sea level signal above this ice-free level. By making this correction it implies that the sea level record when sea level is below the ice-free level is not contaminated by an ocean basin volume signal (Cramer et al., 2011). Note that we do not make this correction here and choose to show the raw record as we believe it is a better representation of the potential sources of error in the record. Müller et al. (2008) reconstructed ocean basin volume using marine geophysical data. Their data did suggest a decrease in sea level caused by an increase in ocean basin volume since 50 Ma of ∼20 m. It should be noted that their reconstruction significantly differs from the NJ record on longer timescales (Müller et al., 2008), as discussed below. This combined total of ∼75 − 86 m does not close the long-term NJ sea level budget and may suggest that the record contains other controls in addition to global sea levels due to changes in ocean volume.

For multiple reasons, a sea level record from any single coastal area should be viewed as a record of regional sea level rather than a record of global eustatic sea level (Kominz et al., 2008). This is because in addition to sea level changes resulting from the movement of water to and from storage as ice on land, the variation in the ocean basin volume, and the thermal expansion of water, there are regional effects that may be recorded (Pekar et al., 2002). If a continental plate moves vertically, e.g., as a result of ice loading, this will be seen as a sea level change in the record (Peltier, 1974). Isostasy due to ice loading will not have affected the NJ record over the period of 100 − 10 Ma as it is unlikely that large-scale North American glaciation occurred prior to the Plio-Pleistocene (e.g. Zachos et al., 2001a). Even though the margin has subsequently been subject to isostasy, the preserved record of water depth was formed free from a glacioisostatic signal. However, there are other tectonic effects that may pose a challenge to the sequence stratigraphy method and that may be contained in the NJ sea level record (Kominz et al., 2008).

It has been suggested that northeast America has subsided since the Late Cretaceous, as the continent over-rode the subducted Farallon slab (Conrad et al., 2004; Spasojević et al., 2008). This would have been synchronous with declining sea level since the Late Cretaceous highstand, having the effect of masking some of the sea level decline in the NJ record (Müller et al., 2008). This subduction could explain the discrepancy between the sea level estimates of Müller et al. (2008), based on the reconstruction of basin volume from geophysical data, and the NJ record

of Miller et al. (2005a). If the NJ margin did subside because of this mechanism, it would only affect the sea level record on long timescales ($10^7 - 10^8$ years). This should be too slow to be confused with the more rapid glacioeustatic signal in the record (Miller et al., 2005a), but it may still have contributed to the broad sea level trend of the last 50 Ma.

More recently, Petersen et al. (2010) suggested that on intermediate timescales ($2 - 20$ Ma) small-scale convection in the mantle could generate vertical plate movements. Using a 2-D thermomechanical model, Petersen et al. (2010) demonstrated that vertical plate movements on the order of $\sim$30 m were possible on intermediate timescales. Such convective cycles could generate sedimentary deposits, due to variations in water depth, which could be misinterpreted as being caused by eustatic sea level fluctuations (Petersen et al., 2010).

Another potential source of local sea level change in the NJ record is due to gravitational and Earth rotational effects. There is a gravitational effect between an ice sheet and the surrounding ocean that influences relative sea levels on a global scale (Mitrovica et al., 2001, 2009; Raymo et al., 2011). Because of this gravitational effect, when a large ice sheet melts its mass is not evenly redistributed across the oceans. Sea level local to an ice sheet can therefore fall once the ice sheet has melted (Mitrovica et al., 2001, 2009). If the Antarctic ice sheet melted, for the NJ region the local sea level change would be greater than if the volume were evenly distributed across the oceans. In addition to the gravitational effect there are other feedbacks from this redistribution of mass, through influences on the Earth's rotation and solid Earth deformation (Mitrovica et al., 2001, 2009). As there have been large changes in the size of the ice sheets, this gravitational effect will be present in the NJ record and is another source of uncertainty.

In order to test the NJ sequence stratigraphy record, additional sea level curves from well-dated deposits from multiple regions need to be generated. The NJ sequence stratigraphy record should be viewed as a regional sea level record that needs to be tested with additional data from other locations. Sequence stratigraphy data from the Russian platform agree well with the NJ record (Sahagian and Jones, 1993), although the Russian platform data are only for the Late Cretaceous and earlier. When applied to the late Pleistocene ($130 - 10$ ka), the sequence stratigraphy sea level record from NJ compares well against other sea level proxies, such as fossil corals (Wright et al., 2009). Additional sequence stratigraphy records are being assembled from expeditions to Australia and New Zealand, and this should provide further tests for the NJ record (Kominz et al., 2008; John et al., 2011). Results from the northeastern Australian margin show large amplitude sea level changes in the Miocene, with events at 14.7

Ma and 13.9 Ma showing a larger sea level change than is evident in the NJ record (John et al., 2011). A recent record from southeast Australia provides an independent sea level record for part of the Oligocene ($32 - 27$ Ma; Gallagher et al., 2012). This record shows some similarities with the NJ record, although the lack of lowstand deposits in the NJ record limits a direct comparison. Additional differences between the record of Gallagher et al. (2012) and the NJ record may be due to different glacio-isotatic responses due to relative proximities to the East Antarctic ice sheet (Gallagher et al., 2012).

### 1.2.2 Temperature Proxies

Proxy methods for calculating palaeo-SSTs include the tetraether index ($TEX_{86}$) (Wuchter et al., 2004), the alkenone unsaturation index $U^{k'}_{37}$ (Brassell et al., 1986), and the Mg/Ca ratio of planktic (surface-dwelling) foraminifera. The Mg/Ca proxy can also be used for benthic (bottom-dwelling) species of foraminifera to calculate DSTs (Nurnberg et al., 1996). Long-timescale ($10^7$ years) temperature records are currently limited to Mg/Ca records of benthic foraminifera (Lear et al., 2000; Billups and Schrag, 2003); for intermediate timescales ($10^6$ years) there are additional DST records using Mg/Ca and SST records using all of the proxies mentioned above for multiple regions over a variety of time periods. We do not cover all of the time periods where intermediate timescale records are available but focus on the EOT as this is a major period of ice sheet expansion and sea level change.

#### 1.2.2.1 Mg/Ca Temperature Proxy

Magnesium ions ($Mg^{2+}$) can be incorporated into the calcite ($CaCO_3$) tests of foraminifera, substituting for calcium; the amount incorporated shows a temperature-dependent relationship (Nurnberg et al., 1996). Both core top samples and culturing experiments show that the Mg/Ca ratio of foraminiferal calcite increases with water temperature (Nurnberg et al., 1996; Rosenthal et al., 1997; Lea et al., 1999; Anand et al., 2003). The Mg/Ca ratios of suitable species of both benthic and planktic foraminifera can therefore be used as a proxy of DST and SST, respectively.

A potential source of error in the Mg/Ca proxy, which is also relevant to other stable isotope proxies using foraminifera, is postmortem changes to the geochemical signal (diagenesis) (Savin and Douglas, 1973; Brown and Elderfield, 1996; Rosenthal et al., 2000; Sexton et al., 2006; Lear, 2007). This source of error can be minimised by carefully selecting well-preserved samples, using multiple proxies, correcting for known effects, and rejecting samples that are at high risk to

15

diagenetic processes (Rosenthal et al., 2000; Rosenthal and Lohmann, 2002; Sexton et al., 2006; Lear, 2007). Billups and Schrag (2003), however, suggest that perhaps the largest source of uncertainty in the Mg/Ca palaeo-temperature proxy is due to temporal changes in the seawater Mg/Ca ratios from changes in $Mg^{2+}$ and $Ca^{2+}$ cycling in the oceans, as discussed below.

Because of the residence times of $Mg^{2+}$ and $Ca^{2+}$ ions in the oceans of $\sim$10 Ma and $\sim$1 Ma, respectively, when used on long timescales ($10^7$ years), the absolute Mg/Ca temperature estimates may contain errors (Lear et al., 2000; Billups and Schrag, 2003; Lear, 2007). To account for this, the Mg/Ca temperature estimates can be corrected for variations in seawater Mg/Ca (Lear et al., 2000; Lear, 2007; Creech et al., 2010).

Reconstruction of past seawater Mg/Ca can be made through proxy measurements or mass balance modelling. Lowenstein et al. (2001) reconstructed past seawater Mg/Ca using fluid inclusions in marine halites. Their data suggest that seawater Mg/Ca has increased over the past 50 Ma from initial values of $2.5 - 3.5$ mol mol$^{-1}$ to the present-day value of 5.2 mol mol$^{-1}$. This was slightly higher than the reconstructed estimate of $\sim$2 mol mol$^{-1}$ at 50 Ma using fossil enchinoderms (Dickson, 2002). This lower estimate was supported by an alternative reconstruction using measurements of $CaCO_3$ veins recovered from oceanic crust. These estimates suggest seawater Mg/Ca was relatively constant prior to 24 Ma at $1.5 - 2.5$ mol mol$^{-1}$ before increasing toward the modern value (Coggon et al., 2010). Mass balance modelled estimates of past seawater Mg/Ca vary, with one model suggesting that ratios increased approximately linearly from a relatively high value of 3.85 mol mol$^{-1}$ at 50 Ma (Wilkinson and Algeo, 1989). To account for this variability, the Mg/Ca palaeo-temperatures can be calculated using these different seawater Mg/Ca scenarios (Lear, 2007).

Creech et al. (2010) looked at multiple SST proxies in the early Eocene, including Mg/Ca and $TEX_86$. They used various seawater Mg/Ca scenarios and suggested a lower limit for seawater Mg/Ca of $\sim$2 mol mol$^{-1}$ in the early Eocene (with preferred scenarios ranging from $2.24 - 3.35$ mol mol$^{-1}$ in order to reconcile the Mg/Ca SSTs with $TEX_{86}$ SSTs (Creech et al., 2010)). Because of these uncertainties regarding the past seawater concentration of Mg/Ca, absolute Mg/Ca temperatures on long timescales ($10^7$ years) should be interpreted with caution (Billups and Schrag, 2003; Lear, 2007). The Mg/Ca proxy is much more reliable when looking at relative Mg/Ca temperature changes over shorter ($10^6$ years) intervals (Lear, 2007).

Lear et al. (2000) created a DST record from Mg/Ca ratios of benthic foraminifera from four sites. This provided a record of DSTs over the past 50 Ma, with an age resolution of $\sim$1

Ma. Lear (2007) calculated a window of DST estimates, based on the data of Lear et al. (2000) (shown in Figure 1.4), using seawater Mg/Ca varying from 1.5 mol mol$^{-1}$ to 5.2 mol mol$^{-1}$ at 50 Ma, which then linearly increases to present day. The modelled seawater Mg/Ca estimate of Wilkinson and Algeo (1989) produces Eocene DSTs that are in closest agreement with oxygen isotope records assuming an ice-free world, although this benthic $\delta^{18}O$ temperature estimate also contains an associated error due to uncertainties in estimating the $\delta^{18}O$ of seawater for an ice-free world.

Evans and Müller (2012) recently suggested an additional source of uncertainty which also explains why using the modelled Mg/Ca seawater estimate of Wilkinson and Algeo (1989) produces a close agreement with the oxygen isotope records, despite the Wilkinson and Algeo (1989) Mg/Ca seawater ratio being higher than all of the independent reconstructions listed above. The correction for changes in the seawater Mg/Ca ratio discussed above assumes a linear relationship between the Mg/Ca ratio of the calcite test and seawater Mg/Ca (e.g. Lear, 2007). More recent culturing studies have suggested that this relationship is better described by a power law (Hasiuk and Lohmann, 2010; Evans and Müller, 2012). Evans and Müller (2012) suggest that two incorrect assumptions, namely a relatively high value for the Mg/Ca ratio of seawater at 50 Ma and a linear relationship between Mg/Ca of calcite and Mg/Ca of seawater, effectively cancel out to provide a reasonable agreement with the temperature estimates from the oxygen isotope record assuming an ice-free world. More culturing studies are required to provide a more accurate calibration between Mg/Ca of calcite and Mg/Ca of seawater (Evans and Müller, 2012).

Since the early work of Lear et al. (2000), there have been numerous higher-resolution benthic Mg/Ca records published, spanning various portions of the Cenozoic. For example, Billups and Schrag (2003) used the Mg/Ca proxy to obtain DST records over the past 50 Ma from Ocean Drilling Program (ODP) Sites 757 and 689. Additional palaeogene (65.5 − 23 Ma) Mg/Ca records include those from Pacific ODP Sites 1218 and 1209 (Lear et al., 2004; Dutton et al., 2005; Dawber and Tripati, 2011), and additional Neogene (23 − 0.05 Ma) records include those from ODP Sites 761 and 1171 (Shevenell et al., 2008; Lear et al., 2010).

#### 1.2.2.2   Surface Temperature Proxies: TEX$_{86}$ and $U^{k'}_{37}$

Alkenones are highly resistant compounds found in sediments from all of the ocean basins and preserved in sediments spanning back to the Eocene and even earlier (Boon et al., 1978;

Marlowe et al., 1990; Muller et al., 1998). They are synthesized by a very limited number of species of phytoplankton, such as the widespread *Emiliania huxleyi* in the modern ocean (Volkman et al., 1980; Marlowe et al., 1990). The reason alkenones are synthesized by these species of phytoplankton remains unknown (Conte et al., 1998; Herbert, 2003). The degree of unsaturation in the alkenone molecules, i.e., the number of double bonds, correlates with the temperature at synthesis (Marlowe, 1984). The degree of alkenone unsaturation was used in a pioneering study to show late Pleistocene climate cycles (Brassell et al., 1986). A simplified alkenone unsaturation index ($U^{k'}_{37}$) was developed as a measure of the degree of alkenone unsaturation and then calibrated to temperature, from laboratory culturing studies and core top analysis (Prahl and Wakeham, 1987; Sikes et al., 1991; Muller et al., 1998). The index can be used for temperatures ranging from $\sim 1 - 28$ °C, meaning that it cannot be used for extremely cool or warm regions and climates (Herbert, 2003). As alkenones are well preserved in ocean sediments, the alkenone unsaturation index is a useful proxy for past SST, although we note that high temperatures at low latitudes might be particularly challenging (Brassell et al., 1986; Prahl and Wakeham, 1987; Muller et al., 1998; Liu et al., 2009; Herbert et al., 2010).

The modern producers of alkenones have evolved relatively recently. For example, the species *E. huxleyi* evolved in the late Pleistocene, although alkenones are found in much older sediments (Marlowe et al., 1990). This has implications for using the $U^{k'}_{37}$ index further back in time, as the index is calibrated against alkenone samples produced by modern species of phytoplankton (Herbert, 2003). A morphologic study suggested that modern alkenone producers share a common evolutionary pathway, evolving from, or belonging to, the same family, Gephyrocapsaceae, dating back to at least the Eocene, $\sim 45$ Ma. The relationship between producers of alkenones in even older sediments, from the Cretaceous, and modern species is less well understood (Marlowe et al., 1990). Furthermore, the form of alkenones found in these older sediments differs from modern alkenones (Herbert, 2003). The $U^{k'}_{37}$ index has been used to estimate SST for the Eocene (Bijl et al., 2010), although it is unlikely that the index would remain valid on even older sediments (Herbert, 2003).

In addition to temperature, the degree of alkenone unsaturation also shows sensitivity to other factors, such as light (Prahl et al., 2003). Modern producers of alkenones live at various depths in the photic zone, and alkenones produced at greater depths could generate $U^{k'}_{37}$ temperatures cooler than the annual mean SST (Prahl et al., 2001). Additionally, the production rate of alkenones varies over an annual cycle, typically peaking in the spring or summer months, meaning that temperatures may not represent the mean annual temperature but may be slightly

biased to warmer months (Prahl et al., 1993; Sprengel et al., 2000). This seasonal bias generally increases with increasing latitude (Sikes et al., 1997; Ternois et al., 1998; Herbert, 2003; Sikes et al., 2009). The potential impacts of these external factors have been studied in detail through culturing studies, performing core top analysis, and using sediment traps (Herbert, 2003).

More recently, another organic palaeothermometer has been developed, based on the composition of the membrane lipids of Thaumarchaeota (formerly classed as Crenarchaeota; Brochier-Armanet et al., 2008), a group of single celled microorganisms. One group of membrane lipids biosynthesized by Thaumarchaeota are glycerol dialkyl glycerol tetraethers (GDGTs; Schouten et al., 2002). The number of cyclopentane rings in the GDGTs shows a strong correlation with temperature at synthesis (Schouten et al., 2002; Wuchter et al., 2004). It is thought that Thaumarchaeota can change the relative amounts of the different GDGTs (containing different numbers of cyclopentane rings) in their membranes, to allow changes to the membrane lipid fluidity, in response to changing temperature (Sinninghe Damsté et al., 2002). The $TEX_{86}$ index was developed as a measure of the relation between the distribution of GDGTs and the temperature at synthesis (Schouten et al., 2002; Wuchter et al., 2004). The calibration has been further refined, although there is still debate as to what calibration is most appropriate, especially at extremely high ($>30$ °C) and low ($<5$ °C) temperatures (Kim et al., 2008; Liu et al., 2009; Kim et al., 2010). The main advantages that the $TEX_{86}$ proxy has over the $U^{k'}_{37}$ proxy are that it can be used for higher temperatures than $U^{k'}_{37}$ and can be used further back in time, when low alkenone concentrations and uncertainties over the evolution of alkenone producers limit the use of the $U^{k'}_{37}$ proxy.

Although the $TEX_{86}$ proxy has some advantages over the $U^{k'}_{37}$ proxy, it also has significant weaknesses. Thaumarchaeota are not restricted to the photic zone but are distributed throughout the ocean depths (Karner et al., 2001). Therefore, it seems unusual that the $TEX_{86}$ index shows such a strong correlation with SST (Huguet et al., 2006). The cells of Thaumarchaeota are too small to sink to the ocean floor postmortem; therefore, the $TEX_{86}$ signal must be transported to the ocean sediments in another way. A likely mechanism is that Thaumarchaeota are consumed and the $TEX_{86}$ signal is incorporated into marine snow. As most food webs are active in the upper ocean, this would also explain why $TEX_{86}$ is well correlated with SST (Wuchter et al., 2005, 2006; Huguet et al., 2006). Support for this interpretation comes from sediment traps set up at different depths, with measurements from deeper sediment traps reflecting SST rather than the ambient ocean temperature (Wuchter et al., 2005, 2006). A core top calibration using samples from multiple regions and ocean depths suggested that the $TEX_{86}$

signal is strongly coupled to mixed layer temperatures, at depths of $0 - 30$ m (Kim et al., 2008). However, another study suggested TEX$_{86}$ temperatures cooler than actual SST, implying that for certain regions the TEX$_{86}$ signal might originate in the subsurface (Huguet et al., 2007).

Potential seasonal biases affect the TEX$_{86}$ proxy as well as the $U^{k'}_{37}$ proxy. Sediment trap studies suggest that the peak concentration of GDGTs occurs in the winter and spring months (Wuchter et al., 2005), but when the TEX$_{86}$ index is applied in sediment trap and core top studies the signal appears to be predominantly an annual mean (Wuchter et al., 2005; Kim et al., 2008). Both TEX$_{86}$ and $U^{k'}_{37}$ may be subject to alteration due to diagenesis (Huguet et al., 2009) and contamination from secondary inputs (Thomsen et al., 1998; Weaver et al., 1999; Weijers et al., 2006), although the diagenetic pathways differ (Liu et al., 2009). Alkenones can be transported laterally and can also be recycled from sediments, placing fossil alkenones or alkenones synthesised in different environments onto core tops and potentially biasing $U^{k'}_{37}$ temperature estimates (Thomsen et al., 1998; Weaver et al., 1999). GDGTs are also found in soils and can be transported to ocean basins by rivers, potentially affecting the TEX$_{86}$ proxy for sites near river outflow (Weijers et al., 2006). To improve SST estimates and to reduce the impact of secondary effects on temperature signals, it is desirable to use multiple proxies whenever possible (Liu et al., 2009).

### 1.2.2.3  Temperature time series

Figure 1.4 shows different temperature records generated using the proxies discussed above, including the Mg/Ca DST record of Lear et al. (2000) and high- and low-latitude SST records for the EOT (Lear et al., 2008; Liu et al., 2009). Although existing Mg/Ca DST records show a net cooling throughout the Eocene, at face value they show either no significant cooling or even warming at the EOT (Lear et al., 2000; Billups and Schrag, 2003; Lear et al., 2004; Peck et al., 2010; Pusz et al., 2011). This is not consistent with the cooling that might be expected during a period of rapid ice growth (Coxall and Pearson, 2007). The lack of cooling in the Mg/Ca records at the EOT initially led to the hypothesis that the majority of the oxygen isotope $\delta^{18}$O shift at the EOT is due to an increase in ice mass (Lear et al., 2000) (also see Section 1.2.3 on $\delta^{18}$O). This would necessitate the growth of a greater ice mass than could be accommodated on Antarctica, implying that Northern Hemisphere ice sheets formed much earlier in the Cenozoic than previously thought (Coxall et al., 2005). Additional evidence for Northern Hemisphere glaciation (albeit as isolated glaciers) much earlier in the Cenozoic was

found in ice-rafted debris (IRD) deposits from the Arctic Ocean (Moran et al., 2006) and off the coast of Greenland (Eldrett et al., 2007). However, it has also been shown that Antarctic land area at the EOT could have been greater than at present, meaning that more of the $\delta^{18}O$ increase can be explained by the growth of Antarctic ice in combination with cooling (Wilson and Luyendyk, 2009). In addition, modelling studies suggest that atmospheric $CO_2$ concentrations were above the threshold for bipolar glaciation at this time (DeConto et al., 2008).

More recently, the lack of apparent cooling witnessed in the deep-sea EOT Mg/Ca records has been attributed to secondary effects in the Mg/Ca proxy related to the synchronous deepening of the calcite compensation depth (CCD) (Lear et al., 2004; Coxall et al., 2005). In addition to the dominant control on Mg/Ca ratios recorded in foraminifera, changes in temperature, the ratio is also affected by the degree of carbonate saturation of seawater (Martin et al., 2002). This secondary control could become significant during large changes in carbonate saturation, such as the lowering of the CCD at the EOT (Lear et al., 2004).

Support for this hypothesis is found from Mg/Ca data from a shallow water site well above the palaeo-CCD, which show a ~2.5 °C cooling across the EOT (shown inset in Figure 1.4; Lear et al., 2008). Additional evidence for this explanation is found in other deep-sea, surface, and terrestrial temperature proxies that also show a cooling across the EOT (Dupont-Nivet et al., 2007; Zanazzi et al., 2007; Katz et al., 2008; Liu et al., 2009; Eldrett et al., 2009). Liu et al. (2009) undertook a modelling study based on their surface temperature results in order to estimate deep-sea cooling. The model was able to reproduce the observed high-latitude surface cooling (~5 °C), and their model generated a deep-sea cooling of ~4 °C across the EOT. This deep-sea cooling could be even greater as Liu et al. (2009) suggest their (~5 °C) high-latitude surface cooling may be a low estimate. Recent work attempting to correct for the simultaneous influence of changing seawater saturation state on the EOT deep-sea Mg/Ca records implies a deep-sea cooling on the order of 1.5 °C, although this estimate will likely be refined as understanding of trace metal proxies advances (Lear et al., 2010; Pusz et al., 2011). This 1.5 °C of deep-sea cooling across the EOT is considerably less than the modelled deep-sea cooling suggested by Liu et al. (2009).

Although the modelling study of DeConto et al. (2008) did not support bipolar glaciation at the EOT, it did suggest that, based on the proxy $CO_2$ records of Pearson and Palmer (2000) and Pagani et al. (2005), the $CO_2$ threshold for bipolar glaciation was crossed ~25 Ma, meaning that ephemeral Northern Hemisphere ice sheets may have been present much earlier than previously
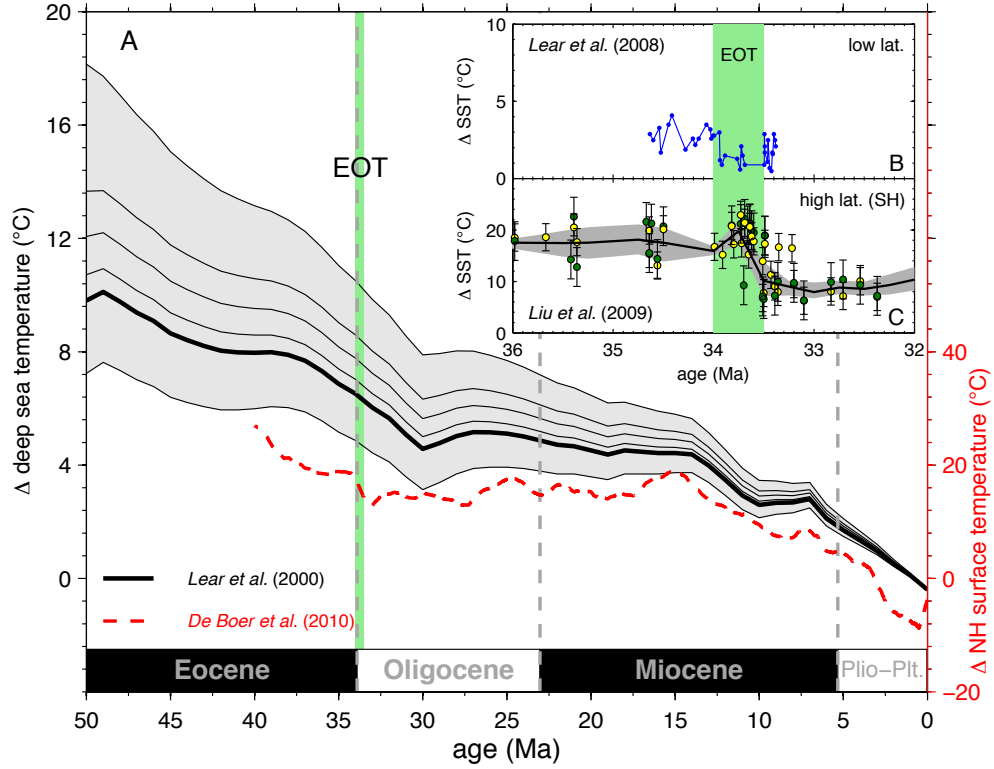
Figure 1.4: *Temperature time series for both deep-sea and surface temperatures. (a) Both deep-sea temperature from Mg/Ca of benthic foraminifera (Lear et al., 2000) (black lines) and Northern Hemisphere surface temperature from observation-constrained forward modelling (de Boer et al., 2010) (red dashed line). de Boer et al. (2010) temperature is scaled so that it can be read on both axes using the deep-sea to Northern Hemisphere surface temperature parameter of de Boer et al. (2010). The error envelope for Lear et al. (2000) data is for different seawater Mg/Ca scenarios from a constant scenario (low estimate) to a linearly increasing seawater Mg/Ca concentration from a value of 1.5 mol $mol^{-1}$ at 50 Ma (high estimate) to present day. The thick line is the best estimate scenario of Lear et al. (2000) for a seawater Mg/Ca value at 50 Ma of 3.85 mol $mol^{-1}$ linearly increasing to present. (b) EOT low-latitude sea surface temperature from Mg/Ca of planktic foraminifera from Tanzania (Lear et al., 2008), shown here as an anomaly relative to a modern SST value of 27.1°C, taken from the coast immediately to the east of the core site. (c) EOT high-latitude Southern Hemisphere sea surface temperature, from $TEX_{86}$ (green dots) and $U^{k'}_{37}$ (yellow dots). Data are shown as an anomaly relative the modern SST for the palaeo-location of each site (Liu et al., 2009, supplementary information); this differs from the work by Liu et al. (2009), where the data are presented as an anomaly relative to the pre-EOT mean for each site and includes additional Northern Hemisphere high-latitude sites. The best fit is calculated using a local weighted regression, with a weighting of 15%.*

thought. This potentially means that some of the sea level variations during the Miocene could be explained by changes in Northern Hemisphere ice mass. However, this is not consistent with the modelling work of de Boer et al. (2010, 2012a), who suggested that the threshold for Northern Hemisphere glaciation was not reached in this period and that sea level variation in the Miocene was caused by the Antarctic ice sheets.

The high-latitude SST record of Liu et al. (2009) is shown in Figure 1.4. The cooling shown in Figure 1.4 at the EOT is greater than the ∼5 °C of cooling suggested by Liu et al. (2009) in their original analysis. Liu et al. (2009) presented the data as a temperature anomaly relative to the mean temperature for each site prior to the EOT. The data are shown here as a temperature anomaly relative to modern temperatures at the palaeo-location for the respective sites (Liu et al., 2009, supplementary information). Only Southern Hemisphere sites are included to allow comparison with Pleistocene Southern Hemisphere data in the later analysis.

The surface temperature records in Figure 1.4 show pre-EOT temperatures significantly warmer than present in the Southern Hemisphere high latitudes and temperatures only a few degrees warmer in the low latitudes. This reduced latitudinal temperature gradient (which is even more pronounced in the early Eocene (Bijl et al., 2009)) presents a paradox: to explain the very warm temperatures in the high latitudes suggests increased heat transport from the equator to the poles; however, the reduced temperature gradient evident from data implies a reduced transport of heat from the equator to the poles (Huber, 2008). A full exploration of this paradox is beyond the scope of this thesis, but it should be noted that this reduced latitudinal temperature gradient in the Eocene remains a significant area of disagreement between data and climate models (Hollis et al., 2009; Lunt et al., 2012).

The Lear et al. (2000) DST record shows little temperature variation during the early Miocene, before a gradual cooling at ∼15 Ma that continues into the Pliocene. This is partly because the resolution of this record is particularly low in the Miocene and is unable to pick out the DST variations observed in higher-resolution Mg/Ca records (Shevenell et al., 2008; Lear et al., 2010). Other palaeoclimate proxies, notably the $\delta^{18}O$ record from benthic foraminifera (see 1.2.3), suggest deep-sea warming and/or a decrease in ice volume into the Miocene followed by deep-sea cooling and/or an increase in ice volume from the middle to late Miocene (Zachos et al., 2008). Regional terrestrial palaeoclimate proxies also show a return to a warmer climate in the middle Miocene followed by cooling in the late Miocene (Utescher et al., 2007, 2009, 2011). A prominent example of the effect of terrestrial warming into the Miocene is the

change in distribution of crocodilians, which after being restricted to the lower latitudes during the Oligocene, returned to higher latitudes of North America in the Miocene. On the basis of modern climate distributions of crocodilians, the fossil crocodilian record suggests terrestrial warming in the Miocene following on from a cooler period in the Oligocene (Markwick, 1998). Modelling studies, although not fully consistent with proxy data, have also simulated the warmth of the middle Miocene followed by cooling to the late Miocene (Micheels et al., 2007; You et al., 2009).

The temporal resolution of the Lear et al. (2000) data set is also too low to resolve the glacial-interglacial cycles of the Quaternary. In the next chapter we will focus on the data set of Lear et al. (2000) for the period $50 - 10$ Ma because of its long duration and as it appears to pick out the broad DST variations of the Cenozoic, although we acknowledge the limitations of this low-resolution multisite data set. Although the Lear et al. (2000) record does not show a pronounced cooling at the EOT, it does not show a warming as the Billups and Schrag (2003) record does, which subsequent records suggest is unlikely (Dupont-Nivet et al., 2007; Zanazzi et al., 2007; Lear et al., 2008; Liu et al., 2009; Lear et al., 2010). Additionally, the Billups and Schrag (2003) data from the Indian Ocean (ODP 757) show little DST variation from the Miocene onward and generates unrealistically high DSTs for the Plio-Pleistocene. We supplement our analysis with the higher-resolution SST data sets (Lear et al., 2008; Liu et al., 2009) across the EOT.

### 1.2.2.4 Deep-sea to surface temperature gradient

Surface temperature changes reach the deep sea primarily at regions of deep-water formation, which is predominantly in the high-latitude regions (Zachos et al., 2001a). DST records are therefore suited to a review of the relationship between temperature and sea level as DST is strongly coupled to the surface climate at regions of ice formation. However, the coupling between the deep sea and the surface may not have remained constant through time. As previously discussed, there is a significant discrepancy between the DST records, based on Mg/Ca, and the surface records of temperature across the EOT due to secondary effects (Lear et al., 2000, 2004; Liu et al., 2009; Eldrett et al., 2009). In addition, changes in ocean circulation and stratification over the past 50 Ma may have affected the deep-sea to surface temperature gradient and may explain some of the changes in DST (Cramer et al., 2009; Katz et al., 2011).

The Drake Passage opened and then gradually widened and deepened in the middle Eocene

through the Oligocene as South America separated from Antarctica (Kennett, 1977; Nong et al., 2000; Scher and Martin, 2009). This opening, in addition to the opening of the Tasman gateway between Antarctica and Australia in the late Eocene to early Oligocene, led to the development of the Antarctic Circumpolar Current (ACC). Modelling studies suggest that the development of the ACC caused a reorganisation of ocean currents, leading to a warming of $\sim 3 - 4$ °C of the high-latitude Northern Hemisphere surface waters and a cooling of a similar magnitude in the high-latitude Southern Hemisphere surface waters (Toggweiler and Bjornsson, 2000; Nong et al., 2000; Najjar, 2002). These model results suggest that the deep sea also cooled by $\sim 2 - 3$ °C, a slightly lower magnitude than the surface southern high latitudes (Nong et al., 2000; Najjar, 2002).

It is possible that feedbacks from the formation of a continental sized East Antarctic Ice Sheet (EAIS) across the EOT generated regional cooling and enhanced sea ice cover (DeConto et al., 2007). If this enhanced cooling were transmitted to the deep sea, this could explain why the $\delta^{18}$O shift across the EOT is greater in deep-sea records than low-latitude surface records (Pearson et al., 2008; Lear et al., 2008). This change in ocean currents due to the opening of gateways, and potentially the regional cooling due to the formation of the EAIS and enhanced sea ice cover, may have changed the surface to DST gradient. However, the coupling between the deep sea and the surface is still strongest with the regions of major ice formation during the study period, the high-latitude Southern Hemisphere. The ocean restructuring that occurred during this period may also have generated inter-basinal divergence (Cramer et al., 2009; Katz et al., 2011), which is discussed in more detail in Section 1.2.3 and has potential implications for multi-basin composite proxy records such as the deep-sea Mg/Ca record of Lear et al. (2000).

### 1.2.3   Benthic Oxygen Isotopes and Ice Volume

The oxygen isotope composition of foraminiferal calcite provides a record of climate changes throughout the Cenozoic. The three stable isotopes of oxygen, $^{16}$O, $^{17}$O, and $^{18}$O, have natural abundances of 99.76 %, 0.04 %, and 0.20 %, respectively (Rohling and Cooke, 1999). The ratio of $^{18}$O to $^{16}$O is generally the more useful for climate research because of the higher natural abundance of $^{18}$O compared to $^{17}$O and the greater mass difference between $^{18}$O and the predominant $^{16}$O. A sample is analysed using a mass spectrometer and conventionally presented using delta ($\delta$) notation relative to an international standard, which is also analysed (Rohling and Cooke, 1999). During evaporation of water from the ocean, fractionation occurs because
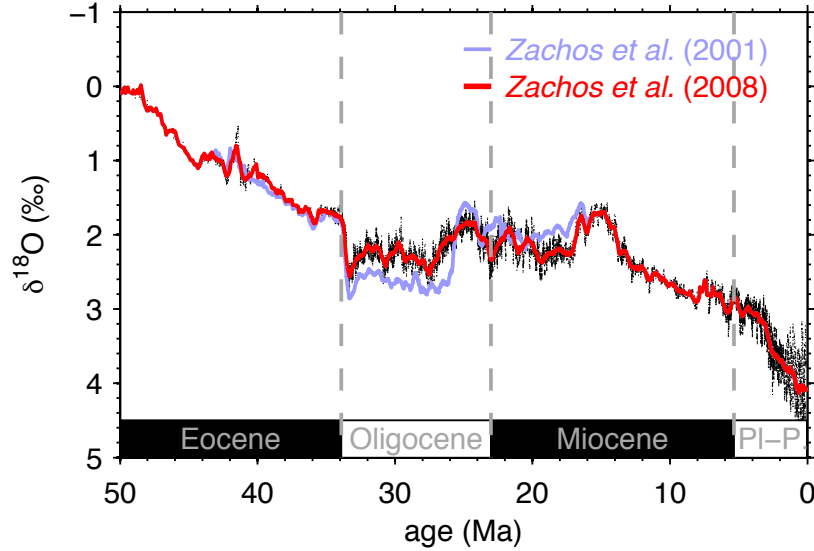
Figure 1.5: *Stack of benthic foraminifera $\delta^{18}O$ data, showing Zachos et al. (2001a) stack (light blue) and updated Zachos et al. (2008) stack with more data (red line and black dots). The additional data remove the artefact of a rapid decrease in benthic $\delta^{18}O$ toward the end of the Oligocene in Zachos et al. (2001a) compilation. Raw data (black points) are smoothed with a 5-point running mean, as per Zachos et al. (2001a), and curves are calculated using the smoothed data with an additional centre-weighted running mean with a constant window size of $\pm 0.2$ Ma.*

of preferential evaporation of the lighter $^{16}O$ isotope. Therefore, freshwater removed from oceans by evaporation has a low $^{18}O$ / $^{16}O$ ratio relative to the source seawater. Fractionation also occurs during condensation, with the heavier $^{18}O$ isotope preferentially condensed. As atmospheric vapour is transported away from its source region, condensation during transport means the remaining vapour becomes more and more depleted in $^{18}O$. Rainout from atmospheric vapour that has been transported a long way, i.e., from the low to high latitudes, will be very depleted in $^{18}O$ (Dansgaard, 1964). The buildup of ice sheets from isotopically light (depleted in $^{18}O$) precipitation, and subsequent storage of $^{16}O$ in ice sheets, causes the oceans to become enriched in $^{18}O$. The $\delta^{18}O$ values of seawater are therefore affected by storage of the lighter $^{16}O$ isotope in ice sheets (Shackleton, 1967). In addition to this ice volume component, temperature-dependent fractionation occurs when the oxygen isotopes are incorporated into calcite tests of foraminifera (Urey, 1947). Increases in benthic foraminiferal $\delta^{18}O$ suggest deep-sea cooling and increased ice storage on land (Zachos et al., 2001a).

Benthic foraminiferal $\delta^{18}O$ data from multiple sites have been compiled to create $\delta^{18}O$ stacks

26

(Miller et al., 1987; Zachos et al., 2001a; Lisiecki and Raymo, 2005; Zachos et al., 2008). The compilation of Zachos et al. (2008) is shown in Figure 1.5. Starting in the early Eocene, Figure 1.5 shows a broad increase in benthic $\delta^{18}O$ throughout the Eocene with a rapid but brief reversal in the $\delta^{18}O$ trend at $\sim$40 Ma, a period known as the Middle Eocene Climatic Optimum (MECO; Zachos et al., 2008). A significant transition at the EOT is seen as an abrupt increase in benthic $\delta^{18}O$ of $\sim$1.5 ‰, due to ice growth and/or declining DST (Zachos et al., 2008; Liu et al., 2009). The most established view of the evolution of Cenozoic ice sheets places the first inception of a continent sized ice sheet on Antarctica at the EOT (Zachos et al., 2001a). In older compilations there was a rapid benthic $\delta^{18}O$ decrease during the late Oligocene ($\sim$1.0 ‰), which had been interpreted as being due to warming and significant ice loss (Miller et al., 1987; Zachos et al., 2001a). More recent records suggest instead that this rapid decrease in benthic $\delta^{18}O$ was an artefact caused by data being combined from regions with contrasting thermal histories (Pekar and DeConto, 2006). A later compilation with data from more regions removes this artefact (Zachos et al., 2008). The benthic $\delta^{18}O$ values remain relatively stable throughout the early Miocene before continuing to increase after the Middle Miocene Climatic Optimum (MMCO) across the middle Miocene climate transition ($\sim$14 Ma; Zachos et al., 2008).

Although a climate trend can be interpreted from the raw benthic $\delta^{18}O$ data, separating the signal into a quantitative record of ice volume or DST, until recently, has required an independent record of one of the components from which the other can then be calculated (Lear et al., 2000; Waelbroeck et al., 2002). However, this leads to the errors in the independent DST or ice volume record being translated to the calculated component. Alternatively, the relative contributions from these components can be estimated using ice sheet models constrained by the $\delta^{18}O$ observational data that solve changes in the ice volume and change in DST simultaneously (de Boer et al., 2010). In principle, the $\delta^{18}O$ data can also be used as a test for independent sea level and DST data, which can be combined to create a synthetic $\delta^{18}O$ record using a simple calibration (see Section 2.2.3).

The benthic $\delta^{18}O$ record is also susceptible to the changes in ocean circulation discussed previously, which occurred during the Eocene and Oligocene with the opening of ocean gateways. Cramer et al. (2009) created a new benthic $\delta^{18}O$ compilation separated by ocean basin, in contrast to the Zachos et al. (2001a, 2008) multi-basin compilation. This showed inter-basinal homogeneity from $\sim$65 Ma to $\sim$35 Ma shifting to heterogeneity from $\sim$35 Ma to present. This was attributed to the development of the ACC and ocean current reorganisation at the EOT (Cramer et al., 2009). Katz et al. (2011) suggest that the modern four layer ocean structure

also developed in the early Oligocene because of the development of the ACC. Inter-basinal heterogeneity is clearly a potential source of uncertainty in multi-basin palaeoclimate compilations (Lear et al., 2000; Zachos et al., 2008) and brings into question how representative multi-basin compilations are of the global climate (Cramer et al., 2009).

## 1.3 Modelling

Modelling approaches to estimating Cenozoic ice volume and temperature can be broadly divided into physics based approximations using general circulation models (GCMs) and ice sheet models (Huybrechts, 1993; DeConto and Pollard, 2003a) and observation-constrained modelling, which also uses ice sheet models (Bintanja et al., 2005a; de Boer et al., 2010).

### 1.3.1 Observation-constrained forward modelling

As the $\delta^{18}$O record is a mixed climate signal, an alternative method of separating the components of the $\delta^{18}$O signal has been developed, which uses ice sheet models constrained by the input $\delta^{18}$O data (Bintanja et al., 2005a,b; de Boer et al., 2010). In summary, this approach uses 1-D models (and 3-D models for $3 - 0$ Ma) of the North American, Eurasian, Greenland, West Antarctic, and East Antarctic ice sheets in a routine that is forced to follow the input benthic $\delta^{18}$O observational data. The work of de Boer et al. (2010) is based on earlier work by Bintanja et al. (2005a,b) but extended over the past 40 Ma. This method creates modelled estimates of Northern Hemisphere surface temperature, DST, ice volume, sea level, and benthic $\delta^{18}$O . The Northern Hemisphere surface temperature and sea level data are shown in Figures 1.3 and 1.4, and the Northern Hemisphere surface temperature and sea level data are plotted against each other in Figure 1.6.

de Boer et al. (2010) use ice sheet models to calculate the separate ice volume and DST components of the benthic $\delta^{18}$O signal. For each time step, the ice sheet models require a temperature anomaly as input. The temperature anomaly is calculated from the difference between the modelled $\delta^{18}$O ($\delta^{18}O_b$) at the current time step and the observed $\delta^{18}$O ($\delta^{18}O_{obs}$) 100 years later (the inverse routine). This $\delta^{18}$O anomaly over the 100 year interval is converted to a Northern Hemisphere temperature anomaly using a Northern Hemisphere temperature to benthic $\delta^{18}$O response parameter. An assumption of this approach is that Northern Hemisphere temperature is the predominant control on the benthic $\delta^{18}$O record through its coupling with
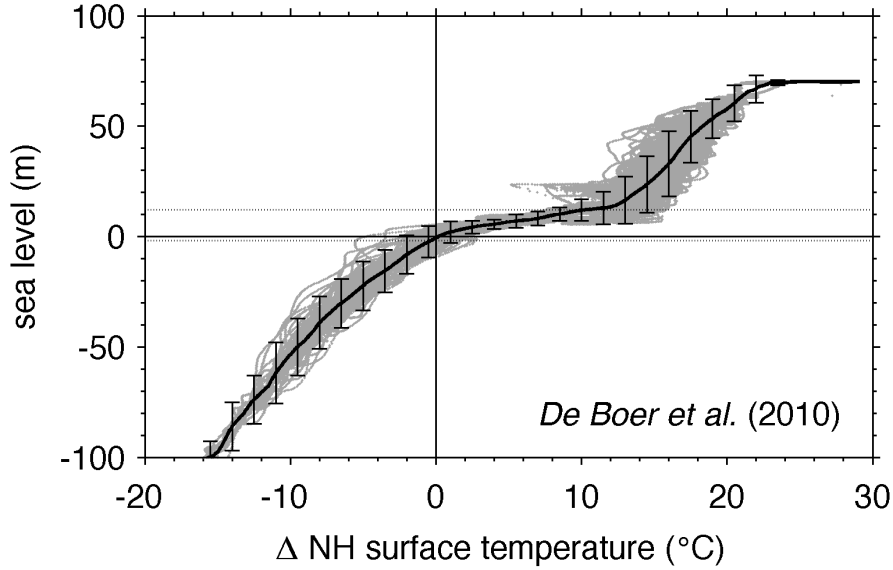
Figure 1.6: *de Boer et al. (2010) observation-constrained forward modelled sea level and Northern Hemi-sphere surface air temperature. Solid line is smoothed using a centre-weighted running mean with a window size of $\pm 0.05\,^\circ C$. Error bars are calculated as 2 standard deviations of the data range $\pm 0.25\,^\circ C$ of each data point.*

DST and forcing of ice growth. With this input, the ice sheet models can calculate a new ice volume, DST, and $\delta^{18}O_b$ signal for the next 100 years. The inverse routine is optimised to min-imise the difference between the modelled and observed $\delta^{18}O$ signals and to satisfy independent climate constraints (Bintanja et al., 2005a,b; de Boer et al., 2010).

The inverse routine is sensitive to multiple parameters that can be tuned to satisfy inde-pendent sea level and temperature data. Northern Hemisphere temperatures are translated to DSTs using a response parameter. Northern Hemisphere temperatures are averaged over 3 ka to take into account the slow response of the oceans to atmospheric temperature change (Bintanja et al., 2005a). To represent changes in the Greenland and Antarctic ice sheets, the Northern Hemisphere temperature is linearly related to these regions by taking into account the different geographical location and altitude of these ice sheets. A sensitivity test suggested that changing these parameters can affect the long-term $(35 - 3\text{ Ma})$ sea level and Northern Hemisphere temperature averages by $\sim$6 m and $\sim$2 $^\circ$C, respectively. de Boer et al. (2010) select optimum values of these parameters based on agreement with the tuning parameters, such as LGM sea level $\sim$120 m lower than present (Rohling et al., 2009) and a sea level fall of $\sim$40 m in the earliest Oligocene (DeConto and Pollard, 2003a).

The study by de Boer et al. (2010) uses 1-D ice sheet models. This method has also been applied using a 3-D model over the past 3 Ma (Bintanja and van De Wal, 2008; de Boer et al., 2012b), and the 1-D results are similar over this period (de Boer et al., 2010). Equilibrium studies using both 1-D and 3-D models over North America suggest that the oversimplified geometry in the 1-D model means that hysteresis effects seen in the 3-D results are not replicated (Wilschut et al., 2006). Indeed, de Boer et al. (2010) suggested that the use of 3-D models was possible scope for a future study. The hysteresis in the study of Wilschut et al. (2006) using 3-D models means that a certain temperature can be related to several sea level stands depending on the evolution of the system over time.

de Boer et al. (2010, 2012a) explore the relationship between sea level and Northern Hemisphere surface temperature in their observation-constrained model results; this is reproduced in Figure 1.6 for Northern Hemisphere surface temperature against sea level. Clearly present in their results are the broad climate states of the past 35 Ma, going from unglaciated conditions to partial glaciation with an East Antarctic Ice Sheet, transitioning to interglacial conditions with the additional growth of the Greenland Ice Sheet and the West Antarctic Ice Sheet (WAIS) and finally, glacial conditions with additional Northern Hemisphere ice sheets (de Boer et al., 2012a). Their results suggest that the relationship between sea level and temperature (both deep sea and Northern Hemisphere surface) has not remained constant (i.e., linear) over the past 35 Ma. Sea level appears less sensitive to temperature for sea levels approximately between -2 and +12 m relative to present (see Figure 1.6). This suggests that interglacial periods, when sea level is similar to present, are relatively stable in the context of variation over the past 35 Ma (de Boer et al., 2010). This is seen in the relative contributions to the $\delta^{18}$O signal from DST and ice volume. From the middle Miocene ($13 - 12$ Ma) until $\sim$3 Ma, when sea level in the reconstruction of de Boer et al. (2010) is $\sim$10 m above present, the dominant contribution is from DST, with very little contribution from changing ice volume. It is likely that the lack of ice volume contribution is due to the EAIS being bound by the limits of the continent and Northern Hemisphere temperatures being above the threshold for widespread Northern Hemisphere glaciation. For temperatures warmer than present, the relationship between Northern Hemisphere surface temperature and sea level (and also DST and sea level, not shown here) shows a single-stepped, sigmoidal form (see Figure 1.6; de Boer et al., 2010).

As this modelling approach is based on the global compilation of benthic $\delta^{18}$O data, it is also susceptible to potential errors from inter-basinal divergence, discussed in the work by Cramer et al. (2009). This modelling approach also assumes a constant deep-sea to surface temperature

ratio (de Boer et al., 2010); for reasons previously discussed, the deep-sea to surface temperature gradient may have changed on this long time-scale (Nong et al., 2000; Najjar, 2002), and this may be a potential source of error in the results of de Boer et al. (2010).

### 1.3.2   GCM-ice sheet modelling

There are various methods of modelling past ice volume using GCMs and ice sheet models (Pollard, 2010). This thesis is interested in how ice sheets have evolved in response to changes in temperature forcing and therefore will focus on modelling studies with transient forcing rather than time slice studies. Ice sheet models can be coupled with general circulation models to simulate long-term climate changes, with approximate feedbacks between the ice and climate systems. Although a full coupling between a GCM and an ice sheet model would be desirable, for multimillion year integrations this is currently not feasible given the high computational expense of running GCMs (e.g. Blatter et al., 2011). Because of the discrepancy between the time taken for the climate system to approach equilibrium and for ice sheets to reach equilibrium, an asynchronous coupling can be used (DeConto and Pollard, 2003a,b). The climate system can be perturbed by slowly changing the atmospheric $CO_2$ concentration with the climate system in quasi-equilibrium and the ice sheets slowly varying because of astronomical and greenhouse gas forcing (Pollard and DeConto, 2005).

DeConto and Pollard (2003a,b) used an asynchronous method to study the thresholds for inception of the EAIS at the EOT. Their method is split into two stages: (1) The GCM is used to provide extrapolated forcings for a much longer ice sheet simulation for different astronomical configurations and $CO_2$ concentrations. An initial GCM run provides a mass balance for a 10 ka ice sheet simulation. At the end of the ice sheet run, and at subsequent 10 ka intervals, the GCM is run again with the updated ice sheet extent and a new astronomical configuration. The ice sheet model provides feedback over each 10 ka interval because of albedo and topography changes. The astronomical configurations are idealised representations of changes in the Earth's orbit and obliquity. This is completed for atmospheric $CO_2$ concentrations of 560 and 840 ppmv ($2 \times$ and $3 \times$ preindustrial $CO_2$). The GCM data are stored for the next stage (Pollard and DeConto, 2005). (2) In this stage, a 10 Ma ice sheet model simulation is completed. This is updated every 200 years with a new mass balance calculated using linear extrapolation of the GCM data. This creates an approximation of astronomical cycles at a high temporal resolution. The extrapolation includes a linearly declining $CO_2$ concentration. The calculations take into

account the logarithmic effect of $CO_2$ forcing on temperature change via radiation theory. The mass balance calculations correct for changing elevation due to changes in the size of the ice sheet, so height-mass balance feedback is represented. Albedo feedbacks on timescales longer than the first integration (10 ka) are not represented (Pollard and DeConto, 2005). This method can be modified to investigate the effect of ocean gateways being opened or closed, the effect of mountain uplift, and the effect of astronomical variations (DeConto and Pollard, 2003a; Pollard and DeConto, 2005).

Modelling studies of the forcings required to form an ice sheet on Antarctica suggest that ice growth responds non-linearly to changing temperature (Oerlemans, 2004). This nonlinearity is caused by feedbacks such as heightmass balance feedback (the additional cooling caused by the temperature gradient in the atmosphere as an ice sheet grows vertically), precipitation feedback, and ice-albedo feedback (Oerlemans, 2002; Notz, 2009). The initiation of glaciation displays a threshold response, with growth starting as the descending snow line intercepts high topographic regions (Oerlemans, 1982; Pollard, 1982; DeConto and Pollard, 2003a).

In Figure 1.7, the model output from Pollard and DeConto (2005) for the formation and melting of the East Antarctic Ice Sheet is shown. The original $CO_2$ axis is converted to a temperature (average global surface) axis using the climate sensitivity of their GCM (2.5 °C per doubling of $CO_2$; Thompson and Pollard, 1997) and accounting for the logarithmic dependence of temperature to $CO_2$. The data are reversed on both axes for consistency with the other figures shown here. Ice volumes are converted to sea levels assuming an ice-free sea level of 64 m above present (Lythe and Vaughan, 2001; Bamber et al., 2001; Lemke et al., 2007) and adjusting for the change in volume with change in state from ice to seawater. The original $CO_2$ forcing and model time is included but converted to a logarithmic scale.

The results of DeConto and Pollard (2003a,b) show the formation of ice on Antarctica in multiple stages under various atmospheric $CO_2$ concentrations. With a high atmospheric $CO_2$ concentration of $8 \times$ pre-industrial $CO_2$ (PIC), equal to 2240 ppmv, ice is limited to mountain glaciers in the Transantarctic Mountains and Dronning Maud Land. Isolated ice caps first form in the high-elevation regions of Dronning Maud Land and the Gamburtsev and Transantarctic Mountains as atmospheric $CO_2$ decreases to $3 - 4 \times$ PIC ($840 - 1120$ ppmv). In the model, as $CO_2$ falls to $\sim 2.7 \times$ PIC ($\sim 760$ ppmv) a threshold is crossed and height-mass balance feedback leads to the three isolated ice caps coalescing into a continent sized ice sheet. Although there are multiple "steps" in their results, there are two major steps marking (1) the transition from
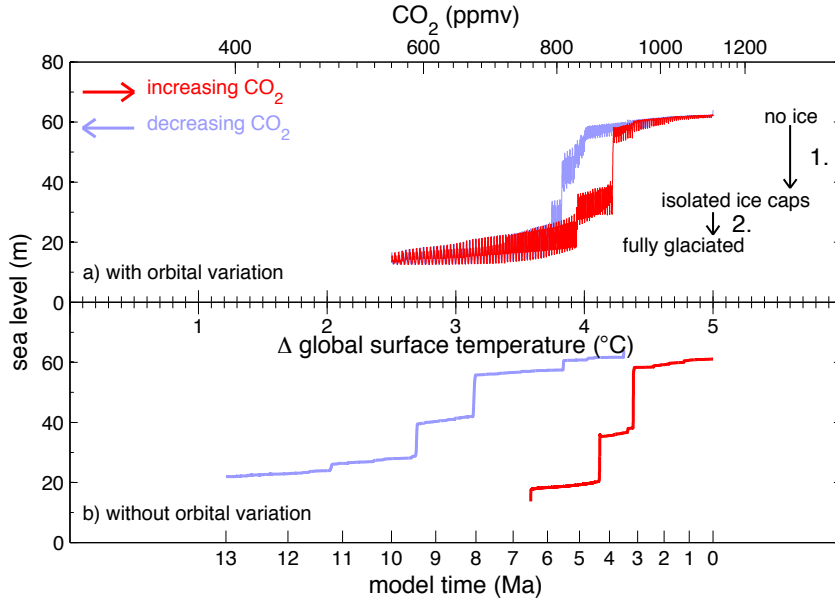
Figure 1.7: *Pollard and DeConto (2005) GCM-ice sheet modelled results, for the East Antarctic Ice Sheet only (the WAIS is not fully represented). Data are converted to a temperature scale from the original $CO_2$ scale using the climate sensitivity of their model (2.5 °C for a doubling of $CO_2$ (Thompson and Pollard, 1997)) and accounting for the logarithmic relationship between temperature and $CO_2$. The original axes of Pollard and DeConto (2005) are included but converted to an appropriate logarithmic scale. The ice volumes of the original figure are converted to sea level assuming ice-free sea level of 64 m above present (Lemke et al., 2007) and accounting for the change in volume with change in state from ice to seawater. The high-frequency oscillations in the data in a) are due to idealised Milankovitch astronomical forcing.*

no ice to isolated mountain ice caps and (2) the transition to a full ice sheet (see Figure 1.7.A). The total sea level shift in this two-step model of Pollard and DeConto (2005) is on the order of 50 m ($\sim$33 m after accounting for hydroisostasy for comparison with the NJ record (Pekar et al., 2002)); Figure 1.7 does not include other causes of sea level change, such as thermosteric sea level change.

A study of forward (inception) and reverse (deglaciation) model runs investigated ice sheet hysteresis (reproduced in Figure 1.7; Pollard and DeConto, 2005). Starting with no ice, a descending snow line generates rapid ice mass gains as it meets the mountain regions. Once a full continental ice sheet has formed, the snow line must rise considerably higher to achieve negative net mass balance and initiate broad-scale retreat. This is because the steep outer slopes of the ice sheet and the atmospheric lapse rate require much warmer conditions to produce enough surface melt area around the margins to overcome the net interior snowfall (which at present is balanced by Antarctic iceberg and shelf discharge; Oerlemans, 2002; Pollard and

33

DeConto, 2005). In the model runs for the EAIS, this hysteresis equates to a difference of $0.5 \times$ PIC between forward and reverse runs. Although the forward run required atmospheric $CO_2$ to descend past $\sim 2.7 \times$ PIC for inception to begin, the reverse run required atmospheric $CO_2$ to rise above $\sim 3.2 \times$ PIC ($\sim 900$ ppmv) for deglaciation to begin. These runs include astronomical variations; without astronomical variations, the hysteresis is greater. The model shows formation of ice in a series of steps between multiple quasi-stable states. There is a stable state just after the formation of ice in mountain regions as further growth is limited by the extent of the mountain ranges. The snow line has to descend further with additional cooling before there is additional growth. With the continent fully glaciated, further growth is inhibited when the ice sheet reaches the coastline (Pollard and DeConto, 2005).

As noted in the work by Pollard and DeConto (2005), the asynchronous coupling method used for Figure 1.7 poorly represents albedo feedback on longer than astronomical timescales. Ongoing work with improved coupling schemes suggests that the major no-ice to continental ice transitions are steeper than in Figure 1.7, and the hysteresis (i.e., difference between $CO_2$ levels of inception and deglaciation) is considerably more pronounced (this is explored in detail in Chapter 5).

The observation-constrained modelling work of de Boer et al. (2010) displays a single-step form for temperatures warmer than present, not a two-step form seen in the work of Pollard and DeConto (2005). The two-stepped hypothesis is based on isolated ice caps initially forming in mountain regions prior to coalescing into a continental sized ice sheet with further cooling (Pollard and DeConto, 2005). A possible reason that the work of de Boer et al. (2010) does not show this form is that the ice sheets used in their initial study used 1-D ice sheet models, with a simplified geometry. It is possible that if this work were completed with 3-D ice sheet models then a two-stepped form could be apparent, with the inclusion of the initial isolated ice cap phase.

# Chapter 2

# The past relationship between temperature and sea level – from proxy records

## 2.1 Sea level versus temperature: methods

Using the data we have discussed in the previous chapter, in this chapter we consider the possible forms for the relationships between temperature (both DST and SST) and sea level over the past 50 Ma. We test three functions, a linear function and single- and double-stepped nonlinear functions, which are based on previous publications covering the past relationship between temperature and sea level (Pollard and DeConto, 2005; Archer, 2007; de Boer et al., 2010). For the period $50 - 10$ Ma the DST data used are the Lear et al. (2000) benthic Mg/Ca record, and the sea level data used are the Kominz et al. (2008) NJ sequence stratigraphy record. For the SST relationship with sea level, we use the same sea level record of Kominz et al. (2008) and additional SST records for the high-latitude Southern Hemisphere (Liu et al., 2009) and low latitudes (Lear et al., 2008) for the EOT. Additional Plio-Pleistocene data are shown on the plots. The past relationship between temperature and sea level for periods cooler than present has been the subject of previous studies (Rohling et al., 2009; Siddall et al., 2010a). In this chapter we focus on the relationship between temperature and sea level for periods warmer than present. The Plio-Pleistocene data are therefore shown as a guide and are not used when fitting the different functions. As the DST record is more complete, the majority of this chapter focuses on the relationship between DST and sea level, with the SST to sea level relationship investigated over the EOT. These changes are for the long-term response of sea level to SST or DST, with ice sheets approaching equilibrium with climate over $10^4 - 10^5$ years.

### 2.1.1 Interpolation

The temporal resolutions of the different records used in this chapter vary. The Mg/Ca data set of Lear et al. (2000) has a resolution of $\sim 1$ Ma and does not resolve shorter climatic events. The sea level record of Kominz et al. (2008) has a temporal resolution of 0.1 Ma, although the age control is significantly worse, at $\pm 0.5$ Ma (Kominz et al., 2008). To compare these two data sets, the sea level data are first reduced to the same lower temporal resolution of the Lear et al. (2000) data set. The higher-resolution sea level data are smoothed using a centre-weighted running mean and a window size of $\pm 0.5$ Ma; the data are then interpolated with a 1 Ma frequency. Smoothing in this manner leads to the loss of some of the high-frequency sea level variability in the record, but major transitions, such as the EOT sea level fall, are preserved. For the SST records, which have a higher temporal resolution than the DST data, the sea level data are interpolated using the same method but to a 0.1 Ma resolution for the low-latitude

record and to a 0.25 Ma resolution for the high-latitude Southern Hemisphere record.

The different records all span the EOT, a period of major sea level change; however, they all have different durations. Kominz et al. (2008) sequence stratigraphy data are not available from 10 Ma to present, so data are shown from $50 - 10$ Ma, which is the maximum age of the Lear et al. (2000) data set. The high-latitude Southern Hemisphere SST data of Liu et al. (2009) are shown from $36.5 - 32$ Ma, which is the period of peak data density in their record. The low-latitude SST data of Lear et al. (2008) cover the period from $34.5 - 33.4$ Ma. Therefore, there are significant data gaps on the plots; in particular, the Miocene is not covered for the SST to sea level synthesis.

Lear et al. (2000) used four core locations for their compilation. The site from which the most recent samples (exclusively for period $6 - 0$ Ma) were obtained was DSDP Site 573. Modern DST for this site is 1.4 °C (from NODC_WOA98). The Mg/Ca DST data are shown as an anomaly relative to this modern-day value. Liu et al. (2009) provide modern palaeo-location temperatures for all of their sites. The high-latitude Southern Hemisphere SST data are presented here as anomalies relative to the modern value for each site. The Lear et al. (2008) record comes from an exposed shelf; the data are shown here as anomalies relative to a modern SST value of 27.1 °C (from NODC_WOA98), taken from the coast immediately to the east of the core site.

A best and a low and high estimate are provided with the NJ highstand data. The low and high estimates are calculated as being 60 % and 150 % of the best estimate, respectively. Therefore, the best estimate is not the midpoint of the estimate range; the skewed errors are a result of using foraminifera habitat ranges as a water depth indicator, the errors of which increase with increasing water depth (Kominz et al., 2008). In order to carry out the regression, we require a symmetric error distribution. We calculate a mid-point from the asymmetrical (triangular) error distribution and create a synthetic data set that has symmetric errors (see Figure 1.3). Errors are not provided for the conceptual low-stand data (Kominz et al., 2008), although lowstand errors are likely to be larger than the highstand errors; here we use lowstand errors of $\pm 50$ m based on the maximum errors suggested by Miller et al. (2005a). The Mg/Ca DST curve is calculated using a weighted local regression of the raw data (Lear et al., 2000). Here we repeat this regression and obtain an error estimate from the raw data. Errors on the DST data are also unevenly distributed, and again we create a synthetic data set with a symmetric distribution.
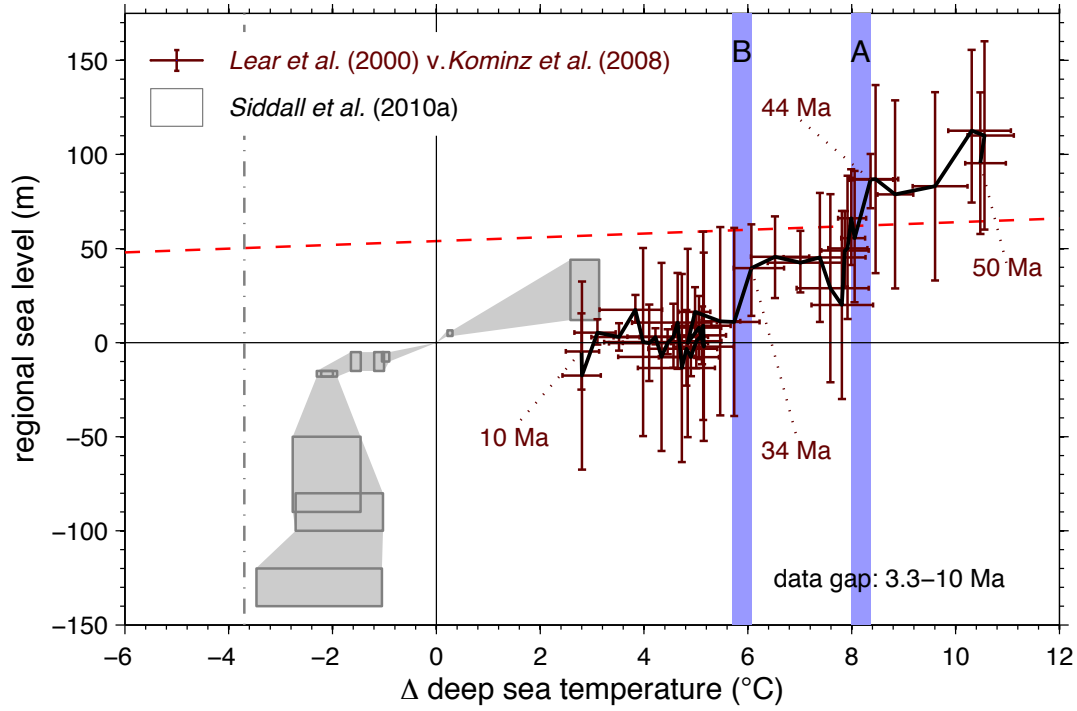
Figure 2.1: *Deep-sea temperature against regional sea level crossplot. Dark red error bars are the Lear et al. (2000) Mg/Ca deep-sea temperature anomaly against Kominz et al. (2008) New Jersey regional sea level data. Shown connected in time order (black line). Blue bars highlight the two steps discussed in the text. Grey boxes are Plio-Pleistocene deep-sea temperature and sea level data from the Red Sea (Siddall et al., 2010a); the vertical grey dot-dashed line is the freezing point for water for the deep-sea temperature data used in the work by Siddall et al. (2010a), showing decreased deep-sea temperature variability as the freezing point is approached. The sloped red dashed line is the ice-free thermal expansion gradient, assuming an ice-free NJ sea level of 54 m and a thermal expansion of 1 m per °C, after Miller et al. (2009b).*

## 2.1.2 Sea level versus temperature crossplots

For each of the crossplots, additional data for the Plio-Pleistocene are shown to provide a reference for the relationship between the relevant temperatures and sea level for cooler climates. Figure 2.1 includes DST and Red Sea sea level data (Siddall et al., 2003) compiled by Siddall et al. (2010a). This highlights that as DSTs approach the freezing point for seawater (also highlighted in Figure 2.1) they show very little variation (Siddall et al., 2010a). Figure 2.2 includes Antarctic air temperature and sea level data for the last 500 ka Rohling et al. (2009); again the sea level data come from the Red Sea reconstruction (Siddall et al., 2003; Rohling et al., 2009). The proxy Antarctic air temperatures come from deuterium isotope ($\delta$D) data
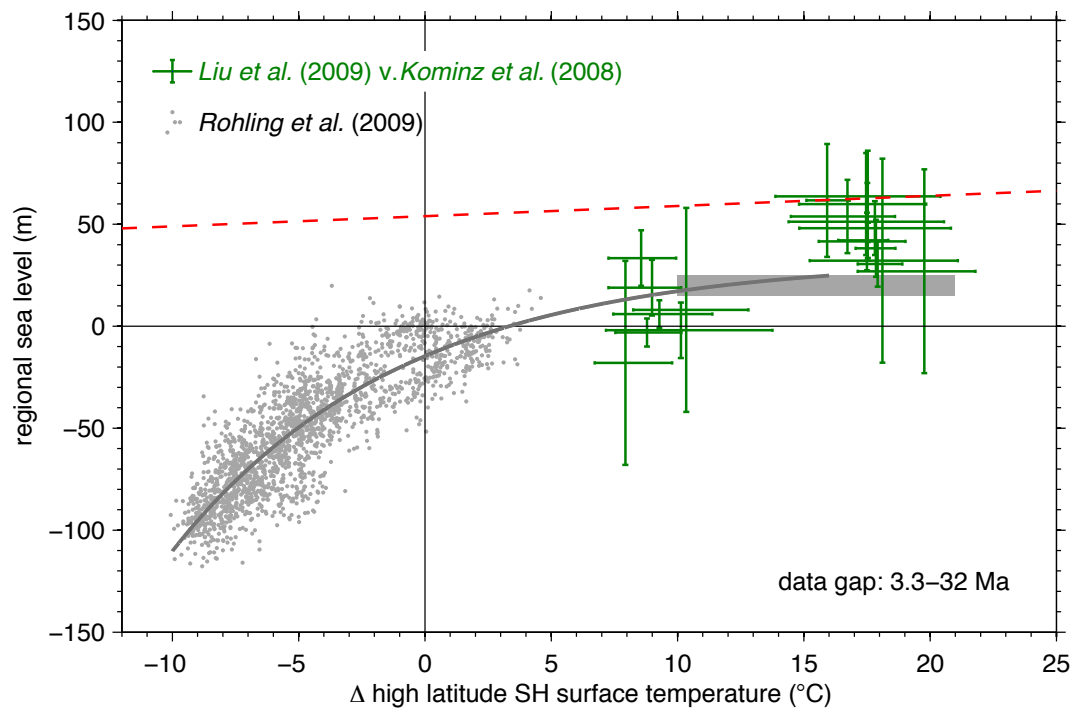
Figure 2.2: *High-latitude Southern Hemisphere surface temperature against regional sea level. Dark green error bars are the Liu et al. (2009) $TEX_{86}$ and $U^{k'}_{37}$ SST data for high-latitude Southern Hemisphere sites, shown as an anomaly relative to modern SST, against Kominz et al. (2008) New Jersey regional sea level data. The dark green data cover the EOT, with data from 36.5 to 32 Ma with a 0.25 Ma resolution. There is a data gap from the end of the dark green data at 32 Ma to the Plio-Pleistocene data. The grey dots show Pleistocene data (500-0 ka); the grey box is for the mid-Pliocene (Rohling et al., 2009). The grey dots from Rohling et al. (2009) are for Antarctic air temperature based on $\delta D$ and sea level data from the Red Sea (Siddall et al., 2003). The grey line is the preferred exponential fit between temperature and sea level of Rohling et al. (2009). The sloped red dashed line is the ice-free thermal expansion gradient, assuming ice-free NJ sea level of 54 m and a reduced thermal expansion gradient of 0.5 m per $^{\circ}C$, to account for polar amplification (e.g., Siddall et al., 2010a).*

from EPICA Dome C (Jouzel et al., 2007) and are presented as an anomaly relative to average temperature over the past 1 ka (Rohling et al., 2009). Figure 2.3 uses temperature data from a low-latitude SST stack from five tropical sites in the major ocean basins using the $U^{k'}_{37}$ proxy (Herbert et al., 2010) and Mg/Ca of planktic foraminifera (Medina-Elizalde and Lea, 2005). We repeat the stacking method outlined by Herbert et al. (2010) but calculate temperatures as an anomaly relative to the average of the past 3 ka. Again the Plio-Pleistocene sea level data come from the Red Sea reconstruction (Siddall et al., 2003; Rohling et al., 2009).

All of the plots of sea level against temperature exhibit a positive correlation. This relationship is expected because of thermal expansion and changing land ice volumes with changing temperature. In addition to the forcing of sea level from changes in temperature, there are potential feedbacks where by changes in ice volume can drive changes in temperature. For example, the vertical growth of a large ice sheet will slightly lower the global mean surface temperature due to the atmospheric lapse rate. There are also potential feedbacks from the growth of ice sheets on sea ice (DeConto et al., 2007), which could influence deep-water formation and hence deep-sea temperatures.

There is an additional component to the sea level record that may not be directly related to temperature: the change in ocean basin volume. However, it is possible that there is a common driving mechanism: decreased seafloor spreading could cause a decline in atmospheric $CO_2$, resulting in increased basin volume (i.e., lower sea level) and decreased temperature (Larson, 1991; Miller et al., 2009b). The sea level record may contain regional tectonic influences, which are not related to temperature change (see 1.2.1). The thermal expansion gradient assuming ice-free conditions (54 m above present at NJ margin for present temperature (Pekar et al., 2002; Miller et al., 2005a)) is shown on all of the plots (Figures 2.1−2.3) as a guide to how much of the NJ sea level variability is likely due to thermal expansion and glacio-eustasy.

In Figure 2.1 when the data are connected in time series (black line in Figure 2.1), it is possible that there is a two-stepped relationship between the DST data of Lear et al. (2000) and the sea level data of Kominz et al. (2008). This is potentially in agreement with the modelling work of Pollard and DeConto (2005) although the total sea level shift is greater than the ∼50 m (∼33 m after accounting for hydro-isostasy) shift seen in the work by Pollard and DeConto (2005; Figure 1.7) as the sea level record used here includes thermosteric and ocean basin volume components. The two-step form seen in the study by Pollard and DeConto (2005) is solely due to glacio-eustasy from the formation of the EAIS. An additional difference between the two-step form seen in the work of Pollard and DeConto (2005) and that seen here is the time scale. The two steps occurring in the Pollard and DeConto (2005) study take place over a duration of ∼200 ka. The two steps in this chapter are separated by ∼10 Ma. A first step occurs at 44 − 42 Ma (hereafter step A), and there is a second step (hereafter step B) at 34 − 33 Ma coinciding with the EOT. The lack of cooling in the DST record at the EOT should be taken into consideration when interpreting these steps. The lack of cooling accentuates step B at the EOT. Other temperature proxies suggest that there was cooling at the EOT (Dupont-Nivet et al., 2007; Zanazzi et al., 2007; Lear et al., 2008; Liu et al., 2009; Lear et al., 2010), and
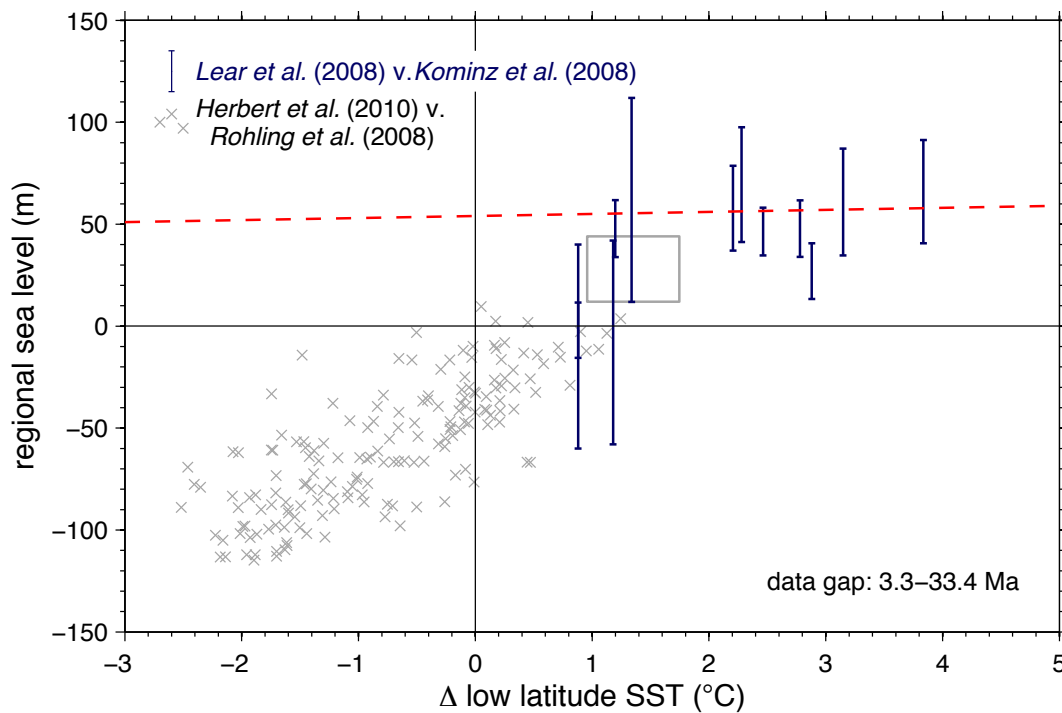
Figure 2.3: *Low-latitude sea surface temperature against regional sea level. The dark blue error bars are for the Lear et al. (2008) Mg/Ca sea surface temperature data from Tanzania against Kominz et al. (2008) New Jersey regional sea level data for the EOT. The dark blue data cover the period from 34.5 to 33.4 Ma, with a resolution of 0.1 Ma. Plio-Pleistocene data are shown in grey, with low-latitude SST data from the stack by Herbert et al. (2010) and sea level data from the Red Sea record (Siddall et al., 2003; Rohling et al., 2009). Pleistocene data for 500-0 ka are shown as grey crosses; a mid-Pliocene data point is shown as a grey box. The sloped red dashed line is the ice-free thermal expansion gradient, assuming an ice-free NJ sea level of 54 m and a thermal expansion of 1 m per °C (Miller et al., 2009b).*

deep-sea cooling may have been on the order of 1.5 °C (Lear et al., 2010; Pusz et al., 2011). In Figure 2.4, the DST data prior to the EOT are shifted by +1.5 °C to take into account cooling at the EOT. This results in the steepness of step B, as seen in Figure 2.1, being reduced. The SST plots (Figures 2.2 and 2.3) also span the EOT. The steep step B seen in the DST plot (Figure 2.1) is not evident in the SST plots. This again suggests that the steepness of step B in the DST plot may be an artefact of the lack of cooling in the DST data across the EOT.

Because the Mg/Ca temperature proxy is affected by past variations in seawater Mg/Ca (see 1.2.2.1; Lear et al., 2000; Billups and Schrag, 2003), the absolute DST values can vary depending on the seawater Mg/Ca scenario used. DSTs using the favoured scenario of Lear et al. (2000) and the extreme scenarios of Lear (2007) are shown in Figure 2.5 plotted against
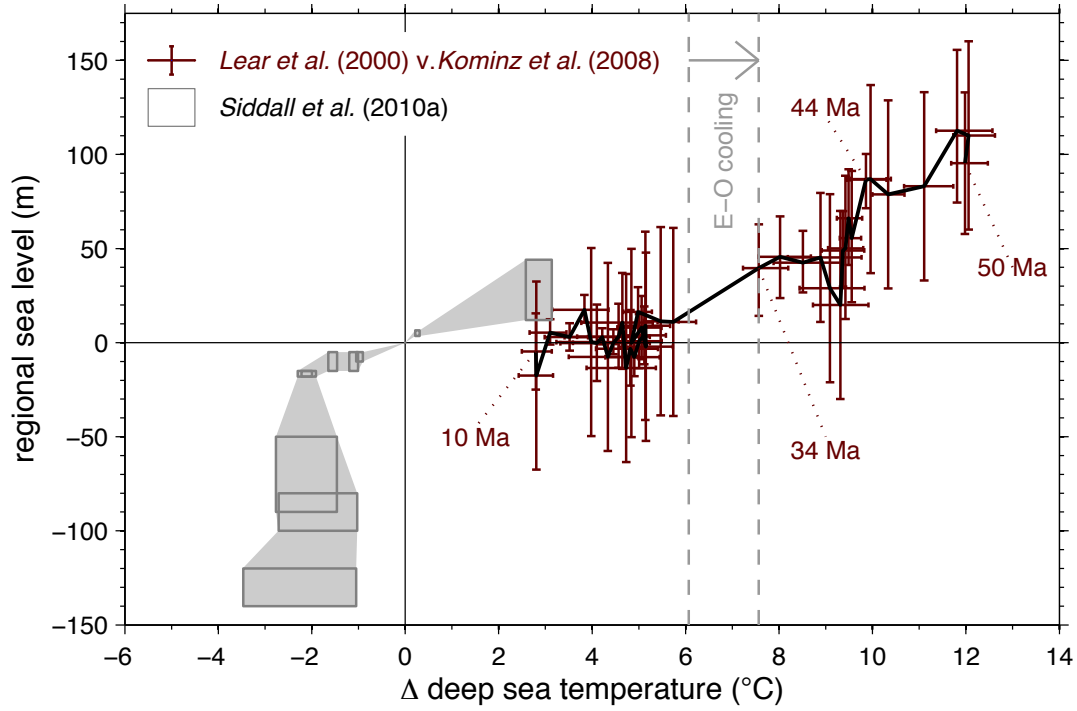
Figure 2.4: *Deep-sea temperature against regional sea level. Data as per Figure 2.1 but with data prior to the EOT shifted by +1.5 °C (Lear et al., 2010; Pusz et al., 2011) to account for EOT cooling not seen in the Lear et al. (2000) record.*

NJ sea level. It is unlikely that seawater Mg/Ca has remained constant over the past 50 Ma (Wilkinson and Algeo, 1989; Lowenstein et al., 2001; Dickson, 2002; Coggon et al., 2010), as per Figure 2.5.A. However, it is possible that seawater Mg/Ca was lower than the preferred scenario of $3.85$ mol mol$^{-1}$ at 50 Ma (Lear et al., 2000; Lowenstein et al., 2001; Dickson, 2002; Coggon et al., 2010; Evans and Müller, 2012), as per Figure 2.5.C, where a value of $1.5$ mol mol$^{-1}$ at 50 Ma, linearly increasing to present, is used; although it is difficult to reconcile this Mg/Ca temperature scenario with the benthic $\delta^{18}$O records assuming early Cenozoic ice-free conditions (Lear, 2007). As such, the absolute Mg/Ca DST values should be interpreted with caution.

The Cenozoic temperature trend is dominated by cooling, with shorter warm reversals. Hysteresis effects mean that the sea level thresholds may be at different temperatures for warming compared to cooling (see 1.3.2 and Figure 1.7). Because of the long response time of the ice sheets, the relationship shown represents sea level in approximate equilibrium with temperature. The very long-term relationship between DST or SST and sea level investigated in this chapter is therefore not directly relatable to potential future surface warming on centennial timescales.
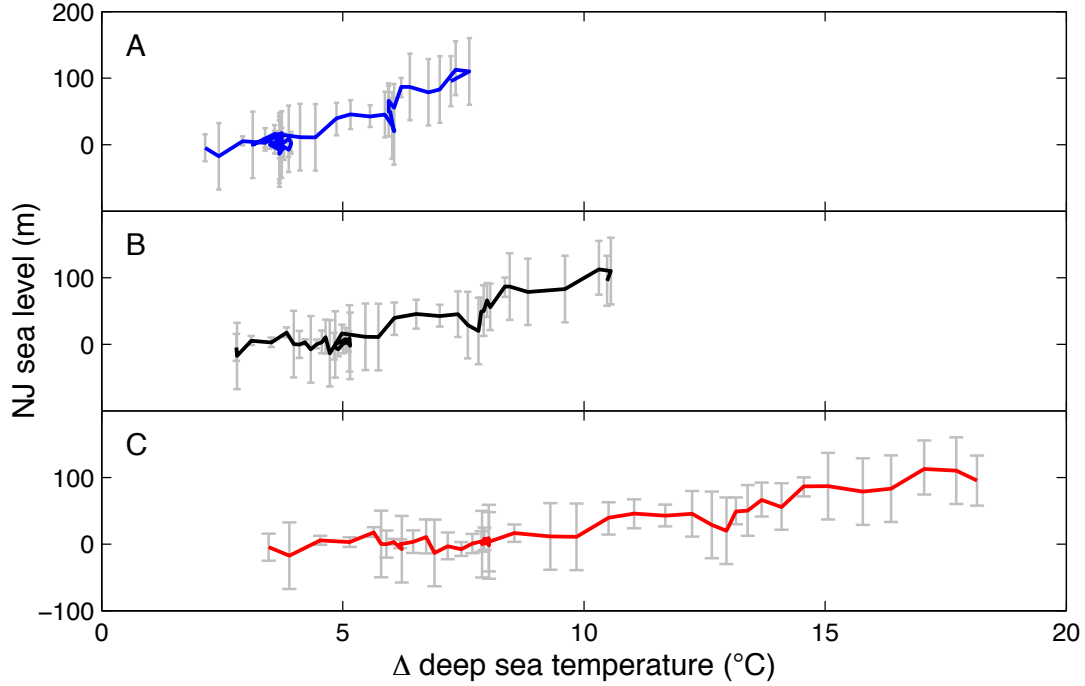
Figure 2.5: *Impact of different past seawater Mg/Ca scenarios on crossplots of Lear et al. (2000) DST data against Kominz et al. (2008) New Jersey regional sea level data. (a) For constant seawater Mg/Ca scenario. (b) Best estimate scenario of Lear et al. (2000) for seawater Mg/Ca linearly increasing from 50 Ma value of 3.85 mol mol$^{-1}$ (Wilkinson and Algeo, 1989) to present-day concentration of 5.2 mol mol$^{-1}$. (c) High temperature estimate for seawater Mg/Ca linearly increasing from 50 Ma value of 1.5 mol mol$^{-1}$ (Lear, 2007)*

### 2.1.3 Function Selection

We next explore various functions which can describe the observed relationship in the temperature and sea level data. Note that we do not claim that sea level is related to temperature by a continuous function, and suggest reasons for why discontinuity may arise later on, but explore possible functions which may describe this relationship as it has implications for semi-empirical sea level projections, which do rely on a continuous function (Rahmstorf, 2007; Grinsted et al., 2008; Orlić and Pasarić, 2013). The first function we test against the temperature and sea level data is a linear function. A linear form for the temperature to sea level relationship is suggested by Archer (2007). This is based on LGM, middle Pliocene, and Eocene temperature and sea level estimates, periods when temperature and sea level were significantly different to present. Archer (2007) used LGM sea level of ∼120 m lower than present (Fairbanks, 1989) and

temperatures of $4 - 7\,°$C colder than present (Waelbroeck et al., 2002; Schneider von Deimling et al., 2006; Rahmstorf, 2007). In the middle Pliocene ($\sim$3 Ma), Archer (2007) suggests that temperatures were $2 - 3\,°$C warmer than present and sea level was $25 - 35$ m higher than present (Dowsett et al., 1994). In the late Eocene (40 Ma), Archer (2007) suggests that temperatures may have been $4 - 5\,°$C warmer than present and sea level was 70 m higher than present, i.e., assuming ice-free conditions but not correcting for isostatic effects (e.g., Miller et al., 2009b). This temperature estimate, comparable to the estimate of Covey et al. (1996), is lower than more recent Eocene temperature estimates. The Covey et al. (1996) Eocene surface temperature estimate was based on an integration of a temperature anomaly against latitude profile. This included Eocene low-latitude temperatures that were cooler than present, based on $\delta^{18}$O of planktic foraminifera (Zachos et al., 1994). It is acknowledged that the planktic $\delta^{18}$O values on which these cool low-latitude SSTs are based are affected by diagenesis, meaning that the signal is contaminated with cooler deeper ocean temperatures (Zachos et al., 1994; Pearson et al., 2007). Therefore, it is likely that this Eocene (40 Ma) temperature estimate is too low.

The approach of Archer (2007) is recreated in the insets of Figures $2.6 - 2.8$ with a linear function that is forced through the origin, i.e., constrained to modern sea level and temperature. Their approach is intended as a tentative approximation only and is not based on physical insights or modelling work. Although a linear model may be a fair approximation of the present-day temperature to sea level relationship, when the greatest contributor to sea level rise is thermal expansion (Vermeer and Rahmstorf, 2009), on longer timescales or for larger temperature changes when the greater contribution comes from glaciers and ice sheets it may be less applicable (Pollard and DeConto, 2005; Vermeer and Rahmstorf, 2009; de Boer et al., 2010). The linear models to be used are shown in equations (1) and (2), where $S_L$ is sea level, $T$ is temperature, $m$ is the rate of change of sea level with change in temperature, and $c$ is the intercept on the sea level axis.

$$S_L = mT \tag{2.1.1}$$

$$S_L = mT + c \tag{2.1.2}$$

In addition to linear functions, both forced (equation 2.1.1) and unforced (equation 2.1.2) through the origin, nonlinear functions are used to describe the relationship between temperature and sea level. The nonlinear relationship is based on both GCM-ice sheet modelling and observation-constrained modelling (Huybrechts, 1993; Pollard and DeConto, 2005; de Boer et al., 2010). The proposed nonlinear relationship varies from a single-stepped relationship (Huybrechts, 1993; de Boer et al., 2010) to a two-step relationship (Pollard and DeConto, 2005). An inverse hyperbolic sine function can be used to describe the single-stepped form (equation 2.1.3) and a double inverse hyperbolic sine function can replicate the two-stepped form (equation 2.1.4):

$$S_L = a \sinh^{-1}\left(\frac{T-b}{c}\right) + d \tag{2.1.3}$$

$$S_L = \left(a_1 \sinh^{-1}\left(\frac{T-b_1}{c_1}\right)\right) + \left(a_2 \sinh^{-1}\left(\frac{T-b_2}{c_2}\right)\right) + d \tag{2.1.4}$$

In equation (2.1.3), $a$ is the magnitude of the sea level change, $b$ is the midpoint on the temperature axis, $c$ is the peak rate of change in sea level with change in temperature, and $d$ is the midpoint on the sea level axis (Siddall et al., 2010b). This function can replicate the form of the modelled results of de Boer et al. (2010), showing the increased sea level to temperature response out of the quasi-stable interglacial state and also how the sea level response asymptotes as ice-free conditions are approached. This function is not based on ice dynamics, but is chosen because it is a sigmoid (s-shaped) function that can replicate the form of the relationships in the data. The single-step model is also consistent with early GCM ice sheet modelling work of Huybrechts (1993). The double inverse hyperbolic sine is also not based on ice sheet dynamics but is chosen because it can replicate the two-stepped form seen in the modelling work of Pollard and DeConto (2005). The double inverse hyperbolic sine function can also take a single-stepped form if it is present in the data and both nonlinear functions can adopt a straight line form (i.e. linear).

46

### 2.1.4 Fitting method

Because there are significant errors in both the proxy sea level and temperature data, when fitting the functions to the data, orthogonal regression is used. Least squares regression attempts to minimise the sum of squared errors on the y-axis (response) and assumes that errors on the x-axis (predictor) are minimal. However, in this instance the predictor, DST or SST, contains significant error. It is likely that this is a common instance when performing regression within paleoclimatology, which is often ignored. Prior to fitting the data are nondimensionalised, by dividing by the standard deviation, to avoid over-fitting to one axis. Orthogonal errors can be calculated for a linear function from the slope of the line. An optimum fit can then be found using an optimisation algorithm (e.g. Krystek and Anton, 2007). For a nonlinear function the orthogonal errors are not as easily calculated, as the closest point on the curve to each data point is unknown.

Here we approximate the orthogonal errors using a finite difference approach. The fit is optimised using a genetic algorithm (GA). The GA we have developed is similar to that described by Gulsen et al. (1995). This "global solver" is used in combination with a "local solver", which is better suited to finding a local minimum (MATLAB fminunc function). As the GA contains a random element, it may not find the same minimum every time it is run, although in practice if the GA is run for long enough the fits are very similar. In summary, the GA contains a population of coefficients. The population members are randomly mixed in each generation, with the worst members in terms of goodness of fit then being culled. This allows the best members of the population to remain and keep improving the fit until there is either no further improvement or the maximum number of generations is reached.

The GA is given the coefficients from a least squares fit as a starting point. Random starting coefficients for the population size are then selected from a normal distribution with the starting coefficient as a mean. The goodness of fit, calculated from the sum of squared orthogonal errors, is calculated for the entire population. The population is ranked by goodness of fit and the bottom half culled. The remaining half are randomly sorted into pairs, and a crossover mechanism creates new members, which are the mean of the parent coefficients. Additionally, a mutation mechanism creates new coefficients from a uniform distribution of 2 times the range of all the parent coefficients. The goodness of fit is calculated for the new members and the cycle repeated. The GA is run for 200 generations but can be terminated earlier if there is no improvement after 50 generations.
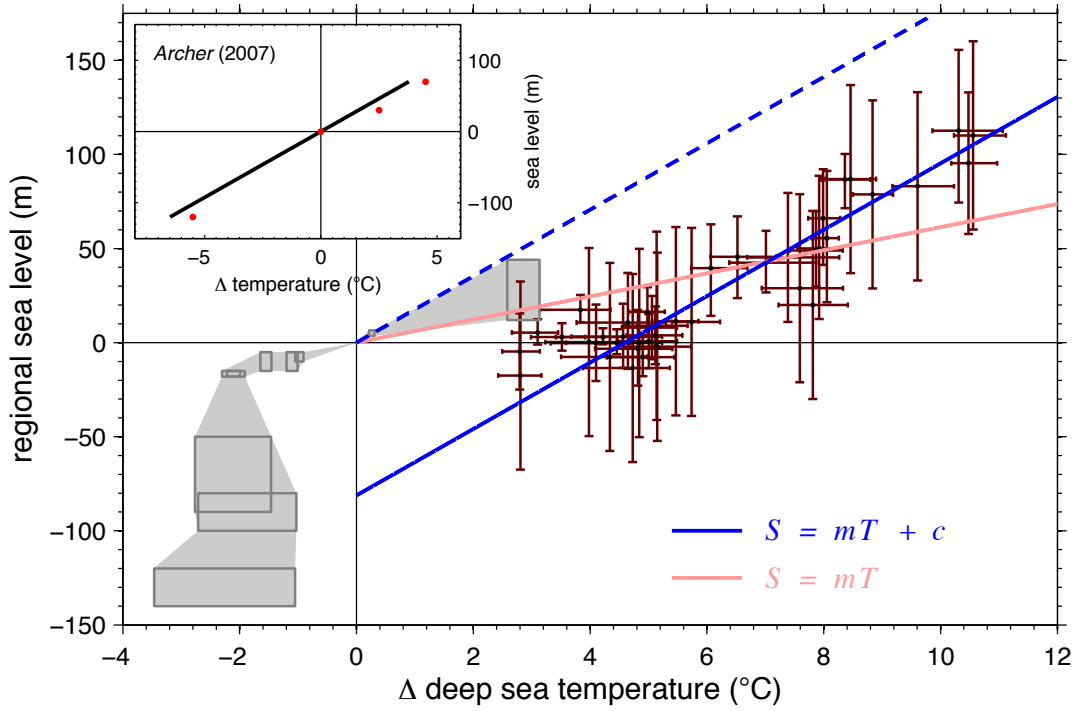
Figure 2.6: *Data as per Figure 2.1, showing deep-sea temperature against regional sea level, with Archer (2007) linear trend shown inset. Linear functions are fit to the data of Lear et al. (2000) and Kominz et al. (2008) using orthogonal regression; functions are not constrained by additional Plio-Pleistocene data (grey boxes) (Siddall et al., 2010a). The pink line is forced through the origin. The dashed line is "corrected" for potential isostatic offset by shifting on the y-axis so that it is consistent with modern temperature and sea level (see text).*

## 2.2 Synthesis

The linear function is fitted to all of the temperature versus sea level plots for high-latitude Southern Hemisphere SST, low-latitude SST, and DST. The single $\sinh^{-1}$ function is fitted to the high-latitude Southern Hemisphere SST and DST plots, and the double $\sinh^{-1}$ function is fitted to the DST plot only. Independent data show the relationship between the relevant temperatures and sea level at several intervals in the Plio-Pleistocene (Rohling et al., 2009; Herbert et al., 2010; Siddall et al., 2010a). These additional Plio-Pleistocene data are included in the figures as a guide; the functions are not constrained by these additional data.
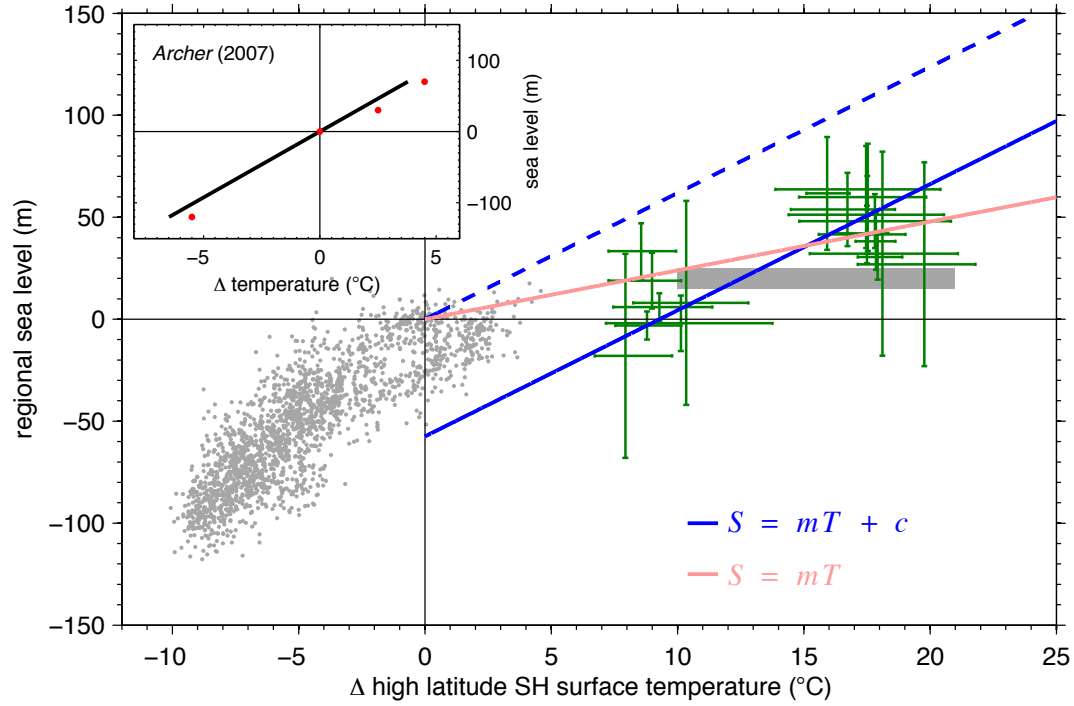
Figure 2.7: *Data as per Figure 2.2, showing high-latitude Southern Hemisphere surface temperature against regional sea level, with Archer (2007) linear trend shown inset. Linear functions are fit to the data of Kominz et al. (2008) and Liu et al. (2009) using orthogonal regression; the functions are not constrained by the additional Plio-Pleistocene data shown in grey. The pink line is forced through the origin. The dashed blue line is "corrected" for potential isostatic offset in the NJ sea level data by shifting on the y-axis so that it is consistent with modern temperature and sea level (see text).*

## 2.2.1   Testing linear functions

The linear function (Figures $2.6 - 2.8$) highlights the positive correlation between sea level and DST or SST. However, there are important constraints that mean a linear model is not necessarily appropriate here. The y-intercept of the linear models suggests that for modern DSTs sea level would be approximately $-81$ m (Figure 2.6), for high-latitude Southern Hemisphere SST it would be $-57$ m (Figure 2.7), and for low-latitude SST it would be $-32$ m (Figure 2.8). Alternatively the linear function can be forced through the origin, i.e., be constrained to modern sea level and temperature, but this produces a poor fit to the DST and high-latitude Southern Hemisphere SST data, although it produces a reasonable fit to the low-latitude SST data

It is possible that the NJ sea level data contain a systematic offset due to isostatic effects
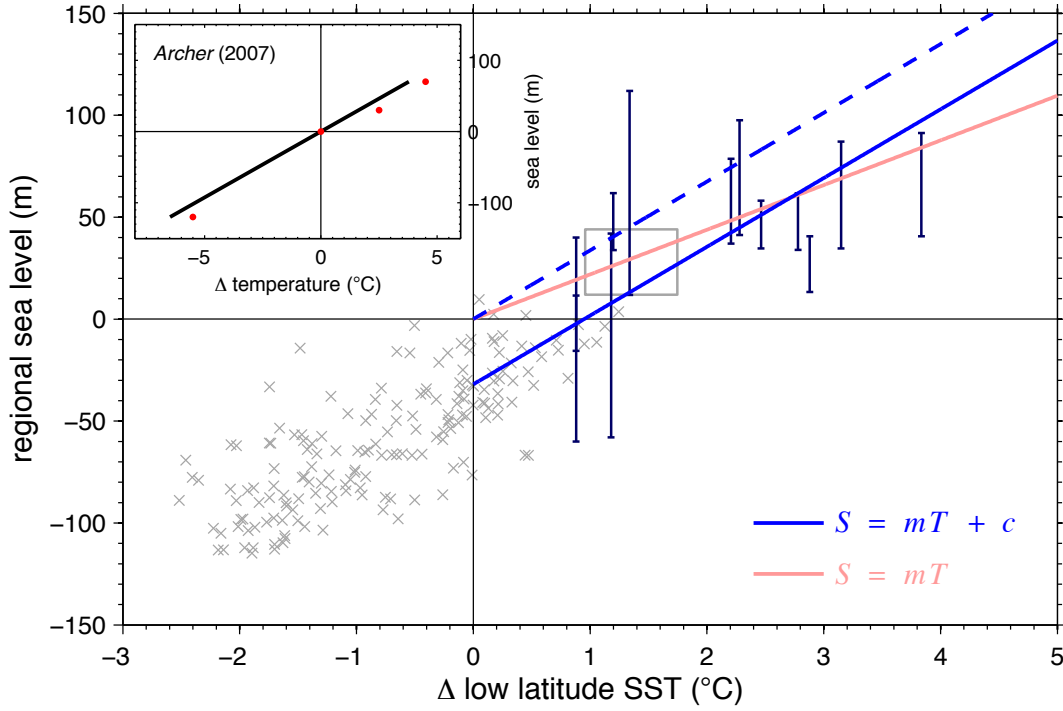
Figure 2.8: *Data as per Figure 2.3, showing low-latitude SST against regional sea level, with Archer (2007) linear trend shown inset. Linear functions are fit to the data of Kominz et al. (2008) and Lear et al. (2008) using orthogonal regression; the functions are not constrained by the additional Plio-Pleistocene data shown in grey. The pink line is forced through the origin. The dashed blue line is "corrected" for potential isostatic offset in the NJ sea level data by shifting on the y-axis so that it is consistent with modern temperature and sea level (see text)*

during the Pleistocene. Sea level on the NJ margin continued to rise throughout the Holocene and is presently on the order of ∼10 m lower than equilibrium, assuming an exponential curve to equilibrium (see Miller et al., 2009a their Figure 3; Raymo et al., 2011). Sea level records from other regions suggest Holocene stabilisation, following a large sea level increase due to the melting of the major glacial period ice sheets, from $9 - 6$ ka (Siddall et al., 2003). A crude "correction" for this potential systematic isostatic effect is to shift the data set on the y axis so that the function passes through the origin (dashed line in Figures $2.6 - 2.8$). However, this would imply an offset due to postglacial isostasy of 81, 57, or 32 m for the DST, high-latitude Southern Hemisphere SST, and low-latitude SST data, respectively. This is significantly larger than the ∼10 m from equilibrium previously mentioned (Raymo et al., 2011). This simple offsetting approach is also applied to the non-linear functions in Figures $2.9 - 2.11$.

A second constraint that means a linear function may be a poor representation of the data is
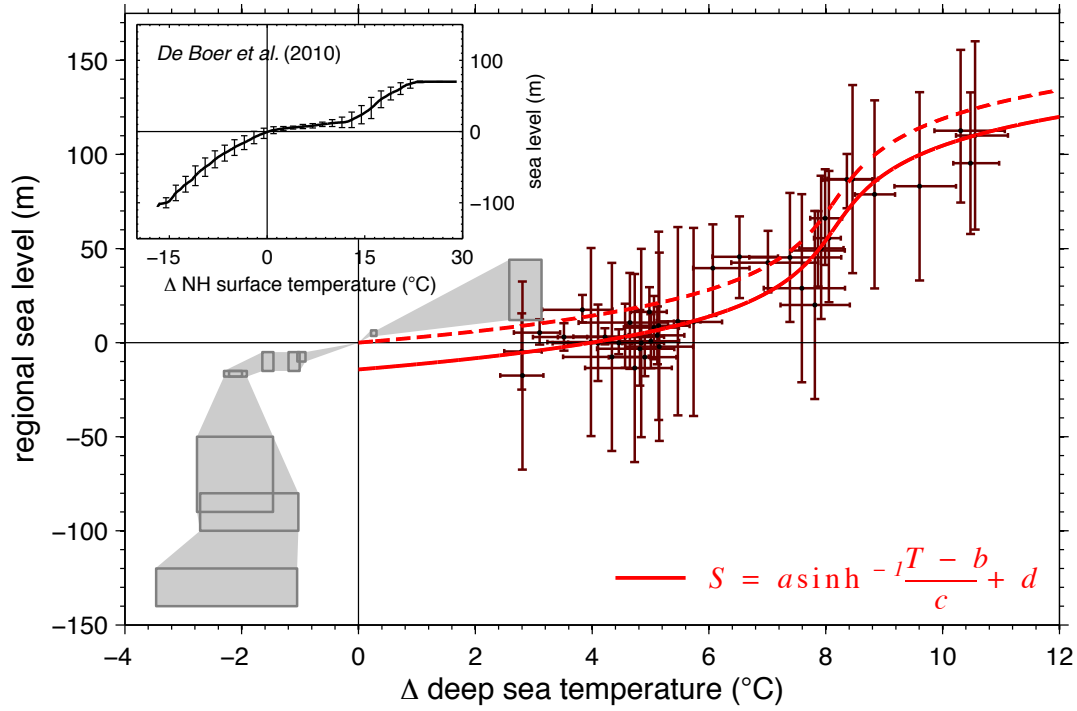
Figure 2.9: *Data as per Figure 2.1, showing deep-sea temperature against regional sea level, with de Boer et al. (2010) observation-constrained modelled results inset. Single inverse hyperbolic sine function fit to Kominz et al. (2008) New Jersey regional sea level data and Lear et al. (2000) Mg/Ca deep-sea temperature. Dashed line is "corrected" for potential isostatic offset by shifting function on y-axis so that it is consistent with modern deep-sea temperature and sea level (see text).*

that once ice-free conditions are reached the function should asymptote to the thermal expansion gradient. The linear function is also not consistent with the independent Plio-Pleistocene data, except for the low-latitude SST data (Figure 2.8). Conceptually, a linear fit is not consistent with the modelling work of de Boer et al. (2010), which clearly showed different temperature thresholds for Northern Hemisphere and Southern Hemisphere glaciation.

## 2.2.2 Testing nonlinear functions

An inverse hyperbolic sine function can describe a single-stepped form, similar to the work of de Boer et al. (2010), for temperatures warmer than present (Figure 1.6). This function is not fitted to the low-latitude SST data, as a single-stepped form is not apparent in these data. This function can partially satisfy the independent constraints highlighted above. For modern DSTs this function predicts sea level of −14 m (Figure 2.9). If there is a sea level
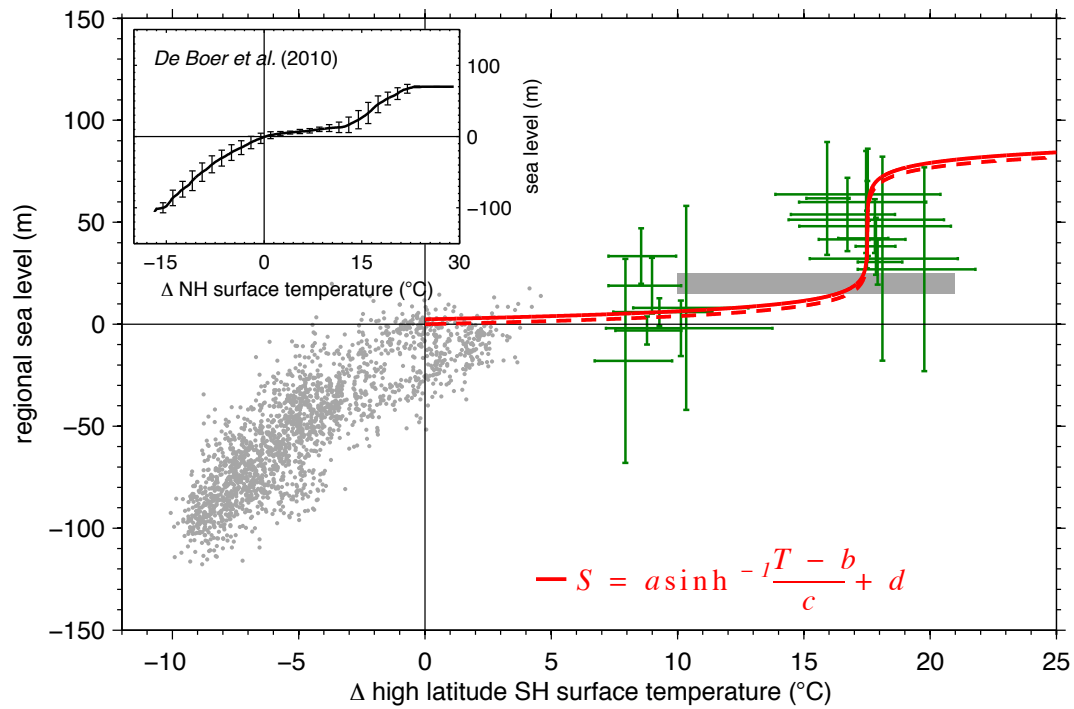
Figure 2.10: *Data as per Figure 2.2, showing high-latitude Southern Hemisphere surface temperature against regional sea level, with de Boer et al. (2010) observation-constrained modelled results inset. Single inverse hyperbolic sine function fit to Kominz et al. (2008) New Jersey regional sea level data and Liu et al. (2009) high-latitude Southern Hemisphere SST data. Dashed line is "corrected" for potential isostatic offset by shifting function on y-axis so that it is consistent with modern temperature and sea level (see text).*

offset due to Holocene isostasy then it could conceivably be of this magnitude (Raymo et al., 2011), although for the high-latitude Southern Hemisphere SST data, the function predicts modern sea level of +2 m (Figure 2.10). For temperatures cooler than present, the sea level to high-latitude Southern Hemisphere surface temperature relationship has been suggested by Rohling et al. (2009) to represent an exponential curve. The single-stepped function asymptotes toward modern temperature, which could join an exponential curve for temperatures cooler than present. The single-stepped form joining an exponential curve is similar to the relationship seen in the modelling work of de Boer et al. (2010).

The upper asymptote for the single-step function suggests a sea level of 110 m for DSTs of +10 °C and a sea level of 80 m for high-latitude Southern Hemisphere SSTs of +20 °C. This is well above the ice-free thermal expansion gradient, as shown in Figures 2.1 and 2.2. This again highlights that the NJ sea level record contains other drivers of sea level change, such as ocean
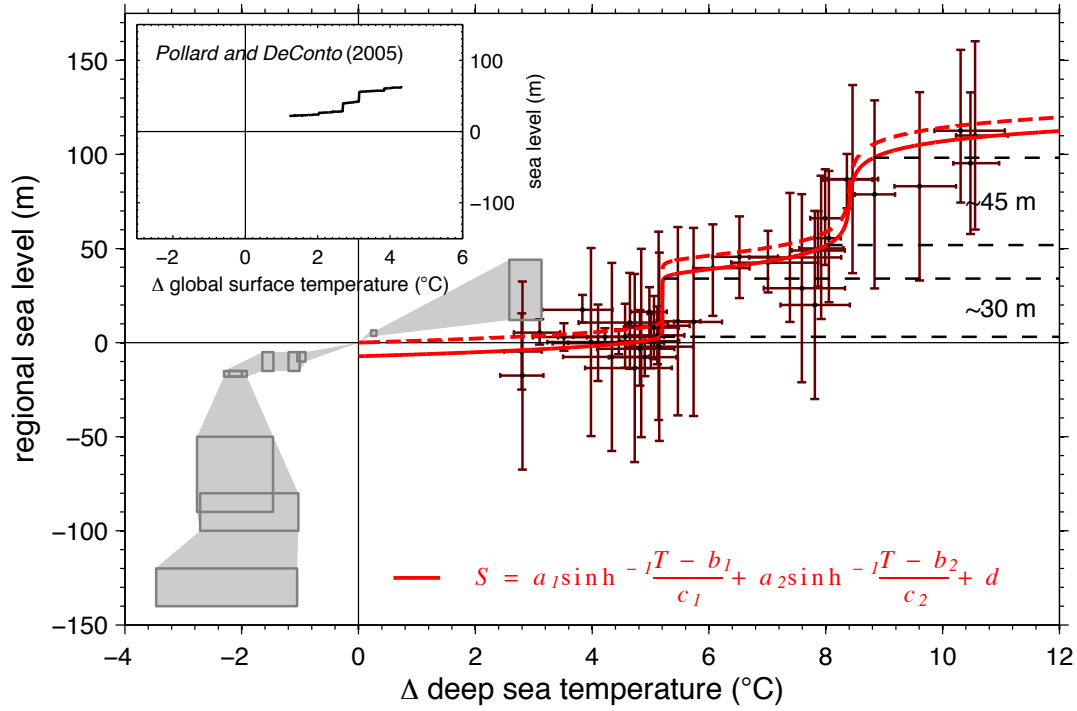
Figure 2.11: *Data as per Figure 2.1, showing deep-sea temperature against regional sea level, with Pollard and DeConto (2005) ice sheet modelled results, for cooling direction without orbital variation, shown inset. Double inverse hyperbolic sine function fit to Kominz et al. (2008) New Jersey regional sea level data and Lear et al. (2000) Mg/Ca deep-sea temperature. Dashed red line is "corrected" for potential isostatic offset by shifting function on y-axis so that it is consistent with modern temperature and sea level (see text). The magnitude of the sea level changes occurring in the steps is highlighted, showing a total sea level change of ∼75 m, which is greater than for the two-step model of Pollard and DeConto (2005), suggesting that the NJ sea level record contains other effects (see text).*

basin volume changes and potential isostatic changes. The high-latitude Southern Hemisphere SST plot against sea level (Figure 2.10) shows a steep transition, with the step occurring in the second cluster of data. It is likely that this is caused by discrepancies in the age models of the two data sets, as the sea level fall in the Kominz et al. (2008) record at the EOT precedes the EOT temperature fall in the record of Liu et al. (2009). It is important to bear in mind the ±0.5 Ma age error estimate of the Kominz et al. (2008) record. If the age models were better matched, the relationship between high-latitude Southern Hemisphere SST and sea level may be different.

In addition to the single-stepped nonlinear function, a two-stepped nonlinear function is fitted to the DST data (Figure 2.11). The function identifies the two steps seen in the time-

ordered data. As previously mentioned, this two-stepped form shows some consistencies with the modelling work of Pollard and DeConto (2005), although the sea level change in the steps of $\sim$75 m is greater than the $\sim$50 m ($\sim$33 m after accounting for hydroisostasy for comparison with the NJ record) shift shown by Pollard and DeConto (2005), and the timescales are significantly different. The function produces extremely rapid rates of sea level change at the thresholds of the steps. Step B is due to the rapid formation of ice at the EOT. As previously discussed, step B is likely to be overly steep because of the lack of temperature change in the Lear et al. (2000) Mg/Ca data set at the EOT. The origin of step A ($\sim 44 - 42$ Ma) is discussed in more detail below. The function is offset on the y axis by $\sim$4 m (dashed line in Figure 2.11) to account for the possible isostatic error.

### 2.2.3 Synthetic $\delta^{18}$O

An alternative way to test the sea level and DST data is to create a synthetic $\delta^{18}$O record using a simple calibration and compare it with the benthic $\delta^{18}$O stack (Figure 2.12). Here we convert the NJ sea level record and Mg/Ca DST record to a $\delta^{18}$O signal using a calibration of 0.01 ‰ m$^{-1}$ (Pekar et al., 2002; Miller et al., 2009b) and 0.25 ‰ °C$^{-1}$ (Zachos et al., 2001a), respectively. Prior to this conversion, the NJ sea level record is adjusted for hydroisostasy by multiplying by 1.48 (Pekar et al., 2002). We remove thermal expansion from the sea level record using the DST record and a calibration of 1 m °C$^{-1}$. This sea level calibration is possibly an oversimplification when used on such a long timescale. It is possible that the first ice caps to form on Antarctica would have had a different isotopic composition to the present-day ice sheets (DeConto et al., 2008; Katz et al., 2008). The modelling work of de Boer et al. (2012a) shows that the scaling factor of seawater $\delta^{18}$O to sea level has not remained constant over the last 40 Ma, although they suggest that the constant calibration, as used here, is a reasonable approximation. Additionally, the NJ sea level data set contains a signal from ocean basin changes and may include regional tectonic effects, which are not related to $\delta^{18}$O . We do not attempt to remove these effects from the NJ record, as attempted by Cramer et al. (2011), and acknowledge that this is a limitation of this very simple approach. The synthetic record is tied to the benthic $\delta^{18}$O stack (Zachos et al., 2008) at 50 Ma. From $10 - 0$ Ma, sea level data are not available (Kominz et al., 2008); in the work by Miller et al. (2005a) sea level in the late Miocene and Plio-Pleistocene is based on a calibration of the benthic $\delta^{18}$O record. We extend the synthetic $\delta^{18}$O from $10 - 0$ Ma using the actual benthic $\delta^{18}$O stack, with the dotted line in Figure 2.12.
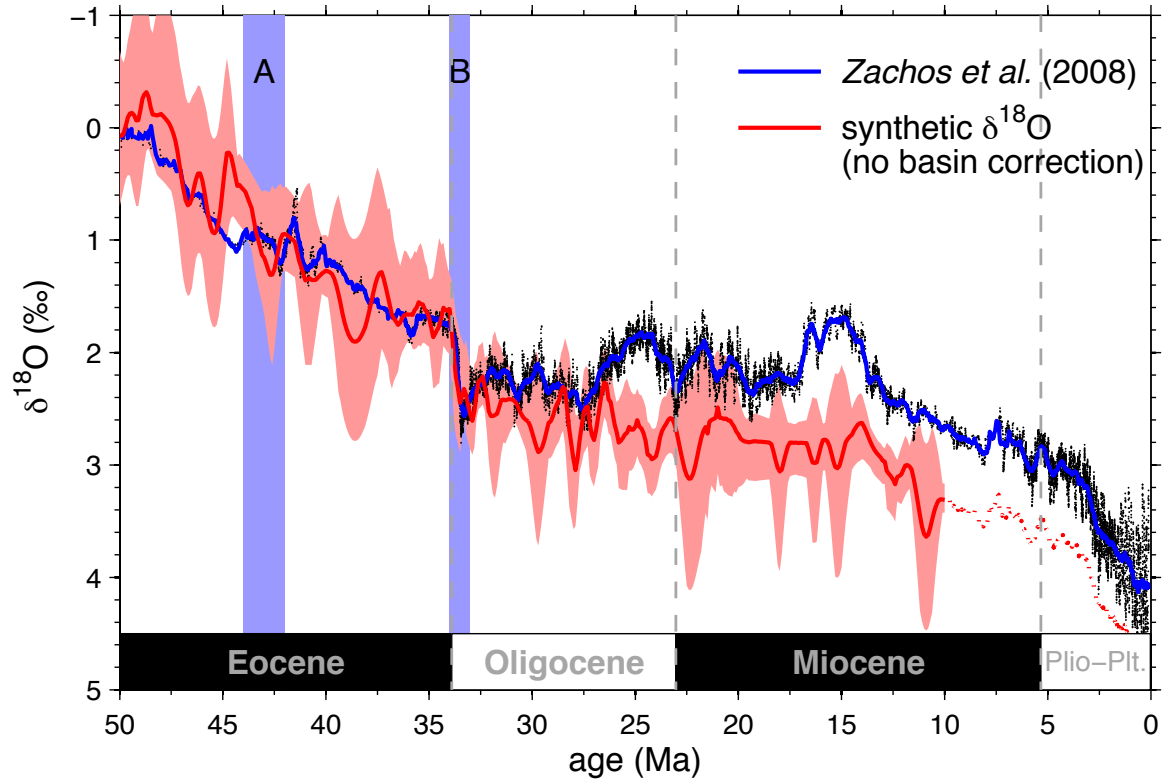
Figure 2.12: *Synthetic $\delta^{18}O$ (red line) plotted with benthic $\delta^{18}O$ stack (blue line) of Zachos et al. (2008). The synthetic record is created using Kominz et al. (2008) sea level record and Lear et al. (2000) temperature record. The sea level data are first multiplied by 1.48 to account for hydroisostasy (Pekar et al., 2002), thermal expansion is removed using the temperature record of Lear et al. (2000) and a factor of 1 m $^\circ C^{-1}$, and sea level is then converted to $\delta^{18}O$ using a 0.01 ‰ $m^{-1}$ calibration (Pekar et al., 2002; Miller et al., 2009b). Ocean basin changes are not removed from the sea level record, and this is a potential source of error. The Lear et al. (2000) temperature record is converted to $\delta^{18}O$ using a 0.25 ‰ $^\circ C^{-1}$ calibration (Zachos et al., 2001a). These two signals are combined to create the synthetic $\delta^{18}O$ curve. From 10 to 0 Ma there are no sea level data, so the synthetic $\delta^{18}O$ curve (dotted red line) tracks the benthic $\delta^{18}O$ stack for the period 10-0 Ma.*

The synthetic record follows the general trend of the benthic $\delta^{18}$O stack (Figure 2.12). The $\sim$1.6 ‰ increase in the benthic $\delta^{18}$O stack from 50 Ma to the EOT is reproduced in the synthetic $\delta^{18}$O record, with $\sim$1.1 ‰ due to temperature and $\sim$0.5 ‰ due to sea level. However, the large increase in the synthetic $\delta^{18}$O record at $\sim 44 - 42$ Ma, which is responsible for step A in the temperature and sea level crossplots, is not seen in the benthic $\delta^{18}$O stack. The large increase in $\delta^{18}$O at the EOT is seen in the synthetic record (step B), although it is of a slightly lower magnitude than the increase in the benthic $\delta^{18}$O stack. This is probably due to the lack of apparent cooling in the uncorrected Mg/Ca DST record. The synthetic $\delta^{18}$O record diverges from the benthic $\delta^{18}$O stack in the Miocene, in particular during the middle Miocene. Both the DST and sea level records used in the synthetic $\delta^{18}$O record have poor data coverage during the Miocene.

## 2.3 Discussion

The sea level and temperature synthesis generates several points for discussion; the majority of this discussion focuses on the DST to sea level relationship as the DST record is more complete than the SST record. The additional surface temperature records for the EOT are useful in determining whether there is a nonlinear response to temperature forcing across this boundary, as may be suggested by the uncorrected (for carbonate saturation effects) DST data. If the two-step function is appropriate, and if the first step (step A) is due to glacioeustasy, then it implies the formation of significant land ice in the Eocene. Not all of the sea level variability is due to the formation of land ice; there are thermosteric and ocean basin volume components and potential regional tectonic effects. However, the rate and magnitude of the sea level decline in the raw NJ sea level record may suggest glacioeustasy as a cause (Miller et al., 2008b). The significance of these steps should be considered in combination with the multiple sources of error in the data discussed in Sections 1.2.1 and 1.2.2. Finally, we discuss the types of nonlinearity that might be expected when looking at the temperature to sea level relationship from ice-free conditions to full Northern Hemisphere glaciation. Broadly, the expected nonlinearity can be divided into two types: (1) as seen in some ice sheet modelling studies (Huybrechts, 1993; Pollard and DeConto, 2005; Langebroek et al., 2009), where a small temperature forcing, near the glacial threshold, generates a large change in ice volume, and (2) nonlinearity caused by the different glacial thresholds for Northern and Southern Hemisphere glaciation. This second nonlinearity occurs as the ice sheet carrying capacity of the Antarctic continent is reached before

the glacial threshold for Northern Hemisphere glaciation (de Boer et al., 2010).

### 2.3.1 Eocene ice and the origins of step A

The extent of Antarctic glaciation prior to the EOT and whether Northern Hemisphere ice sheets existed before the Pliocene are two questions still subject to much debate (Miller et al., 2005a; Pekar et al., 2005; Moran et al., 2006; Eldrett et al., 2007; Coxall and Pearson, 2007; Cox et al., 2010; Dawber and Tripati, 2011; Dawber et al., 2011). Shackleton and Kennett (1975) used the $\delta^{18}O$ record to hypothesise that a continent-sized ice sheet first formed on Antarctica $\sim$15 Ma. Matthews and Poore (1980) proposed an alternative theory, which suggested that there was an earlier ice formation event between the Eocene and Oligocene. As previously discussed (Sections 1.2.3 and 2.2.3), the $\delta^{18}O$ record of benthic foraminifera shows a rapid increase in $\delta^{18}O$ at the EOT (Zachos et al., 2008).

The sequence stratigraphy record of sea level from the NJ margin shows large changes earlier than the Oligocene (Miller et al., 2005a). The rate and magnitude of these sea level changes may imply that they are due to changes in ice volume. In the raw NJ sea level data, step A is seen as a sea level fall of $\sim$35 m over $\sim$0.7 Ma (Figure 1.3; Kominz et al., 2008). The relatively fast rate of these sea level changes has been suggested to rule out other factors that could cause a sea level change of this magnitude, such as variations in ocean basin volume (Miller et al., 2005a). A thermosteric response could explain the rate of sea level change but not the magnitude. This points to at least ephemeral ice sheets on Antarctica during the Eocene. This is controversial, as this same argument used to justify ice mass changes in the Eocene can be extended for the whole of the 100 Ma NJ record and would imply that ephemeral ice sheets were present during the whole of the Cenozoic and into the Late Cretaceous, a time that was thought to be ice free (Miller et al., 2005b).

Miller et al. (2008b) used the modelled ice sheet maps of DeConto and Pollard (2003a) to estimate how large an ice sheet would be required to explain each of the transitions in the Miller et al. (2005a) sea level record. Clearly, a larger sea level transition would require the formation or loss of a larger ice sheet than a smaller sea level transition. Smaller ice sheets could form under the higher atmospheric $CO_2$ concentrations of the Eocene in the Antarctic mountain regions (DeConto and Pollard, 2003a; Pagani et al., 2005). A larger ice sheet would require a lower atmospheric $CO_2$ concentration than that shown in the Eocene proxy $CO_2$ records. All of the pre-Oligocene transitions in the Miller et al. (2005a) record are of a small enough magnitude

to be explained by the formation or loss of isolated ice caps in the Antarctic mountain regions (Miller et al., 2008b). Only the larger sea level transition at the EOT would require growth of a continental sized Antarctic ice sheet.

A potential problem with this hypothesis is that it is dependent on the existence of high-topographic regions during the Late Cretaceous and Eocene. However, the paleo-topography of Antarctica is poorly known. Although some authors suggest that uplift of the trans-Antarctic mountains began in the Cretaceous (Fitzgerald, 2002), others place uplift much later, in the Eocene (ten Brink et al., 1997). The hypothesis of Miller et al. (2008b) partially breaks down if trans-Antarctic mountain uplift did indeed occur more recently. However, even if the trans-Antarctic mountains were not uplifted, the other high-elevation regions of the Gamburtsev Mountains and Dronning Maud Land could have harboured isolated ice caps; indeed, the Gamburtsev Mountains are considered to be the major early ice nucleation centre for ice growth (Huybrechts, 1993; DeConto and Pollard, 2003a,b) and to have formed considerably before the Cenozoic (e.g., Cox et al., 2010).

Browning et al. (1996) looked at links between $\delta^{18}O$ data in the Eocene with an earlier version of the NJ sequence stratigraphy sea level record. They suggested that increases in benthic and planktonic $\delta^{18}O$ correlate well with hiatuses in the sea level record from the late to middle Eocene onward (later than $43 - 42$ Ma) and may suggest a glacioeustatic control. There is little correlation in the earlier Eocene ($49 - 43$ Ma) between the sea level record and the $\delta^{18}O$ record, meaning that a glacioeustatic control is unlikely. Therefore, they suggest that the late to middle Eocene ($43 - 42$ Ma) could mark the onset of Antarctic glaciation. This is consistent with the timing of the first step ($\sim 44 - 42$ Ma) in the two-step model. This is slightly earlier than proposed by Billups and Schrag (2003) as the possible onset of glaciation. They suggested that the good agreement between their Mg/Ca record and the benthic $\delta^{18}O$ record in the early Eocene implied DST as a sole control on benthic $\delta^{18}O$. From $\sim 40$ Ma the Mg/Ca record diverges from the $\delta^{18}O$ record, suggesting that ice growth may have started to affect the benthic $\delta^{18}O$ ratios (Billups and Schrag, 2003).

If ephemeral glaciation did begin in the late to middle Eocene and ice caps were present in Antarctica, then it would seem likely that the rapid increase in atmospheric $CO_2$ during the MECO ($\sim 40$ Ma) (Bijl et al., 2010) would have had an impact on ice volumes. This event is characterised by a rapid and large decrease in benthic $\delta^{18}O$ (Zachos et al., 2008). This benthic $\delta^{18}O$ shift suggests a rapid increase in DSTs, which may have been combined with decreasing

ice volume. If this shift in benthic $\delta^{18}O$ was due to surface warming alone then it would require an increase in DST of $\sim 4 - 5$ °C (Bijl et al., 2010). Bijl et al. (2010), using both TEX$_{86}$ and $U^{k'}_{37}$ inferred a surface warming of 3 °C and 6 °C, respectively. This means that if this surface warming reached the deep sea, a reduction in ice volume is not needed to explain the large benthic $\delta^{18}O$ shift at the MECO (Bijl et al., 2010). This would suggest that either ice sheets were not present prior to this event or that they were not significantly affected by this rapid but brief warm interval.

Dawber et al. (2011) suggested that stratigraphic sequences from the Hampshire Basin, United Kingdom, show large amplitude regional water depth changes in the middle Eocene. A negative benthic $\delta^{18}O$ excursion at the same site, comparable to the MECO $\delta^{18}O$ excursion seen in open ocean sites (Bohaty et al., 2009), correlates with a large regional increase in water depth (Dawber et al., 2011). Although it is difficult to determine the cause of this regional change in water depth at the MECO, glacioeustasy is a possibility (Dawber et al., 2011). Dawber and Tripati (2011) could not precisely identify the MECO in their high-resolution middle Eocene benthic $\delta^{18}O$ record from Site 1209 in the Pacific. However, they did identify multiple $\delta^{18}O$ excursions in the middle Eocene (at $\sim 44 - 43$ Ma, $\sim 42 - 40$ Ma and $\sim 39 - 38$ Ma), which could not be reconciled with Mg/Ca based DST estimates from the same site. Although there are age model uncertainties, these events appear to correlate with sequences in the NJ record, including step A (Kominz et al., 2008; Dawber and Tripati, 2011). This could suggest that these $\delta^{18}O$ excursions were caused in part by a change in ice volume (Dawber and Tripati, 2011).

In the smoothed sea level record used in this chapter, the period between 44 Ma and 34 Ma shows little sea level variation. However, the raw sea level record does show significant fluctuations (Kominz et al., 2008). Even if isolated ice caps formed at step A, it is likely that they were ephemeral in this 10 Ma period in order to explain the continued sea level fluctuations in the raw record, whereas step A represents a permanent shift in our DST to sea level crossplot (Figure 2.11). Additionally, the large sea level fall at the EOT, if it can be explained solely by the formation of ice on Antarctica, requires that there was very little ice on Antarctica before the event (Miller et al., 2009b). A closer analysis of the $\delta^{18}O$ data suggested that the EOT (step B) also occurred in two steps, representing the isolated ice cap phase prior to full inception of a continental sized East Antarctic Ice Sheet (Coxall et al., 2005). The two-step function in this chapter might not represent the noise in the data. In summary, while we are confident that there is a glacioeustatic origin behind step B, there is limited supporting evidence for step A in the middle Eocene being caused by glacioeustasy, although this arguably remains the best

explanation for this large and relatively rapid sea level fall in the NJ sea level record.

An independent means of determining the origin of the two steps in our crossplot is the synthetic $\delta^{18}$O record created from the sea level and temperature data for comparison with the benthic $\delta^{18}$O stack (Section 2.2.3). Although there is an increase in the synthetic $\delta^{18}$O record at step A, there is no obvious increase in the benthic $\delta^{18}$O record at the same period in the Eocene (Figure 2.12; Zachos et al., 2008). Therefore, the global compilation of benthic $\delta^{18}$O data do not lend support to step A being caused by glacioeustasy and instead, perhaps, points to either regional tectonic influence on the NJ record or ocean basin changes at this time. When interpreting these steps, it is important to bear in mind the large sources of uncertainty in the NJ sea level record.

### 2.3.2   Causes of nonlinearity in the temperature to sea level relationship

It is useful to separate the nonlinearities that might be expected in the relationship between temperature and sea level into two types: (1) as seen in some ice sheet modelling studies (Huybrechts, 1993; Pollard and DeConto, 2005; Langebroek et al., 2009) where a small temperature forcing, near the glacial threshold, generates a large change in ice volume, and (2) caused by the different glacial thresholds of Northern and Southern Hemisphere glaciation and the ice sheet carrying capacity of the Antarctic continent (de Boer et al., 2012a). The steps that are shown in the DST against sea level plots may suggest the first type of nonlinearity, where a small temperature change leads to a large sea level change. However, as we have discussed, it is likely that data artefacts alter, enhance, or even generate these steps. The lack of cooling in the DST record of Lear et al. (2000) at the EOT is most likely responsible for the steepness of step B, and there is uncertainty as to whether step A in the Eocene is due to glacioeustasy. Additionally, the EOT step is not seen in the surface temperature plots (Figures 2.2 and 2.3). Instead, we suggest that the second type of nonlinearity mentioned above is more evident in the data.

Both the one-step and two-step functions suggest that once a large continental sized EAIS has formed, sea level becomes less sensitive to changing DST; the function asymptotes toward modern sea level and temperature. There is a gap in the sequence stratigraphy sea level data set between 10 and 0 Ma (Kominz et al., 2008), and so the temperature-sea level relationship is not represented in this time period. The sea level record of Miller et al. (2005a) uses a calibration of the benthic foraminifera $\delta^{18}$O record for this time period. Between 10 and 3

Ma in the Miller et al. (2005a) record there is very little sea level variation prior to large sea level fluctuations starting ∼3 Ma associated with the formation of the Northern Hemisphere ice sheets and Pleistocene glacial cycles. In the modelling work of de Boer et al. (2010, 2012a) sea level is also remarkably stable in the period $10 - 3$ Ma, with the majority of variation in the input $\delta^{18}$O data explained by temperature variation. Therefore, the lack of data for the period of $10 - 0$ Ma does not significantly affect this conclusion, although ideally a complete sea level record for this period is needed.

The relationship between both deep-sea and surface air temperature and sea level has previously been studied for temperatures colder than present (Rohling et al., 2009; Siddall et al., 2010a,b). These studies suggest that there is also an asymptotic relationship toward modern sea level from colder temperatures (Rohling et al., 2009; Siddall et al., 2010a,b). The work on temperature and sea level relationships for temperatures colder than present, in addition to this chapter and the work of de Boer et al. (2010), suggests that the present interglacial state is relatively stable in the context of sea level variations over the past 50 Ma, while supporting the existence of "critical thresholds" within the Earth's climate system. The "warm threshold" corresponds to the early Cenozoic major East Antarctic glaciation, whereas the "cold threshold" corresponds to the major Northern Hemisphere glaciations of the Pleistocene. In between these two large thresholds are the glaciations of the West Antarctic and Greenland, which we cannot resolve in this analysis because of the large errors (>10 m) in the sea level data used.

## 2.4   Summary

In this chapter, the relationship between sea level and DST has been synthesised using the Mg/Ca DST record of Lear et al. (2000) and the regional sequence stratigraphy sea level record from the NJ margin (Kominz et al., 2008). This DST to sea level relationship may differ from the surface temperature to sea level relationship on this long timescale if the surface to DST gradient has changed, which could have occurred because of ocean circulation (Nong et al., 2000; Najjar, 2002; Cramer et al., 2009; Katz et al., 2011). We emphasise the significant sources of error and the regional nature of the currently available long-duration data sets. We have investigated the relationship at the low temporal resolution of the available DST data, ∼1 Ma, as such some of the higher-frequency details of the sea level record are not included. In addition to the DST data, we have used SST data across the EOT, as this is a period of major sea level change and a period poorly represented by the current Mg/Ca DST records.

Different functions, justified by previous publications (Huybrechts, 1993; Pollard and De-Conto, 2005; Archer, 2007; de Boer et al., 2010), have been fitted to the data. Important constraints, for example, that a function should pass through modern sea level and temperature, mean that it is unlikely that there is a linear relationship between DST and sea level or high-latitude Southern Hemisphere SST and sea level. However, the relationship between low-latitude temperature and sea level remains ambiguous and could be explained by a linear relationship. A linear function is not consistent with ice sheet modelling studies (Huybrechts, 1993; Pollard and DeConto, 2005; de Boer et al., 2010).

Nonlinear functions, in both one-step and two-step forms, are a more plausible fit to the DST and Southern Hemisphere high-latitude data against sea level plots. It is difficult to determine whether the single-step or two-step function is the most appropriate function given the wide errors in the currently available data. The two-step hypothesis originates from GCM and ice sheet modelling studies where ice build up on Antarctica occurs nonlinearly in a series of steps in response to declining atmospheric $CO_2$ and temperature (Pollard and DeConto, 2005). The first step occurs with the formation of isolated ice caps in the mountain regions of Antarctica before the formation of a continent sized ice sheet in the second step. We underline an important caveat of using the NJ sea level record: the long-term sea level change contains thermosteric and ocean basin volume components and potentially regional tectonic effects. The two-step hypothesis is a glacioeustatic concept, yet when it is applied to the DST and sea level data in this chapter it shows a greater sea level range ($\sim$75 m in the two steps, 100 m in total) than can be explained solely by the formation of the modern ice sheets ($\sim$43 $-$ 54 m as seen from the NJ margin). Additionally, the first step occurs at $\sim$44 $-$ 42 Ma, implying that large, permanent Antarctic ice caps formed in the Eocene, for which there is at present limited supporting evidence. The second step at the EOT in the DST against sea level plot is, at least in part, an artefact of the lack of cooling in the Lear et al. (2000) Mg/Ca DST data set across the EOT. A steep step is not apparent for the SST against sea level plots for the EOT.

The asymptotic relationship between modern temperature and sea level relative to glacial temperatures (i.e., cooler than present, Rohling et al., 2009; Siddall et al., 2010b) or pre-Pleistocene temperatures (i.e., warmer than present, this chapter) suggests that the present interglacial state is relatively stable compared to the overall sea level change observed for the past 50 Ma. However, the implied nonlinear relationship in the DST and high-latitude Southern Hemisphere SST data suggests there are large sea level thresholds for temperatures warmer and colder than present. These are caused by the different glacial thresholds for Northern Hemi-

sphere and Southern Hemisphere glaciation and the size of the Antarctic continent restricting further growth of the East Antarctic Ice Sheet. Given the significant limitations of the currently available DST data, due in part to uncertainties in the past seawater Mg/Ca concentration, it is difficult to determine precisely the temperatures of these thresholds. Unfortunately, the uncertainties within the sea level and temperature proxy data used here are currently too large to resolve potential thresholds associated with smaller-scale glaciation (e.g., <10 m, which could, for example, include the Greenland Ice Sheet and West Antarctic Ice Sheet).

The sea level to temperature relationships in this chapter are based on long-term changes (>1 Ma), which, given that the response time of the ice sheets is <1 Ma (Miller et al., 2005a), we assume is representative of the major ice sheets and sea level in near equilibrium with the climate. Therefore, this relationship is not directly applicable to anthropogenic warming on a centennial timescale. In addition, the current uncertainties in the sea level and temperature proxies used in this chapter precludes an assessment of thresholds that may potentially be associated with todays least stable continental ice sheets (the West Antarctic Ice Sheet and the Greenland Ice Sheet). Hysteresis effects mean that any thresholds are likely to be at higher temperatures for warming than for cooling (we explore this in detail in Chapter 5); this chapter uses Cenozoic data that predominantly show cooling. The temperature thresholds visible in the figures should therefore be seen as low estimates. The temperature to sea level relationships investigated in this chapter use data over a very long time period, which includes significant tectonic change, continental movement, mountain building, and ocean circulation change. All of these effects could have an influence on the palaeo-long-term sea level to temperature relationships and are not relevant to short-term future warming. These important caveats are relevant to all attempts at temperature to sea level synthesis on this long timescale, including that shown in this chapter.

# Chapter 3

# Ice sheet modelling – methods and evaluation

This thesis makes use of existing climate model simulations from a variety of sources, no new climate simulations were performed for this thesis. All ice sheet model simulations shown in this thesis were performed by the author, unless otherwise stated.

## 3.1 Introduction

To address the overall aims of this thesis we use ice sheet modelling to investigate variations in sea level on million-year timescales. Throughout the Cenozoic, the formation and melting of the ice sheets has been the main cause of sea level variation (Miller et al., 2005a). By using modelling, led by the insight gained from the data in the previous chapter, we can gain further understanding of the broad relationship between the Earth's temperature (whether that is the average surface temperature or deep-sea temperature) and sea level. During periods cooler than present the formation and retreat of the North American and Eurasian ice sheets generated large sea level variations (Fairbanks, 1989; Clark et al., 2009). Although the Antarctic ice sheets did expand in periods cooler than present (Anderson et al., 2002; Denton and Hughes, 2002; Huybrechts, 2002), they were largely constrained by the extent of the continent (de Boer et al., 2010, 2012a). The East Antarctic ice sheet was arguably more dynamic in past warm periods (Wilson, 1995; Zachos et al., 2001a) and contributed to large sea level fluctuations in the Oligocene ($33.9-23.0$ Ma) and Miocene ($23.0-5.3$ Ma), and possibly the Eocene ($55.8-33.9$ Ma; Miller et al., 2005a, 2008b). In this thesis we focus on the formation of the large ice sheets, by modelling the Northern Hemisphere ice sheets during the last glacial cycle ($\sim$120 ka $-$ present) and also the formation of the East Antarctic ice sheet at the Eocene-Oligocene transition (EOT). In this chapter we discuss the different model components required to simulate the long term ($10^4 - 10^7$ year) evolution of the ice sheets.

The Quaternary (2.6 Ma $-$ present) is a relatively data-rich time period in the context of paleoclimate and includes several cycles of large-scale glaciation and deglaciation (Martinson et al., 1987; Lisiecki and Raymo, 2005), it is therefore a good test period for ice sheet modelling. This is the period we address first, by modelling the North American and Eurasian ice sheets through the last glacial cycle. There is also a large body of ice sheet modelling literature for this period from which to draw (e.g. Pollard, 1982; Oerlemans, 1982; Abe-Ouchi and Blatter, 1993; Siegert et al., 2001; Zweck and Huybrechts, 2005; Abe-Ouchi et al., 2007; Ganopolski et al., 2010; Gregoire et al., 2012). Modelling this period is not straightforward and there are a number of challenges still subject to much debate, such as the mechanism(s) for deglaciation (e.g. Anderson et al., 2009; Ganopolski et al., 2010; Shakun et al., 2012) and the cause(s) of the Mid-Pleistocene transition (e.g. Raymo et al., 2006; Bintanja and van De Wal, 2008; Elderfield et al., 2012). We do not attempt to enter such debates here, and focus on using the last glacial cycle in order to test our modelling approach. What we learn from modelling the Northern

Hemisphere ice sheets through the last glacial cycle will be applied to our modelling of the East Antarctic ice sheet at the EOT and contribute to our assessment of the qualitative uncertainty in our approach. This objective should be borne in mind when considering the results of this chapter – we are not just attempting to model the last glacial cycle, we are attempting to model the last glacial cycle with a method which can then be applied on much longer timescales and to other regions. It should also be noted that simulating the Northern Hemisphere ice sheets through the last glacial cycle may present additional challenges that are not relevant to simulation of the EAIS. In the Northern Hemisphere, the pattern of ice growth is arguably more complex due to the growth and coalescence of multiple ice sheets. It is therefore possible that this is an overly stern test of our modelling approach.

It would be desirable to directly couple a complex climate model to an ice sheet model (ISM) in order to fully represent any feedbacks between these two systems (Pollard, 2010; Blatter et al., 2011). However, due to limitations of computing power this is presently not feasible for the very long duration simulations ($10^4 - 10^7$ years) performed for this thesis. Such a coupling is only presently feasible for centennial-scale simulations (Blatter et al., 2011). In this chapter, various methods of accounting for potential feedbacks from the growth of an ice sheet on the climate system are discussed, ultimately leading to a preferred method for indirectly coupling a climate model to an ISM. We use a suite of climate model simulations of the last glacial cycle to test these various methods (Singarayer and Valdes, 2010; hereafter referred to as the BBC simulations because they were originally commissioned by the British Broadcasting Corporation for their TV series *The Incredible Human Journey*). The ice sheets respond to various climate forcings, such as changes in the Earth's orbit or atmospheric greenhouse gas (GHG) concentrations (e.g. Abe-Ouchi et al., 2007). The BBC simulations were performed with various climate forcings included and others kept constant (Singarayer and Valdes, 2010). We can therefore use the BBC simulations as a control to test our parameterisation of each of the major climate forcings.

## 3.2   The ice sheet model

The Glimmer ISM used in this thesis follows the conventions of a number of previous large-scale, whole ice sheet ISMs (e.g. Huybrechts, 1993; Abe-Ouchi and Blatter, 1993; Ritz et al., 1997; DeConto and Pollard, 2003a). It makes use of the shallow ice approximation (SIA), a simplification of the ice sheet physics that significantly reduces computational expense (Hutter,

1983). Although higher-order and full Stokes ice sheet models exist (e.g. Morlighem et al., 2010; Seddik et al., 2012), their computational expense currently prohibits their use for the very long duration ($10^4 - 10^7$ years), whole ice sheet simulations conducted in this thesis. For example, Seddik et al. (2012) limited their simulations of the Greenland ice sheet using a full Stokes model to 100 years due to the computational expense of the model. The use of the SIA approximation prohibits the accurate simulation of ice streams or the transfer of mass across the grounding line from terrestrial ice to floating ice shelves. In this thesis we focus on the slow response of the large and predominantly terrestrial ice sheets on long timescales. Similar to previous studies, we consider the SIA acceptable for these purposes (DeConto and Pollard, 2003a).

The mechanics of the Glimmer ice sheet model are fully documented in Rutt et al. (2009), but are summarised here for convenience. The evolution of ice thickness ($H = s - h$, where $s$ is the elevation of the ice surface and $h$ is the elevation of the bed) is based on the continuity equation for an incompressible material:

$$\frac{\partial H}{\partial t} = -\nabla \cdot (\bar{\mathbf{u}}H) + B - S, \tag{3.2.1}$$

where $t$ is time, $\nabla$ is the horizontal divergence operator, $\bar{\mathbf{u}}$ is the ice velocity vector ($\mathbf{u} = u, v$) averaged over the ice thickness, $B$ is the surface mass balance and $S$ is the basal melt rate. This equation states that local ice thickness varies over time based on ice flow (first term on right-hand side), the surface mass balance and the melting or freezing of ice at the base of the ice sheet. Each of these 3 components will be dealt with in turn, starting with the surface mass balance. Additional components of the ice sheet model, which calculate the geothermal heat flux and solid earth deformation through isostasy are also described.

### 3.2.1 Surface mass balance

The surface mass balance ($B$) of an ice sheet is calculated from the inputs of mass (precipitation; $P$) minus the outputs of mass (ablation; $a$). There are various approaches for representing the surface mass balance in an ISM. Here we use the precipitation and temperature output from a climate model to calculate the mass balance, using the commonly adopted positive degree day (PDD) scheme to calculate ablation (Reeh, 1991). The PDD scheme is based on the assumption
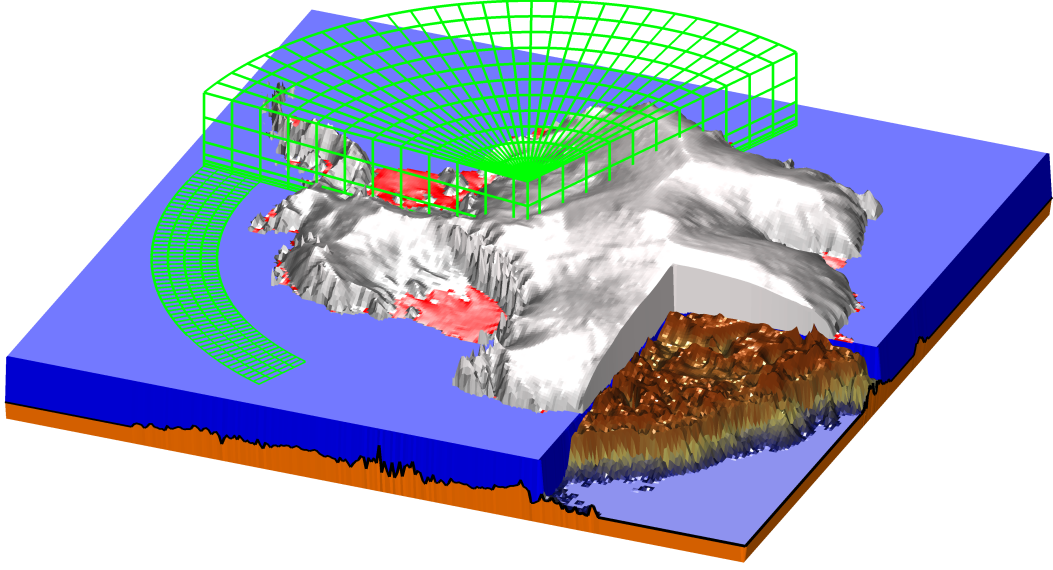
Figure 3.1: *Schematic of the different model components. Part of the GCM grid for HadCM3 is shown in green, the ice sheet is rendered at the much finer resolution grid of the ice sheet model (20 × 20 km for Antarctica), the z-axis is exaggerated. Note the different projections and spatial resolutions of the climate model and ISM. The ice shelves are highlighted in red and cannot be simulated by the version of Glimmer used in this thesis*

that the total annual ablation is related to the annually integrated surface air temperature above freezing point.

The mean annual air temperature $\bar{T}_a$ and annual air temperature half range $\Delta T_a$ are calculated from the monthly surface air temperatures ($T_a$) output from the climate model. Daily surface air temperatures $T'_a$ are then calculated assuming a sinusoidal cycle with random variations.

$$T'_a = \bar{T}_a + \Delta T_a \cos\left(\frac{2\pi t}{A_t}\right) + \mathbf{R}(0, \sigma_T), \tag{3.2.2}$$

where $A_t$ is the period of the year and random variations $\mathbf{R}$ are applied with a mean of 0 °C and a standard deviation $\sigma_T$ of 5 °C. The number of positive degree days $D_p$ can then be calculated using equation 3.2.3 (Reeh, 1991):

$$D_p = \frac{1}{\sigma\sqrt{2\pi}} \int_0^{A_t} \int_0^{T'_a + 2.5\sigma_T} \bar{T}_a \exp\left(\frac{-(\bar{T}_a - T'_a)^2}{2\sigma_T^2}\right) dT dt. \tag{3.2.3}$$

70

The number of positive degree days is related to a total melt amount using separate empirically based degree day factors for the melting of snow $\alpha_s$ and of ice $\alpha_i$ (Braithwaite, 1995). The potential for some melt to be retained in the snowpack is accounted for, as is the melting of snow prior to the melting of ice. Depending on the potential amount of melt, total amount of precipitation and the refreezing capacity of the snowpack, one of three outcomes is possible:

$$a = \begin{cases} 0 & \text{if} \quad a_s < b_0 \\ a_s - b_0 = \alpha_s D_p - b_0 & \text{if} \quad b_0 < a_s < P \\ a_s + a_i = P - b_0 + \alpha_i(D_p - P/\alpha_s) & \text{if} \quad a_s > P \end{cases} \quad , \qquad (3.2.4)$$

where $b_0$, the refreezing capacity of the snowpack, is first calculated as a fraction of precipitation $b_0 = w_{max}P$, with the parameter $w_{max}$ set to a default value of 0.6. Equation 3.2.4 also first requires the potential amount of snow melt, which is calculated as $a_s = \alpha_s D_p$. As can be seen from equation 3.2.4 if the potential snowmelt is less than the refreezing capacity of the snowpack, there is no melt. If the potential snowmelt is greater than the refreezing capacity of the snowpack, but less than total precipitation, then some snowmelt occurs. Finally, if the potential snowmelt is greater than the total precipitation then there is additional ice melt (Rutt et al., 2009), i.e. the mass balance $B$ becomes negative.

Although the PDD surface mass balance scheme is widely used for both paleoclimate and future simulations (e.g. Ritz et al., 1997; DeConto and Pollard, 2003a; Ridley et al., 2005; Lunt et al., 2008), it does have limitations. Because the PDD factors are based on modern empirical relationships there is uncertainty as to how applicable the PDD surface mass balance scheme is to studies of future climates (Bougamont et al., 2007) and palaeoclimates, especially under a different astronomical configuration (van de Berg et al., 2011). For example, van de Berg et al. (2011) using a regional climate model suggested that only 55% of the reduced surface mass balance of the Greenland ice sheet during the last interglaciation was a result of changes in ambient temperature. The remaining reduction in the surface mass balance was a result of changes in insolation (van de Berg et al., 2011). To simulate the reduced Greenland ice sheet during the last interglaciation required tuning of the PDD factors to enhance the ambient temperature contribution to the lower surface mass balance (van de Berg et al., 2011). If the last interglaciation were considered an analogue for future warming then these tuned PDD factors

could overestimate the surface melt from ambient warming (van de Berg et al., 2011).

Alternatives to the PDD surface mass balance scheme exist, such as physically based energy balance models (e.g. Bougamont et al., 2005; Calov and Ganopolski, 2005), however these also have limitations. Energy balance models require additional climate input variables (Bougamont et al., 2005). The additional variables required by such energy balance models may include the cloud cover, wind speed, relative humidity, surface pressure and the incoming longwave- and shortwave-radiation (Bougamont et al., 2005; Calov and Ganopolski, 2005). The representation of clouds is a known weakness of HadCM3 (Pope et al., 2007), a GCM which has been widely used for paleoclimate applications (Lunt et al., 2007; Haywood et al., 2010; Singarayer and Valdes, 2010; Taylor et al., 2012) and which we use in this chapter. Ganopolski et al. (2010) used an energy balance model for their simulations of the Northern Hemisphere ice sheets during the last glacial cycle. Although the surface mass balance scheme is physically based, many of the required input variables are parameterised within an intermediate complexity climate model (Ganopolski et al., 2010). Although we can criticise the PDD surface mass balance because of its reliance on modern empirical relationships, for paleoclimate applications the more complex energy balance approach also has limitations due to its reliance on additional, and often parameterised, climate variables.

### 3.2.2 Ice flow

The Glimmer ice sheet model makes use of the commonly adopted shallow ice approximation for simulating the flow of grounded ice (Hutter, 1983). This approximation is considered valid if the spatial extent of the ice sheet greatly exceeds its thickness (height / width $\ll 1$). In this instance the ice surface and bedrock slopes are sufficiently small to ignore the normal stress components ($\sigma_{xx}, \sigma_{yy}, \sigma_{zz}$) and longitudinal shear stresses ($\tau_{xy}, \tau_{zy}, \tau_{yx}, \tau_{zx}$) (see Figure 3.2; Van der Veen, 1999). Only horizontal shear stresses, the gravitational driving stress and basal drag are represented. The horizontal shear stresses ($\tau_{xz}$ and $\tau_{yz}$) are calculated as follows:

$$\tau_{xz}(z) = -\rho_i g(s-z)\frac{\partial s}{\partial x}, \tag{3.2.5}$$

$$\tau_{yz}(z) = -\rho_i g(s-z)\frac{\partial s}{\partial y}, \tag{3.2.6}$$

where $\rho_i$ is the density of ice, which remains constant (there is no compaction), and $g$ is accel-
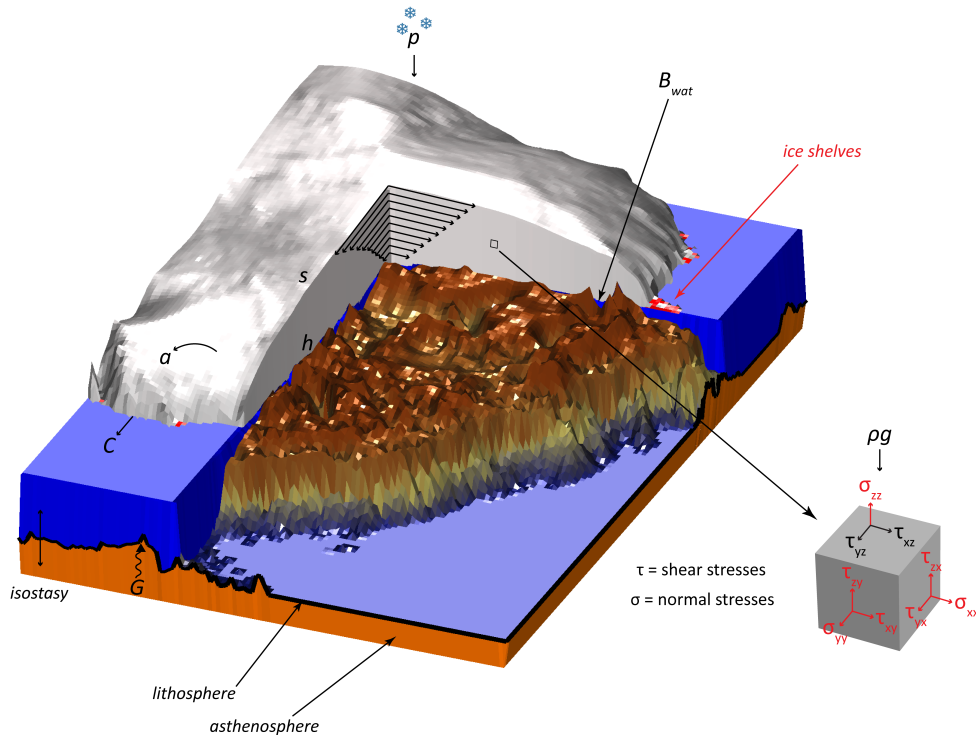
Figure 3.2: *Schematic of the ice sheet mechanics of the Glimmer ISM. The components highlighted in red, such as the ice shelves, are not represented.*

eration due to gravity. The way ice deforms when stresses are applied depends on its rheology. The ice rheology is represented in the numerical model using Glen's flow law (Van der Veen, 1999; Rutt et al., 2009):

$$\dot{\varepsilon}_{xz} = A(T^*)\tau_*^{n-1}\tau_{xz}, \tag{3.2.7}$$

$$\dot{\varepsilon}_{yz} = A(T^*)\tau_*^{n-1}\tau_{yz}. \tag{3.2.8}$$

Deformation is shown as a strain rate $\dot{\varepsilon}$, $A$ is the temperature dependent flow law coefficient, $\tau_*$ is the effective shear stress $\left(\tau_* = (\tau_{xz}^2 + \tau_{yz}^2)^{1/2}\right)$ and $n$ is the flow law exponent, typically given a value of 3 (Blatter et al., 2011). As the flow law is temperature dependent, absolute temperatures $(T^*)$, corrected for the influence of pressure on the melting point, are calculated throughout the ice column. Values for $A$ have been approximated based on experiment, with the following Arrhenius relationship commonly adopted:

73

$$A(T^*) = fa_0e^{-Q/RT^*}, \tag{3.2.9}$$

where $f$ is the tuneable flow enhancement factor, $a_0$ is a temperature independent material constant, $Q$ is the activation energy for creep and $R$ is the universal gas constant. The flow enhancement factor is included to account for non-uniformites in the ice crystal structure (anisotropy), for pure isotropic ice a value of 1 should be used (Blatter et al., 2011). Values for $f$ typically vary between 1 and 5, with higher values also found in the literature (Tarasov and Peltier, 2004; Ganopolski et al., 2010), higher values lead to increased ice flow. Using the above equations, it is possible to derive the vertical gradient of $\mathbf{u}$ (the ice velocity vector):

$$\frac{\partial \mathbf{u}}{\partial z} = -2A(T^*)(\rho_i g(s-z))^n|\nabla s|^{n-1}\nabla s. \tag{3.2.10}$$

Integrating with respect to $z$ gives the horizontal velocity profile:

$$\mathbf{u}(z) - \mathbf{u}(h) = -2(\rho_i g)^n|\nabla s|^{n-1}\nabla s \int_h^s A(s-z')^n dz', \tag{3.2.11}$$

where $\mathbf{u}(h)$ is the basal velocity, which can be set to zero if basal sliding is turned off. Experiments are conducted in this thesis with basal sliding turned both on and off. If turned on, the basal velocity is calculated as proportional to the basal shear stress (Payne, 1995):

$$\mathbf{u}(h) = -B_s \rho_i g H \nabla s. \tag{3.2.12}$$

The basal sliding parameter $B_s$ can be assigned in various ways and can vary spatially across the ice sheet domain $B_s = B_0(x,y)$. The basal sliding parameter can also be set to vary if meltwater $(B_{wat})$ is present at the ice sheet bed. It should be noted that the validity of including basal sliding in a shallow ice approximation model is questioned (Bueler and Brown, 2009). Integrating equation 3.2.11 again with respect to $z$ gives the vertically averaged ice velocity vector $\bar{\mathbf{u}}$ :

$$\bar{\mathbf{u}} = -\frac{2}{H}(\rho_i g)^n|\nabla s|^{n-1}\nabla s \int_h^s \int_h^z A(s-z')^n dz' dz + \mathbf{u}(h). \tag{3.2.13}$$

74

### 3.2.3 Thermodynamics and basal melt rate

As noted above, the ice flow law (equations 3.2.7 and 3.2.8) contains a temperature dependent term, as ice becomes more viscous with increasing temperature. It is therefore necessary to calculate temperatures throughout the ice column using:

$$\frac{\partial T}{\partial t} = \frac{k_i}{\rho_i c_i}\left(\nabla^2 T + \frac{\partial^2 T}{\partial z^2}\right) - \mathbf{u} \cdot \nabla T + \frac{\Phi}{\rho_i c_i} - w\frac{\partial T}{\partial z}, \tag{3.2.14}$$

where $k_i$ is the thermal conductivity of ice, $c_i$ is the specific heat capacity of ice, $\Phi$ is the heat generated by internal friction (calculated from the horizontal shear strain rate and stresses) and $w$ is the vertical velocity. In this equation, the first term on the right is the vertical diffusion of heat (horizontal diffusion is assumed minimal), the second term is horizontal advection, the third term is internal heat generated by friction and the final term is vertical advection. At the surface, ice temperatures are calculated from the mean annual surface temperature. At the base of the ice sheet, heat is provided by the geothermal heat flux ($G$) and basal friction. Ice temperatures are kept constant at the pressure melting point, with excess heat used to calculate the basal melt rate ($S$):

$$S = \frac{k_i}{\rho_i L}\left(\frac{\partial T^*}{\partial z} - \frac{\partial T}{\partial z}\right), \tag{3.2.15}$$

where $L$ is the specific latent heat of fusion. The geothermal heat flux can be set to a constant value or can be allowed to vary across the ice sheet domain (Rutt et al., 2009).

### 3.2.4 Isostasy

The Glimmer ISM includes various representations of the isostatic loading and unloading of the lithosphere and asthenosphere with the build-up and melting of ice. The model has two layers, a thin lithosphere floating on top of the asthenosphere. The lithosphere can either be described as local, in which case there are no lithospheric effects and the ice effectively floats on the asthenosphere, or it can be elastic, in which case it has some flexural rigidity

which affects the geometry of the isostatic response (Lambeck and Nakiboglu, 1980). The asthenosphere can either be treated as a non-viscous fluid, in which case isostatic equilibrium is reached immediately, or it can be set to respond slowly with a relaxing asthenosphere. With the relaxing asthenosphere, a characteristic time constant is estimated and the rate of response is assumed to be proportional to the difference between the loaded equilibrium and the current profile, and inversely proportional to the time constant. In this thesis a relaxing asthenosphere is used with a time constant of 3,000 years, coupled with an elastic lithosphere (Rutt et al., 2009).

### 3.2.5 Marine margin

The version of the Glimmer ISM used in this thesis currently has no representation of floating ice, therefore it cannot simulate ice shelves. When ice reaches the marine margin it is simply removed through calving (either all of the ice reaching the margin is removed or some fraction is removed). This is clearly a problem when attempting to simulate the modern West Antarctic ice sheet, where large parts of the ice sheet are grounded below sea level and stabilisation is provided by buttressing from the surrounding ice shelves. Although some ice does grow on the terrestrial parts of West Antarctica in simulations using the Glimmer ISM, a full WAIS cannot form due to these missing processes. This problem is common to all shallow ice approximation ISMs.

In a previous study using the Glimmer ISM (Gregoire et al., 2012), ice growth across shallow seas was enabled by significantly lowering the marine margin (effectively lowering sea level). This approach has also been adopted in other SIA studies (Tarasov and Peltier, 1999; Abe-Ouchi et al., 2007). This allows the spread of ice across the continental shelf. This is necessary to simulate the growth of the Laurentide ice sheet across Hudson Bay, or the spread of the Eurasian ice sheets across the North Sea and Baltic Sea, for example. A problem with this solution is that it increases the accommodation space of the ice sheet, potentially leading to a large overestimate of the ice sheet size. An alternative approach is to impose a fixed grounding line, for example based on reconstructions of the LGM ice sheet extent or sea level records (Siegert et al., 2001). Both of these solutions lead to the growth of an ice sheet across shallow seas for the wrong physical reasons.

Alternative hybrid ISMs exist which make use of the SIA for the main grounded part of the ice sheet but have an alternative scheme for ice shelves, the shallow shelf approximation (SSA).

The SIA allows deformation of grounded ice by horizontal shearing, with basal drag balancing the gravitational driving stress. For a floating ice shelf, the SSA assumes there is negligible basal drag and the main deformation is through longitudinal stretching, which balances the driving stress. Areas where both types of flow are relevant, e.g. across the grounding line and for ice streams, are more problematic (Van der Veen, 1999). The hybrid model of Pollard and DeConto (2009, 2012b) uses a parameterisation for the flow of ice across the grounding line based on the theory of Schoof (2007). This allows for the migration of the grounding line and the transfer of ice across the grounding line from one flow regime to another (Pollard and DeConto, 2012b).

This thesis includes results from the Glimmer (SIA-only) ISM and focuses on the formation of the large and predominantly terrestrial ice sheets (i.e. not the WAIS). We acknowledge that the large ice sheets (the North American, Eurasian and East Antarctic) may have instabilities resulting from marine processes (Winsborrow et al., 2010; Williams et al., 2010; Joughin and Alley, 2011), and that because we are not able to correctly simulate these processes using the Glimmer ISM we may overestimate the stability of these ice sheets.

### 3.2.6 Bedrock topography

The ISM operates over a limited region on a cartesian grid (the ISM domain). We run the ISM over three regions in this thesis: North America, Eurasia and Antarctica. The Northern Hemisphere simulations are for the last glacial cycle and the Antarctic simulations are for the formation of the EAIS at the Eocene/Oligocene transition.

For the last glacial cycle simulations, the bedrock topography is the modern bedrock topography. There are various bedrock topographies available for the EOT, the most basic is the modern topography (Lythe and Vaughan, 2001) which is isostatically adjusted following the removal of the Antarctic ice sheet and rotated into its EOT position. In addition, Wilson et al. (2011) have created an EOT bedrock topography which takes into account rifting and replaces sediment lost by erosion. We use both of these bedrock topographies in a later chapter. This chapter focuses on last glacial cycle simulations of the Northern Hemisphere ice sheets.

The ISM can be initiated with varying ice sheet extents, although we typically initiate from modern conditions for the last glacial cycle simulations and ice-free conditions for the EOT simulations. The ISM is set to a horizontal resolution of 40 × 40 km for the Northern Hemisphere simulations and 20 × 20 km for the smaller domain of the Antarctic simulations. The ISM has 11 vertical levels, arranged as sigma levels (some fraction of ice thickness rather
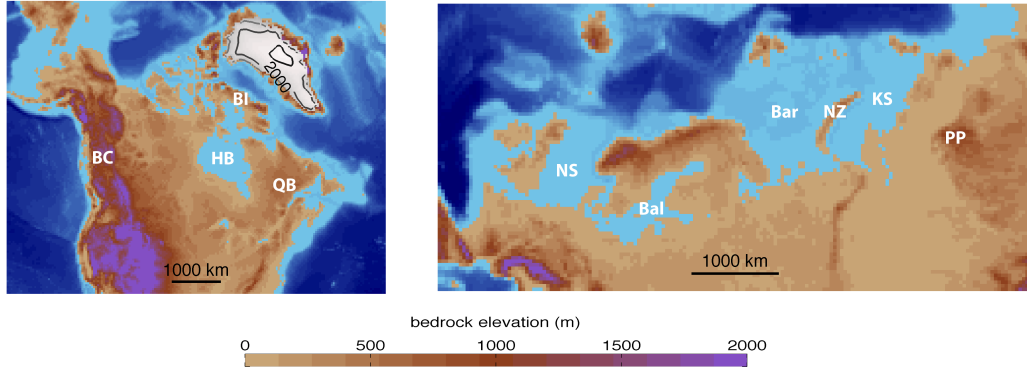
Figure 3.3: *Northern Hemisphere bedrock topography, for North American and Eurasian domains. Approximate locations of regions referred to in the text: BC - British Columbia; HB - Hudson Bay; BI - Baffin Island; QB - Quebec; NS - North Sea; Bal - Baltic Sea; Bar - Barents Sea; NZ - Novaya Zemlya; KS - Kara Sea; PP - Putorana Plateau. Data from Gregoire (2010)*
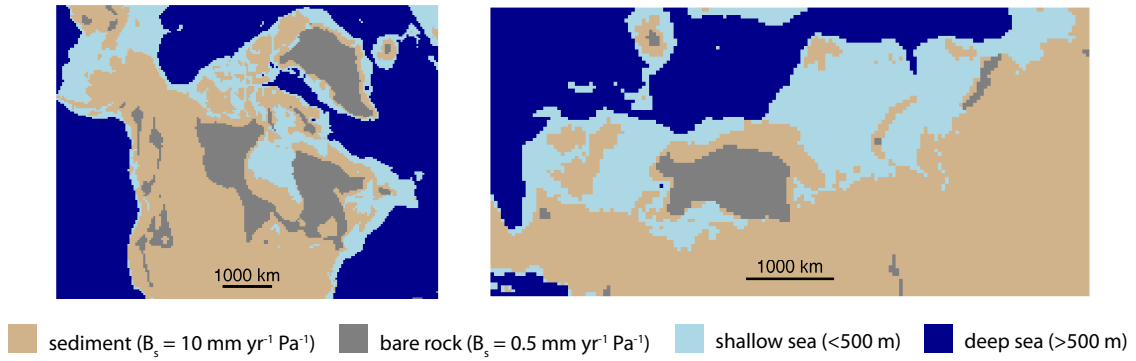


Figure 3.4: *Bedrock topography for North America and Eurasia, showing regions of sediments and bare rock. Also shown is the extent of shallow seas, over which ice is allowed to extend. Data from Gregoire (2010)*

than a fixed thickness) so that their depth varies as the ice thickness evolves.

The basal sliding parameter ($B_s$) can be set to vary spatially if basal sliding is turned on. This can vary depending on whether there are deep sediments underneath the ice sheet or bare rock. We use 3 scenarios for the last glacial cycle simulations of the Northern Hemisphere ice sheets, either no sliding (BS1), a uniform sliding (BS2, 10 mm yr$^{-1}$ Pa$^{-1}$) or a spatially varying sliding (BS3). The spatially varying basal sliding parameter is based on the sediment maps of Lakse and Masters (1997), following the method of Gregoire et al. (2012) (see Figure 3.4).

Where there are shallow sediments (less than 20 m), the basal sliding parameter is set to a lower rate of 0.5 mm $yr^{-1}$ $Pa^{-1}$ for bare rock. Everywhere else the basal sliding parameter is set to a rate of 10 mm $yr^{-1}$ $Pa^{-1}$.

In Figure 3.4 we also highlight the shallow seas ($< 500$ m deep) over which the ice sheet is allowed to grow. This is due to the previously discussed problem of representing the marine margin using the Glimmer ISM. Because the continental shelf will be pushed down as the ice sheets grow due to isostasy and the water depth will increase, the shallow seas highlighted here are at their maximum extent. The border between the shallow and deep seas, which we fix at 500 m depth, will retreat slightly towards the continent as the ice sheet grows. Note that eustatic sea level does not change within the ice sheet model during a simulation, even if a large ice sheet forms.

## 3.3   Climatology

In order to calculate the surface mass balance, the ISM requires some representation of the climate. Approaches include using a parameterised climate or a climate model (e.g. Pollard, 1982; Pollard and DeConto, 2009; Huybrechts, 2002; DeConto and Pollard, 2003a; de Boer et al., 2010; Ganopolski et al., 2010). Parameterisations include simple temperature relationships based on latitude (e.g. Pollard, 1982), to more complex translations of deep-sea temperature records (Pollard and DeConto, 2009; de Boer et al., 2010) or ice core records using a glacial index (Huybrechts, 2002; Zweck and Huybrechts, 2005; Charbit et al., 2007). A limitation of such parameterisations is that they have to make assumptions about the geographic distribution of temperature and precipitation based on a limited number of sites. This usually means adopting the modern distribution and assuming it remains constant through time. Imposing a parameterised climate on the ISM often implies that there is no or incomplete representation of ice sheet feedback on the climate. Using a climate index to drive an ISM also imposes ice sheet evolution on the ISM, limiting the use of this approach in determining causes of the glacial cycles or for undertaking simulations of the future (Pollard, 2010).

Climate models are available in various orders of complexity. Lower complexity models have a reduced number of equations which need to be solved by the model and/or have a reduced resolution, but have the advantage of increased computational efficiency (e.g. CLIMBER-2; Calov and Ganopolski, 2005). This means that for certain applications, reduced complexity climate models can be directly coupled to ice sheet models (Ganopolski et al., 2010). However,

this reduction in complexity and increase in efficiency has a disadvantage. The simplification of the atmospheric physics means more processes need to be parameterised, often based on modern observations. It is therefore likely that such models will become less reliable as they are applied to periods significantly different from modern, such as paleoclimate applications (Pollard, 2010). By reducing climate model resolution, a large discrepancy between the climate grid and the ISM grid develops. For example the intermediate complexity climate model CLIMBER-2, with a latitudinal resolution of $10°$ and a longitudinal resolution of $51°$ (equivalent to $\sim 1110 \times 2330$ km at $65°$N) has been dynamically coupled to an ice sheet model with a resolution of approximately 100 km (Calov and Ganopolski, 2005).

### 3.3.1 Climate models

General Circulation Models (GCMs; also Global Climate Models) solve equations for fluid dynamics and thermodynamics on a 3-D spherical shell. These equations stem from the laws governing the conservation of mass, energy and momentum, the equations of state such as the ideal gas law and the hydrostatic approximation in the atmosphere. They account for the transport of various tracers, such as moisture in the atmosphere (McGuffie and Henderson-Sellers, 2005). Various other processes are included that operate at a scale below that of the climate resolution (such as the formation of clouds), these processes are parameterised, often based on empirical relationships. Other components, such as vegetation, may be represented by additional coupled models. Boundary conditions are fixed inputs which are imposed on the GCM. These include the atmospheric concentration of greenhouse gases (if the GCM has no carbon cycle model), solar insolation and the extent of the ice sheets. These boundary conditions can be changed between different GCM runs (McGuffie and Henderson-Sellers, 2005).

The GCM can include an atmosphere or ocean, and the two systems can be dynamically coupled to form ocean-atmosphere GCMs (OAGCMs). If the ocean is deemed to be less important for the problem being addressed, then atmosphere-only GCMs can also be used. These may have some representation of the ocean, often as a shallow slab, but no deep ocean (Thompson and Pollard, 1997). This thesis makes use of simulations from both OAGCMs and atmosphere-only GCMs. Because of the large archive of GCM simulations available to us, we make use of the output from existing climate model simulations throughout this thesis.

The UK Met Office model HadCM3 is an OAGCM that was originally released in 1999 (Gordon et al., 2000). Although it has been superseded by subsequent versions (Pope et al., 2007), it

remains popular for a number of applications, including paleoclimate and ensemble simulations, due to its computational cheapness and relatively good climatology compared to subsequent releases (Taylor et al., 2012; Rowlands et al., 2012). HadCM3 has a higher resolution ocean grid ($1.25° \times 1.25°$) than atmosphere grid ($2.5° \times 3.75°$) in the horizontal, whereas HadCM3L has the same lower resolution grid for the atmosphere and ocean. This results in HadCM3L being approximately twice as fast to run than HadCM3. Due to this computational advantage and the relative ease of changing boundary conditions (such as the land-sea mask) because of its even grid, HadCM3L is a useful model that has been used in a number of paleoclimate applications (Lunt et al., 2007; Haywood et al., 2010; Taylor et al., 2012) and future projections (Rowlands et al., 2012).

The atmospheric dynamics of HadCM3 (HadAM3) are solved on a finite difference grid, with a resolution of $2.5° \times 3.75°$ (approximately equivalent to a spectral resolution of T42), with 19 levels in the vertical and a time-step of 30 minutes (Gordon et al., 2000). The grid is constant in latitude and longitude, therefore the grid boxes become increasingly small at higher latitudes as the meridians converge towards the poles. This is useful when simulating the ice sheets, in that the spatial resolution increases at higher latitudes. However, the increase in spatial resolution at the poles can generate computational instabilities. A solution to this is to use a suitably fast time-step or to incorporate filtering procedures (Pope and Stratton, 2002; McGuffie and Henderson-Sellers, 2005).

There is a known cool bias in HadCM3 surface temperatures, this is particularly strong during the Northern Hemisphere winter, especially over Eurasia. The cold bias extends over North America, but is less pronounced, and there is a slight warm bias to the east of North America (Pope et al., 2000). Over Antarctica, HadCM3 produces large temperature anomalies when compared to the limited observational data. This varies from a strong warm bias over the south pole, to a cold bias over most other regions where data exists. This temperature anomaly is partially due to incorrect orographic height in the GCM over Antarctica. These temperature anomalies are also caused by an overestimation of the low-level temperature inversion over Antarctica (Turner et al., 2006).

### 3.3.2 Ice sheet - climate coupling

The different response times of the large scale ice sheet processes ($10^3 - 10^5$ years) and the climate system (days to $10^3$ years), and the vast computational expense of running complex
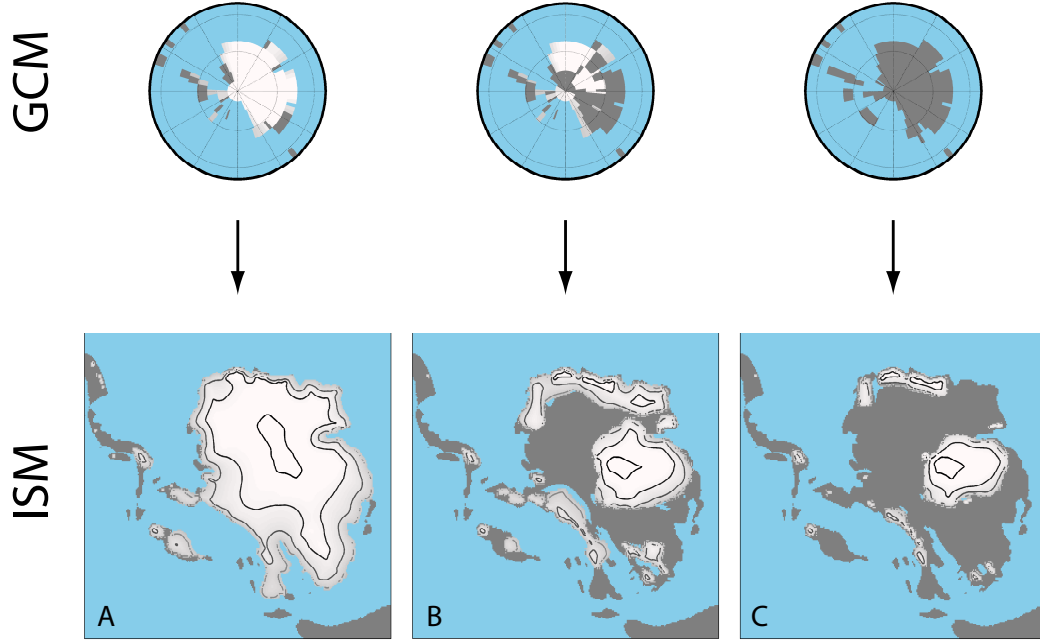
Figure 3.5: *Glimmer ISM forced with climate from 3 GCM runs with A) full and B) medium sized Antarctic ice sheets and C) no Antarctic ice sheet. All other GCM boundary conditions (atmospheric $CO_2$ concentration, insolation) are equal. ISM started from ice-free conditions. Note the difference in ISM response to these different GCM boundary conditions, ice volumes output by the ISM are: A) 24.9 $\times 10^6$ $km^3$; B) 7.2 $\times 10^6$ $km^3$ and C) 3.4 $\times 10^6$ $km^3$.*

climate models (GCMs) presents a challenge when attempting to couple ice sheet models to climate models (Pollard, 2010). For example, based on current computing power the FAMOUS climate model (a faster version of HadCM3L) can simulate 120 years of climate per wall-clock day (Smith et al., 2008), whereas whole continent sized ice sheet simulations of $10^4 - 10^7$ years using the SIA can be computed in a few days to weeks of wall-clock time (Pollard, 2010). Reducing the complexity of a climate model goes some way to resolving this issue, but the temporal mismatch still remains (Ganopolski et al. (2010) estimate that ISM is responsible for only 1% of total CPU time in their simulations using a reduced complexity climate model and SIA ISM).

One way around this problem adopted in a number of studies is to use a constant climate forcing (Huybrechts and de Wolde, 1999; Lunt et al., 2008; Stone et al., 2010; Dolan et al., 2011). This has advantages in that once a climate simulation has been performed; it is then relatively easy (and quick) to run an ice sheet model simulation. This means many ice sheet

model runs can be conducted exploring the ice sheet model parameter space. Typically with this approach, the only feedback from the ice sheet model on the climate is from a change in temperature as the ice sheet grows vertically through the atmosphere (height-mass balance feedback). Other feedbacks, such as albedo feedbacks and changes in atmospheric circulation are not represented. This is a problem if the ice sheet configuration in the climate model is significantly different from that simulated by the ISM, because such a change in the climate model boundary conditions can have a large impact on the climate (Hofer et al., 2012). An example is given in Figure 3.5, where the GENESIS GCM is set-up in an identical way for 3 runs, except with a different Antarctic ice sheet extent. When an ISM is then forced with these 3 climates there is a very large difference in ice volume, from $3-25\times10^6$ km$^3$. This is due to the presence of a large Antarctic ice sheet in the GCM, with albedo changes reducing temperature and the height of the ice sheet generating changes in atmospheric circulation.

Another problem with constant forcing simulations is that they are often run to equilibrium. This generally means running the ice sheet model until the change in ice sheet volume between time-steps becomes very small. Depending on the size of the ice sheet and how far from equilibrium the ice sheet was when it was initiated, this can take $50-100$ ka (Dolan et al., 2012). This timescale is comparable to the frequencies of the major astronomical forcings, of precession ($19-23$ ka), obliquity (41 ka) and eccentricity ($\sim$100 ka) (Hays et al., 1976). Therefore the climate which is forcing the ISM is no longer synchronous to its appropriate astronomical forcing. This is illustrated in Figure 3.6.

Figure 3.6 uses GCM simulations from the last interglaciation to present. Only the astronomical forcing changes in these simulations, with the greenhouse gas concentrations and ice sheet extent in the GCM kept at modern. These simulations are then used to drive equilibrium ISM simulations of the Northern Hemisphere ice sheets. This is compared to a transient simulation, where the ISM model is forced by linearly interpolating between these simulations through time. By forcing the ISM with a constant astronomical forcing for 50 ka, the ice sheet response to astronomical forcing is greatly exaggerated, especially as the ice sheets get larger. In reality the forcing does not remain constant for 50 ka and the ice sheet never reaches equilibrium with the climate. This is clearly evident from the much less extreme ice sheet response in the transient simulation.

One solution to these problems is to asynchronously couple a climate model to an ISM, i.e. sequentially running the climate model then running the ISM (see 1.3.2). This allows for a
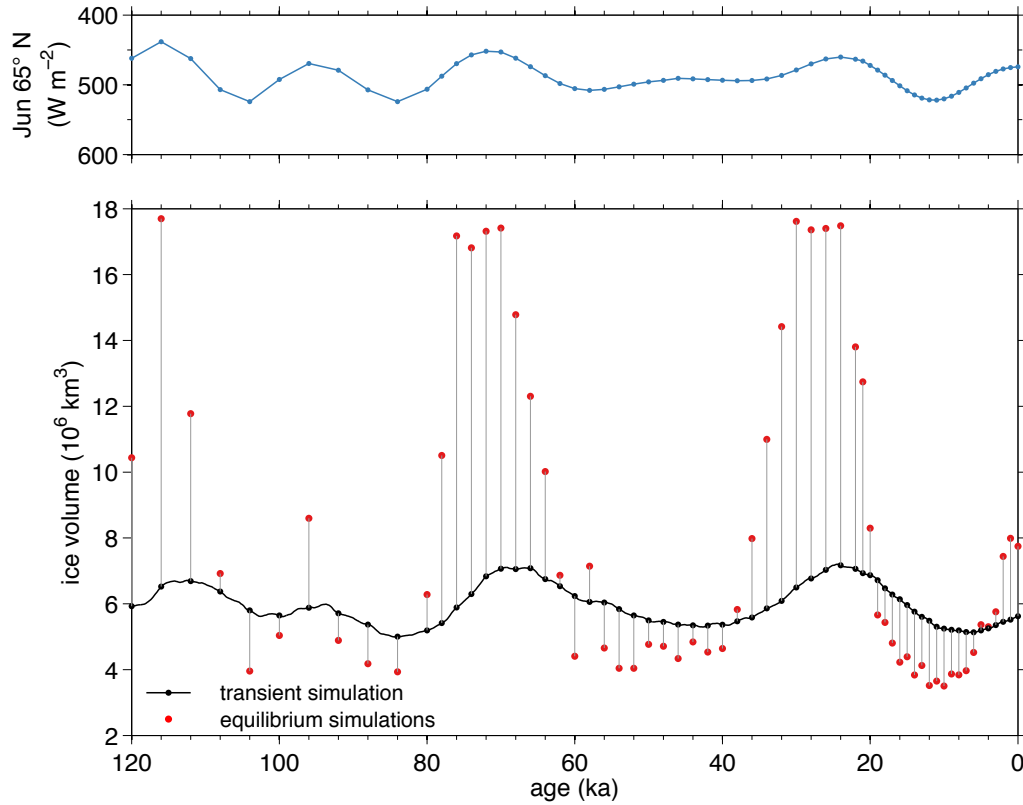
Figure 3.6: *Comparison of transient simulation (black line) with equilibrium simulations (red dots) for same astronomical only simulations. Note that by running the ISM for 50 ka with a constant forcing, the ISM response to astronomical forcing is greatly exaggerated. The upper subplot shows solar insolation for June 65° N.*

delayed climate feedback to any change in the size of the ice sheets. This technique has been used for very long simulations ($10^6$ years) of the EAIS (DeConto and Pollard, 2003a), but is still relatively computationally expensive. An alternative approach is to build a multi-dimensional matrix of climate simulations (the GCM matrix method), with a dimension for each of the long-term climate forcings (atmospheric $CO_2$, astronomical, ice sheet extent). The climate can then be updated by interpolating between these different climate simulations (Pollard, 2010). This is the method that is adopted and tested in this thesis.
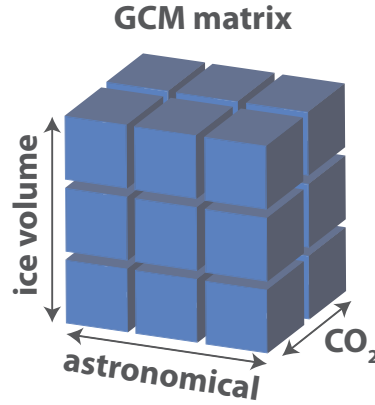
**GCM matrix**

Figure 3.7: *Schematic of the GCM matrix method, each box represents a GCM simulation with different boundary conditions which cause a different climate forcing. The climate at the current time-step is calculated by interpolating between these simulations*

### 3.3.3 GCM matrix method

The GCM matrix used here has three dimensions for varying the astronomical forcing, atmospheric $CO_2$ and ice sheet extent (see Figure 3.7). It may be possible to add additional dimensions for other large-scale climate forcings, such as the uplift of mountain ranges or the opening and closing of ocean gateways, though these are not included here. Adding too many dimensions would result in a large increase in the number of simulations required, which would defeat the purpose of adopting this method. The climate at the current time-step is calculated for each dimension in turn, starting with astronomical variability. Although we only show equations for temperature, precipitation is calculated in the same way unless otherwise stated.

#### 3.3.3.1 Astronomical forcing in the GCM matrix method

The astronomical forcing accounts for variations in the Earth's orbit and obliquity which affects incoming insolation at the top of the atmosphere, resulting in changes in the surface climate ($T_i$). The astronomical dimension of the GCM matrix includes 3 simulations with different astronomical configurations, categorised as cold $T_c$, medium $T_m$, and a warm $T_w$, with respect to the summer of the relevant hemisphere. Astronomical variability is commonly shown as a time series of insolation for one latitude and month. This is typically June 65°N for Northern Hemisphere glaciation (Paillard, 1998). We can therefore calculate the climate by interpolating between 2 of the GCM simulations based on the insolation at June 65°N for our Northern

Table 3.1: *Summary of astronomical interpolation methods. For AST1-AST3 the target of optimisation is a time series, i.e. the average insolation for the specified latitude and months. For AST4 and AST5 the target of optimisation is the specified area of the TOA insolation field.*

|      | latitude ($\lambda$) | month ($m$) |
|------|------------|-----------|
| AST1 | 65°N       | June      |
| AST2 | 65°N       | JJA       |
| AST3 | 65°N       | 6 max     |
| AST4 | 50-70°N    | JJA       |
| AST5 | all        | all       |

Hemisphere simulations (we will use January 70°S for our Antarctic simulations). This is based on the method suggested by Pollard (2010) as is shown below:

$$T_i = \begin{cases} T_m + \frac{I-I_m}{I_w-I_m}(T_w - T_m) & \text{if} \quad I > I_m \\ T_c + \frac{I-I_c}{I_m-I_c}(T_m - T_c) & \text{if} \quad I \leq I_m \end{cases}, \tag{3.3.1}$$

where, $I$ is the insolation at June 65°N for the current timestep, based on the astronomical solutions of Laskar et al. (2004), and $I_c$, $I_m$ and $I_w$ are the insolation values at June 65°N from the GCM simulations. We test whether June (AST1) is the most suitable time period by also testing June-July-August (JJA; AST2) and the 6 summer months (AST3).

Although it is common to represent astronomical variability as a 1-dimensional time series, astronomical variability in a climate model is actually realised as a changing 2-dimensional field of top of the atmosphere (TOA) insolation by latitude $\lambda$ and month $m$ (see Figure 3.8). This TOA insolation field depends on the parameters for the Earth's orbit (eccentricity and precession) and obliquity. We therefore explore an alternative method for interpolating between the different GCM simulations by using the TOA insolation field. The climate ($T_i$) at each time-step can be calculated using the sum of various fractions of the 3 GCM scenarios:

$$T_i = \beta_1 T_c + \beta_2 T_m + \beta_3 T_w. \tag{3.3.2}$$

We can calculate the coefficients $\beta$ with respect to the TOA insolation $I_{\lambda,m}$, with the implicit assumption that this relationship is linearly related to the surface climate:
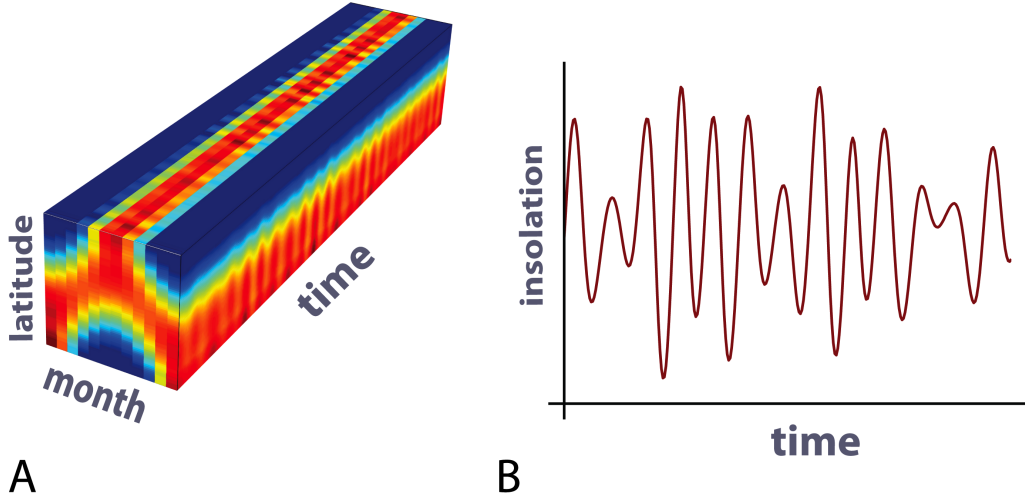
Figure 3.8: *Schematic of the 2 ways of representing astronomical variability: A) the top of the atmosphere insolation field by month and latitude through time and B) as a time series of insolation for a given month and latitude through time*

$$f(I, \beta) = \beta_1 I_c + \beta_2 I_m + \beta_3 I_w, \tag{3.3.3}$$

where $I_c$, $I_m$ and $I_w$ is the TOA insolation field for the GCM simulations. A pragmatic solution to avoid negative insolation is to impose a constraint, such that the sum of the coefficients must equal 1:

$$\beta_3 = 1 - (\beta_1 + \beta_2). \tag{3.3.4}$$

It is possible to optimise equation 3.3.3 for various combinations of latitudes and months. Using the astronomical reconstructions of Laskar et al. (2004), TOA insolation fields $I_{Laskar(\lambda,m)}$ are created for the past 50 Ma. This is used as a target for the function $f(I, \beta)$, for various combinations of $\lambda$ and $m$, including the full TOA insolation field (i.e. all latitudes and months):

$$r_{\lambda,m} = I_{Laskar(\lambda,m)} - f(I_{(\lambda,m)}, \beta). \tag{3.3.5}$$

An optimisation algorithm (MATLAB fminunc) is then used to optimise the fit using least squares regression, by minimising $S$:

$$S = \sum_{\lambda=1}^{n} \sum_{m=1}^{k} r_{\lambda,m}^2. \tag{3.3.6}$$

If we optimise to the full TOA insolation field then the solution should be equally valid for Northern and Southern Hemisphere glaciation, which is not the case for the 1-D time series approach. The different ways of representing astronomical variability are summarised in Table 3.1. We test all of these methods in a later section.

### 3.3.3.2 $CO_2$ forcing in the GCM matrix method

The next dimension in the GCM matrix is the $CO_2$ forcing. We use 2 GCM simulations at different $CO_2$ concentrations, $T_a$ and $T_b$. The climate is then interpolated between these 2 simulations based on the $CO_2$ concentration at that time-step ($C$), following a logarithmic relationship between temperature and atmospheric $CO_2$ based on the equation for climate sensitivity (Solgaard and Langen, 2012):

$$T_{ghg} = T_a \frac{\ln(C/C_b)}{\ln(C_a/C_b)} + T_b \frac{\ln(C/C_a)}{\ln(C_b/C_a)}. \tag{3.3.7}$$

For the last glacial cycle simulations $C_a$ is 185 ppmv and $C_b$ is 280 ppmv, for the EOT experiments conducted later on in this thesis $C_a$ is 560 ppmv and $C_b$ is 1120 ppmv. Temperatures can also be extrapolated outside of these $CO_2$ ranges.

### 3.3.3.3 Ice sheet - climate feedback in the GCM matrix method

The final dimension of the GCM matrix is the ice sheet extent. This allows for potential feedbacks from the growth of an ice sheet on the climate system. Again there are various approaches which we test here, starting with the method proposed by Pollard (2010), where interpolation between the different ice sheet extents is based on the total ice volume ($V$, or alternatively the total area) for the domain (hereafter FB1). In this case there are 3 different ice sheet extents, a full ice sheet ($V_f$), an intermediate ice sheet ($V_m$) and no ice, with the feedback $\alpha$ calculated as follows:

$$\alpha = \begin{cases} \frac{V - V_m}{V_f - V_m} & \text{if} \quad V > V_m \\ \frac{V}{V_m} & \text{if} \quad V \leq V_m \end{cases}, \tag{3.3.8}$$

$$T_{albedo} = \begin{cases} \alpha T_f + (1 - \alpha)T_m & \text{if} \quad V > V_m \\ \alpha T_m + (1 - \alpha)T_n & \text{if} \quad V \geq V_m \end{cases}, \tag{3.3.9}$$

where $T_{albedo}$ is the resulting climate accounting for ice sheet feedback and $T_f$, $T_m$ and $T_n$ are the climates for a full ice sheet, medium ice sheet and no ice sheet, respectively. Solgaard and Langen (2012) suggest that ice volume is preferable to ice area when performing such interpolation due to high frequency fluctuations in ice area depending on whether the time-step ends in summer or winter.

With this method there is no guarantee that the feedback from the growth of an ice sheet will be applied to the correct region within the ISM domain. Taking North America as an example, the intermediate ice sheet in the GCM may have a small ice sheet over the Rockies and an ice free region in the continental interior. Because this method is based on the total ice volume for the entire domain, if an ice sheet starts to grow in the continental interior the feedback would be applied incorrectly to the Rockies. Such an extreme example is unlikely as the ice sheet extent in the GCM is originally based on an ISM run. Nevertheless we develop and test an alternative method to attempt to address this problem.

### 3.3.3.4 Patchwork method

The patchwork feedback method attempts to overcome the problem of misplaced ice sheet feedbacks across the ISM domain (hereafter FB2). The feedback is calculated on a grid-point by grid-point basis. We consider this reasonable because the major feedback, albedo feedback, is largely a local effect. However, this method will potentially under/overestimate regional scale circulation effects. The resulting climate is therefore a patchwork of 2 GCM simulations:

$$T_{albedo(x,y)} = \begin{cases} T_{f(x,y)} & \text{if} \quad H_{(x,y)} > 0 \\ T_{n(x,y)} & \text{if} \quad H_{(x,y)} = 0 \end{cases}, \tag{3.3.10}$$

where $H_{(x,y)}$ is the local ice thickness. The Glimmer ISM requires the climate data to be provided on a latitude-longitude grid. In order to calculate the patchwork feedback we first transfer the ice thickness data from the ISM domain onto a latitude-longitude grid. This is a slightly higher resolution grid ($0.5° \times 0.5°$) than the original GCM data, requiring that the GCM data is upscaled onto this new grid. We use a slightly higher latitude-longitude grid to prevent

89

the growth of a small amount of ice at the edge of the ice sheet from creating an unrealistically large feedback.

This method attempts to account for local effects from the growth of an ice sheet, namely the albedo effect. Any regional scale climate effects such as impacts on the jet stream and storm systems (Clark et al., 1999; Hofer et al., 2012), are not directly accounted for. We test both ice sheet feedback methods later in this chapter.

### 3.3.4 Height-mass balance feedback

One ice sheet feedback is calculated within the ISM itself. This is the effect on temperature from the vertical growth of the ice sheet through the atmosphere, height-mass balance feedback. This is applied using a fixed lapse rate for the entire ISM domain. This also accounts for the discrepancy in spatial resolution between the GCM orography and the ISM orography. Because we are interpolating from a number of different GCM simulations potentially with different orographies, we first translate all temperatures to sea level equivalent temperatures ($T_{SL}$) using the lapse rate:

$$T_{SL} = T_{GCM} + (\gamma O_g), \tag{3.3.11}$$

where, ($\gamma$) is the lapse rate and $O_g$ is the GCM orography. The temperatures are then translated to ice sheet surface temperatures ($T_s$) within the ISM using the same lapse rate and the ISM orography ($O_l$):

$$T_s = T_{SL} - (\gamma O_l). \tag{3.3.12}$$

Note that it is unlikely that the environmental lapse rate is constant for the continental sized regions we are investigating (Krinner and Genthon, 1999). However the Glimmer ISM does not allow for a spatially varying lapse rate. The value that should be assigned to the lapse rate is also uncertain and is therefore one of the parameters which is often used to tune the ISM.

## 3.4 Evaluation of the GCM matrix method during the last glacial cycle

We next use the BBC GCM simulations (Singarayer and Valdes, 2010) as a control to test our representation of the different climate forcings in the GCM matrix method.

### 3.4.1 The BBC runs

The BBC simulations are a suite of 186 (3 sets of 62) GCM snapshot simulations (individual simulations with fixed boundary conditions) performed by Singarayer and Valdes (2010) for different periods between the last interglaciation (120 ka) and present. For the last glacial maximum (21 ka) to present, one simulation was performed every 1 ka with different boundary conditions. These simulations include 3 climate forcings: astronomical, GHG concentration and ice sheet extent. Sets of simulations were performed with some of these forcings varying through time and others fixed. The first set of simulations were performed with just astronomical variability, with the GHG concentrations and the ice sheet extent fixed at modern (BBC_AST). The second set of simulations includes astronomical and GHG forcing, with the ice sheet extent fixed at modern (BBC_AST_GHG). The final set of simulations has all forcings varying through time (BBC_ALL). The ice sheet extent in the BBC_ALL set of simulations is based on the ICE-5G reconstruction (Singarayer and Valdes, 2010), which is based on glacioisostatic modelling (Peltier, 2004). Because no GHG-only set of simulations was performed as part of the BBC suite, we approximate a BBC_GHG set by removing the BBC_AST anomaly from the BBC_AST_GHG set of simulations, this set is referred to as BBC_GHG*.

We create control ISM simulations by forcing the ISM with each of the 62 simulations from any given set. The climate is created by linearly interpolating between each of these snapshot simulations, from 120 ka to present. We then test our representation of individual climate forcings in the GCM matrix method against these control simulations.

First we perform an ISM simulation using the BBC_ALL set of GCM simulations. We compare this simulation against a sea level reconstruction for the last interglaciation to present (Siddall et al., 2003). This will enable us to tune the ISM by varying certain parameters. Note that because this first ISM simulation using the BBC_ALL set includes varying ice sheet extent, ice sheet evolution is being imposed on the ISM. The ice sheet extent in the BBC_ALL set of simulations was partially based on an ice volume record (Singarayer and Valdes, 2010). It is

91

Table 3.2: *Default values and ranges for key parameters in the ISM. The default values are the values used by Gregoire et al. (2012) for their simulation of the North American and Eurasian ice sheets using the Glimmer ISM. Ranges from the literature:* [a] *Hebeler et al. (2008);* [b] *Stone et al. (2010);* [c] *Gregoire (2010)*

|  |  | default value (P1) | range | units |
|---|---|---|---|---|
| $\alpha_s$ | PDD factor for snow | 3 | $3 - 8$[a] | mm d$^{-1}$ °C$^{-1}$ |
| $\alpha_i$ | PDD factor for ice | 8 | $8 - 20$[b] | mm d$^{-1}$ °C$^{-1}$ |
| $f$ | flow enhancement factor | 5 | $1 - 10$[c] | - |
| $G$ | geothermal heat flux | -50 | $-35 - -65$[a] | mW m$^{-2}$ |
| $\gamma$ | lapse rate | 5 | $5 - 9$[a] | °C km$^{-1}$ |

therefore expected that the ISM simulation forced by the BBC_ALL set should closely match the sea level reconstruction.

Our forcing of the ISM model using the BBC_ALL set of simulations is similar in methodology to Gregoire et al. (2012), except that they used a lower resolution version of HadCM3L (FAMOUS) and included an additional freshwater forcing. We use the same ISM as in Gregoire et al. (2012) with the same initial set-up. As the Glimmer ISM has no treatment of ice shelves, we lower the marine limit to -500 m to allow the formation of an ice sheet over shallow seas, such as the North Sea, consistent with Gregoire et al. (2012).

### 3.4.2   Ice sheet model tuning

The values for a number of the parameters in the ISM are poorly constrained. Varying these parameters can have a large impact on the spatial extent, volume and response times of an ice sheet to a climate forcing. Previous studies have identified key parameters which can have a large impact on the ISM simulations (Ritz et al., 1997; Hebeler et al., 2008; Stone et al., 2010; Applegate et al., 2012). These include the PDD factors for snow and ice, the flow enhancement factor, the geothermal heat flux and the lapse rate. These are summarised in Table 3.2, with the default values (hereafter P1) and ranges for these parameters from the literature.

The PDD factors ($\alpha_i$ and $\alpha_s$) relate the surface temperature to surface ablation, higher values lead to increased ablation. Values for these factor(s) are based on empirical relationships (Reeh, 1991). Typical default values for the PDD factors in modelling studies of the Greenland,

Antarctic, Eurasian and North American ice sheets are 3 mm d$^{-1}$ °C $^{-1}$ for $\alpha_s$ and 8 mm d$^{-1}$ °C $^{-1}$ for $\alpha_i$ (Huybrechts, 1993; Ritz et al., 1997; Lunt et al., 2008; Gregoire et al., 2012). Empirical data from a number of modern glaciers and time periods suggests that these factors could be higher (Hock, 2003). The study of Hock (2003) also highlighted that there are no universal PDD factors, but that they vary considerably between glaciers. As such, many modelling studies have used ranges for the PDD factors and used them as tuning parameters. Energy-balance modelling of the Greenland ice sheet suggested that $\alpha_i$ could be as high as 20 mm d$^{-1}$ °C $^{-1}$ and that $\alpha_s$ is generally less than half of the value for $\alpha_i$ (Braithwaite, 1995), which is comparable to the values from empirical data (Hock, 2003). We base our ranges for these parameters on existing modelling studies, using ranges of $3 - 8$ mm d$^{-1}$ °C $^{-1}$ for $\alpha_s$ and $8 - 20$ mm d$^{-1}$ °C $^{-1}$ for $\alpha_i$ (Ritz et al., 1997; Hebeler et al., 2008; Stone et al., 2010).

The flow enhancement factor $f$ is a tuning parameter which accelerates ice flow. Higher values for $f$ lead to increased flow. $f$ is included in Glen's flow law (see Section 3.2.2) to account for non-uniformities in the orientation of ice crystals (anisotropy), a value of 1 should be used for pure isotropic ice (Blatter et al., 2011). A default value of 3 is often used in modelling studies (Ritz et al., 1997). In previous studies using this parameter to tune ice sheet response, a range of $1 - 5$ for the flow enhancement factor has been used (Hebeler et al., 2008; Ritz et al., 1997; Stone et al., 2010). Values higher than 5 can also be found in the literature: Tarasov and Peltier (2004) use a standard value of 6.5 for $f$ whilst Ganopolski et al. (2010) used a maximum value of 12 for $f$ in their sensitivity tests when simulating the Northern Hemisphere ice sheets through the last glacial cycle. We adopt a range of 1 to 10 for $f$, consistent with Gregoire (2010).

The geothermal heat flux $G$ affects the basal mass balance and can affect basal sliding if basal sliding is dependent on the presence of basal meltwater. Default values for $G$ in modelling studies are typically -42 mW m$^{-2}$, based on values for Precambrian shields (Lee, 1970; Ritz et al., 1997). However the geothermal heat flux can vary significantly regionally (Lee, 1970). Rogozhina et al. (2012) investigated this effect by using various spatially varying geothermal heat flux maps for Greenland. They found that the currently available spatially varying maps produced larger errors than a simple uniform geothermal heat flux. Previous modelling sensitivity studies have used a range of -35 to -65 mW m$^{-2}$ for the Geothermal heat flux, (Ritz et al., 1997; Hebeler et al., 2008), which we adopt here.

The final tuneable parameter is the vertical lapse rate ($\gamma$). This accounts for the cooling of

the ice sheet surface as it grows vertically through the atmosphere. It is also used to translate temperatures from the coarse GCM grid onto the finer ISM grid. Values for $\gamma$ vary from region to region largely dependent on the moisture content of the atmosphere. In a GCM study, Krinner and Genthon (1999) found values as high as $10\,^{\circ}\mathrm{C}\,\mathrm{km}^{-1}$ for the dry interiors of large continental sized ice sheets, such as the East Antarctic ice sheet. For the coasts, and for smaller ice sheets such as the Greenland ice sheet, values as low as $\sim 5\,^{\circ}\mathrm{C}\,\mathrm{km}^{-1}$ were found. Therefore values for $\gamma$ when simulating large ice sheets are typically $7-9\,^{\circ}\mathrm{C}\,\mathrm{km}^{-1}$ (Pollard and Thompson, 1997) and $5-7\,^{\circ}\mathrm{C}\,\mathrm{km}^{-1}$ when simulating the smaller Greenland ice sheet (Lunt et al., 2008). Because we are simulating ice sheets over a wide variety of regions, including continental interiors and coastal regions, we adopt a range of $5-9\,^{\circ}\mathrm{C}\,\mathrm{km}^{-1}$ for the lapse rate, following Hebeler et al. (2008)

Previous studies addressing the impact of parametric uncertainty on ice sheet response have varied the same parameters that we have selected. Broadly, they found that the spatial extent of the ice sheet was most affected by the parameters which affect ablation, these being the PDD factors and the lapse rate (Ritz et al., 1997; Stone et al., 2010; Hebeler et al., 2008). These parameters had little impact on the ice thickness. The ice thickness was most affected by changing the flow enhancement factor $f$ (Ritz et al., 1997; Stone et al., 2010; Hebeler et al., 2008). The geothermal heat flux had a limited influence on ice sheet geometry (Ritz et al., 1997; Hebeler et al., 2008), although some of these studies did not include basal sliding (e.g. Stone et al., 2010).

Two approaches are typically adopted when looking at parametric uncertainty in ISMs. The first approach is to vary each parameter individually through its plausible range, with all of the other parameters held at their default value (Ritz et al., 1997; Huybrechts and de Wolde, 1999). This has advantages in that it is easy to determine the response to individual parameters, however it neglects the potential interactions between parameters (Stone et al., 2010). The second approach is to adopt a sampling strategy that varies all parameters at once. With this approach the parameters can either be randomly sampled, although there is no guarantee that all of the parameter space will be sampled, or an alternative sampling approach can be used (Stone et al., 2010). Latin hypercube sampling is a more efficient sampling strategy than random sampling (McKay et al., 1979). With this method, each parameter is divided into $N$ evenly spaced bins, with a sample taken from a uniform distribution within each bin. This therefore ensures that the tails of each parameter are sampled. The samples from each parameter are then randomly sorted with the samples from the other parameters, producing parameter sets
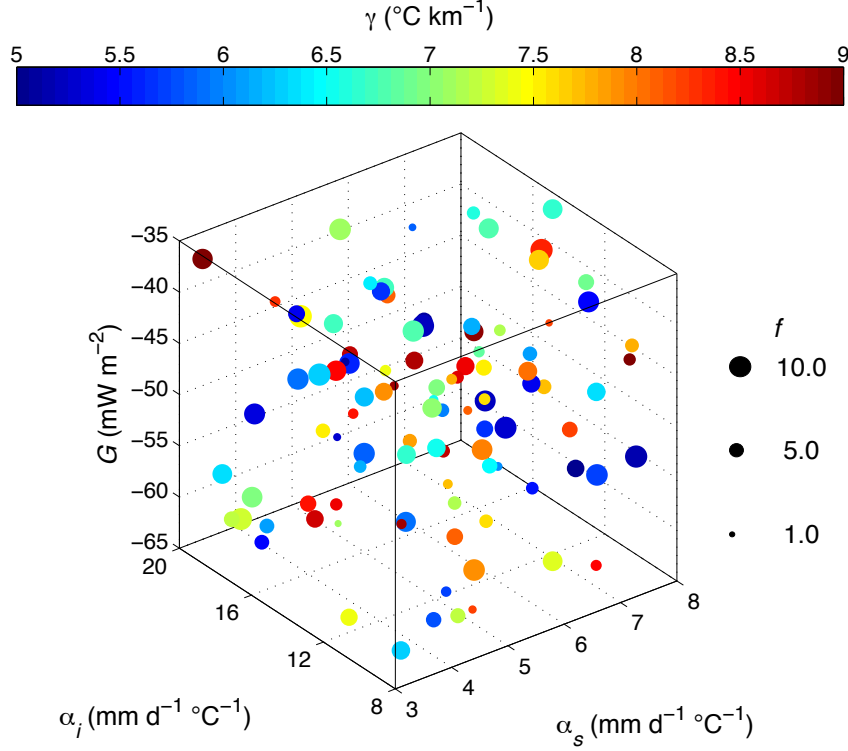
Figure 3.9: *Distribution of 5 ISM parameters using Latin hypercube sampling. On the x and y axes are the PDD factors for snow and ice, on the z axis is the geothermal heat flux, shown by the colour-scale is the lapse rate and the size of the circles shows the flow enhancement factor. 100 parameter sets were created from the ranges for each parameter given in Table 3.2. All parameter values are included in Appendix A*

(McKay et al., 1979; Stone et al., 2010).

It is suggested that the value for $N$, the number of parameter sets created, should be at least 5 times the number of variables (Iman and Helton, 1985). For our control BBC_ALL simulations we conduct 100 simulations (i.e. $N$ is 20 times the number of variables) using latin hypercube sampling. Note that the default parameter set is not in the centre of the latin hypercube. This is because the default values for the PDD factors and the lapse rate are at the lowest values for the plausible range given in Table 3.2.

### 3.4.3 Simulations with BBC_ALL ensemble

The first set of ISM simulations performed are forced by the BBC_ALL set of GCM simulations. Because we are using snapshot GCM simulations, we linearly interpolate the temperature and

precipitation data from each of these 62 simulations through time, from the first simulation at 120 ka to the last simulation at modern. We allow an initial ice sheet to grow at the start of the simulations by including a 20 kyr spin-up phase using the climate from the first simulation. This spin-up phase is not shown on the figures, the initial conditions are a modern ice sheet extent. The BBC_ALL GCM simulations include evolving ice sheet extent, based on the ICE-5G reconstruction from the LGM to present. From the LIG to the LGM the ice sheet extent in the GCM is scaled from ICE-5G using the SPECMAP record of $\delta^{18}$O (Singarayer and Valdes, 2010; see Appendix B). This therefore assumes that the ice sheets glaciated with the same geometry that they deglaciated.

We conduct simulations using the default ISM parameter set (P1) and also conduct a 100 member ensemble. ISM simulations are conducted for the North American domain and the Eurasian domain. We combine the ice volume output from both regions and convert this into a sea level record. This enables us to compare our model simulation with sea level reconstruction. Ice volumes are converted to sea level by first adjusting volumes for a change in state, assuming a density for ice of 918 kg m$^{-3}$ and a density for seawater of 1028 kg m$^{-3}$ (Bamber et al., 2009), and then dividing by the total modern ocean surface area. The sea level reconstruction we use is the Red Sea estimate (Siddall et al., 2003; Rohling et al., 2009), which has been shown to be representative of other independent estimates (Siddall et al., 2010a). Note that we ignore the impact of changes in the Antarctic ice sheets over the glacial cycle. The reason for this is twofold, firstly the expansion of the Antarctic ice sheets was a small contributor to the sea level fall at the LGM ($\sim 8 - 14$ m; Denton and Hughes, 2002; Pollard and DeConto, 2009; Mackintosh et al., 2011; de Boer et al., 2012b) and secondly the expansion was largely of the marine based WAIS (Denton and Hughes, 2002), which we cannot correctly simulate using the Glimmer ISM. Basal sliding is included in these experiments, using the spatially varying parameters of Gregoire et al. (2012) (BS2).

The first thing to note from the BBC_ALL control ensemble is that the default parameter set (blue dashed line in Figure 3.10), as used by Gregoire et al. (2012), overestimates the volume of the North American ice sheets and significantly overestimates the volume of the Eurasian ice sheets. This results in sea level much lower than is suggested by the Red Sea sea level record (Siddall et al., 2003; Rohling et al., 2009). Our method in these experiments is similar to Gregoire et al. (2012), except we use a higher resolution version of the same GCM. This highlights why tuning the ISM is often necessary. The best parameter set produces a root-mean squared error (RMSE) of $\sim 12$ m sea level equivalent (SLE), when compared to the Red Sea
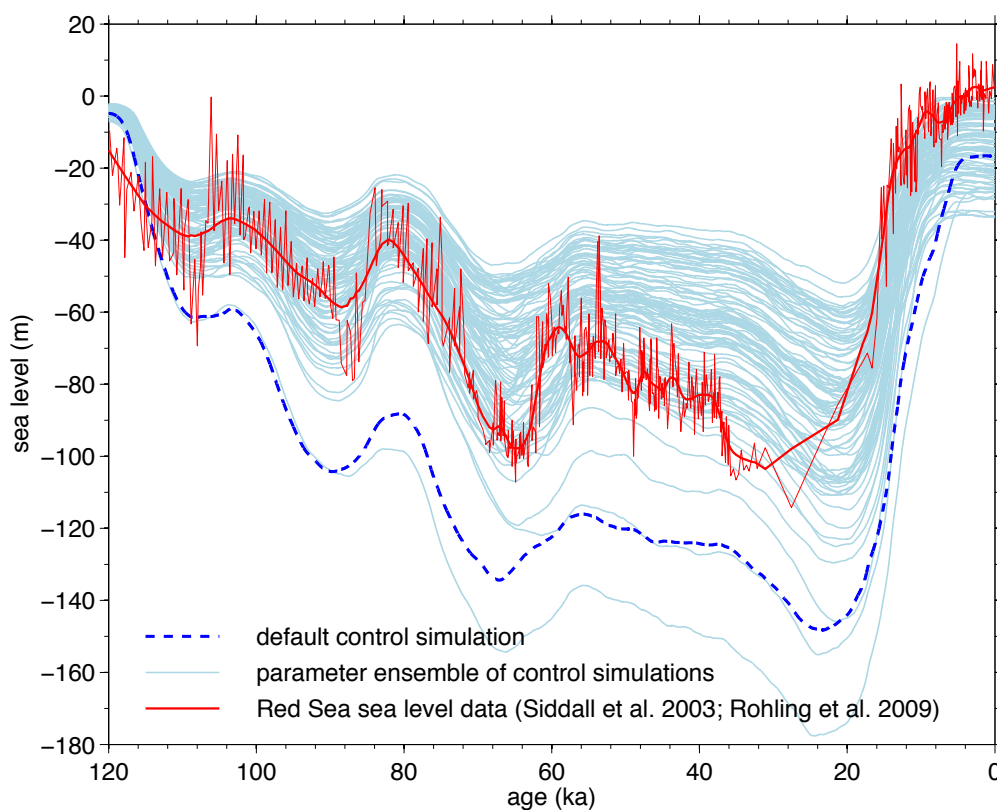
Figure 3.10: *Ensemble simulation of the last glacial cycle compared to the Red Sea sea level record. Simulations performed by forcing the Glimmer ISM with the BBC_ALL set of GCM simulations. Ensemble of 100 simulations, with 5 parameters varied using latin hypercube sampling. The ice volume from simulation of the North American and Eurasian ice sheets is converted to sea level to compare with the Red Sea record. 2 ensemble members failed. The default parameter set, based on Gregoire et al. (2012) is shown as a blue dashed line.*

record.

The majority of the simulations have too much ice remaining at modern, shown by sea levels of −10 to −30 m at modern. This is largely due to the lowering of the marine margin. This means that the Greenland ice sheet is able to spread over the continental shelf. It is difficult to overcome this problem with the current version of Glimmer (see Section 3.2.5). Some of the simulations also have large ice caps remaining in other regions where there are no large ice caps today, such as Baffin Island, British Columbia and Novaya Zemlya. The large ice cap that often remains over Novaya Zemlya in northern Russia is especially large because of the marine limit

Table 3.3: *Ensemble members producing good agreement with Red Sea record, RMSE: 12.2 m SLE, and best agreement with ICE-5G ice volumes at LGM, North America: 36.6 $\times 10^6$ km$^3$ and Eurasia: 9.6 $\times 10^6$ km$^3$. Parameter values referred to as P2 in the text*

|  |  | North America (95) | Eurasia (45) | units |
|---|---|---|---|---|
| $\alpha_s$ | PDD factor for snow | 3.172 | 6.206 | mm d$^{-1}$ °C $^{-1}$ |
| $\alpha_i$ | PDD factor for ice | 16.365 | 19.766 | mm d$^{-1}$ °C $^{-1}$ |
| $f$ | flow enhancement factor | 8.649 | 8.966 | - |
| $G$ | geothermal heat flux | -48.909 | -62.251 | mW m$^{-2}$ |
| $\gamma$ | lapse rate | 5.321 | 5.833 | °C km$^{-1}$ |

problem. Evaluating the ensemble members based on the total contribution to sea level from the formation of the Northern Hemisphere ice sheets, does not take into account whether ice has formed in the correct regions. Indeed, we find that generally too much ice forms in the Eurasian domain, which is compensated for by too little ice forming in the North American domain for the best ensemble members.

In response to the problem of too much ice forming in the Eurasian domain we impose a criteria in order to pick the best ensemble members. We rank ensemble members based on the ice volumes for each domain at the LGM. The ICE-5G reconstruction suggests that there was $37 \times 10^6$ km$^3$ of ice in the North American domain and $9 \times 10^6$ km$^3$ of ice in the Eurasian domain at the LGM (Peltier, 2004; Gregoire, 2010). We therefore select members which are $\pm 25$ % of the ICE-5G reconstruction at the LGM. As none of the ensemble members can meet this criteria for both domains, we mix the ensemble members which do meet this criteria (8 members for Eurasia and 16 members for North America) for each domain. This therefore creates 128 additional ensemble pairs, which we can then compare against the Red Sea record. Note that it is only possible to select the 'good' ensemble members because there is some independent data for the ice sheet extent at the LGM, we could not currently adopt this approach for the subsequent simulations of the East Antarctic ice sheet at the EOT due to a lack of data.

The ensemble pair which is closest to the ICE-5G ice volumes at the LGM is member 95 for the North American domain (36.6 $\times 10^6$ km$^3$) and member 45 for the Eurasian domain (9.6 $\times 10^6$ km$^3$). This ensemble pair (hereafter P2) is highlighted on Figure 3.11 and the parameter values are given in Table 3.3. Note that the PDD factors and the flow enhancement factor are close to the upper range of the plausible ranges given in Table 3.2, especially for Eurasia.
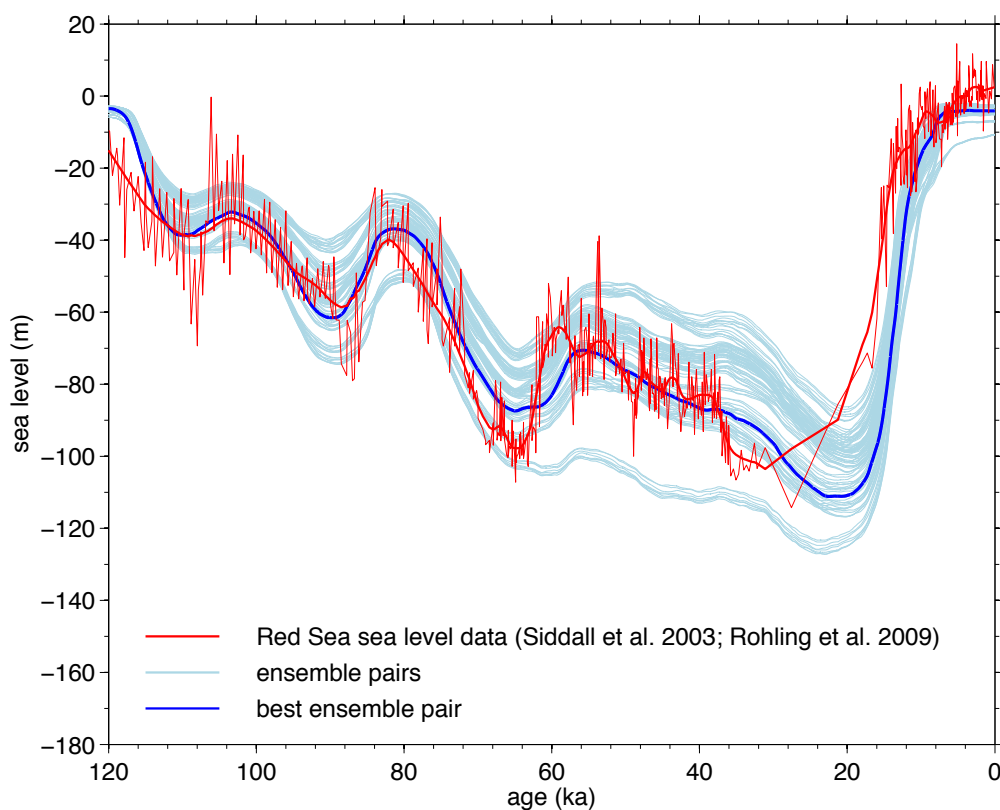
Figure 3.11: *Paired ensemble simulation of the last glacial cycle compared to the Red Sea record. Ensemble of 128 ensemble pairs, formed of 8 members from Eurasia and 16 members from North America which are within ± 25% of the ICE-5G reconstruction at the LGM. The best ensemble pair with the lowest RMSE compared with the Red Sea sea level record is highlighted in dark blue (member 45 for Eurasia and 95 for North America).*

Although following tuning the Eurasian ice sheets are close in volume to the ICE-5G reconstruction, the distribution of ice is generally different to empirical reconstructions (Svendsen, 2004). Typically the Barents Sea ice sheet extends too far south-east in our simulations at the LGM. Although the ice sheet did extend onto the main Asian continent, reaching as far south-east as the Putorana Plateau at around 80-90 ka, it had retreated significantly by the LGM to the Kara Sea (Lambeck, 1996; Svendsen, 2004). Because the Barents Sea ice sheet extends over a much greater area in our simulations, its volume is also too large. For the ensemble member which best matches the ICE-5G volume for Eurasia (member 45), the large Barents Sea ice sheet is balanced by Fennoscandian and British Isles ice sheets which are much smaller than
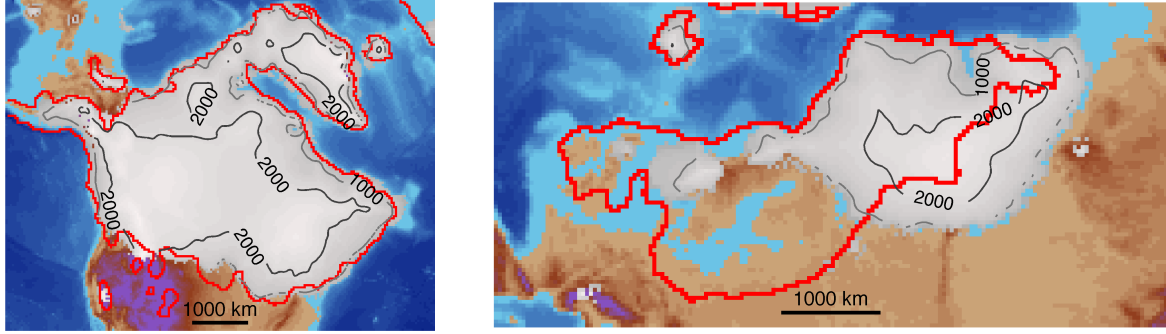
Figure 3.12: *Ice sheet extent at LGM for ensemble member 95 (North America) and member 45 (Eurasia). Glacioisostatic reconstruction (ICE-6G) is shown as a red outline.*

suggested by glaciological evidence (Svendsen, 2004). The Barents Sea ice sheet was a marine based ice sheet, which was therefore sensitive to sea level fluctuations. Because we cannot accurately simulate marine based ice sheets using the present version of the Glimmer ISM, we are not confident that we can successfully simulate the Eurasian ice sheets. Nevertheless we use ensemble member 45 for the subsequent Eurasian simulations as it is the best match to the ICE-5G volume and hence sea level, which we are ultimately interested in. The spatial extent of the North American ice sheets in our simulations are generally much closer to empirical and glacioisostatic reconstructions at the LGM (see Figure 3.12; Dyke, 2002; Laskar et al., 2004).

This tuning exercise illustrates the sensitivity of the ISM to certain parameters. As previously noted, the GCM we use, HadCM3, has a slight cool bias (Pope et al., 2000). By tuning the ISM parameters to the sea level data we are overcoming deficiencies in both the ISM and the GCM. It is therefore unlikely that the best parameter sets in this experiment would be the same if another GCM were used.

One interesting result of the study of Gregoire et al. (2012) was the nonlinear ice sheet response to climate forcing (see Figure 3.13). The authors found an acceleration in the deglaciation of the North American ice sheets as the Cordilleran and Laurentide ice sheets separated. As these two ice domes separate, height-mass balance feedback increased the surface ablation. This 'saddle-collapse' mechanism is seen in their results as a sharp increase in the meltwater flux. They suggested that this mechanism could be responsible for meltwater pulses, such as MWP-1a and the 8.2 ka event. Our method using the BBC_ALL simulations to force the ISM is similar to Gregoire et al. (2012) and we also see this nonlinear response in our results. We plot the meltwater flux from our optimum ensemble members in Figure 3.13.
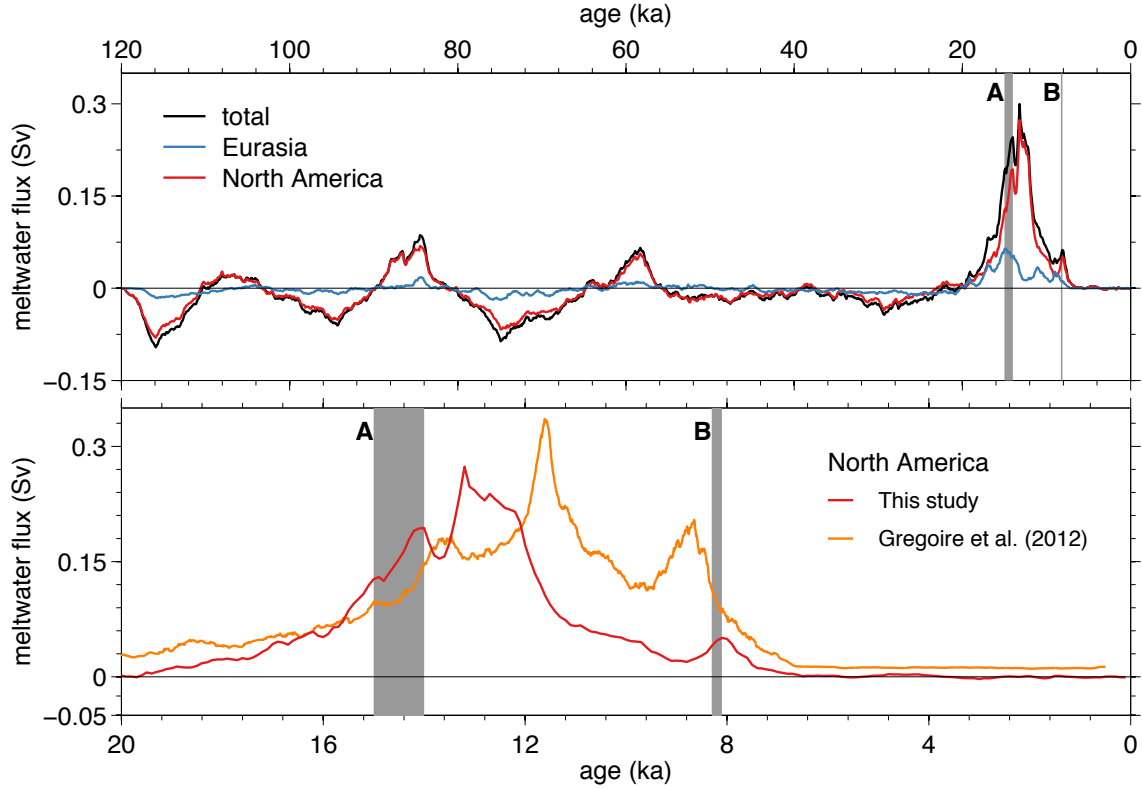
Figure 3.13: *Meltwater flux from North American and Eurasian ice sheets. Some of the peaks in the meltwater flux are attributed to the 'saddle-collapse' mechanism. The grey bars mark the timing of A) the separation of the Cordilleran and Laurentide ice sheets in ICE-5G and B) the 8.2 ka event. Also shown in the lower subplot is the meltwater flux from North America from the study of Gregoire et al. (2012)*

We find a pulse of 0.3 Sv at 13.2 ka which coincides with the separation of the Cordilleran and Laurentide ice sheets in our simulations. This is slightly later than the separation of these ice sheets in the ICE-5G reconstruction (Peltier, 2004) and as suggested by empirical evidence (Dyke, 2004). The grey bar 'A' on Figure 3.13 marks the separation of the Cordilleran and Laurentide ice sheets in the ICE-5G reconstruction at $15 - 14$ ka. Although there is a peak in the meltwater flux in our simulations at this time, this is caused by the rapid retreat of the southern limit of the Laurentide ice sheet, rather than through the 'saddle-collapse' mechanism, which causes the larger peak immediately afterwards. The timing of the separation of these two ice sheets was also late in the simulations of Gregoire et al. (2012), where it occured at 11.6 ka. The next meltwater peak, marked 'B' on Figure 3.13, coincides with the 8.2 ka event. In our simulations this is caused by the separation of two ice domes, one over Baffin Island (Fox dome)

Table 3.4: *RMSE for astronomical methods against control simulation. Astronomical methods are summarised in Table 3.1. RMSE compared with control simulation for both domains.*

|        | North America RMSE | Eurasia RMSE | Northern Hemisphere RMSE |
|--------|--------------------|--------------|--------------------------|
| AST1   | $0.36 \times 10^6$ | $0.54 \times 10^6$ | $0.83 \times 10^6$ |
| AST2   | $0.53 \times 10^6$ | $0.71 \times 10^6$ | $1.21 \times 10^6$ |
| AST3   | $0.27 \times 10^6$ | $0.47 \times 10^6$ | $0.68 \times 10^6$ |
| AST4   | $1.02 \times 10^6$ | $1.09 \times 10^6$ | $2.07 \times 10^6$ |
| AST5   | $0.65 \times 10^6$ | $0.99 \times 10^6$ | $1.60 \times 10^6$ |

and one over Quebec (Labrador dome), again the peak in the meltwater flux can be attributed to the 'saddle-collapse' mechanism (Gregoire et al., 2012).

Some of the earlier meltwater peaks, in particular the peak at ∼85 ka, can also be attributed to the 'saddle-collapse' mechanism. The peak at ∼85 ka is caused by the separation of the Cordilleran ice sheet from another ice dome, which resembles the later separation of the Cordilleran and Laurentide ice sheets. The peak at ∼60 ka is not a full separation of ice sheets, but there are 3 large ice domes and there is significant ice loss from the saddles between them, accelerated by mass-balance feedback (ice maps through time for these events are included in Appendix C).

### 3.4.4   Simulations with BBC_AST

The BBC_ALL simulations will be used as a control to test the full GCM matrix method. We first test our parameterisation of individual dimensions within the GCM matrix, starting with the parameterisation of astronomical variability. We use all of the simulations within the BBC_AST set to create a control ISM simulation. The climate forcing is provided by interpolating between each of the GCM simulations within the BBC_AST set, using the same method we adopted for the BBC_ALL simulations previously discussed. We test each of the insolation interpolation methods (AST1-AST5) against this control simulation. These simulations use the default parameter set, P1.

As can be seen from Figure 3.14 and Table 3.4, the closest match the BBC runs is AST3, for both the North American and Eurasian domains. For the Northern Hemisphere, this results in a root mean squared error (RMSE) of $0.68 \times 10^6$ km$^3$ (1.8 m SLE) compared to the BBC_AST control. Averaging over the 6 summer months (AST3) generated a closer match to the control
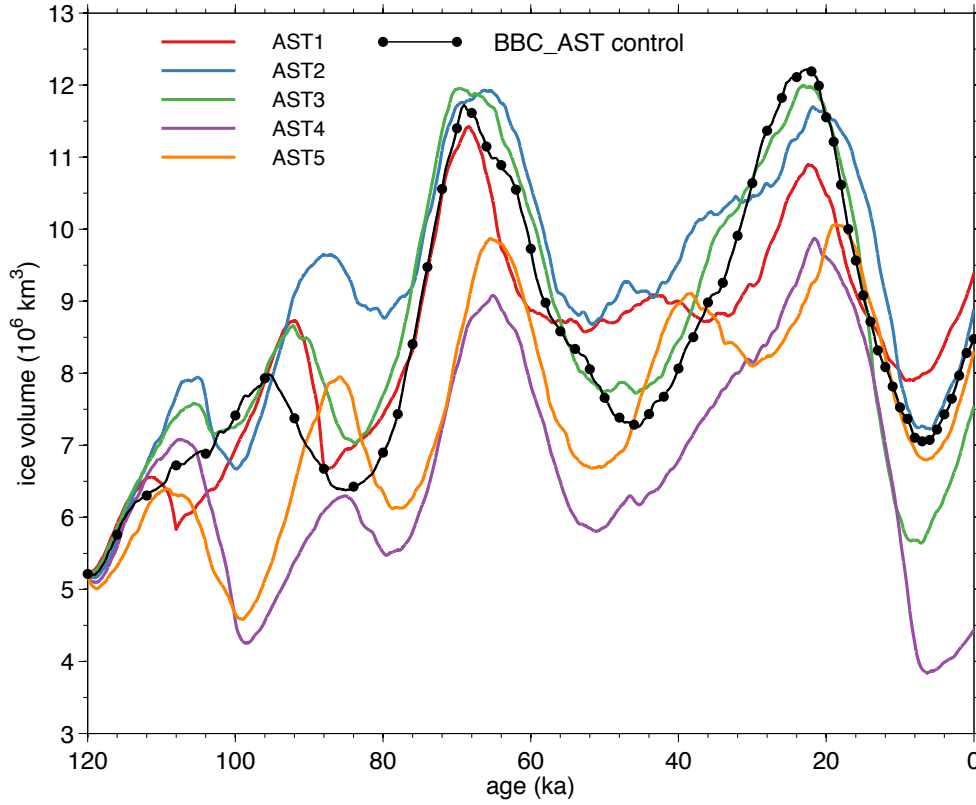
Figure 3.14: *Time series of the different insolation interpolation methods (summarised in Table 3.1). The BBC astronomical only control run is shown in black, the black dots are the 62 time-slice GCM simulations used for the control simulation*

simulation than using the June 65°N insolation (AST1). It is interesting that AST1, which is typically shown to represent Northern Hemisphere glaciation, underestimates ice volume at the LGM and shows a much smaller deglaciation than the control simulation. The experimental methods using the TOA insolation fields to represent astronomical variability (AST4-5) generated larger errors than the time series methods (AST1-3). Although AST3 is closest to the astronomical control it does deviate in certain periods, such as the last deglaciation where it generates too large of a reduction in ice volume compared to the control. Based on the results of this experiment we will use the method AST3, which is based on the summer insolation at 65°N, for the simulations using the full GCM matrix.

103

### 3.4.5 Simulations with BBC_GHG*

We next test our parameterisation of GHG forcing within the GCM matrix. As no GHG-only set of simulations were performed as part of the BBC suite of simulations, we approximate a GHG only set by removing the BBC_AST anomaly from the BBC_AST_GHG set of simulations. We force the ice sheet model with the resulting BBC_GHG* set of simulations to create the control simulation. The BBC_GHG* set of simulations includes varying atmospheric concentrations of $CH_4$ and $N_2O$, in addition to $CO_2$. For our parameterised GHG forcing we scale 2 GCM simulations using the $CO_2$ record used in the control simulation (Petit et al., 1999; Singarayer and Valdes, 2010). The additional GHGs vary approximately in phase with $CO_2$ so we consider this reasonable. The default method we test (GHG1) is to interpolate between the GCM simulation with the maximum (280 ppmv, 0 ka) and the lowest (185 ppmv, 22 ka) atmospheric $CO_2$.

As can be seen from Figure 3.15, the interpolation of GHG forcing from just 2 GCM simulations is able to reproduce the control simulation based on 62 GCM simulations relatively well. The RMSE for GHG1 is $0.929 \times 10^6$ km$^3$, which is equivalent to 2.5 m of sea level. One thing to note is that the deglaciation after the LGM in the interpolated simulation lags the control simulation by $\sim$4 ka. This could be important for correctly simulating the last deglaciation with the full GCM matrix method. Interestingly, by switching to interpolating between the simulation at 17 ka and modern (GHG2), the timing of the deglaciation is better matched to the BBC_GHG* control. However, for GHG2 the RMSE compared to the control is slightly higher than for GHG1, at $0.961 \times 10^6$ km$^3$ (2.6 m SLE). For GHG3 we tested interpolating between the GCM simulation at 19 ka and modern, this produced a slightly higher RMSE than GHG1 ($0.931 \times 10^6$ km$^3$) and also has a late start to the deglaciation. We will use GHG1 as our default method for GHG interpolation within the full GCM matrix.

### 3.4.6 Simulations with full GCM matrix

Finally we test the full GCM matrix against the BBC_ALL simulation. For this experiment we are testing all of the parameterisations, the previously tested astronomical and GHG forcings in addition to the ice sheet-climate feedback. For the astronomical forcing, we use AST3 for these experiments because it produced the smallest errors compared to the astronomical control. We test the 2 ice sheet feedback methods described previously. These are FB1, for which the feedback is based on interpolation between 3 GCM simulations based on the total ice volume
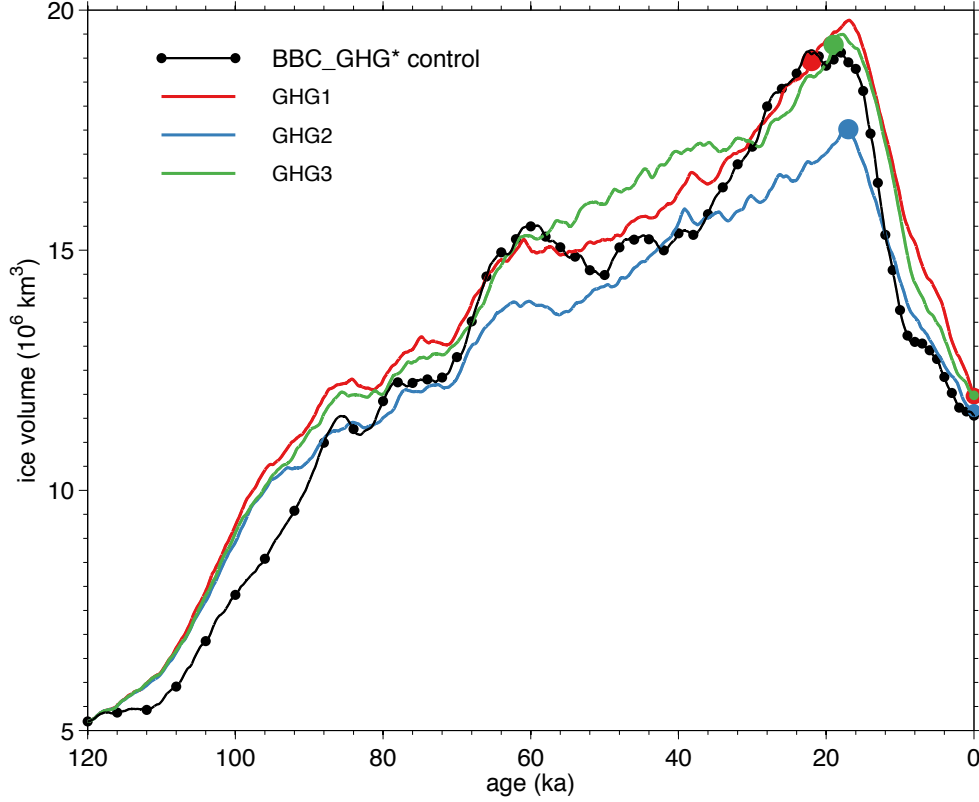
Figure 3.15: *Time-series of the $CO_2$ interpolation method. GHG1 uses GCM simulations from 0 ka and 22 ka, GHG2 from 0 ka and 17 ka and GHG3 from 0 ka and 19 ka. Dots show GCM simulations used to force the ISM.*

for the domain and FB2, for which the feedback is applied on a grid-box by grid-box basis depending on whether ice is present in that grid-box (the patchwork method).

As can be seen from Figure 3.16, there is mixed success in reproducing the BBC_ALL control ISM simulation using the GCM matrix method. Firstly, the simulation using the ice sheet feedback method FB1 and the parameter set P2 (see Table 3.3) significantly underestimate ice volumes and is unable to grow a significant ice sheet on either continent. These particular parameter values used generate high rates of ablation because the PDD factors are close to the upper plausible range. We therefore performed a simulation using FB1 and the default parameters (P1, after Gregoire et al. (2012), see Table 3.2). These default parameter values have lower values for the PDD factors and for the flow enhancement factor, thus aiding ice growth. The FB1 simulation with parameter set P1 leads to increased ice growth and is much
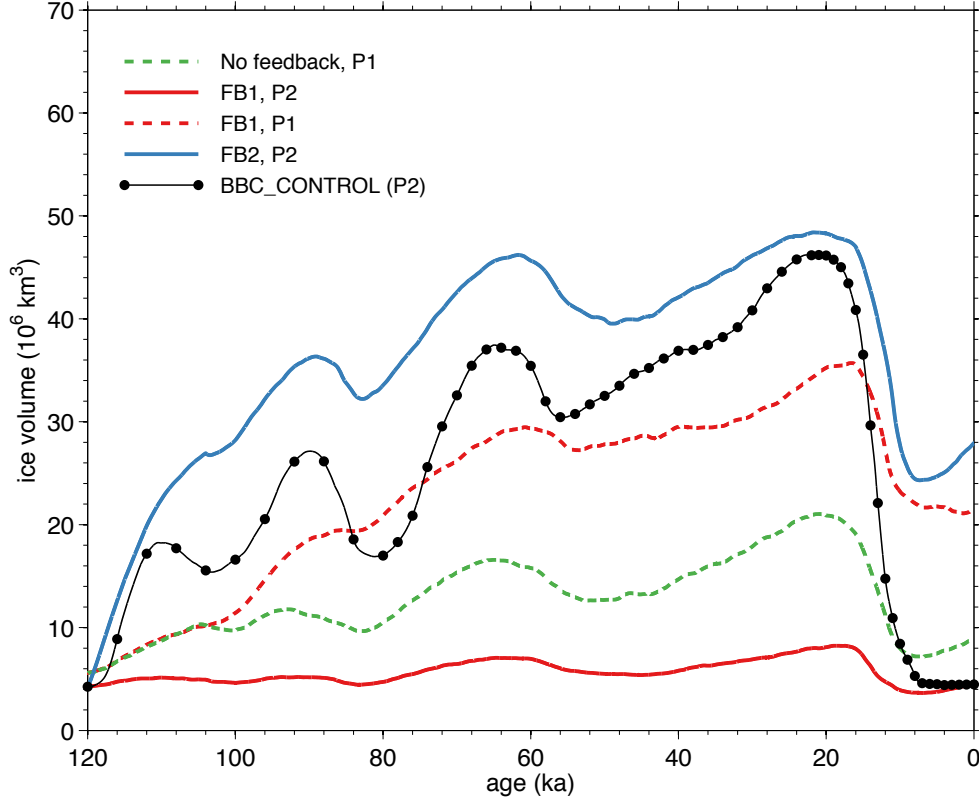
Figure 3.16: *Time-series of the full GCM matrix method against the BBC_ALL control. Shown are the 2 ice sheet feedback methods, FB1 and FB2. A simulation with no feedback is also included. Parameter values are either P1, the default parameter values from Table 3.2 or P2, the best parameter pair from the ensemble, see Table 3.3*

closer to the control simulation. For the simulation with FB1 and the P1 parameter set there is limited reduction in ice volume during the last deglaciation, resulting in $\sim 20 \times 10^6$ km$^3$ of ice remaining at modern. The RMSE compared to the control simulation is $8.5 \times 10^6$ km$^3$ ($\sim 21$ m SLE).

We next compared the results of the patchwork feedback method, FB2. The growth of ice is faster for this simulation than for the control simulation, with a less 'saw-toothed' build-up of ice than is seen in the control simulation. This is likely due to the feedback method, where the climate provided to the ice sheet model is in effect the LGM climate for regions where ice has grown. Ice volumes at the LGM are similar to the BBC_ALL control; however there is only a partial deglaciation with significant ice volumes remaining at modern. The deglaciation is also
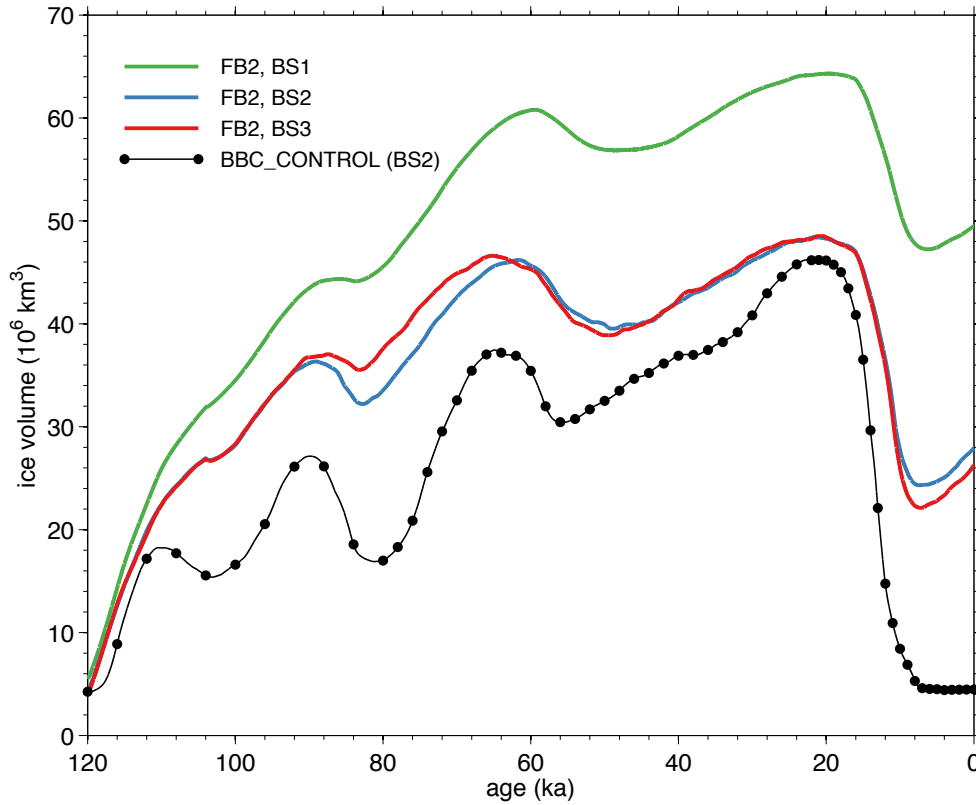
Figure 3.17: *Impact of basal sliding on the GCM matrix method. Simulations using the full GCM matrix method with either no basal sliding (BS1), spatially varying basal sliding (BS2) or uniform basal sliding (BS3)*

later than the control simulation. It is possible that this is caused by the GHG interpolation method, which also showed late deglaciation. However, also shown on Figure 3.16 is a simulation with GHG and astronomical forcing only (i.e. no ice sheet albedo feedback), this does not show a late start to deglaciation. This would therefore suggest that the late deglaciation shown in the FB2 simulation is due to deficiencies in the ice sheet feedback method, rather than the GHG interpolation method. The RMSE for the FB2 method compared with the control simulation is $11.0 \times 10^6$ km$^3$ ($\sim 27$ m SLE).

Another potential factor limiting deglaciation is basal sliding. All of the simulations in Figure 3.16 have a spatially varying basal sliding parameter (BS2). The ice remaining after the deglaciation is often in regions where this parameter is set to the lower value (0.5 mm yr$^{-1}$ Pa $^{-1}$). We perform a simulation with a universal basal sliding, where the basal sliding parameter
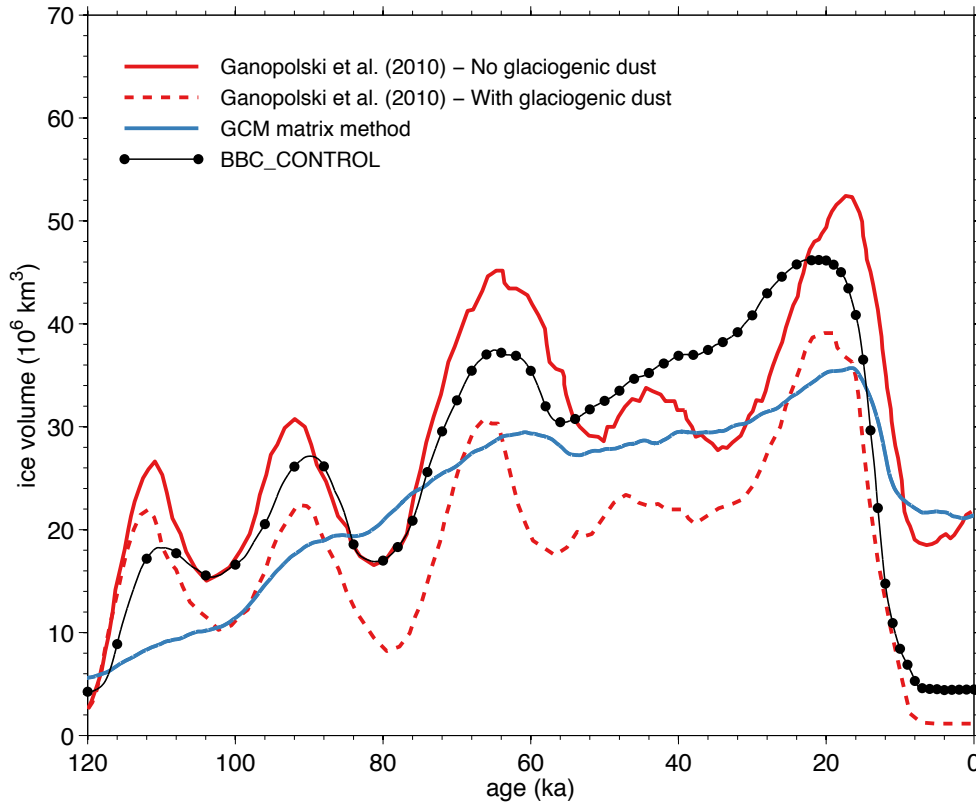
Figure 3.18: *Comparison of the best simulation using the GCM matrix method with the results of Ganopol-ski et al. (2010). The GCM matrix method simulation uses FB1, BS2 and P1. The Ganopolski et al. (2010) simulations are digitised from their Figure 11c, for simulations with and without the glaciogenic dust flux.*

is set to 10 mm yr$^{-1}$ Pa$^{-1}$ across the entire domain (BS3). This leads to a slight reduction in ice volume during the last deglaciation, but there is still a significant ice volume remaining (see Figure 3.17). To investigate the importance of including basal sliding, we also performed a simulation with basal sliding turned off (BS1). This resulted in higher ice volumes than the BBC_ALL control.

The problems we are facing in simulating a complete deglaciation have been encountered in previous studies. There have been various solutions proposed to these problems, although some of these are likely to be model specific. Ganopolski et al. (2010) simulated the last glacial cycle using a climate model of intermediate complexity. The authors included a simple dust deposition model, composed of a 'background' and a 'glaciogenic' dust flux, which had a large

impact on ice surface albedo. In sensitivity experiments without the glaciogenic dust model included, only a partial deglaciation was achieved, with $> 20 \times 10^6$ km$^3$ of ice remaining at modern, comparable to the volume of ice remaining in our best simulation (see Figure 3.18). The Ganopolski et al. (2010) simulation without the glaciogenic dust model also showed a late start to deglaciation, as seen in some of our simulations.

In the simulations of Ganopolski et al. (2010) the 'background' flux is based on interpolating between the modern and LGM dust flux based on total ice area. The 'glaciogenic' dust flux is based on the assumption that some proportion of the sediment transported at the ice front becomes airborne through erosion. Because this is only produced in ice-free cells neighbouring ice-covered cells, and because there is a characteristic timescale for erosion of 1000 years, the dust flux is low when the ice sheet is advancing and high when the ice sheet has stopped advancing. Both the 'background' and 'glaciogenic' ice flux peak at the LGM, encouraging deglaciation once LGM ice volumes have been reached and the ice sheet has stopped advancing. Because the dust model is partially based on empirical data and modern maps of sediment thickness, Ganopolski et al. (2010) suggest it would be inappropriate to apply the model for periods earlier than the last glacial cycle. It would also be problematic to implement a similar dust flux model in our simulations as we do not use the surface energy balance method to calculate the surface mass balance but use the positive degree-day method, which does not include an albedo term. Additionally we are interested in simulating the ice sheets for periods earlier than the last glacial cycle.

## 3.5  Summary

In this chapter we have described and evaluated a method for providing a time evolving climate to an ISM in order to simulate the long term evolution of the ice sheets. This method, which is based on a matrix of GCM simulations, is based on the method outlined by Pollard (2010). Using this method we can represent the main climate forcings on an ice sheet, these being astronomical forcing, GHG forcing and ice sheet feedbacks on the climate system. We have tested this method against Northern Hemisphere control simulations of the last glacial cycle. We have provided examples as to why an offline forcing method, where the climate output from one GCM simulation is used to force an ISM to equilibrium, can generate large errors. In particular the offline forcing method can significantly overestimate astronomical forcing. Although other methods exist for simulating the long term evolution of the ice sheets (e.g.

DeConto and Pollard, 2003a), these have often been applied to data poor periods (the EOT) without first being shown capable of reproducing the evolution of the ice sheets in more data rich periods (such as the last glacial cycle). By first testing our method against the last glacial cycle we have been able to refine our method and understand its limitations.

The results of this chapter suggest that the individual representation of astronomical forcing and GHG forcing within the GCM matrix can reproduce the results of our control simulations with errors on the order of a few metres SLE. However, there was limited success in simulating the last glacial cycle when using the full GCM matrix method, in particular for simulating the last deglaciation. The RMSE compared to our control simulation was $\sim$21 m SLE for our best simulation using the full GCM matrix method. The largest source of error in the GCM matrix method is in the representation of ice sheet feedbacks on the climate. The limitations of this method should be borne in mind when interpreting the results from the subsequent chapters.

In the following chapters we will use the GCM matrix method to simulate the EAIS under Eocene / Oligocene boundary conditions. The exercise presented in this chapter of simulating the Northern Hemisphere ice sheets during the last glacial cycle will aid our simulation of the EAIS in the next chapters. Following this evaluation of the GCM matrix method, we will use the astronomical forcing AST3 and the ice sheet feedback method FB1 for these next simulations. This work on the Northern Hemisphere ice sheets also illustrates the importance of including basal sliding in these simulations. The difficulties in simulating the deglaciation of the Northern Hemisphere ice sheets may also have implications for the high stability of the EAIS seen in previous ISM studies (Pollard and DeConto, 2005; Langebroek et al., 2009), some of which have used a methodology similar to that used here (Pollard, 2010).

# Chapter 4

# Modelling the onset of Antarctic glaciation – ice in the Eocene?

## 4.1 Introduction

The aim of this chapter is to address some of the questions which have arisen from the discussion in earlier chapters, in particular whether small ice sheets could have existed and contributed to sea level fluctuations in the Eocene (Miller et al., 2005a, 2008a; Eldrett et al., 2007; Dawber et al., 2011). Miller et al. (2008a) have used the results of a previous ice sheet modelling study (DeConto and Pollard, 2003a) to argue in support of the existence of ephemeral ice sheets in the Eocene. DeConto and Pollard (2003a) suggested that the onset of Antarctic glaciation was driven by declining atmospheric $CO_2$ at the EOT. Proxy records of atmospheric $CO_2$ suggest that the modelled $CO_2$ threshold for Antarctic glaciation may have been crossed at times in the Eocene, earlier than the EOT which is generally considered the period when continental scale Antarctic glaciation first occurred in the Cenozoic (DeConto and Pollard, 2003a; Zachos et al., 2008; Beerling and Royer, 2011).

For consistency with the modelling work in the previous chapter, it was our original intention to use HadCM3L to provide the climate forcing for all of the Antarctic ISM simulations, a version of the same GCM used in the previous chapter (HadCM3). Using HadCM3L would have had advantages over previous work (DeConto and Pollard, 2003a) in that HadCM3L is a coupled ocean-atmosphere GCM rather than a simpler atmosphere-only GCM with a slab ocean, as used by DeConto and Pollard (2003a). Another apparent advantage of using HadCM3L is that a number of the simulations that would make up the GCM matrix are already available, following the early Eocene simulations of Lunt et al. (2010b, 2011). Therefore fewer additional simulations would need to be performed. These pre-existing simulations are early Eocene simulations at $1\times$, $2\times$, $4\times$ and $6\times$ pre-industrial atmospheric $CO_2$ (PIC, 280 ppmv). Simulations are also available with variations in the astronomical forcing (Lunt et al., 2011). All of these simulations were performed with an ice-free Antarctic, meaning that the only additional runs which would need to be performed are simulations with an added Antarctic ice sheet, in order to include ice sheet-climate feedbacks using the previously discussed GCM matrix method.

After conducting initial offline ISM simulations using the climate forcing from the HadCM3L simulations (Lunt et al., 2010b, 2011), the results were unexpected when compared with previous simulations (Huybrechts, 1993; Pollard and DeConto, 2005; Langebroek et al., 2009). In order to test the HadCM3L results, additional simulations were performed using simulations from another 4 GCMs (CCSM3, ECHAM5, GISS (ModelE-R) and GENESIS). The results from this inter-model comparison also suggest that the ISM simulations using HadCM3L are unusual.

This inter-model comparison also lends new insights to the question of whether ice sheets could have existed in the warmth of the Eocene, and will form much of the focus of this chapter.

All of the GCMs used in this chapter have been used to perform modern day control experiments. Here we first discuss their performance over Antarctica relative to modern observations. It should be noted that modern day performance may not be relevant to performance under Eocene boundary conditions. Connolley and Bracegirdle (2007) evaluated 4 of the GCMs used in this chapter (excluding GENESIS) against 15 other GCMs (used in the IPCC AR4) for their performance compared with Antarctic re-analysis output. They assigned skill scores based on 5 variables (mean sea level pressure, height and temperature at 500 hPa, sea surface temperature, surface mass balance), giving a skill score between 0 (low skill) and 1 (high skill). Over the Antarctic region (defined at areas south of 45°S), ECHAM5 had the highest skill score (0.45) of the 15 GCMs based on the 5 chosen variables, with HadCM3 (0.36) and CCSM3 (0.28) 4th and 7th, respectively, and GISS (0.11) 14th. For Antarctic sea surface temperatures the skill of all of the models was low, in part due to the method used to measure skill, however ECHAM5, GISS and HadCM3 were in the top half of the 15 GCMs. HadCM3 had the joint best skill score for surface mass balance over the Antarctic, with CCSM3 and ECHAM5 also scoring highly (>0.9), however GISS had a low skill score (0.07) (Connolley and Bracegirdle, 2007).

## 4.2   Bedrock topography

Our choice of bedrock topography for the Antarctic ISM simulations is less straightforward than for the Northern Hemisphere simulations in the previous chapter, for which we could use the modern topography. Because we are investigating the onset of Cenozoic Antarctic glaciation, the bedrock topography we use needs to be ice-free. In addition, the palaeo-geography differs slightly from modern due to continental movement and erosion (Wilson et al., 2011). There are 4 bedrock topographies which we use for these simulations, these being the modern Bedmap1 topography (Lythe and Vaughan, 2001; note that the Bedmap2 topography was recently published Fretwell et al., 2013) with the ice sheet removed and accounting for isostatic adjustment (the approach adopted by DeConto and Pollard (2003a)), which is our default topography. In addition we use the proprietary topography used by Lunt et al. (2010b) and the 2 reconstructed topographies of Wilson et al. (2011), which take into account past ice sheet erosion, thermal subsidence and plate movement. In the following paragraphs we will discuss each of these in turn.

As can be seen from Figure 4.1.B, large parts of the modern Antarctic bedrock are below
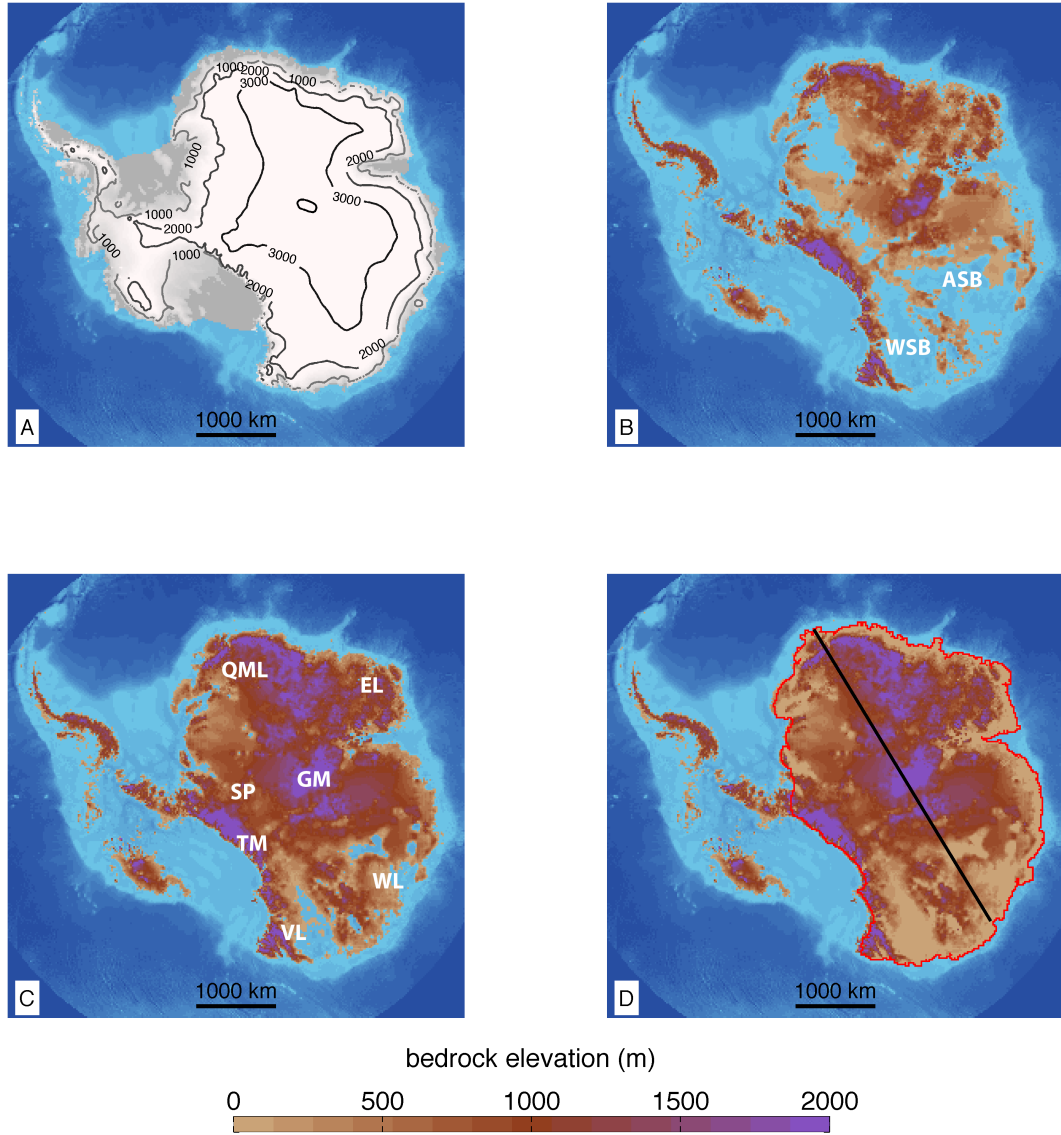
Figure 4.1: *Antarctic topographies: A) the modern topography of Antarctica; B) the modern bedrock of Antarctica from Bedmap1, note that large parts of East Antarctica are below sea level due to the isostatic loading of the EAIS, approximate locations of regions referred to in the text: ASB – Aurora Subglacial Basin; WSB – Wilkes Subglacial Basin; C) The bedrock of Antarctica following the removal of the ice sheets and allowing for isostatic adjustment using the isostasy model within Glimmer. Approximate locations of regions referred to in the text: QML – Queen Maud Land; EL – Enderby Land; GM – the Gamburtsev Mountains; SP – South Pole; TM – the Transantarctic Mountains; WL – Wilkes Land; VL – Victoria Land; D) Relaxed Bedmap1 topography, with subglacial lakes and coastal valleys in filled to a minimum height of 10 m above modern sea level within the bounds of the East Antarctic continent, marked in red. The black line marks a transect used in later Figures.*

modern sea level due to the pressure of the large ice sheets above (Figure 4.1.A). The large basins to the south of the continent, in particular Wilkes Subglacial Basin and Aurora Subglacial Basin, have been suggested as potential sources of past marine instability of the EAIS (Williams et al., 2010; Pierce et al., 2011). Upon removing the ice sheets we take into account the isostatic adjustment of the Antarctic continent using the isostasy model within Glimmer. The ice sheet is removed by performing a simulation with very high ablation and no accumulation, with the simulation then continued for 50 ka to allow for isostatic adjustment (Figure 4.1.C).

The marine margin problem we faced for the Northern Hemisphere simulations is also an issue for the Antarctic simulations. The current lack of treatment of ice shelves within the Glimmer ISM means that we cannot simulate the WAIS correctly. Although we significantly lowered the marine margin (500 m) in the previous Northern Hemisphere simulations to allow the growth of ice sheets across shallow seas, this would be an inappropriate solution for simulating the WAIS, as the buttressing of the ice sheet from the surrounding ice shelves is so important (Pollard and DeConto, 2009). We therefore make no attempt to simulate a marine based WAIS using the Glimmer ISM, an approach also adopted by Hill et al. (2007) who also used a SIA-ISM.

The marine margin problem also affects our simulation of the EAIS. Although the starting ice-free East Antarctic continent is largely above sea level, as the ice sheet grows isostatic loading means that areas of bedrock may be pushed below sea level. Although the Glimmer ISM maintains ice even if the bedrock has been pushed below sea level, with the setup we have adopted it cannot grow new ice on regions below sea level. Therefore as the EAIS regrows, it creates regions of topography below sea level on which it cannot grow, resulting in the ice sheet growing around these isolated regions of low topography.

To overcome this problem we can lower the marine limit (in effect lowering sea level). For our simulations, lowering the marine limit by 50 m is sufficient to avoid isolated ice-free regions in the middle of the ice sheet. By lowering the marine limit 50 m there is limited advance of the ice sheet onto the continental shelf. In addition, we fill in the sub-glacial lakes by raising the topography of the East Antarctic continent to a minimum of 10 m above sea level (see Figure 4.1.D). We consider this reasonable because a) the modern topography has been subject to significant erosion since the Eocene/Oligocene transition (Wilson et al., 2011) and b) the alternative is to lower the marine limit even further, resulting in further advance of the ice sheet onto the continental shelf. The volume of sediment we are adding to the East Antarctic continent is small ($0.68 \times 10^6$ km$^3$) compared to the volumes added in the erosion model of

Wilson et al. (2011) for the East Antarctic ($2.21 - 2.87 \times 10^6$ km$^3$). Our approach to the marine limit problem differs from that of DeConto and Pollard (2003a), who also used a shallow ice approximation ISM but simply constrained the ice sheet to the modern continental shoreline. Imposing such a barrier is more problematic to implement using the Glimmer ISM, hence the adoption of a slightly different approach here. Note that because of this approach, and due to the ISM used, we cannot simulate potential marine instability around the East Antarctic basins that at present day are below sea level.

The Antarctic continent has been subject to tectonic plate movements since the Eocene. The relaxed Bedmap1 topography is therefore rotated anti-clockwise into its early Eocene position. This varies depending on which palaeo-geography has been used in the GCM simulation. For example, we rotate the Antarctic continent $6°$ anti-clockwise when using the climate from the GCM simulations of Lunt et al. (2010b). Similarly, we rotate the bedrock topography so that it is consistent with the palaeo-geography of whichever GCM simulation we are using. This is the default topography we use for the Antarctic simulations, which we denote TOPO1 (see Figure 4.2.A).

The second bedrock topography we use (denoted TOPO2) is the proprietary data used by Lunt et al. (2010b). This data set (a reduced resolution version of this topography is shown in Figure 4.2.B) is similar to our default topography but has some key differences. The main difference is the inclusion of a region of high topography along the coast of the northwest of East Antarctica, between Queen Maud Land and directly north of the South Pole. As this data is proprietary we do not have knowledge as to why this reconstruction includes this region of high topography. It is not present in our default relaxed Bedmap1 topography, nor is it included in the reconstructed topographies of Wilson et al. (2011) which we discuss below. The Gamburtsev Mountains extend over a greater area and are higher in elevation than our default topography. It is also at a relatively low effective spatial resolution, therefore the surface is much smoother than the relaxed Bedmap1 topography. Due to these uncertainties with this topography we only use this topography for the purposes of sensitivity tests.

The final 2 topographies we use are from the reconstructions of Wilson et al. (2011), extended from the earlier work of Wilson and Luyendyk (2009). These reconstructions attempt to take into account the erosion, thermal subsidence and plate movements which have occurred since the Eocene. The reconstructions make use of models for sediment erosion and thermal subsidence. The sediment erosion models are constrained by observed sediment volumes deposited around
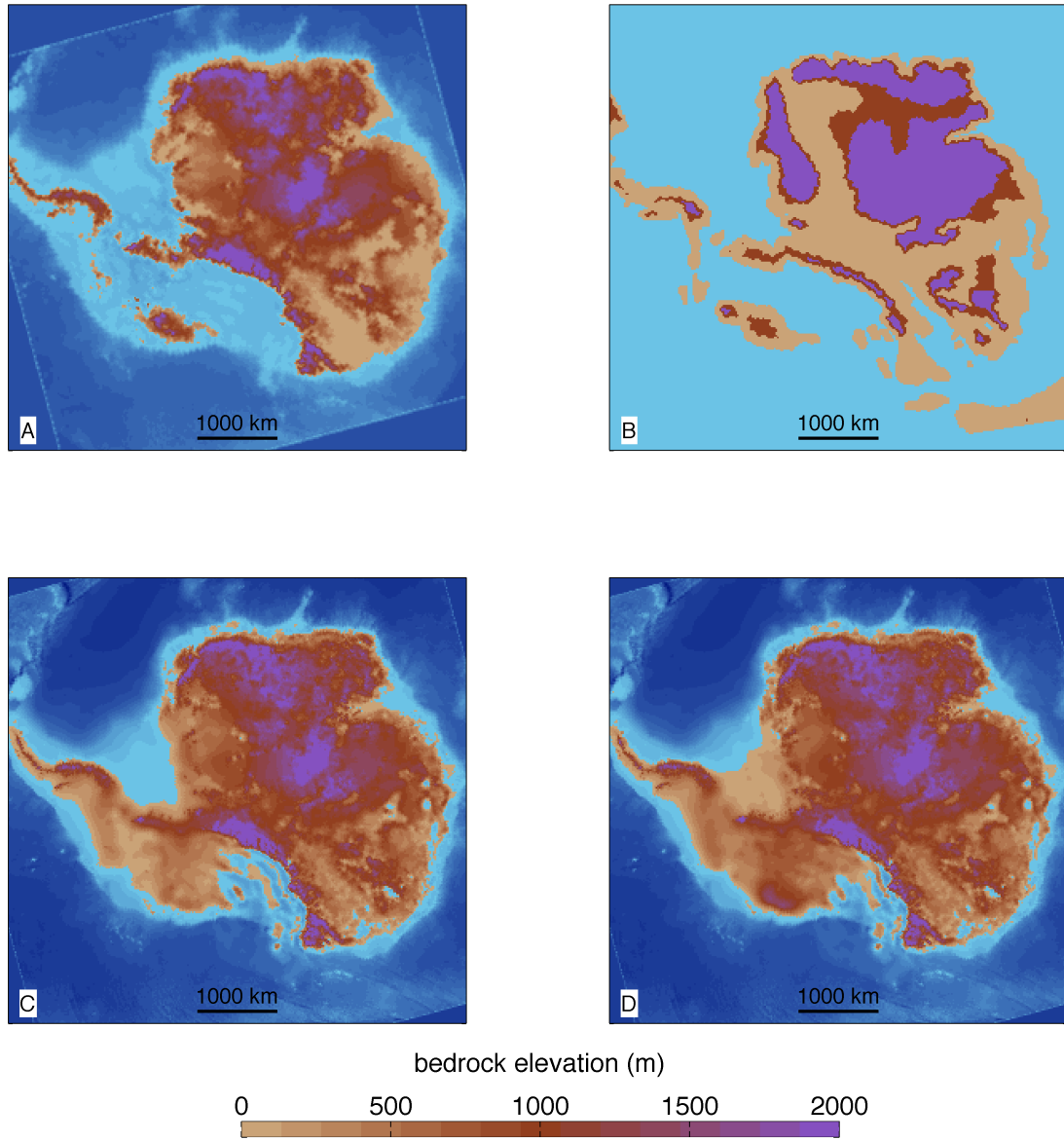
Figure 4.2: *A) Isostatically relaxed Bedmap1 topography of Lythe and Vaughan (2001), rotated into early Eocene position (TOPO1); B) A reduced resolution version of the proprietary topography used by Lunt et al. (2010b), we use a higher resolution version for our ISM simulations than that shown here (TOPO2) C) Minimum (TOPO3) and D) maximum extent reconstructed Eocene/Oligocene topography of Wilson et al. (2011). Note the increase in land surface area above modern sea level, in particular for the West Antarctic.*

the Antarctic continent. Wilson et al. (2011) generated minimum (we denote as TOPO3) and maximum (TOPO4) reconstructions based on different target sediment volumes, due to uncertainties in offshore sediment volumes (see Figure 4.2.C-D). Wilson et al. (2011) do not claim that these are accurate reconstructions of the Eocene/Oligocene topography, but argue that they are 2 plausible end-members. The reconstruction of Wilson and Luyendyk (2009) results in an increase in the total area of the Antarctic continent of $10 - 20$ %. Based on these reconstructions, the accommodation space of the Antarctic continent would have been greater at the Eocene/Oligocene transition than present. For the minimum reconstruction of Wilson et al. (2011), the total area above modern sea level is $12.4 \times 10^6$ km$^2$ compared to the relaxed Bedmap1 topography which has a total area of $10.5 \times 10^6$ km$^2$. The total area of the maximum reconstruction is $13.0 \times 10^6$ km$^2$ (Wilson et al., 2011). The majority of this increase in continental area is for the West Antarctic. Importantly, Wilson et al. (2011) suggested that the during the Eocene/Oligocene the West Antarctic continent could have supported a largely continental based ice sheet, rather than a marine based ice sheet as is present today.

All of the Eocene GCM simulations available to us have a deglaciated Antarctic and largely submerged West Antarctic. As such, it is possible that the climate would differ if the reconstructions of Wilson et al. (2011) were used for the GCM boundary conditions. Although we will use the Wilson et al. (2011) topographies for sensitivity tests, it is with the caveat that the climate forcing provided to the West Antarctic is from GCM simulations which may have ocean cells over regions which are land in the reconstruction of Wilson et al. (2011). To test the significance of the Wilson et al. (2011) topographies to the formation of the ice sheets at the Eocene/Oligocene transition more accurately, it would be necessary to repeat the GCM simulations using a palaeo-geography which incorporates the Wilson et al. (2011) Antarctic topography.

## 4.3 Offline simulations

The first ISM simulations we perform are simple offline simulations using the HadCM3L GCM simulations of Lunt et al. (2010b). Although we criticised the offline forcing method in the previous chapter it does have certain relevant advantages, for example it is a useful method for inter-model comparisons (Dolan et al., 2012). These offline simulations allow us to estimate the Antarctic glacial $CO_2$ threshold for simulations using HadCM3L. In previous simulations using the GENESIS GCM, the Antarctic glacial threshold was $\sim 2.7\times$ PIC concentrations ($\sim$750

Table 4.1: *Default parameter values for Antarctic simulations, based on Lunt et al. (2008), referred to as P3 in the text*

|  |  | default (P3) values | units |
|---|---|---|---|
| $\alpha_s$ | PDD factor for snow | 3 | mm d$^{-1}$ °C$^{-1}$ |
| $\alpha_i$ | PDD factor for ice | 8 | mm d$^{-1}$ °C$^{-1}$ |
| $f$ | flow enhancement factor | 3 | - |
| $G$ | geothermal heat flux | -50 | mW m$^{-2}$ |
| $\gamma$ | lapse rate | 7 | K km$^{-1}$ |

ppmv) for large-scale, continental glaciation (DeConto and Pollard, 2003a). Offline simulations are performed with the Glimmer ISM forced by the $1\times$, $2\times$, $4\times$ and $6\times$ PIC simulations of Lunt et al. (2010b). These simulations use the same parameter values as Lunt et al. (2008), which we refer to as P3 and are shown in Table 4.1. The P3 values differ slightly from the default values used in the previous chapter (P1, see Table 3.2, based on Gregoire et al. (2012)), in that we use the more commonly adopted value for the flow enhancement factor of 3 (Ritz et al., 1997), and use a slightly higher value for the lapse rate (Pollard and Thompson, 1997). Our default ISM setup does not include basal sliding (BS1). The impact of including basal sliding will be investigated in sensitivity tests in the next chapter.

The offline ISM simulations using HadCM3L are shown in Figure 4.3. Very little ice forms on Antarctica, even in the $1\times$ PIC experiment (280 ppmv) using HadCM3L, in which only $1.1 \times 10^6$ km$^3$ of ice has formed. The ice that has formed is composed of isolated ice caps in the mountain regions. The GCM simulations used to drive the ISM have ice-free boundary conditions over Antarctica, therefore there is no albedo feedback. The only feedback from the growth of an ice sheet is height-mass balance feedback, which is calculated within the ISM. However, it is surprising that no ice forms at pre-industrial atmospheric $CO_2$ concentrations.

### 4.3.1 EoMIP simulations

For comparison with our ISM simulations forced by HadCM3L, we perform a number of similar offline simulations using the climate output from a number of different GCMs. These simulations are from the EoMIP project (Eocene Modelling Inter-comparison Project), a GCM inter-comparison of early Eocene simulations (Lunt et al., 2012). The synthesis of these GCM simulations was undertaken after the publication of a number of independent studies, as such this
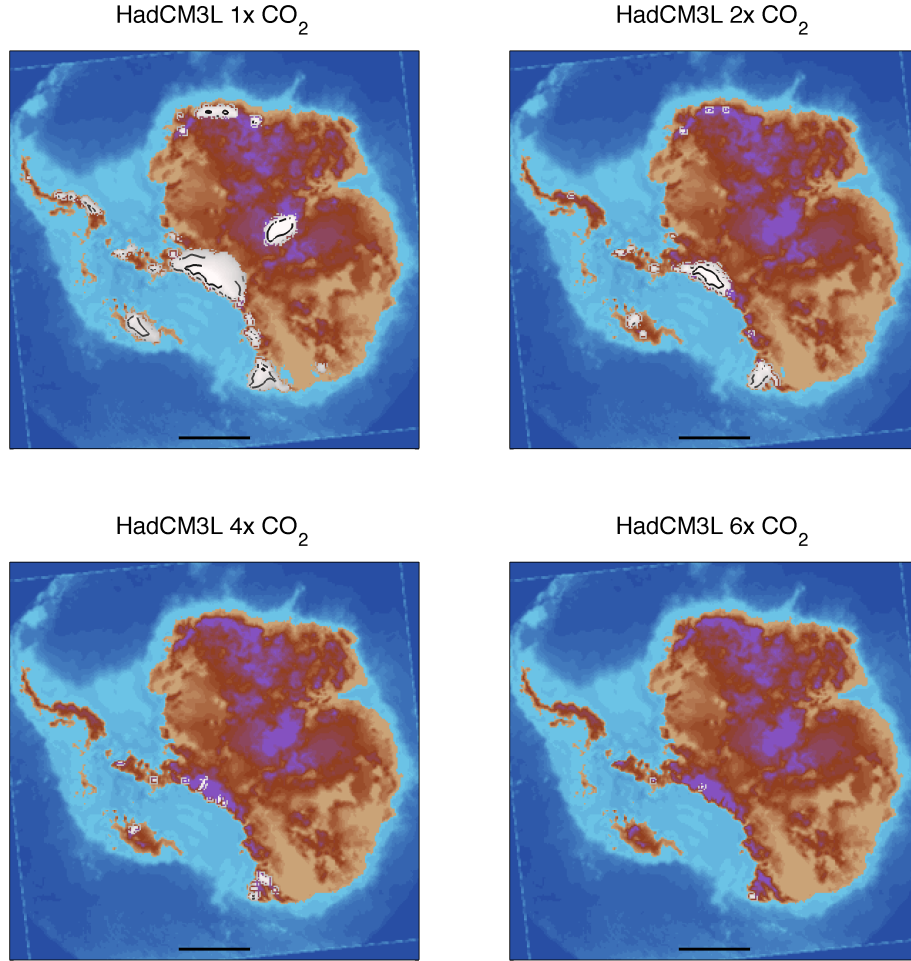
Figure 4.3: *Offline simulations of the Antarctic ice sheets forced by the HadCM3L early Eocene simulations of Lunt et al. (2010b)*

is an informal model inter-comparison in that the GCM boundary conditions are not identical (Lunt et al., 2012). Although the GCM simulations have slightly different boundary conditions, they are broadly similar in that they use an early Eocene palaeo-geography and have ice-free conditions over Antarctica. They can therefore be used to give an indication of the glacial $CO_2$ threshold of these different GCMs and show whether the offline results using HadCM3L are anomalous. To compare with our offline simulations using HadCM3L, we perform additional offline simulations using the climate output from early Eocene simulations using CCSM3 (Liu et al., 2009; Huber and Caballero, 2011), ECHAM5 (Heinemann et al., 2009) and GISS (Roberts et al., 2009). In addition we use the climate output from Eocene/Oligocene simulations using the GENESIS GCM (not included in EoMIP; DeConto et al., 2008). All of these GCMs are coupled ocean-atmosphere models, with the exception of GENESIS which is configured in
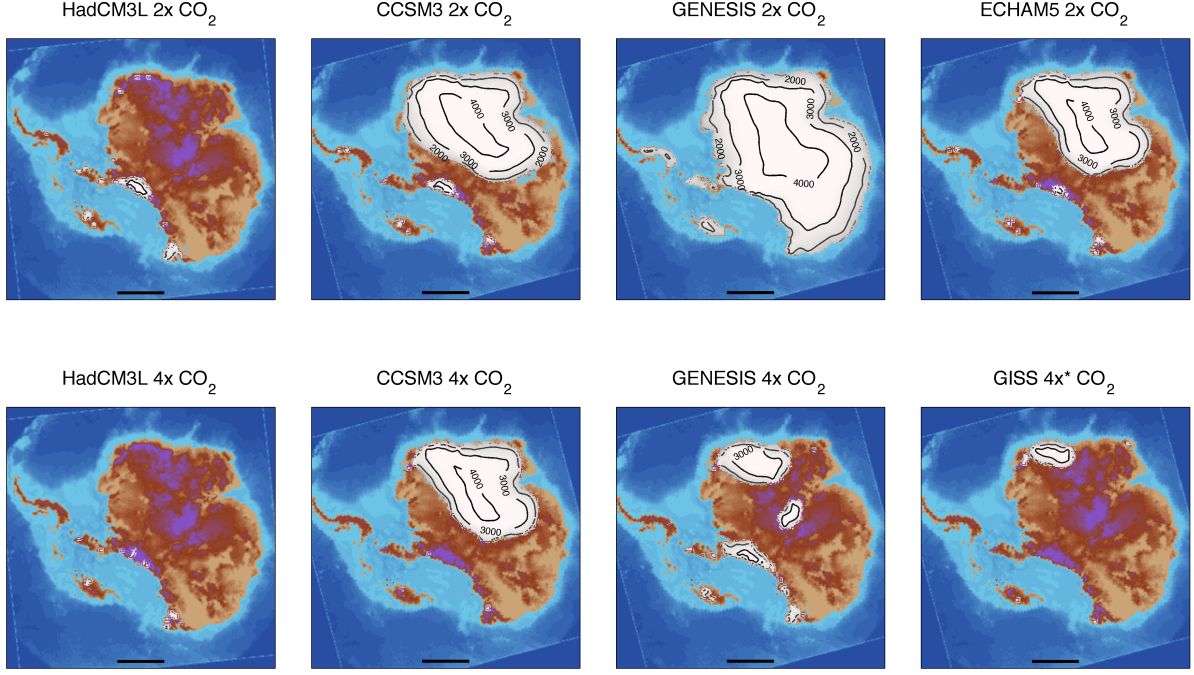
Figure 4.4: *Offline simulations of the Antarctic ice sheets forced by the HadCM3L early Eocene simulations of Lunt et al. (2010b), CCSM3 simulations of Huber and Caballero (2011), GENESIS simulations of DeConto et al. (2008), ECHAM5 simulations of Heinemann et al. (2009) and GISS simulations of Roberts et al. (2009). The $4\times$ PIC GISS simulation includes an additional $CH_4$ forcing, which Roberts et al. (2009) estimate makes this simulation equivalent to a $4.3 \times$ PIC simulation. Note that there are no $2\times$ PIC GISS simulations or $4\times$ PIC ECHAM5 simulations available to us.*

atmosphere-only mode with a slab ocean.

As can be seen from Figure 4.4, the offline simulations using the climate output from CCSM3 and ECHAM5 produce large ice sheets over much of East Antarctica at $2\times$ PIC ($10.3 - 14.6 \times 10^6$ km$^3$) and GENESIS produces a full continental sized EAIS at $2\times$ PIC ($28.6 \times 10^6$ km$^3$). However, there is minimal ice in the equivalent $2\times$ PIC simulation using HadCM3L ($0.3 \times 10^6$ km$^3$). For CCSM3 and ECHAM5, ice nucleates over Queen Maud Land and the Gamburtsev Mountains. These 2 smaller ice sheets have combined to generate an intermediate sized ice sheet in the $2\times$ PIC simulations. Between $4\times$ and $2\times$ PIC a full continental sized ice sheet forms in the offline simulations using the GENESIS model. This is the same GCM used by DeConto and Pollard (2003a) and produces a similar result to their glacial $CO_2$ threshold. Another interesting result of these offline simulations is the relatively large ice sheet which has formed at $4\times$ PIC in the simulation using CCSM3 ($9.4 \times 10^6$ km$^3$). The ice sheet in the $4\times$ PIC simulation using

CCSM3 is only $\sim 35\%$ smaller than for the $2\times$ PIC simulation. This is plausibly a result of the relatively low $CO_2$ sensitivity of CCSM3 (Huber and Caballero, 2011). We also performed offline simulations using the output from CCSM3 at $8\times$ and $16\times$ PIC (not shown). The simulation with CCSM3 at $8\times$ PIC generated minimal ice, with a total volume of $0.2 \times 10^6$ km$^3$, and the simulation at $16\times$ PIC was ice-free. This suggests that the glacial threshold for these CCSM3 simulations is between $8\times$ and $4\times$ PIC. The simulation using the GISS model is for $4\times$ PIC and $7\times$ CH$_4$ compared to pre-industrial concentrations. Roberts et al. (2009) estimate that this GISS simulations is equivalent to a $4.3 \times$ PIC simulation. When we use the climate output from the GISS simulation to force the ISM it generates a small ice cap over Queen Maud Land, this is a slightly higher volume than the $4\times$ PIC HadCM3L simulation.

### 4.3.2   Diagnosing differences in EoMIP simulations

It is not immediately clear why the ISM simulations using the HadCM3L early Eocene simulations of Lunt et al. (2010b) should generate such low ice volumes. Although Lunt et al. (2012) noted certain differences between the GCM simulations within EoMIP, their analysis did not identify a disagreement which could explain our ISM results. The variables which are passed to the ISM from the GCM output data are the annual mean air temperature ($\bar{T}_a$), annual air temperature half range ($\Delta T_a$) and the total precipitation ($P$). Much of the analysis by Lunt et al. (2012) focused on the annual means from the GCMs. Interestingly, their analysis suggested that when looking at the annual mean air temperatures, HadCM3L is cooler than CCSM3 and ECHAM5 for the $2\times$ PIC simulations. This cool bias in the annual mean air temperatures is especially pronounced for the Southern Hemisphere high latitudes.

The surface mass balance in the ISM is calculated using the climate output from the GCM. The lack of ice in the simulations using HadCM3L is a result of the outputs of mass (ablation) exceeding the inputs of mass (precipitation). The 3 variables which are passed to the ISM from the GCM are summarised in Table 4.2 as averages over the East Antarctic continent and also as averages over the mountainous regions ($> 1500$ m), the regions where ice tends to first nucleate. The annual air temperatures are averaged over the ice-free surface (i.e. at the first time-step). As can be seen from Table 4.2, HadCM3L has the lowest annual mean air temperature of the 4 GCM simulations over the East Antarctic continent for the $2\times$ PIC simulations. It also produces the coolest temperatures of the 4 GCMs used in the $4\times$ PIC simulations.

The total annual precipitation averaged over the East Antarctic is lower for HadCM3L

Table 4.2: *Climate variables passed to the ISM from GCM simulations, shown as averages over the East Antarctic continent (the East Antarctic continent is defined using the same mask as was used in Figure 4.1.D), with averages at elevations above 1500 m in parenthesis. $\bar{T}_a$ is the annual mean air temperature, $\Delta T_a$ is the annual air temperature half range (difference between the warm month and the annual mean temperature) and $P$ is total annual precipitation.*

|  |  | $\bar{T}_a$ (°C) | $\Delta T_a$ (°C) | $P$ (m yr$^{-1}$) |
|---|---|---|---|---|
| HadCM3L | 2× PIC | -12.4 (-19.4) | 25.7 (28.2) | 0.38 (0.31) |
| CCSM3 | 2× PIC | -3.4 (-12.0) | 13.4 (16.0) | 0.61 (0.60) |
| GENESIS | 2× PIC | -8.4 (-16.1) | 14.2 (14.7) | 0.46 (0.39) |
| ECHAM5 | 2× PIC | -1.1 (-9.3) | 12.2 (13.9) | 0.74 (0.64) |
| HadCM3L | 4× PIC | -7.0 (-13.8) | 25.0 (27.3) | 0.51 (0.38) |
| CCSM3 | 4× PIC | -0.7 (-9.2) | 12.6 (15.1) | 0.69 (0.68) |
| GENESIS | 4× PIC | -3.1 (-10.7) | 12.8 (13.0) | 0.56 (0.49) |
| GISS | 4×* PIC | 0.6 (-6.7) | 14.6 (15.9) | 0.78 (0.74) |

(0.38 m yr$^{-1}$) than for the other simulations. This is also evident in the precipitation maps shown in Figure 4.5 (Equivalent maps for the 4× PIC simulations are included in Appendix D). Note the especially low precipitation for the HadCM3L simulation over Queen Maud Land, the Gamburtsev Mountains and the Transantarctic Mountains, the regions where ice first forms in the simulations of DeConto and Pollard (2003a). However the total precipitation for GENESIS, which generated the largest ice sheet of the ISM simulations at 2 × PIC, is also relatively low (average 0.46 m yr$^{-1}$ over the East Antarctic) compared to the other 2 GCMs. ECHAM5 has the highest total precipitation over the East Antarctic (average 0.74 m yr$^{-1}$), with CCSM3 the second highest (average 0.61 m yr$^{-1}$).

The relatively low total precipitation from the HadCM3L simulations may partially explain the low ice volumes in the ISM simulations. However, it is the very high seasonality within HadCM3L which is the most striking anomaly when compared to the other GCMs (see also Figure 4.7). The seasonality of the GCM affects the ablation as the PDD mass balance scheme uses the annual air temperature half range, which is the difference between the warmest month and the annual mean (see Table 4.2). The annual air temperature half range of East Antarctica is 25.7 °C for the 2× PIC HadCM3L simulation, compared to 12.2 - 14.2 °C for the other 3 GCMs. The HadCM3L simulations are therefore anomalous compared to the other GCM simulations in that they have the lowest annual mean air temperature, lowest precipitation and
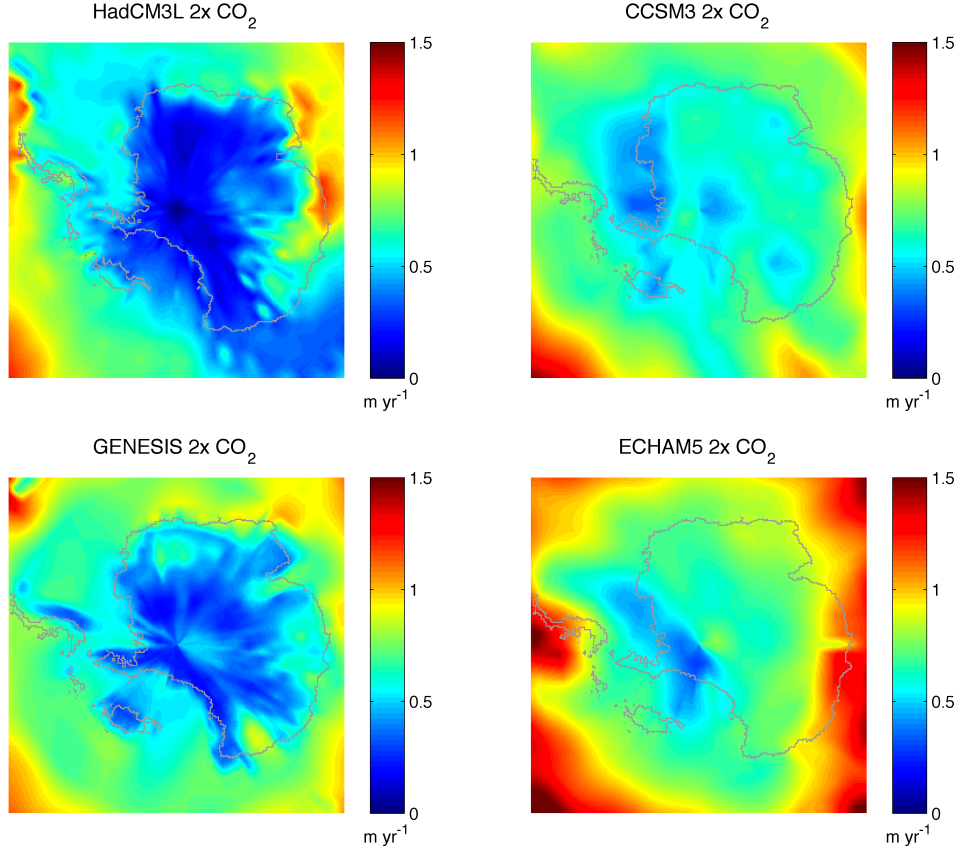
Figure 4.5: *Total annual precipitation from EoMIP GCM simulations at 2× PIC*

also the highest annual air temperature half range.

To determine which of these 3 variables results in the lack of ice-growth in the HadCM3L simulations we use the PDD mass balance scheme to calculate the potential snowmelt ($\hat{a}_s$) for various annual mean air temperatures and annual air temperature half ranges. If the total annual precipitation (which is assumed to all fall as snow) exceeds the potential snowmelt then snow will accumulate. If the total annual precipitation is less than the potential snowmelt than there is no year to year snow accumulation and an ice sheet cannot grow. We will therefore be able to determine whether it is the low precipitation or the high seasonality (or some combination of both) which results in the anomalous HadCM3L results. The potential snowmelt is calculated from the PDD sum and the PDD factor for snow (Reeh, 1991):

$$\hat{a}_s = \alpha_s D_p, \tag{4.3.1}$$

125

where $\alpha_s$ is the PDD factor for snow (3 mm d$^{-1}$ °C$^{-1}$) and $D_p$ is the PDD sum. We use the mass balance scheme described in the previous chapter to calculate $D_p$ using:

$$D_p = \frac{1}{\sigma\sqrt{2\pi}} \int_0^{A_t} \int_0^{50} \bar{T}_a \exp\left(\frac{-(\bar{T}_a - T_a')^2}{2\sigma_T^2}\right) dTdt, \qquad (4.3.2)$$

where, $\sigma_T$ is equal to 5°C, $A_t$ is the period of the year and $T_a'$ is the daily surface air temperature calculated using:

$$T_a' = \bar{T}_a + \Delta T_a \cos\left(\frac{2\pi t}{A_t}\right). \qquad (4.3.3)$$

Note that we ignore the random noise which is normally added to the daily surface air temperature signal (see Equation 3.2.2). We can then numerically evaluate Equation 4.3.2 for various values for the annual mean air temperature and annual air temperature half range, and therefore calculate the potential snowmelt. This is plotted in Figure 4.6, with the values for these two variables from the different GCM simulations also shown.

Figure 4.6 shows that despite the low annual mean air temperatures of the HadCM3L simulations over the mountainous regions of Antarctica, the potential snowmelt is still higher than for the other 3 GCM simulations at 2× PIC. This is due to the large annual air temperature half range in the HadCM3L simulations. The potential snowmelt in the HadCM3L 2× PIC simulation is comparable to the CCSM3 4× PIC simulation. This CCSM3 4× PIC simulation generated a large ice sheet, whereas the HadCM3L simulation did not. The total annual precipitation for the CCSM3 4× PIC simulation is approximately double that of the HadCM3L 2× PIC simulation over the East Antarctic. This would suggest that the low precipitation in the HadCM3L simulations is also a significant factor. Based on the Clausius-Claperon relation, the low precipitation is itself likely to be a result of the low air temperatures. In an idealised simulation where we arbitrarily double the HadCM3L precipitation, a large ice sheet ($18.1 \times 10^6$ km$^3$ ) forms for the 2× PIC simulation. This ice sheet differs from the other simulations, which nucleated between Queen Maud Land and the Gamburtsev Mountains, instead this area is ice-free and the ice-sheet has grown over Victoria Land and Wilkes Land. This would suggest that even with precipitation arbitrarily doubled, the region around Queen Maud Land and the Gamburtsev Mountains is still precipitation limited for the HadCM3L simulation.
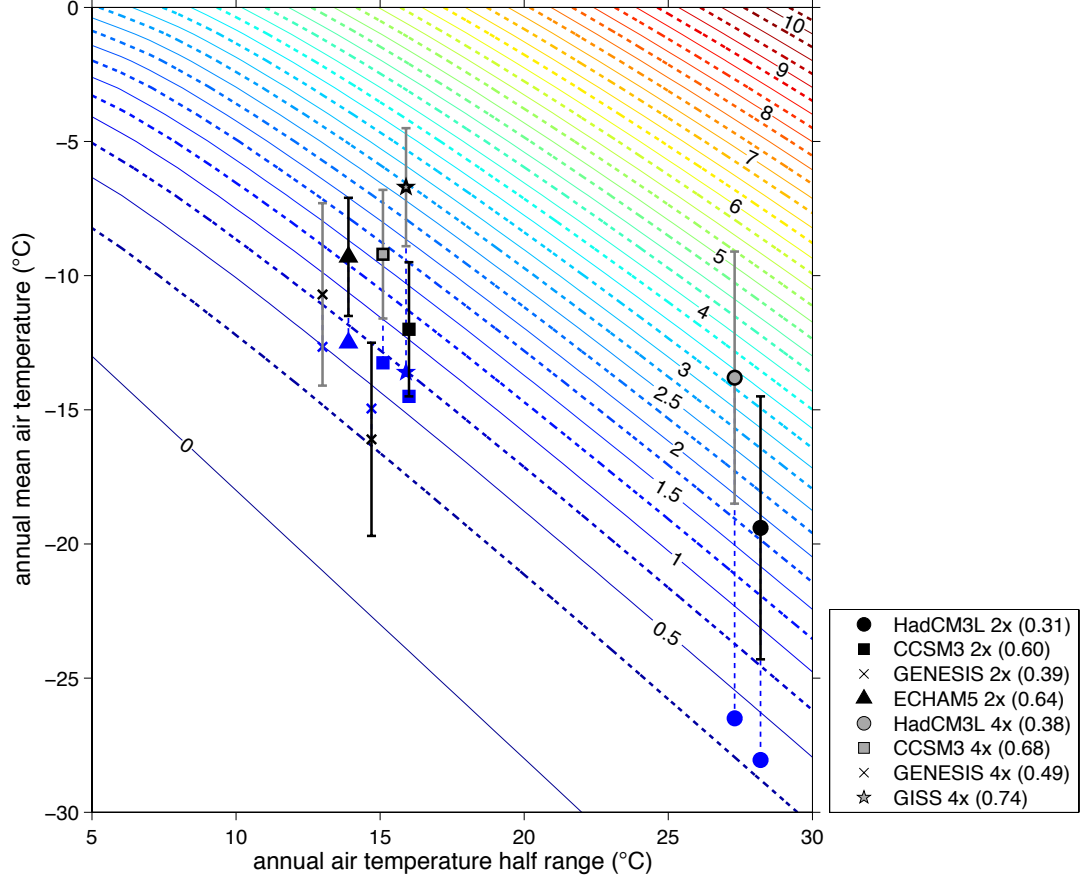
Figure 4.6: *Contours show potential snowmelt (m yr$^{-1}$) for various annual mean air temperatures and annual air temperature half ranges. If the total annual precipitation exceeds this amount then snow will accumulate. Also shown are the values for $\bar{T}_a$ and $\Delta T_a$ from the GCM simulations, averaged over the mountainous regions (> 1500 m). Error bars for $\bar{T}_a$ are 1 standard deviation of $\bar{T}_a$ above 1500 m. The mean precipitation over mountainous regions is included in parenthesis in the legend (m yr$^{-1}$), and is also shown on the plot as the blue markers. Note that for HadCM3L the precipitation, shown by the blue markers, is significantly lower than the potential snowmelt.*

The total annual precipitation values we have shown in Figure 4.6 are averages over the mountainous regions. There is variability from this mean which explains why ice grows for simulations where the mean annual precipitation is lower than the potential snowmelt. For example, the potential snowmelt for the 4× PIC CCSM3 simulation is above the mean annual precipitation for the mountainous regions yet still produced a large ice sheet. Additionally, this data is for ice-free conditions at the first time-step, and therefore does not include height-mass balance feedback or ice-flow from regions of initial ice nucleation.

127

## 4.4 HadCM3L seasonality

Although we have identified the reason for the lack of ice growth in the simulations using HadCM3L as a consequence of the relatively low precipitation and in particular the strong seasonality, it is not clear why the HadCM3L simulations are different. As previously mentioned, the boundary conditions for these GCM simulations are not identical; for example the differences in the palaeo-geography are clearly visible in Figures 4.7 and 4.8. The strong seasonality in the HadCM3L simulations is not just a result of very warm summers, but also cool winters. As can be seen from Figure 4.7, for the early Eocene $2\times$ PIC simulations using HadCM3L there is a very large annual temperature range over Antarctica. For HadCM3L, the annual range in surface air temperature over Antarctica exceeds 60 °C in certain regions. The HadCM3L $4\times$ PIC simulation has a slightly lower seasonality than the $2\times$ PIC simulation, but the seasonality is still greater than for any of the other GCMs at $4\times$ PIC. This very large annual temperature range for HadCM3L is also apparent in the high latitude Northern Hemisphere. None of the other GCMs exhibit such a large annual temperature range in both hemispheres. This may suggest that this anomaly is a result of differences in the astronomical forcing between GCM simulations. Although the GCM simulations do not have identical boundary conditions, the simulations shown here are all for either a low seasonality or modern astronomical forcing. Sensitivity tests using HadCM3L simulations with different astronomical forcing, including a simulation favourable to Southern Hemisphere glaciation (minimum seasonality / cool summers), did not generate any significant increase in ice volumes (not shown).

It is interesting to note that the GENESIS simulation has a relatively high annual temperature range over the Northern Hemisphere, but not the Southern Hemisphere. This pattern is unique to GENESIS amongst the $2\times$ PIC simulations, although the GISS $4\times^*$ PIC simulation also shows a similar pattern. GENESIS is the GCM used by DeConto et al. (2008) in their study investigating the thresholds for Northern Hemisphere glaciation. Their study suggested that the threshold for Northern Hemisphere glaciation is $\sim$280 ppmv, providing evidence against the early Northern Hemisphere glaciation hypothesis. This hypothesis was based on evidence from ice-rafted debris in the Eocene and Oligocene (Tripati et al., 2005; Eldrett et al., 2007), and discrepancies between benthic $\delta^{18}$O and Mg/Ca records across the EOT (Lear et al., 2000), although this second issue has now largely been resolved (DeConto et al., 2008; Liu et al., 2009; Wilson and Luyendyk, 2009). Given the strong seasonality seen in the GENESIS simulations in the Northern Hemisphere, it would perhaps be interesting to repeat the experiment of DeConto
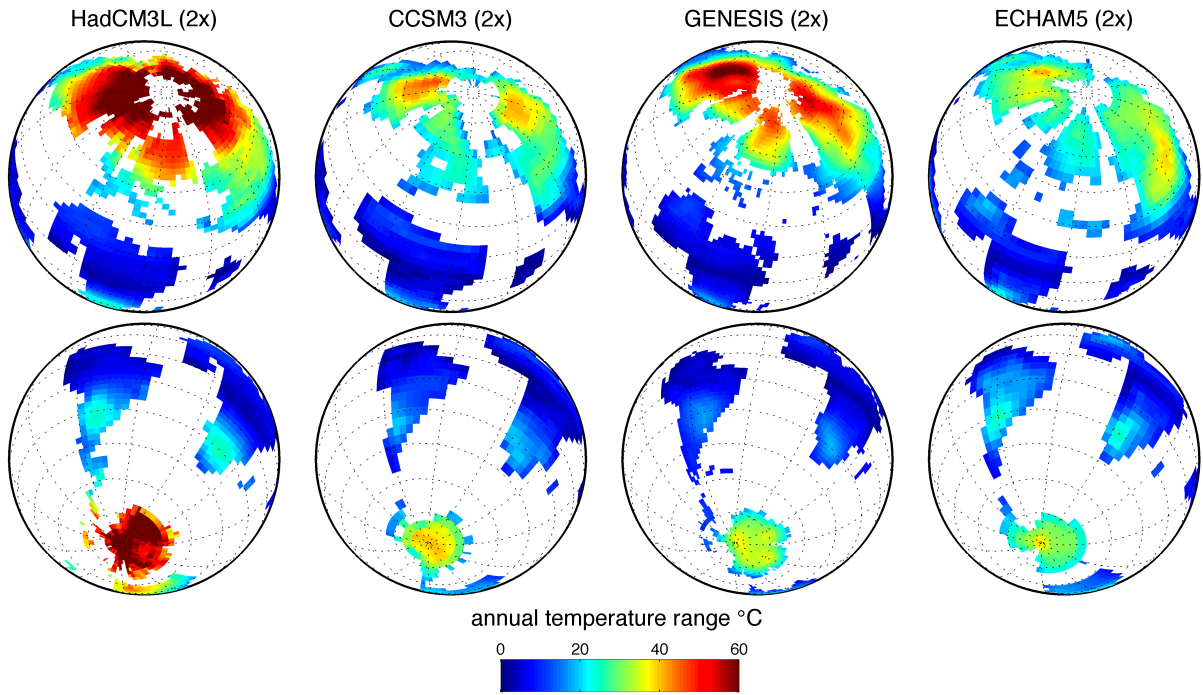
Figure 4.7: *Annual surface air temperature range over land from EoMIP GCM simulations at 2× PIC*
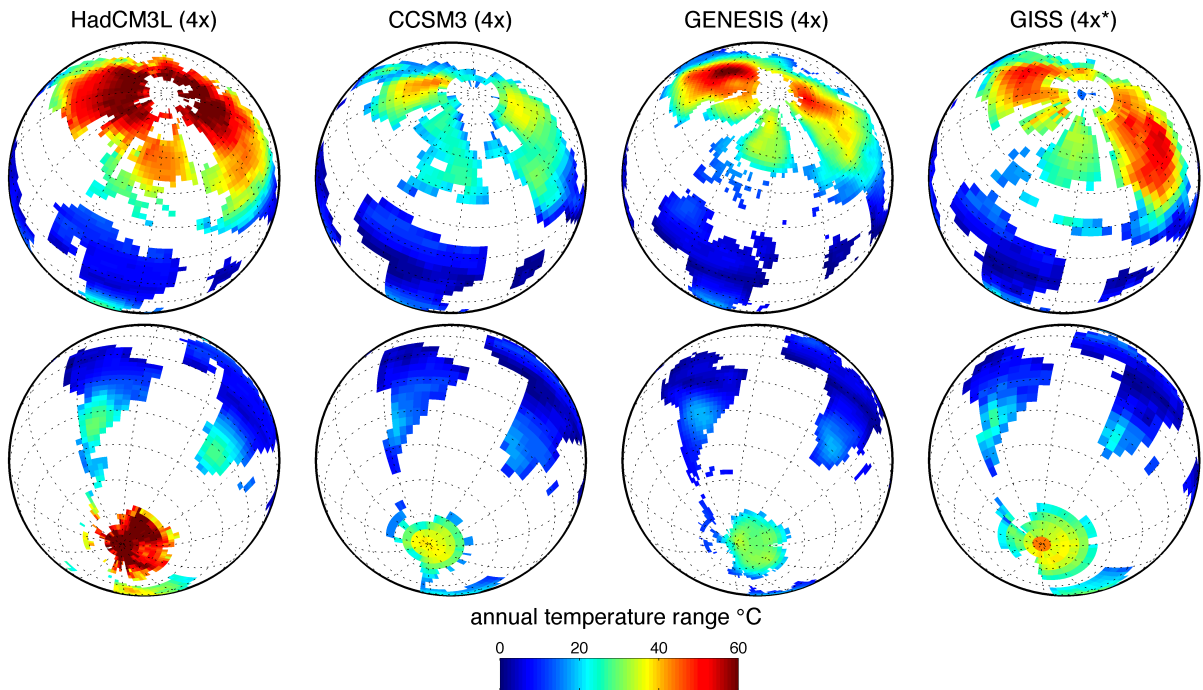


Figure 4.8: *Annual surface air temperature range over land from EoMIP GCM simulations at 4× PIC*
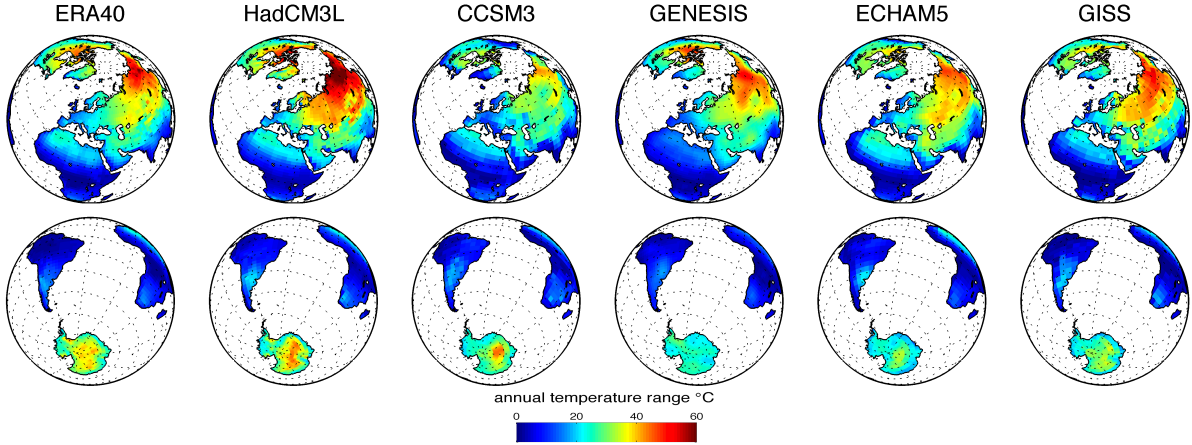
Figure 4.9: *Annual surface air temperature range from modern / pre-industrial control GCM simulations and ERA-40 re-analysis dataset.*

et al. (2008) using another GCM; especially considering that the regions of low seasonality in the Northern Hemisphere, the west of North America and northeast Asia, are also the regions where ice first nucleates in their ISM simulations (DeConto et al., 2008).

To investigate whether the strong HadCM3L seasonality is a result of the early Eocene boundary conditions, or a model bias, we have plotted seasonality maps for modern control simulations from the 5 GCMs in Figure 4.9. The seasonality of the ERA-40 dataset is also shown. Although the modern control HadCM3L simulation has a relatively high seasonality compared with the other GCMs, especially over northern Asia, it is not significantly higher than the ERA-40 dataset. Over Antarctica, which has a large ice sheet in these control simulations, all of the GCMs have a similar seasonality. This suggests that the strong HadCM3L seasonality is caused by the change to early Eocene boundary conditions.

The main differences in the change to Eocene boundary conditions from modern boundary conditions is the removal of the Antarctic ice sheet and the opening and closing of various ocean gateways following changes in the palaeo-geography. The opening of ocean gateways was suggested by Kennett (1977) as a possible cause of Antarctic glaciation (originally thought to have occurred in the middle Miocene). This idea has subsequently been supported by some as the cause of Antarctic glaciation at the EOT, in part due to the approximately coincident timing of the abrupt shift in the benthic $\delta^{18}$O record and the opening of the Drake Passage (seaway between South America and the Antarctic Peninsula) in the late Eocene (Livermore et al., 2005). A number of studies have used climate models to investigate the impact of opening and

closing ocean gateways on ocean circulation and climate throughout the Cenozoic (Huber et al., 2004; von der Heydt and Dijkstra, 2008; Lunt et al., 2008; Sijp et al., 2009, 2011). Huber et al. (2004) and Sijp et al. (2011) argued that the opening of seaways in the Southern Ocean generated limited cooling over Antarctica, suggesting this was not the mechanism for the abrupt Antarctic glaciation at the EOT. In the simulations used here, the palaeo-geographies are not identical, but broadly they all have an open but shallow Drake Passage and all, with the exception of the CCSM3 simulations (Huber and Knutti, 2011), have an open Tasman Gateway (seaway between southeast Australia and the East Antarctic). No study, to our knowledge, has yet investigated the impact of opening Southern Ocean gateways using HadCM3(L). It is possible that HadCM3(L) is more sensitive to ocean circulation changes than the models used in previous studies (Huber et al., 2004; Sijp et al., 2009, 2011), however it is difficult to envisage how this would explain the strong seasonality seen in both hemispheres of the HadCM3L experiments of Lunt et al. (2010b). Hill et al. (2013) have recently submitted a study using HadCM3L which may address some of these issues.

Other attempts at understanding why HadCM3L generates such a strong seasonality have included additional HadCM3L simulations using a dynamic vegetation model (TRIFFID) as opposed to the homogenous shrub-land used by Lunt et al. (2010b) (Lopston 2012, *personal communication*) and GENESIS simulations using the proprietary palaeo-geography used by Lunt et al. (2010b) (Pollard 2012, *personal communication*). These additional GENESIS simulations were also performed with a variety of vegetation types, although the GENESIS simulations are without a coupled-ocean. The HadCM3L simulations with a dynamic vegetation model had an equally strong seasonality, whereas the GENESIS simulations were similar to the standard Eocene/Oligocene simulations (see Appendix D). Further diagnostic work is needed to understand why HadCM3L has a strong seasonality under early Eocene boundary conditions, this could include experiments replacing the East Antarctic ice sheet (similar to the experiments of Goldner et al., 2012) and including changes to ocean gateways. This work is beyond the scope of this thesis.

## 4.5   Glacial $CO_2$ thresholds

Although the offline simulations lack albedo feedbacks and astronomical forcings, we can approximate the thresholds for Antarctic glaciation to allow further comparison between the different climate models. Using the $CO_2$ forcing method described in the previous chapter (3.3.3.2), we

can calculate the $CO_2$ threshold for the formation of an intermediate (which we define here as 25 m Eocene sea level equivalent (SLE)) and large (40 m Eocene SLE) ice sheet. Ice volumes are converted to Eocene sea levels by accounting for the change in state from ice to seawater and dividing by the total Eocene surface area ($372.9 \times 10^6$ km$^2$; DeConto et al., 2008). This is only possible for the GCMs where simulations are available at more than one atmospheric $CO_2$ concentration, these being HadCM3L, CCSM3 and GENESIS. In the simulations of Pollard and DeConto (2005) using an earlier version of the GENESIS GCM with a constant astronomical forcing, the glacial threshold was 2.1$\times$ PIC for an intermediate ice sheet and 1.6$\times$ PIC for a large ice sheet. For the equivalent simulations including astronomical forcing, the $CO_2$ thresholds were higher, at $\sim$ 3.0$\times$ PIC and $\sim$ 2.8$\times$ PIC (Pollard and DeConto, 2005; reproduced in Figure 1.7). Similar results were also found by Langebroek et al. (2009) using a reduced complexity model, in their study focusing on Antarctic glaciation in the middle Miocene. The thresholds for the formation of a large ice sheet in their study were 2.2$\times$ PIC for the experiment including astronomical forcing and 1.6$\times$ PIC for the constant astronomical forcing experiment (Langebroek et al., 2009).

In these transient $CO_2$ experiments, we scale between 6$\times$ and 0.5$\times$ PIC using the climate data from HadCM3L, CCSM3 and GENESIS. Although experiments are available at additional $CO_2$ concentrations, we interpolate between and extrapolate the simulations at 2$\times$ and 4$\times$ PIC for consistency. Because simulations are only available at one atmospheric $CO_2$ concentration for ECHAM5 and GISS, we cannot estimate the $CO_2$ thresholds for these models. However, based on the results of the offline simulations, for the 2$\times$ simulation using ECHAM5 an intermediate ice sheet has formed ($\sim$25 m Eocene SLE), suggesting the threshold for a large ice sheet ($\sim$40 m Eocene SLE) is below 2$\times$ PIC. For GISS, the threshold for glaciation is likely to be below $\sim$ 4.3$\times$ PIC.

In the transient $CO_2$ experiments (see Figure 4.10) there is important inter-model disagreement. An intermediate ice sheet (25 m Eocene SLE) forms at 3.3$\times$ PIC in the experiment using CCSM3 and 2.5$\times$ PIC in the experiment using GENESIS. Again the lack of ice in the experiment using HadCM3L is clearly evident, with ice volumes increasing slowly towards $\sim$ 1$\times$ PIC. Interestingly, a large ice sheet ($>$40 m Eocene SLE) does not form in any of the experiments, with the exception of the experiment using GENESIS where it occurs at 2.4$\times$ PIC. Recall that none of these experiments include albedo feedbacks.

The pattern of ice growth also varies between GCMs. The CCSM3 experiment has 3 distinct
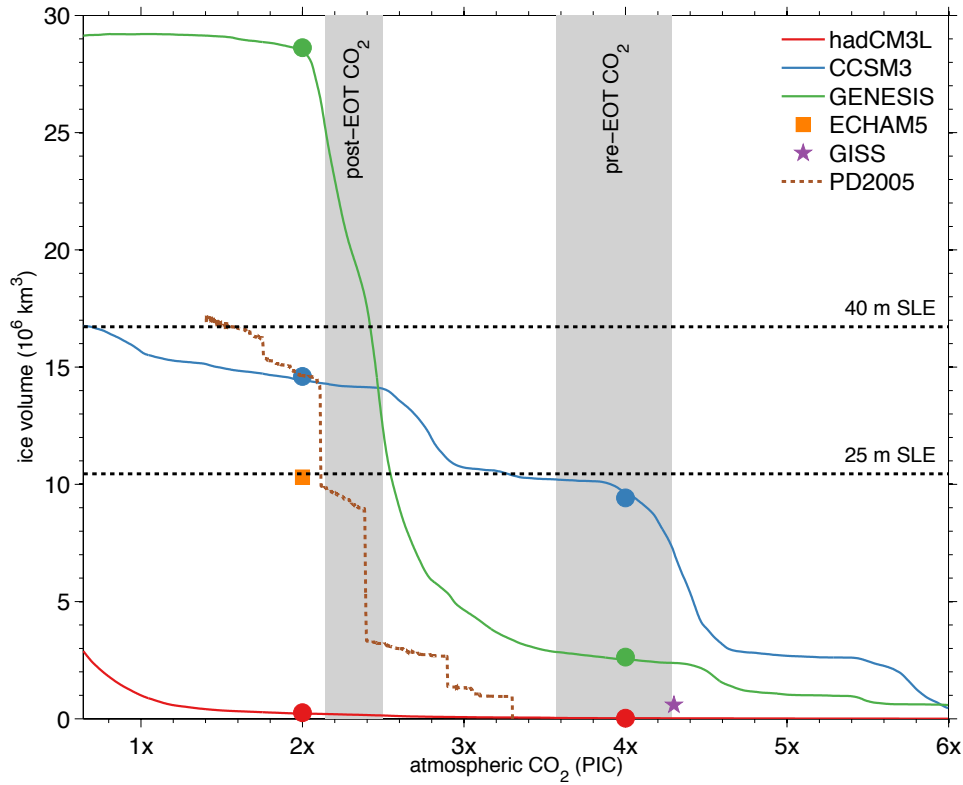
Figure 4.10: *Transient $CO_2$ ISM experiments using climate output from hadCM3, CCSM3 and GENESIS simulations. Offline simulations are shown as solid markers, with additional simulations from ECHAM5 and GISS. The climate for the transient experiments is calculated by interpolating between the $2\times$ and $4\times$ GCM simulations. Horizontal dotted lines are the thresholds for an intermediate (defined here as 25 m Eocene SLE) and a large ice sheet (40 m Eocene SLE). Also shown is the simulation of Pollard and DeConto (2005) for a reduction in atmospheric $CO_2$ and without astronomical forcing. The vertical bars are the pre- and post-EOT atmospheric $CO_2$ proxy estimates of Pagani et al. (2011).*

steps in ice growth, whereas for GENESIS there is one major threshold. The study of DeConto and Pollard (2003a), using an earlier version of the GENESIS GCM, showed the growth of ice in a series of steps as ice first formed as isolated ice caps in the mountain regions. It therefore appears unusual that our experiment using a later version of GENESIS does not show this pattern. However, more recent simulations based on a modified method of that used by DeConto and Pollard (2003a) and the same version of GENESIS we use here, also lack the stepped pattern to ice growth (Pollard 2012, *personal communication*). Also note the greater ice volume of our GENESIS simulations compared with that of Pollard and DeConto (2005) at equivalent atmospheric $CO_2$ concentrations.

Figure 4.11: *Transient $CO_2$ experiments with varying values for the lapse rate parameter. A) Using climate output from CCSM3 simulations B) Using climate output from GENESIS simulations. The horizontal dashed lines are the ice volumes for an intermediate and large ice sheet. Note the high sensitivity to the lapse rate parameter of the CCSM3 simulations.*

### 4.5.1   Highlighting key sensitivities

We next perform sensitivity tests to determine how changing certain poorly constrained parameters affects the glacial $CO_2$ thresholds. Firstly, we highlight the impact of changing the lapse rate. The lapse rate serves two purposes, it is used to allow for the cooling of the ice sheet surface as it rises vertically through the atmosphere. Additionally, the lapse rate is used to scale from the coarse GCM surface topography onto the finer topography used within the ISM. We repeat the transient $CO_2$ experiments for CCSM3 and GENESIS using lapse rates of 6, 7 and 8 K km$^{-1}$ (see Figure 4.11), the default value used in the previous experiments was 7 K km$^{-1}$.

As can be seen from Figure 4.11.A, the simulations using CCSM3 are highly sensitive to the value chosen for the lapse rate parameter. With the threshold for the growth of an intermediate ice sheet varying between $1.2\times$ and $5.7\times$ PIC for lapse rates between 6 and 8 K km$^{-1}$. With the higher value for the lapse rate, the threshold for the growth of a large ice sheet is crossed at $2.4\times$ PIC. The simulations using GENESIS (Figure 4.11.B) are less sensitive to the value for the lapse rate, with the threshold for the growth of an intermediate ice sheet varying between $2.2\times$ and $3.0\times$ PIC for the three values for the lapse rate. Similar simulations were also performed using HadCM3L, however these had little impact on the low ice volumes seen in the previous
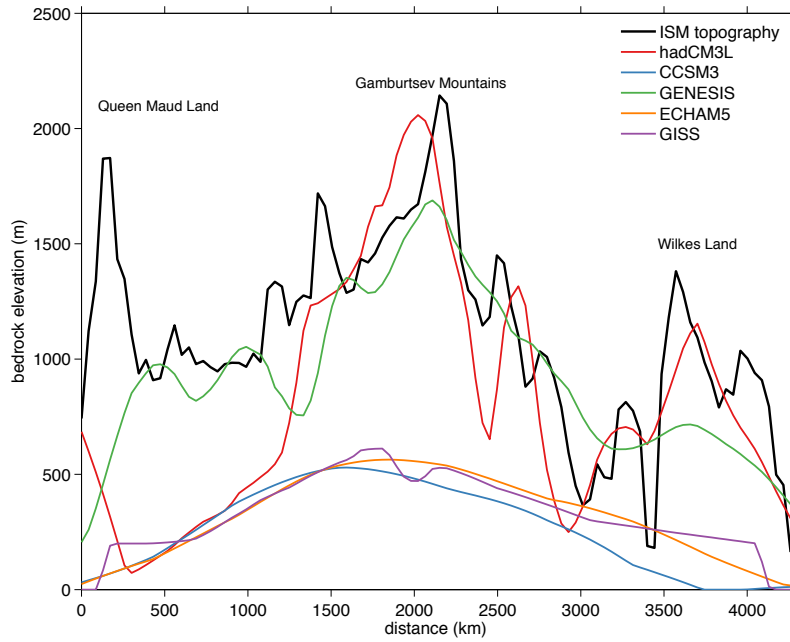
Figure 4.12: *Bedrock elevation transect, see Figure 4.1.D for map of transect. Shown is the ISM topography and the surface topography from the different GCM simulations. Note the significantly lower elevation of the CCSM3, ECHAM5 and GISS simulations. Additional GCM elevation maps are included in Appendix D.*

HadCM3L transient $CO_2$ experiments, due to the previously discussed high seasonality, and are therefore not shown here.

The reason for the strong sensitivity of the CCSM3 experiment to the lapse rate parameter is due to the Antarctic topography within the GCM. For the simulations using CCSM3, the Antarctic topography within the GCM (from the Sewall et al. (2000) palaeo-topography) is significantly lower than the ISM topography. This is evident in the transect shown in Figure 4.12. The discrepancy between the GCM and ISM topography for the CCSM3 simulations exceeds 1 km in certain regions. The Antarctic GCM topography within CCSM3 (and also ECHAM5 and GISS) resembles the modern Antarctic bedrock topography without isostatic adjustment. Because of this, there is a large lapse rate correction to the surface temperatures as they are scaled from the GCM topography to the ISM topography. This results in the high sensitivity to the value for the lapse rate parameter. This would also explain the results of Huber and Nof (2006), which did not find snow accumulation over the Antarctic in an

experiment with an earlier version of CCSM. They used the same GCM boundary conditions as the CCSM3 experiment used here (Huber and Caballero, 2011). Similarly, Heinemann et al. (2009) noted ice-free conditions over the Southern Hemisphere high latitudes in their simulation using ECHAM5 (the same simulation used here).

For the GCM simulations using GENESIS, the GCM topography is much closer to the ISM topography, therefore the ISM simulations are less sensitive to the lapse rate parameter. The Antarctic topography in the simulations using CCSM3, ECHAM5 and GISS are all significantly less mountainous than the ISM topography (GCM elevation maps are included in Appendix D). The Gamburtsev mountain range in the centre of the East Antarctic continent is much lower in elevation for these GCM simulations. Although there is uncertainty as to the past uplift history of the Antarctic, the Gamburtsev Mountains are thought to have formed earlier than the Eocene (Cox et al., 2010). This difference in GCM topography over the Antarctic may also affect precipitation patterns, in addition to surface temperatures. Therefore the significant disagreement between the ISM simulations in Figure 4.10 may be due to differences in the GCM boundary conditions, in addition to differences between the GCMs. To undertake a more formal GCM inter-model comparison it would be necessary to repeat the GCM simulations with identical boundary conditions. However, as noted by Lunt et al. (2012), the early-Eocene boundary conditions are poorly constrained, therefore the broad range of GCM boundary conditions used in this inter-model comparison may better represent the actual uncertainties.

We undertake further sensitivity tests using the 4 different Antarctic ISM topographies available to us, which are described in an earlier section. Note that all of these topographies are more mountainous than the GCM topography used in the CCSM3, ECHAM5 and GISS simulations. The ISM topographies we use are: TOPO1, the default topography used in the previous experiments; TOPO2, the proprietary topography used by Lunt et al. (2010b); and TOPO3 and TOPO4, the minimum and maximum reconstructed topographies of Wilson et al. (2011), respectively (see Figure 4.2).

The glacial $CO_2$ threshold is sensitive to the choice of Antarctic bedrock topography. When using the Wilson et al. (2011) topographies (TOPO3 and TOPO4), the onset of glaciation is at a slightly higher atmospheric $CO_2$ concentration than the default topography (TOPO1). This is especially evident for the experiments using CCSM3 (Figure 4.13). This is due to a slightly higher elevation of the mountains in Queen Maud Land and the Gamburtsev Mountains, the regions where ice first nucleates. The difference in mountain elevation is likely a result of the
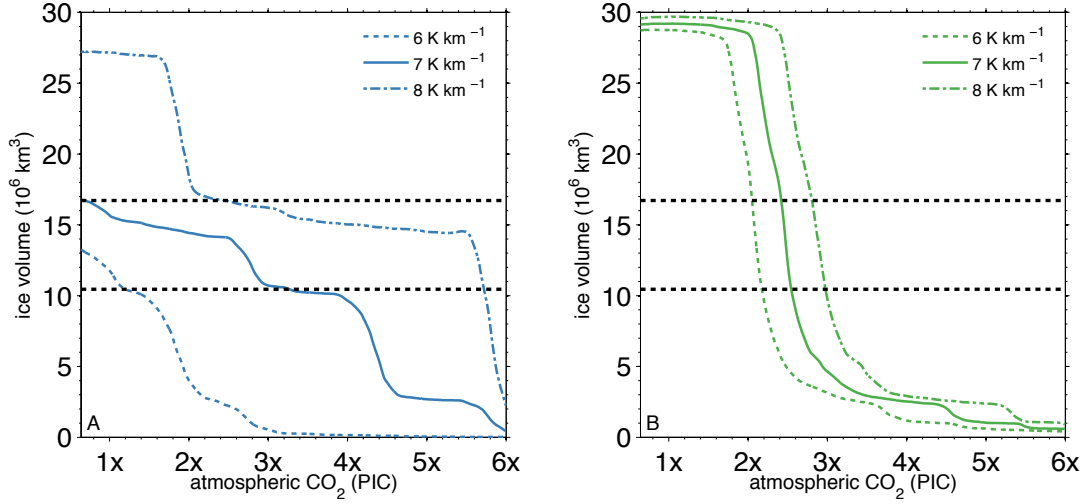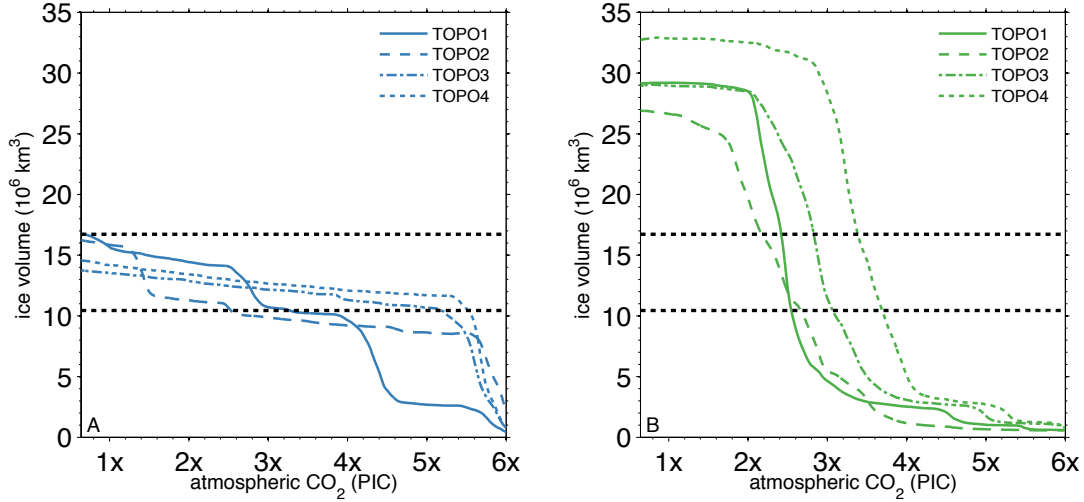
Figure 4.13: *Transient $CO_2$ experiments with varying ISM bedrock topography. A) Using climate output from CCSM3 simulations B) Using climate output from GENESIS simulations. The ISM bedrock topographies are shown in Figure 4.2.*

different isostasy models used for our default topography and that used by Wilson et al. (2011). Similar to the previous experiments, a large ice sheet does not form in the CCSM3 experiments (the lapse rate is 7 K km$^{-1}$). For the GENESIS experiments, the maximum size of the ice sheet varies due to differences in the total Antarctic surface area between the different topographies. For the maximum reconstruction of Wilson et al. (2011) (TOPO4), an ice sheet of $32.5 \times 10^6$ km$^3$ (78 m Eocene SLE) has formed at $2\times$ PIC. This increased ice volume compared to the default topography experiment is largely due to the growth of a continental based WAIS.

## 4.6 The case for Eocene ice

Our interest in the possibility of land ice being present in the Eocene stems from the need to constrain the upper end-member of the temperature / sea-level cross-plots discussed in Chapters 1 and 2, that being ice-free conditions. If there was significant ice present earlier than the EOT it also has implications for certain geochemical proxies, such as Mg/Ca, which make assumptions based on ice-free conditions (Lear et al., 2000). Based on previous modelling studies (DeConto and Pollard, 2003a; Langebroek et al., 2009), and proxy records of atmospheric $CO_2$ concentrations (Pagani et al., 2005, 2011; Pearson et al., 2009; Beerling and Royer, 2011), it is plausible that Antarctica could have been partially glaciated at times during the Eocene. The
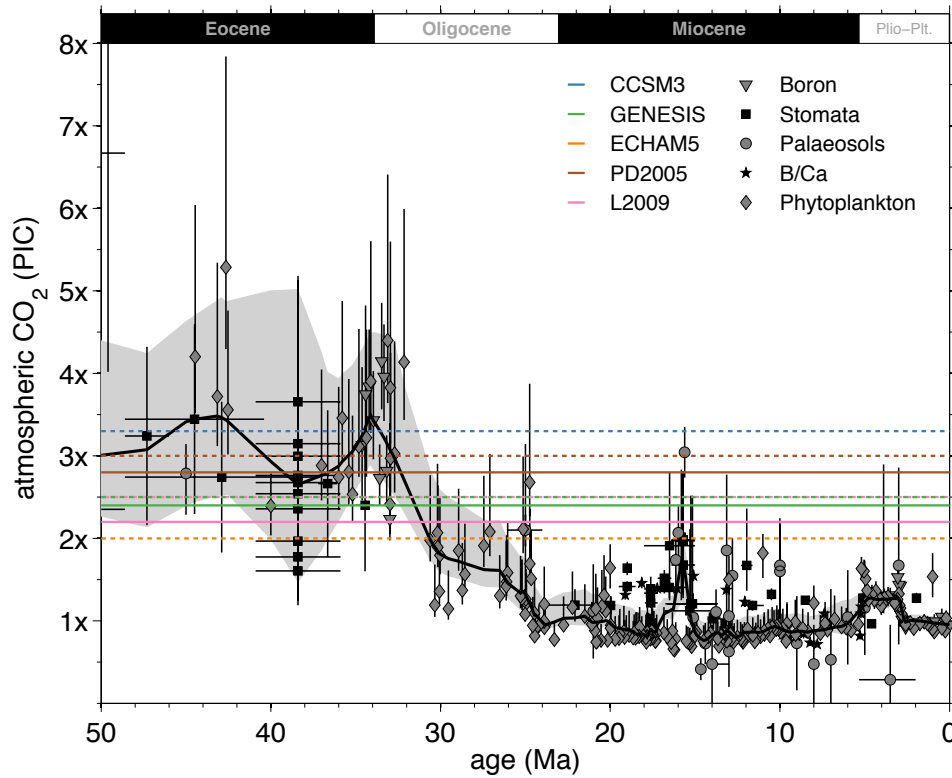
Figure 4.14: *Proxy estimates of atmospheric $CO_2$, reproduced from Beerling and Royer (2011), with Antarctic glacial thresholds from GCM-ISM inter-comparison. The dotted lines are the thresholds for an intermediate ice sheet (25 m Eocene SLE) and the solid lines are the thresholds for a large ice sheet (40 m Eocene SLE), PD2005 is the Pollard and DeConto (2005) simulation with astronomical forcing and L2009 is the Langebroek et al. (2009) simulation with astronomical forcing.*

composite of proxy atmospheric $CO_2$ records from Beerling and Royer (2011) is reproduced in Figure 4.14. This would support the argument of Miller et al. (2008a) that Antarctica experienced ephemeral glaciation earlier than the EOT, based on evidence from the sea level records of Kominz et al. (2008) which show significant fluctuations in the Eocene. The offline simulations undertaken in this chapter, which include no representation of ice albedo feedbacks, suggest that the modelled glacial $CO_2$ is highly climate model dependant.

The ISM simulations using the climate from HadCM3L (Lunt et al., 2010b) do not support the early Antarctic glaciation hypothesis, however, due to the strong seasonality and low precipitation over Antarctica using this model, there is also no significant glaciation at atmospheric $CO_2$ concentrations lower than PIC. Given that Antarctica is glaciated today this result seems unlikely and is also anomalous when compared with previous modelling studies (Huybrechts, 1993; DeConto and Pollard, 2003a; Langebroek et al., 2009) and the other 4 GCMs used in the

inter-model comparison presented here. At 4× PIC small ice caps (< 25 m Eocene SLE) have formed in the experiments using the climate output from CCSM3 and GENESIS. At 2× PIC, an intermediate ice sheet (> 25 m Eocene SLE) has formed in the experiments using CCSM3, ECHAM5 and GENESIS. The compilation of atmospheric $CO_2$ proxies of Beerling and Royer (2011) suggests that atmospheric $CO_2$ was likely between 4× and 2× PIC throughout much of the Eocene (see Figure 4.14). With the exception of the experiment using HadCM3L, none of the experiments support ice-free conditions during the Eocene based on current atmospheric $CO_2$ reconstructions.

An alternative way of addressing the question of land ice in the Eocene is to instead ask why the Eocene was ice-free if indeed it was. Although our modelling, coupled with the proxy records of atmospheric $CO_2$, suggests that isolated ice caps would have existed, we do not assume that this is correct. This caution is warranted given the significant inter-model disagreement. It seems plausible that a mountainous continent located over the pole would support ice caps. However, there are a number of additional factors which we have not yet fully addressed.

The opening of ocean gateways, in particular the Drake Passage, was proposed as a mechanism for the onset of Antarctic glaciation (Kennett, 1977). The modelling studies of DeConto and Pollard (2003a) and Huber et al. (2004), coupled with the synchronous decrease in atmospheric $CO_2$ at the EOT (Pagani et al., 2011), suggest decreasing atmospheric $CO_2$ rather than the opening of ocean gateways as the primary mechanism for continental Antarctic glaciation. However, DeConto and Pollard (2003a) suggest that the opening of ocean gateways could have lowered the $CO_2$ glacial threshold. This is because prior to the opening of the Drake Passage and the development of the Antarctic Circumpolar Current (ACC) there was greater meridional heat transport towards the Southern Hemisphere high latitudes. All of the early Eocene GCM simulations we have used have an open but shallow Drake Passage, resulting in partial development of the ACC. The CCSM3 experiment has a closed Tasman Gateway (Huber and Caballero, 2011; Sewall et al., 2000). It is possible that if the experiments were repeated with a closed Drake Passage then the glacial $CO_2$ threshold would be lower, potentially below that suggested by the proxy records for the Eocene. In an idealised experiment where the meridional heat transport was increased by 20 % to represent a closed Drake Passage, DeConto and Pollard (2003a) noted a slight lowering of the glacial $CO_2$ threshold to 2.3× PIC, compared with 2.8× PIC for an open Drake Passage experiment. The GCM simulations used here have a partially opened Drake Passage, so it is possible that the increase in the glacial $CO_2$ threshold would be less than for the DeConto and Pollard (2003a) open / closed experiment, if additional GCM

simulations with a closed Drake Passage were undertaken.

Proxy sea surface temperature records suggest that there was a reduced meridional temperature gradient in the Eocene, in particular the early Eocene, with the high latitudes significantly warmer than modern (Bijl et al., 2009; Hollis et al., 2009; Liu et al., 2009; Bijl et al., 2010) and the low latitudes only slightly warmer than modern (Sexton et al., 2006; Lear et al., 2008; Keating-Bitonti et al., 2011). Climate models, including those used here, have had limited success in reproducing this reduced meridional temperature gradient (Roberts et al., 2009; Winguth et al., 2010). For HadCM3L and CCSM3, the best model-data agreement requires high atmospheric $CO_2$ concentrations, in the range of $\sim 9 - 18\times$ PIC (Lunt et al., 2012). These atmospheric $CO_2$ concentrations appear high when compared with the proxy estimates. However, Huber and Caballero (2011) suggest that this increased radiative forcing is not necessarily just due to atmospheric $CO_2$, but could include feedbacks from other greenhouse gases, cloud feedbacks or other unknown factors. This increased radiative forcing could be sufficient to prevent snow accumulation, for example our CCSM3 simulation at $16\times$ PIC is ice-free. Alternatively, the $CO_2$ sensitivity could be higher than that suggested by the GCMs, which is particularly low for CCSM3 and GENESIS (Huber and Caballero, 2011). Indeed, simulations using ECHAM5 require only moderate atmospheric $CO_2$ concentrations ($2\times$ PIC) to show reasonable agreement with the sea surface temperature data, a result of the higher $CO_2$ sensitivity of ECHAM5 (Heinemann et al., 2009). It is interesting therefore that our ISM simulations using the climate from this ECHAM5 simulation produced a large ($10.3 \times 10^6$ km$^3$) ice sheet. This is perhaps dependent on the large lapse rate correction required from the relatively low Antarctic topography used in the ECHAM5 simulation to the ISM topography we use.

As discussed in previous chapters, there is a large ($\sim$1.5 ‰) increase in the benthic $\delta^{18}$O record at the EOT, caused by deep-sea cooling (Liu et al., 2009; Lear et al., 2010; Pusz et al., 2011) and/or the growth of a continental sized Antarctic ice sheet (Zachos et al., 2001a; Houben et al., 2012). Recent independent estimates suggest that part of this shift was due to $\sim 1.5 - 5$ °C of deep-sea cooling (Liu et al., 2009; Lear et al., 2010), which would imply the remainder was due to the growth of an ice-sheet with a volume of $\sim 10 - 45 \times 10^6$ km$^3$ (using a calibration of 0.0246 ‰ $10^6$ km$^{-3}$ of grounded ice, DeConto et al., 2008). Based on our simulations, the lower ice volume estimate could easily be accommodated on Antarctica, even if the continent was partially glaciated before the event. Our largest ice volume estimate is $32.5 \times 10^6$ km$^3$ using the GENESIS simulation at $2\times$ PIC and the upper estimate of Wilson et al. (2011) for the bedrock topography. Therefore if the EOT $\delta^{18}$O shift was caused by the growth of an ice

sheet of $45 \times 10^6$ km$^3$ (i.e. deep-sea cooling was 1.5 °C), it would require ice-free conditions prior to the event and potentially the additional growth of Northern Hemisphere ice sheets.

## 4.7  Summary

The inter-model comparison which has formed much of this chapter highlights that the modelled Antarctic $CO_2$ threshold is highly model and model configuration dependant. The threshold for the growth of an intermediate ice sheet (25 m Eocene SLE) varies between 2 and 3.3 $\times$ PIC when using the climate output from GENESIS, CCSM3 and ECHAM5 Eocene simulations and our default parameters. A significant part of this disagreement is due to differences in the GCM boundary conditions, in particular the topography over the Antarctic. Of the pre-existing early Eocene GCM simulations we have used here, 3 have relatively low topography over the Antarctic. The higher resolution ISM topographies we use are significantly more mountainous, requiring a large lapse rate correction. Because the lapse rate is a poorly constrained parameter and likely to vary spatially, the lapse rate correction is a large potential source of error. We have not investigated ISM dependance in this chapter, and we have only used one ISM and one surface mass balance scheme. It is possible that the $CO_2$ threshold could also vary if a different ISM or surface mass balance scheme were used.

The simulations using the HadCM3L simulations of Lunt et al. (2010b) have relatively low precipitation and a very high seasonality, which results in little snow accumulation, even at low atmospheric $CO_2$ concentrations. This result is anomalous when compared to the results of 4 other GCM simulations. The ISM simulations using the climate output from CCSM3, GENESIS and ECHAM5, suggests that grounded ice could have existed earlier than the EOT, based on current estimates of atmospheric $CO_2$. This would be in support of evidence from sea level records (Miller et al., 2005a; Kominz et al., 2008). If the Antarctic was ice-free in the Eocene it may suggest than some other mechanism prevented glaciation. For example, it is possible that stronger net radiative forcing, in addition to $CO_2$ forcing, resulted in warmer high latitudes than shown in the GCM simulations used here. Alternatively, the impact of the opening of ocean gateways and changes in ocean circulation could be greater than suggested by recent studies (DeConto and Pollard, 2003a; Huber et al., 2004).

The ISM simulations shown in this chapter have used a simple offline forcing, with no albedo feedbacks or changes in the astronomical forcing. In the next chapter we will use a more sophisticated forcing method, using the climate output from 18 GENESIS GCM simulations.

This will include astronomical forcing and a representation of albedo feedback. Unfortunately we cannot use any of the other GCMs for this alternative forcing method as we do not have the required GCM simulations available. In addition to investigating how these additional forcings affect Antarctic glaciation, this forcing method will allow us to investigate another issue which has proved problematic for previous coupled ice sheet - climate simulations of the Cenozoic, the hysteresis problem. The strong hysteresis shown by previous modelling studies (Pollard and DeConto, 2005; Langebroek et al., 2009) means that the EAIS is very stable once a continental sized ice sheet forms, as occurred at the EOT. This could be problematic for explaining the subsequent sea level fluctuations in the Oligocene and Miocene, if the EAIS was indeed stable (Kominz et al., 2008).

# Chapter 5

# Antarctic ice sheet hysteresis

## 5.1 Introduction

In this chapter we will use the GCM matrix method to perform idealised ISM simulations for the glaciation and possible deglaciation of the East Antarctic ice sheet (EAIS) under Eocene/Oligocene boundary conditions. There has been a longstanding argument regarding how stable the EAIS was in the Oligocene, Miocene and Pliocene, the period after a continental sized ice sheet formed at the EOT (Huybrechts, 1993; Zachos et al., 2001a; Pollard and DeConto, 2005; Hill et al., 2007; Kominz et al., 2008; Langebroek et al., 2009).

There is evidence for fluctuations in sea level during the Oligocene, from records of benthic $\delta^{18}O$ (Zachos et al., 2001a; Wade and Palike, 2004; Pälike et al., 2006) and sequence stratigraphy (Miller et al., 2005a; Kominz et al., 2008; Gallagher et al., 2012), which have been attributed to changes in the volume of the Antarctic ice sheets. Across the Oligocene/Miocene transition, there is a large glacial event (Mi-1) (Miller et al., 1991; Zachos et al., 2001b; Liebrand et al., 2011), implying that there was a reduced ice volume before the event. This is followed by a number of subsequent glacial / deglacial events in the Miocene (Miller et al., 1991; Pekar and DeConto, 2006; Shevenell et al., 2008; Liebrand et al., 2011; John et al., 2011). During the mid-Pliocene climate optimum, sea level was ~25 m higher than modern (estimates vary between +5 and +40 m; Dowsett and Cronin, 1990; Wardlaw and Quinn, 1991; Kaufman and Brigham-Grette, 1993; Miller et al., 2005a; Naish and Wilson, 2009; Miller et al., 2012), which cannot be explained solely by the loss of ice from the Greenland ice sheet and the West Antarctic ice sheet (WAIS), suggesting additional mass loss from the EAIS (Raymo et al., 2009). It should be noted that these sea level estimates are complicated by glacio-isostatic adjustments, which are often not accounted for (Raymo et al., 2011). The proxy records of sea level therefore suggest that the EAIS was dynamic after a continental sized ice sheet formed at the EOT.

Ice sheet modelling studies have struggled to achieve a significant deglaciation of the EAIS once a continental sized ice sheet has formed (Huybrechts, 1993; Pollard and DeConto, 2005; Langebroek et al., 2009). This is due to a strong hysteresis which means that the deglacial $CO_2$ threshold is higher than the glacial $CO_2$ threshold (Pollard and DeConto, 2005; Langebroek et al., 2009). This problem is exacerbated by the relatively low (typically $< 750$ ppmv) atmospheric $CO_2$ in the Oligocene, Miocene and Pliocene suggested by proxy records (Pagani et al., 2005, 2009, 2011; Beerling and Royer, 2011; Foster et al., 2012). The ice sheet modelling studies which have achieved partial deglaciation of the EAIS have either required a climate forcing using GCM boundary conditions which already have a reduced EAIS (Hill et al., 2007;

Dolan et al., 2011), or have used an inverse forcing method which is constrained by $\delta^{18}O$ data (de Boer et al., 2010).

Our interest in this hysteresis effect is twofold; firstly it remains a significant source of disagreement between data and models (Pollard and DeConto, 2005; Miller et al., 2005a). Secondly we are using data from the Cenozoic, broadly a period of cooling (Lear et al., 2000), to investigate the past temperature / sea level relationship. Because of the ice sheet hysteresis effect, the temperature / sea level relationship could be different for a period of warming, like that predicted for the coming century (Solomon et al., 2007), than for the cooling which has made up much of the Cenozoic.

## 5.2   Ice sheet hysteresis

The first type of hysteresis we discuss in this chapter is that arising from height-mass balance (HMB) feedback operating on a continent bound by an ocean, such as the Antarctic continent (Oerlemans, 1981, 2002; Pollard and DeConto, 2005). Beginning with no ice and a warm climate, the snowline (the point at which accumulation exceeds ablation) is above the continental floor and there is no large-scale glaciation. As the snowline descends due to cooling, for example from a reduction in atmospheric $CO_2$ or astronomical forcing, it intercepts the continental floor and large scale glaciation occurs. Due to the atmospheric lapse rate, as the ice sheet grows vertically through the atmosphere its surface is cooled (Oerlemans, 1981). For the Antarctic, as the ice sheet grows it becomes bound by the limits of the continent, with ice lost through calving at the coast and a positive mass balance existing over the ice sheet interior (see Figure 5.1.A). For deglaciation to occur, the snowline must rise above the ice sheet surface, which is now significantly higher than the ice-free continental floor (see Figure 5.1.C). The stability is enhanced by the steep slopes at the ice sheet edge, as the ice sheet is bound by the ocean, meaning that there is limited melt at the ice sheet flanks. This hysteresis effect is therefore especially strong when the Antarctic is covered with a continental sized ice sheet. Once deglaciation has started, the feedback works in reverse, with the ice sheet surface descending due to surface melting, which is then enhanced as the lapse rate generates increased warming (Pollard and DeConto, 2005). Because of this effect the deglacial threshold is above the glacial threshold (Pollard and DeConto, 2005; Langebroek et al., 2009). This effect occurs regardless of whether the ice albedo effect is accounted for (Pollard and DeConto, 2005).

The higher albedo of the ice sheet surface compared with bare bedrock generates additional
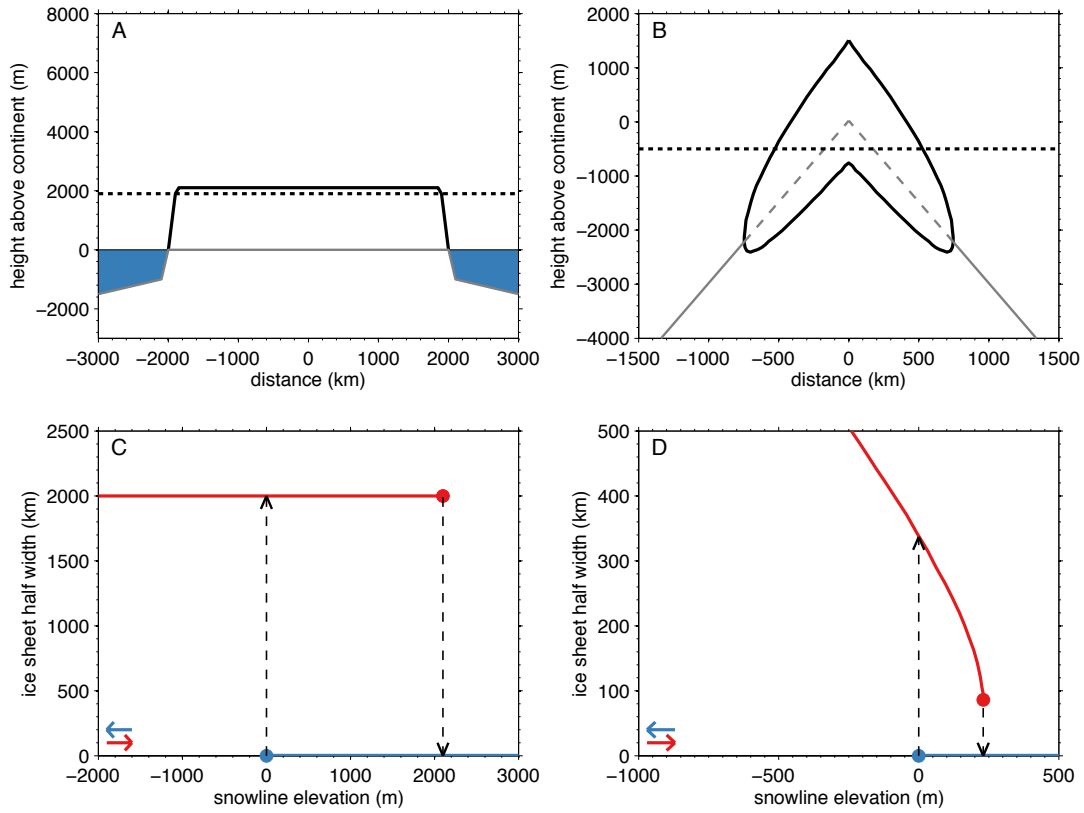
Figure 5.1: *Schematic of height-mass balance feedback. A) representation of the geometry of a large ice sheet on a flat continent bound by ocean, grey line is the continental floor, the ice sheet surface is shown as a black line, the horizontal dotted line is the snowline for an ice sheet in equilibrium. B) geometry of a small ice sheet on sloping terrain with a central peak (after Pollard and DeConto, 2005, their Figure A.1; Weertman, 1976), grey line is the bedrock, the ice sheet surface is shown as a black line, the horizontal dotted line is the snowline for an ice sheet in equilibrium. C) hysteresis for a large ice sheet on a flat continent bound by ocean (after Pollard and DeConto, 2005, their Figure 1.B; Oerlemans, 2002), snowline elevation is with respect to the continental floor, the blue line is for a cooling and lowering of the snowline from an ice-free state, the blue dot is the last stable state, the red line is for a warming and raising of the snowline from a glaciated state, the red dot is the last stable state, the dashed black arrows show possible transitions. D) hysteresis for a small ice sheet on a sloping terrain with a central peak (after Pollard and DeConto, 2005, their Figure 1.A; Weertman, 1976), snowline elevation is with respect to the central mountain peak, the blue line is for a cooling and lowering of the snowline from an ice-free state, the blue dot is the last stable state, the red line is for a warming and raising of the snowline from a glaciated state, the red dot is the last stable state, the dashed black arrows show possible transitions. Note the different sizes of the ice sheets and hysteresis.*

147

cooling as a greater proportion of the incoming solar radiation is reflected by the ice. The inclusion of ice albedo generates a hysteresis effect in the same sign as the HMB feedback (Pollard and DeConto, 2005). Brooks (1949) proposed that the growth of a "small" sea ice cap from a modest cooling would generate an additional cooling from the albedo feedback. This additional albedo cooling would be proportional to the ice cap area, which would increase nonlinearly as a circular ice cap grew outwards from the pole. In an idealised Earth covered with water, the increased cooling from the growth of an ice cap at the pole could exceed the meridional warming (depending on the meridional temperature gradient), generating a runaway increase in the ice cap area until a sufficiently warm latitude were reached. This would lead to the growth of a "large" sea ice cap, which would extend much further than the limit of the initial cooling. For a climate warming, this nonlinear response would operate in reverse, and there would be an abrupt loss of ice after sufficient warming. The climate would need to cool beyond the point of this abrupt ice loss to re-establish a sea ice cap, therefore exhibiting a hysteresis effect (Winton, 2006). Brooks (1949) suggested that the only stable solutions were an unglaciated state and a fully glaciated state, with an ice cap large enough to control its own climate (Notz, 2009). Although this argument was based on a sea ice cap, Brooks (1949) suggested that the same argument could hold for land ice. Whether such a situation would actually exist in nature has been subject to some debate, with the effect becoming known as the 'small ice cap instability' (North, 1984; Crowley et al., 1994; Winton, 2006; Notz, 2009).

An effect similar to that originally described by Brooks (1949) has been seen in some diffusive energy balance model studies, although the effect has been attributed to both albedo feedback (North, 1975, 1984; Birchfield et al., 1982; Mengel et al., 1988) and HMB feedback (Weertman, 1961, 1976; Oerlemans, 1981, 1982). The HMB small ice cap instability differs from the large scale HMB hysteresis described above in that it involves relatively small terrestrial ice caps on sloping (e.g. mountainous) terrain (Figure 5.1.B; Weertman, 1976; Pollard and DeConto, 2005). The magnitude of this hysteresis is also significantly smaller than that described above (Pollard and DeConto, 2005). The albedo feedback small ice cap instability seen in certain energy balance models has been attributed to the parameterisation of the albedo feedback and of the diffusion of heat from the interior of the ice cover (North, 1984; Notz, 2009). This effect was often considered a modelling quirk of these relatively simple models which should be removed by altering the parameterisation, for example by smoothing the albedo feedback at the ice edge or by using a nonlinear diffusive heat transport (North, 1984). However, a similar effect was also seen in a GCM study with a more sophisticated representation of heat transport (Crowley

et al., 1994). More recent GCM studies are inconclusive as to whether such an instability exists for a sea ice cap (Winton, 2006), although there is some support for such an instability existing for the transition from seasonal sea ice cover to an ice-free state (Eisenman and Wettlaufer, 2009).

Pollard and DeConto (2005) attributed the significant hysteresis seen in their Antarctic ice sheet modelling study to the HMB feedback caused by continental scale glaciation on an ocean bound continent. However the study of Pollard and DeConto (2005) had only a rough representation of albedo feedback and the authors suggested that the hysteresis would be even greater with an improved representation of albedo feedback. The hysteresis was found to be sensitive to the inclusion of astronomical forcing (Pollard and DeConto, 2005), which was also shown by the study of Langebroek et al. (2009) using a reduced complexity model. The inclusion of this astronomical 'noise' in addition to the background forcing from changes in atmospheric $CO_2$ was capable of generating an earlier transition between the two stable states (Pollard and DeConto, 2005; Langebroek et al., 2009). In this chapter we will perform various sensitivity studies investigating ice sheet hysteresis. Because of the computationally efficient method we have developed, our work will build on previous studies by using a complex climate model to perform many ice sheet simulations.

## 5.3 Hysteresis experiments

In this section we perform idealised ice sheet hysteresis experiments using Eocene/Oligocene simulations from the GENESIS GCM. Our representation of albedo feedback will be based on the GCM matrix method (Pollard, 2010), discussed in Chapter 3. The GCM matrix will also be used to include astronomical forcing and atmospheric $CO_2$ forcing, using the methods described and tested in Chapter 3. We will perform a number of sensitivity tests with these forcings turned on and off, to determine their effect on the ice sheet hysteresis. In addition we will perform simulations with enhanced basal sliding.

In these hysteresis experiments we decrease atmospheric $CO_2$ from $8\times$ PIC down to $1\times$ PIC and perform the same simulation in reverse, starting at $1\times$ PIC. Note that rather than performing a continuous simulation decreasing and then increasing atmospheric $CO_2$ we choose to perform two simulations to reduce the time taken for computation. The initial conditions for the forward (cooling) run are an ice-free Antarctic, and for the reverse (warming) run are full scale glaciation. The glaciated starting conditions are achieved by performing a 100 ka
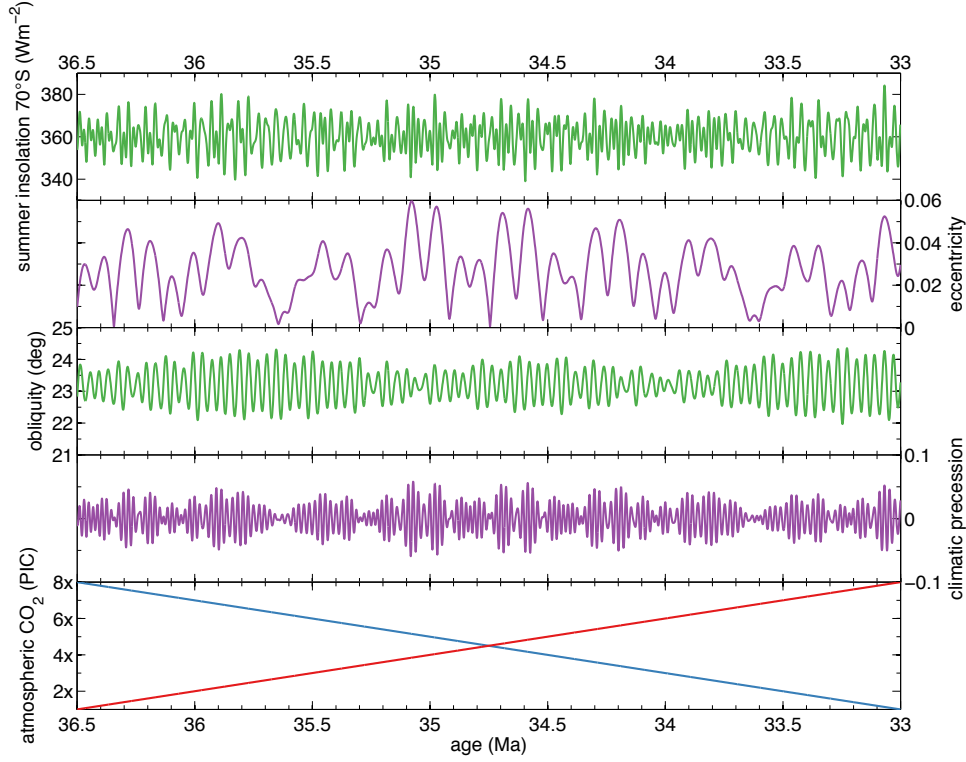
Figure 5.2: *Forcing used for hysteresis experiments. Astronomical forcing used is for the 6 warmest months at 70°S (see Chapter 4), for fixed astronomical forcing a constant value of 360 Wm$^{-2}$ is used. Based on the astronomical solutions of Laskar et al. (2004), the astronomical parameters are also shown for reference. Atmospheric $CO_2$ is either increased or decreased linearly between 8× and 1× PIC.*

equilibrium simulation at 1× PIC at the start of the reverse simulation. Each simulation lasts 3.5 Ma, resulting in a rate of $CO_2$ change of 280 ppmv per 500 ka. This rate of $CO_2$ change is an order of magnitude faster than the rate used by Pollard and DeConto (2005) and Langebroek et al. (2009) who performed similar hysteresis experiments with a rate of $CO_2$ change of 28 ppmv per 500 ka. However, faster rates of $CO_2$ change are recorded across the EOT (Pagani et al., 2011), leading us to assume that we are not changing atmospheric $CO_2$ too quickly for the purposes of these idealised experiments. For the astronomical forcing experiments we use the astronomical solutions of Laskar et al. (2004), starting at 36.5 Ma and ending at 33 Ma (see Figure 5.2).
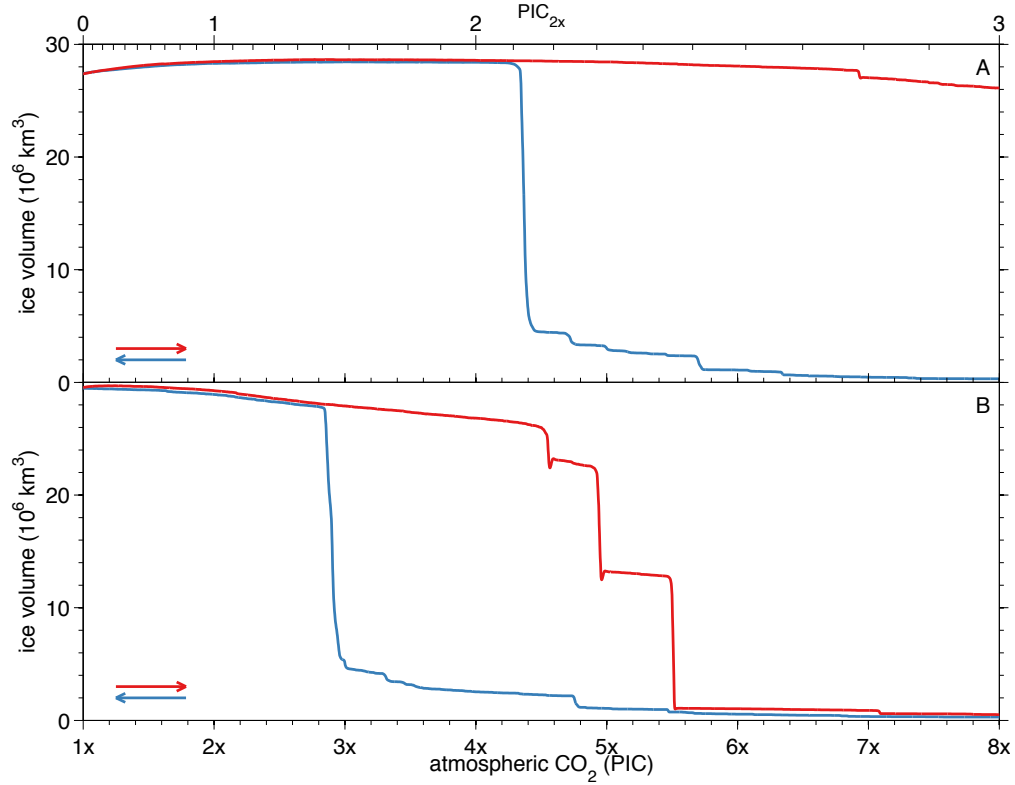
Figure 5.3: *Hysteresis experiment with A) ice sheet feedbacks turned on and B) ice sheet feedbacks turned off. The blue lines are for the cooling direction and the red lines for the warming direction. These experiments are for a constant astronomical forcing which is similar to the modern astronomical forcing. Basal sliding is turned off in these experiments. The upper x-axis, in units of doublings of atmospheric $CO_2$ takes into account the logarithmic dependence of $CO_2$ forcing, see text for an explanation.*

### 5.3.1 Ice sheet – climate feedback

The first simulations we perform are constant astronomical forcing simulations with ice sheet feedback turned either on or off. We refer to this feedback as ice sheet feedback as it includes feedbacks from the growth of an ice sheet on albedo, atmospheric circulation and precipitation patterns. We interpolate between GCM simulations with the following Antarctic boundary conditions: no ice over the Antarctic, an intermediate ice sheet and a full ice sheet over the Antarctic. This interpolation is based on the total volume of ice which has grown in the ISM (see Chapter 3 for a detailed discussion of the GCM matrix method). The feedback does not include HMB feedback, which is calculated by the ISM itself. Therefore both the ice sheet feedback on and ice sheet feedback off simulations include HMB feedback.

As can be seen from Figure 5.3, the inclusion of ice sheet feedbacks results in the earlier onset of glaciation at a higher atmospheric $CO_2$ concentration. A large ice sheet (40 m sea level equivalent) forms at $4.4\times$ PIC in the simulation with ice sheet feedbacks, compared with $2.9\times$ PIC for the simulation without ice sheet feedbacks. In the simulation with ice sheet feedback, once a continental sized ice sheet has formed, there is a slight reduction in ice volume with further decrease in atmospheric $CO_2$. It is likely that this is due to decreased precipitation with decreasing temperature. The precipitation is also lower in the simulation with ice sheet feedback turned on because of changes in atmospheric circulation from the growth of an elevated, dry ice sheet. This feedback on precipitation does not occur in the simulation shown in Figure 5.3.B.

For the warming simulations, shown as red lines in Figure 5.3, a deglaciation does not occur in the simulation with ice sheet feedback included, even towards the end of the simulation when atmospheric $CO_2$ has reached $8\times$ PIC. We do not extend the simulations by extrapolating beyond $8\times$ PIC as this is already a large extrapolation from the $4\times$ PIC GCM simulation, note that we do not have a GCM simulation available higher than $4\times$ PIC. This is similar to the preliminary results of Pollard and DeConto (2005), in their simulation without astronomical forcing and an improved representation of albedo feedback to that shown in Pollard and DeConto (2005). In the simulation without ice sheet feedback a multiple stepped deglaciation occurs, in contract to the glaciation which occurred in a single step, with only small ice caps remaining at $5.5\times$ PIC. Another interesting effect is evident during the deglaciation, with small increases in ice volume after each of the deglacial events. This is caused by isostatic unloading as ice is removed, leading to a rebounding of the bedrock and cooling of the remaining ice sheet surface through HMB feedback. A similar effect was observed in the simulations of Oerlemans (1981).

There is significant hysteresis in both of the simulations shown in Figure 5.3. In the simulations without ice sheet feedback, this is caused by HMB feedback which is enhanced by the constraints of the Antarctic continent after a large ice sheet has formed. The hysteresis is further enhanced by the representation of ice sheet feedbacks from the GCM matrix method, to the extent that a deglaciation does not occur in our constant astronomical forcing simulation with ice sheet feedback.

### 5.3.2  Astronomical forcing

In the next set of simulations we include astronomical forcing. The 2 simulations shown in Figure 5.4 also have the albedo feedback turned on (Figure 5.4.A) and off (Figure 5.4.B). The
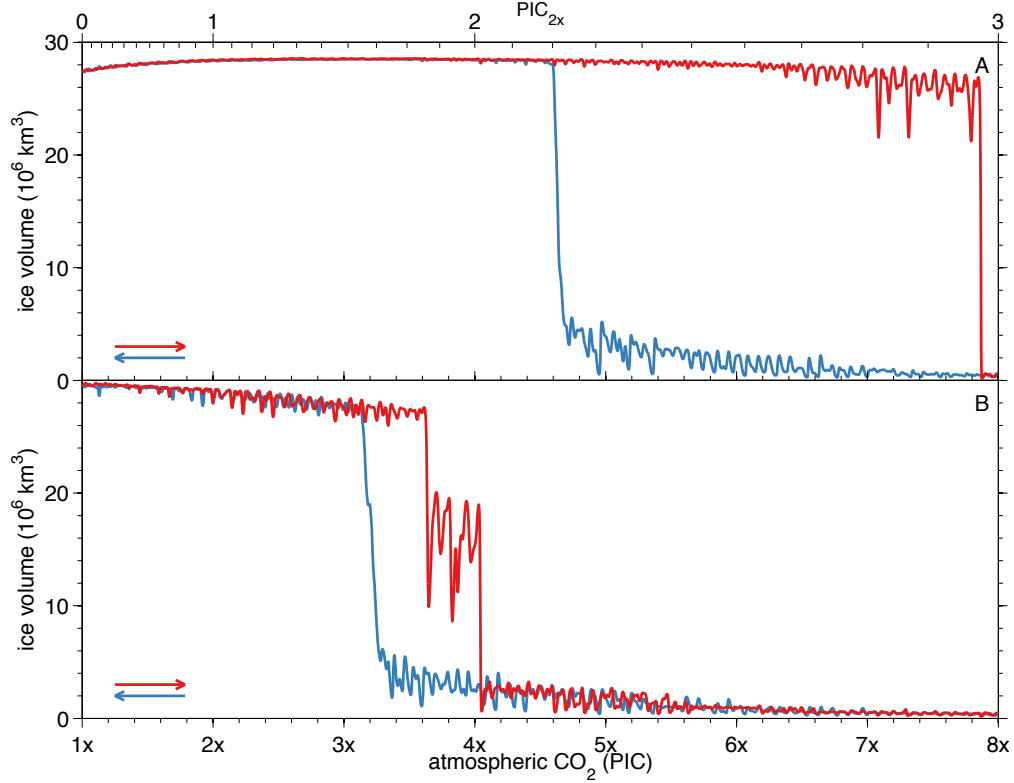
Figure 5.4: *Hysteresis experiment with astronomical forcing A) with ice sheet feedback and B) without ice sheet feedback*

astronomical forcing method is described in Chapter 3 and is based on the summer (6 peak months) insolation at 70 °S, based on the astronomical solutions of Laskar et al. (2004). This differs from the astronomical forcing of Pollard and DeConto (2005), who used a synthetic astronomical forcing which was repeated throughout the duration of their simulation. Our method is similar to Langebroek et al. (2009), who also used an astronomical reconstruction but with a reduced complexity model. The astronomical forcing is evident in Figure 5.4 as the high frequency oscillations superimposed on the broader trend. These oscillations are significantly dampened in Figure 5.4.A when a continental sized ice sheet is present.

The inclusion of astronomical forcing has a small impact on the atmospheric $CO_2$ threshold in our simulations, which occurs at $4.6\times$ and $3.2\times$ PIC for the simulations with and without ice sheet feedback, respectively. This is slightly higher ($\sim 0.2 - 0.3\times$ PIC) than the constant astronomical forcing simulations. The deglacial thresholds occur at a lower atmospheric $CO_2$ concentration than for the constant astronomical forcing simulations. The deglaciation occurs at $7.9\times$ (with ice sheet feedback) and $4.0\times$ PIC (without ice sheet feedback). It is interesting

that we get a deglaciation at all for the simulation with ice sheet feedback, in comparison with the constant astronomical forcing experiment which did not deglaciate. However, we are careful not to read too much into the exact nature of the astronomical configuration which caused this collapse, because this could change if we varied the start date of the experiment (discussed in 5.3.4). There is still a pronounced hysteresis evident in these simulations. We suggest that instead of measuring the width of the hysteresis in atmospheric $CO_2$ ppmv (Pollard and DeConto, 2005; Langebroek et al., 2009), that the logarithmic dependance of $CO_2$ forcing should be taken into account and the width of the hysteresis should be normalised:

$$H_s = \frac{\ln(a) - \ln(b)}{\ln(2)}, \qquad (5.3.1)$$

where, $H_s$ is the width of hysteresis in doublings of $CO_2$ ($PIC_{2\times}$), $a$ is the deglacial threshold and $b$ is the glacial threshold.

The hysteresis for the simulation with astronomical forcing and ice sheet feedback is 0.78 $PIC_{2\times}$ and 0.32 $PIC_{2\times}$ for the simulation without ice sheet feedback. Note that the width of the hysteresis may be affected slightly by the phasing of the astronomical forcing. By comparing the ice sheet feedback on/off simulations we can estimate that $\sim$41 % (0.32 $PIC_{2\times}$) of this hysteresis is due to HMB feedback and $\sim$59 % (0.46 $PIC_{2\times}$) is due to other ice sheet feedbacks. This does not take into account possible nonlinearities between HMB feedback and other ice sheet feedbacks. Ideally we would perform a simulation with other ice sheet feedbacks (albedo, atmospheric circulation) and no HMB feedback, which would require a lapse rate of zero. This is problematic as the lapse rate is used to scale from the coarse GCM topography onto the finer ISM topography, in addition to calculating HMB feedback.

For the ice sheet feedback off simulations, the inclusion of astronomical forcing reduces the width of the hysteresis to 0.32 $PIC_{2\times}$ compared with 0.92 $PIC_{2\times}$ for the constant astronomical forcing simulation. Because the simulation in Figure 5.3.A did not deglaciate, we cannot calculate the width of the hysteresis for that simulation, although it is greater than 1 $PIC_{2\times}$. For comparison, in the simulations of Pollard and DeConto (2005) the width of the hysteresis was 0.25 $PIC_{2\times}$ for the simulation with astronomical forcing and 0.59 $PIC_{2\times}$ for the constant astronomical forcing simulation. Their simulations had a limited representation of albedo feedback (Pollard and DeConto, 2005). In the simulations of Langebroek et al. (2009), the hysteresis was 0.24 $PIC_{2\times}$ for the simulation with astronomical forcing and 1.20 $PIC_{2\times}$ for the constant

astronomical forcing simulation. The study of Langebroek et al. (2009) used a much higher value for the lapse rate of 12 K km$^{-1}$, which would have enhanced the HMB feedback. The parameters we use here are the same as the previous chapter, the lapse rate is 7 K km$^{-1}$.

### 5.3.3 Basal sliding

The previous simulations have all had no basal sliding (see Chapter 3 for a description of basal sliding in the ISM). In the following simulations we include basal sliding by adjusting the basal sliding parameter to a low rate (0.5 mm yr$^{-1}$ Pa$^{-1}$) and a high rate (10 mm yr$^{-1}$ Pa$^{-1}$), similar to Gregoire et al. (2012). These basal sliding rates were used by Gregoire et al. (2012) for regions of either bare rock (low rate) or deep ($> 20$ m) sediments (high rate). In these idealised simulations we apply either the low rate (Figure 5.5.A) or the high rate (Figure 5.5.B) for the entirety of the Antarctic continent for the duration of the simulation. We do not take into account the removal of sediment (Pollard and DeConto, 2003). Both of these simulations include astronomical forcing and ice sheet feedbacks.

As can be seen from Figure 5.5.A, including a low rate of sliding has limited impact compared with the equivalent no sliding simulation (Figure 5.4.A). The total ice volume is slightly reduced, for example at 2× PIC the ice volume is 28.4 ×10$^6$ km$^3$ for the no sliding simulation and 27.2 ×10$^6$ km$^3$ for the low basal sliding simulation. However, there is a larger difference between the low and high basal sliding simulations. The onset of glaciation is delayed in the high basal sliding simulation, occurring at 3.0× PIC, compared with 4.1× PIC for the low basal sliding simulation. Although the continent is fully glaciated in the high basal sliding simulation at low atmospheric CO$_2$, the ice volume is much lower than the low basal sliding simulation. At 2× PIC the ice volume is 17.8 ×10$^6$ km$^3$ for the high basal sliding simulation. This is due to a reduced average ice thickness for the simulation with increased basal sliding (see Figure 5.6). In these simulations, a difference in total ice volume of up to 10.6 ×10$^6$ km$^3$ (∼25 m SLE) can occur on a fully glaciated continent due to changes in basal sliding.

The hysteresis is also significantly reduced in the simulation with the high rate of basal sliding, to 0.26 PIC$_{2×}$, compared with 0.95 PIC$_{2×}$ for the low basal sliding simulation. The deglaciation for the high basal sliding simulation occurs at 3.6× PIC, despite the inclusion of ice sheet feedbacks. Part of this reduction in hysteresis is due to the reduced thickness of the ice sheet, which will limit the HMB feedback. In addition, because the ice sheet feedback is calculated based on total ice volume for the domain, this will be reduced for the simulation
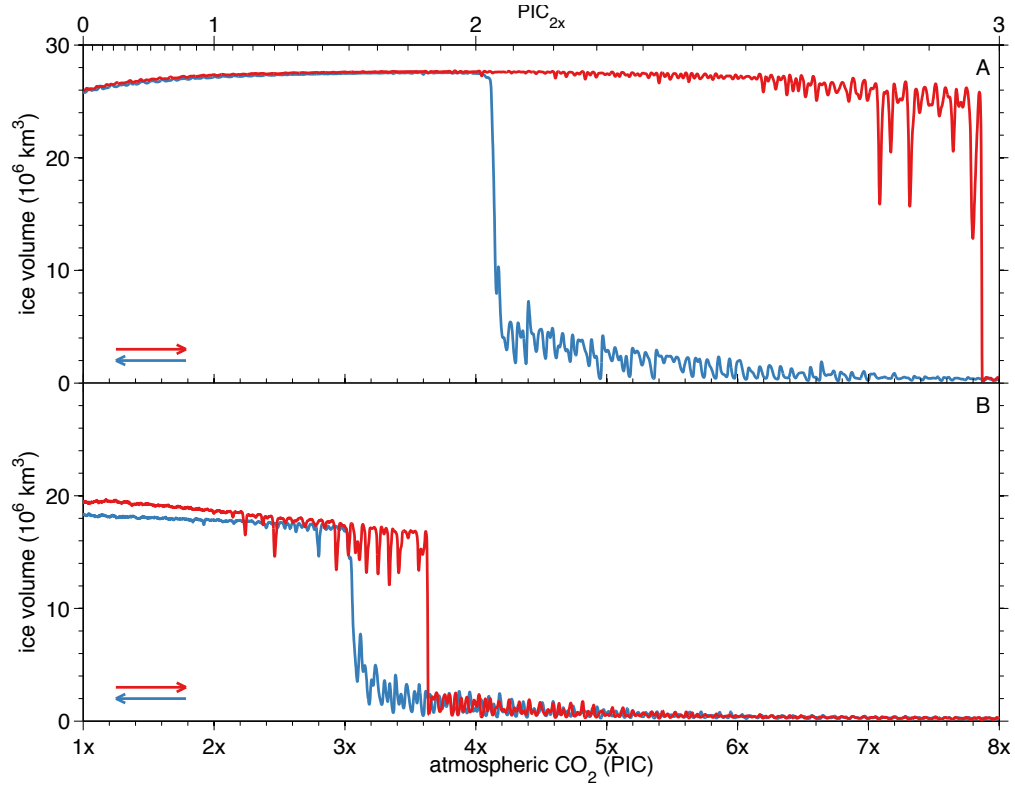
Figure 5.5: *Hysteresis experiments including basal sliding A) low rate for basal sliding parameter (0.5 mm yr$^{-1}$ Pa$^{-1}$) applied uniformly over the continent B) high rate for the basal sliding parameter (10 mm yr$^{-1}$ Pa$^{-1}$) applied uniformly over the continent. Both simulations included astronomical forcing and ice sheet feedbacks*
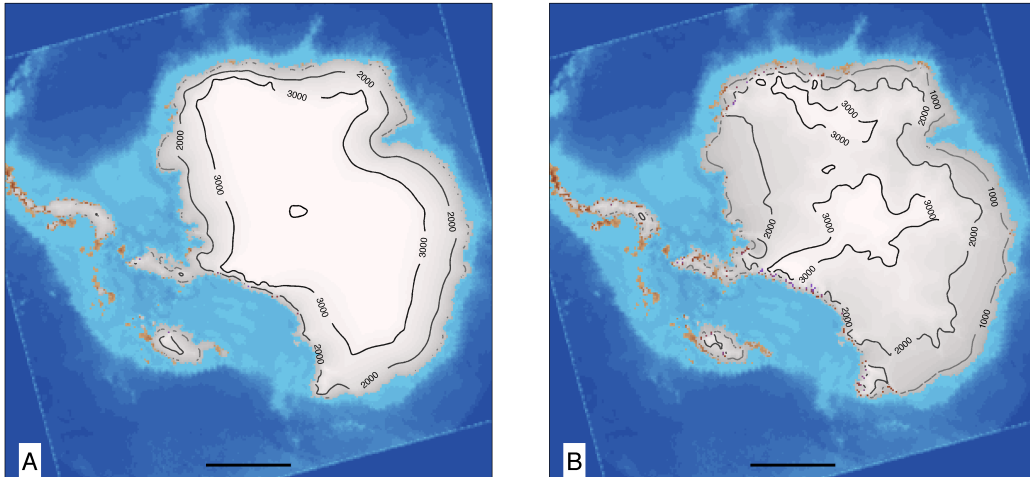


Figure 5.6: *Impact of basal sliding on ice surface elevation through changes in ice thickness. A) low rate for basal sliding at 2× PIC B) high rate for basal sliding at 2× PIC.*

156

with high basal sliding due to its lower volume. If the ice sheet feedback was instead calculated based on total ice area for the domain, this would not be the case.

It is important to bear in mind the idealised nature of these experiments. The high rate of basal sliding is applied uniformly over the entire continent, assuming that there are thick sediments present. These sediments are assumed to remain for the duration of these 3.5 Ma simulations. In the ISM simulations of Pollard and DeConto (2003) which included a model of basal sediments, the sediment thickness was rapidly reduced within a few astronomical cycles ($10^4$ years). Sediments remained where basal temperatures were well below the pressure melting point and there was limited basal sliding. Where basal temperatures were close to the pressure melting point and basal sliding occurred, sediment was quickly removed (Pollard and DeConto, 2003). A stable sediment thickness was reached when the removal of sediment from the bed was replenished by new sediment from erosion (Pollard and DeConto, 2003). The basal environment of the modern Antarctic is poorly known due to its inaccessibility, and is a significant source of uncertainty in ISM simulations of the modern Antarctic ice sheet (e.g. Pollard and DeConto, 2012a). There is considerable uncertainty as to the past basal environment of the Antarctic (e.g. Jamieson et al., 2010).

### 5.3.4 Ensemble simulations

A number of important parameters within the ISM are poorly constrained and are often varied in ISM sensitivity studies (Ritz et al., 1997; Hebeler et al., 2008; Stone et al., 2010; Applegate et al., 2012). Here we perform an ensemble of ISM simulations with parameter values perturbed from their default values. The sampling method we use to vary the parameters is latin hypercube sampling, discussed in Chapter 3. Due to computational constraints, we limit this ensemble to 25 members and vary the value of 5 parameters. The study of Pollard et al. (2005) showed limited impact of changing the geothermal heat flux on Cenozoic Antarctic ice volumes and on the timing of glaciation. We therefore do not include the geothermal heat flux as one of the parameters in our ensemble, as we did in Chapter 3, and instead vary the basal sliding parameter. The geothermal heat flux is fixed at the default value of -50 mW m$^{-2}$. The 5 parameters we vary and the ranges for these values are shown in Table 5.1, the ensemble parameter values are included in Appendix E.

For this ensemble, the simulations we perform are the same as that shown in Figure 5.4.A, which includes astronomical forcing and has ice sheet feedback turned on. To reduce the com-

Table 5.1: *Default values and ranges for key parameters in the ISM. The default values are those used for all other Antarctic ISM simulations in this thesis. Ranges from the literature: [a] Hebeler et al. (2008); [b] Stone et al. (2010); [c] Gregoire (2010); Marshall et al. (2002)*

|  |  | default value | range | units |
|---|---|---|---|---|
| $\alpha_s$ | PDD factor for snow | 3 | 3 to 8[a] | mm d$^{-1}$ °C$^{-1}$ |
| $\alpha_i$ | PDD factor for ice | 8 | 8 to 20[b] | mm d$^{-1}$ °C$^{-1}$ |
| $f$ | flow enhancement factor | 3 | 1 to 10[c] | - |
| $B_s$ | basal sliding parameter | - | 0.5 to 10[c] | mm yr$^{-1}$ Pa$^{-1}$ |
| $\gamma$ | lapse rate | 7 | 5 to 9[a] | °C km$^{-1}$ |

putational expense of these simulations we accelerate the rate of atmospheric $CO_2$ change so that the combined simulations are now 1.5 Ma in duration, instead of 7 Ma. This results in a reduced number of astronomical cycles throughout the simulation. This reduction in the number of astronomical cycles has a small impact on the glacial/deglacial $CO_2$ thresholds as glaciation/deglaciation may be delayed until a favourable astronomical configuration is reached. An equivalent simulation to that shown in Figure 5.4.A but for the shorter 1.5 Ma duration is shown as a black line on Figure 5.7, with the non-accelerated simulation shown in grey. The shorter duration of the simulation results in a glacial threshold of 4.1× PIC, compared with 4.6× PIC for the longer duration simulation, as a favourable astronomical configuration is reached sooner.

The parameter ensemble is shown in Figure 5.7. The first thing to note is that the simulations with the default parameter values (black lines) are far outside the range of the ensemble simulations (blue / red lines), with glaciation and deglaciation occurring at higher atmospheric $CO_2$ concentrations. This is likely because the default parameter values for the positive degree day (PDD) factors are at the lower limit of the plausible parameter range. Therefore all of the ensemble simulations will have higher values for the PDD factors, which will lead to increased ablation. A similar result was shown in the parameter ensemble in Chapter 3 for the Northern Hemisphere simulations. The default parameters also have no basal sliding, whereas basal sliding is included for all of the ensemble simulations. The default value for the flow enhancement factor is also towards the lower end of the plausible parameter range (see Table 5.1). The majority of the ensemble simulations will have greater ice loss through surface ablation and ice flow than the default parameter simulation.

Figure 5.7: *Parameter ensemble, with basal sliding. Transient simulation with ice sheet feedback and astronomical forcing. The default simulation is shown in black, with the non-accelerated default simulation shown in grey (see text). A) decreasing $CO_2$ from ice-free starting conditions B) Increasing $CO_2$ from glaciated starting conditions.*

The shorter duration of the ensemble simulations and associated reduction in the number of astronomical cycles has resulted in clustering of the simulations around favourable astronomical configurations, this is especially evident for deglaciation (Figure 5.7.B). We calculate the hysteresis for the ensemble simulations from the difference between the glacial and deglacial atmospheric $CO_2$ thresholds. Because there are partial glacial / deglacial events, we define glaciation as the earliest formation of an ice sheet $> 12 \times 10^6$ km$^3$ in volume, and deglaciation as the earliest reduction in ice volume to $< 6 \times 10^6$ km$^3$ in volume. For the parameter ensemble, the glacial threshold is crossed on average at 1.7 $\pm$0.3 (1 std.) $\times$ PIC, and the deglacial threshold is crossed on average at 3.3 $\pm$0.7$\times$ PIC. All of the simulations show hysteresis, the deglacial threshold is always at a higher atmospheric $CO_2$ concentration than the glacial threshold. The hysteresis is on average 0.94 $\pm$0.26 PIC$_{2x}$. The average hysteresis of the parameter ensemble is therefore slightly below the hysteresis of the default simulation.

Due to the latin hypercube sampling method we have adopted for this ensemble it is difficult to determine the influence of individual parameters. However, the correlation between each of the parameters and the hysteresis gives some indication as to which of the parameters have the most influence on the magnitude of the hysteresis (Stone et al., 2010). Of the parameters included in the ensemble, the basal sliding parameter has the greatest correlation with hysteresis (-0.67), which is consistent with the results from the basal sliding sensitivity test. The PDD factor for ice (0.53) and the lapse rate (0.45) had the next greatest correlation (see Appendix E). This suggests that low values for the PDD factor for ice and the lapse rate and high values for the basal sliding parameter lead to a reduction in the ice sheet hysteresis.

The parameter ensemble simulations also show large variability in ice volumes once the EAIS has formed and the continent is fully glaciated. At $1.5\times$ PIC for the simulations with increasing $CO_2$ (Figure 5.7.B), a large scale deglaciation has not yet occurred for any of the simulations, but the range of ice volumes varies from 16.1 to $26.5\times10^6$ km$^3$. There is a strong negative correlation (-0.82) between the basal sliding parameter and the ice volume at $1.5\times$ PIC. Because of the strong influence of the basal sliding parameter on the ensemble, and uncertainties as to the basal environment of the Antarctic during the Cenozoic, we repeat the ensemble simulations but with the basal sliding parameter set to zero.

The results of this second ensemble without basal sliding are shown in Figure 5.8. The impact of removing basal sliding is similar to the previous experiments (Figure 5.5), with the average glacial and deglacial thresholds slightly higher at $2.1\times$ PIC and $4.8\times$ PIC, respectively. The mean hysteresis is also slightly larger (1.1 $\pm0.3$ PIC$_{2x}$) in these simulations without basal sliding. The clustering of deglaciation around favourable astronomical configurations is clearly evident. To prevent this was happening it would be necessary to either conduct much longer simulations, or to randomly vary the starting time slightly (it is currently 36.5 Ma) so that the phasing of the astronomical forcings is different between simulations. We suggest this as scope for future work, it would also enable us to explore the astronomical configurations which generate collapses in more detail.

## 5.4   Discussion

The simulations presented in this chapter show that a number of factors affect EAIS hysteresis. All of the simulations display a hysteresis response and the deglacial atmospheric $CO_2$ threshold is always higher than the glacial atmospheric $CO_2$ threshold in our simulations. Height-mass
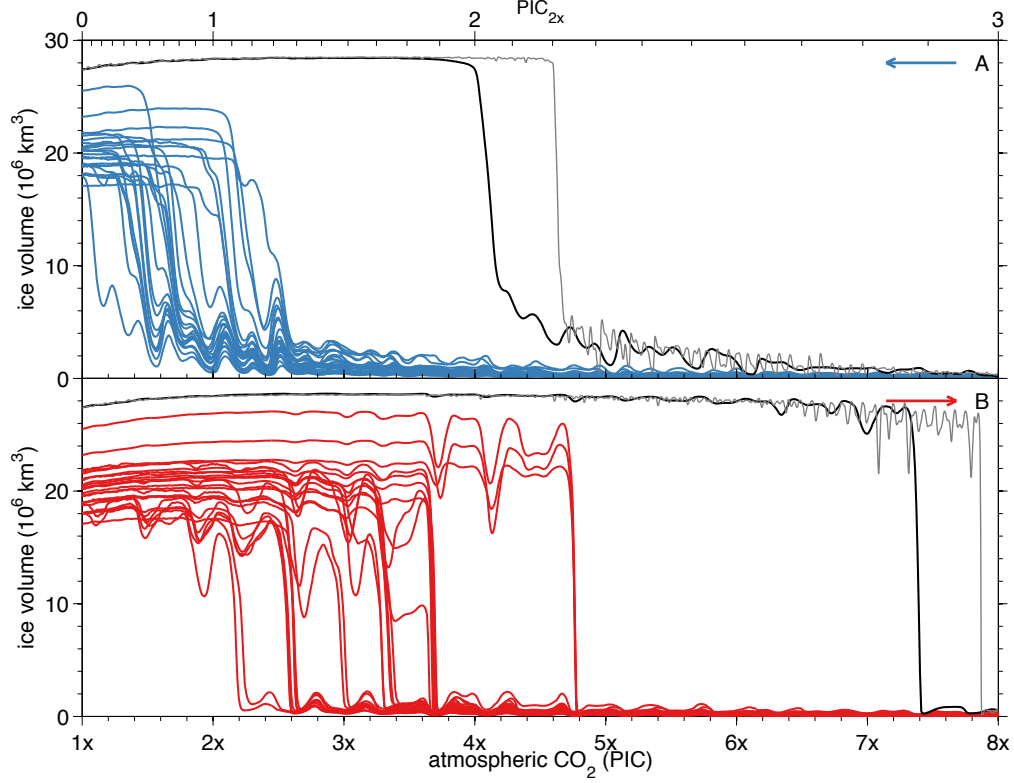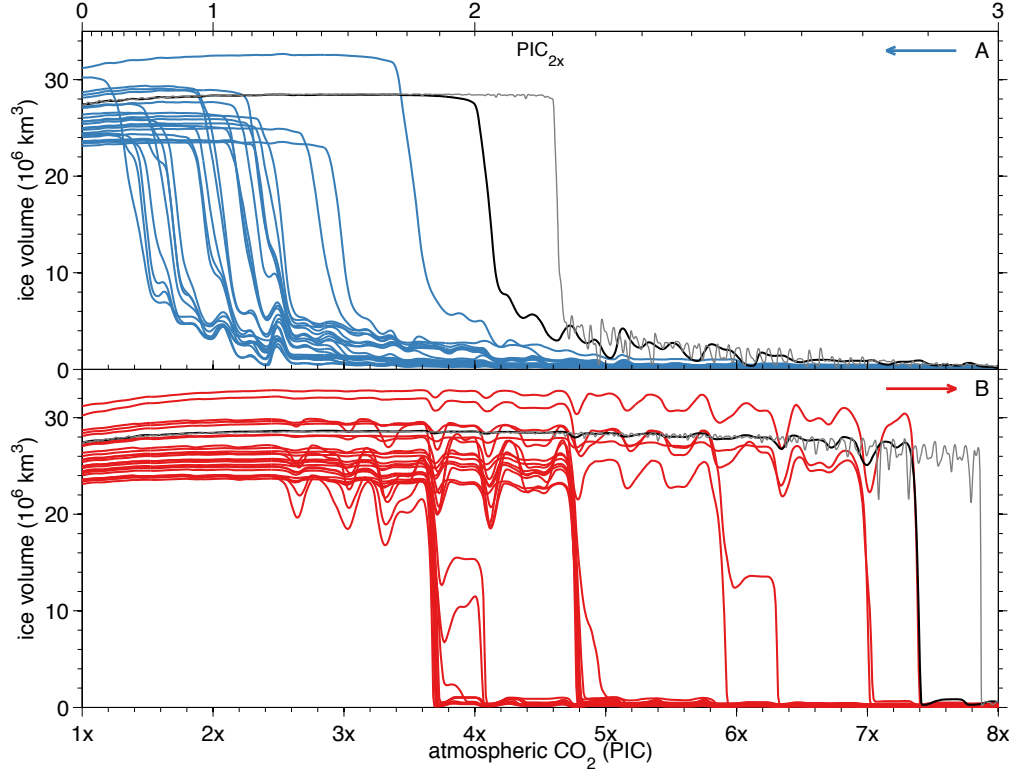
Figure 5.8: *Parameter ensemble, without basal sliding. Transient simulation with ice sheet feedback and astronomical forcing. The default simulation is shown in black, with the non-accelerated default simulation shown in grey (see text). A) decreasing $CO_2$ from ice-free starting conditions B) Increasing $CO_2$ from glaciated starting conditions.*

balance feedback generates a hysteresis of 0.32 $PIC_{2x}$, which is approximately doubled when other ice sheet feedbacks (albedo, atmospheric circulation) are included. The ensemble of simulations suggests that when astronomical forcing and ice sheet feedback are included, the deglacial threshold is 3.3 $\pm 0.7 \times$ PIC if basal sliding is turned on and 4.8 $\pm 1.1 \times$ PIC if basal sliding is turned off. Previous transient ISM simulations have also shown a pronounced Antarctic ice sheet hysteresis of a similar magnitude (Pollard and DeConto, 2005; Langebroek et al., 2009).

Proxy records show astronomically paced fluctuations in ice volume during the Oligocene (Wade and Palike, 2004; Pälike et al., 2006) and Miocene (Pekar and DeConto, 2006; Liebrand et al., 2011). In our simulations during the small ice sheet phase before the main glacial threshold has been crossed, there are significant fluctuations in volume which are paced by astronomical forcing. However, once a large ice sheet has formed the majority of simulations show limited sensitivity to astronomical forcing and the ice sheet is very stable. This suggests that even if

atmospheric $CO_2$ was relatively high in the Oligocene and Miocene, for example at $2\times$ PIC, there would be limited contribution from the Antarctic ice sheet to sea level fluctuations based on our model, even under a favourable astronomical configuration. Significant ice loss in our simulations only occurs at the deglacial threshold.

The inclusion of basal sliding has a large impact on ice sheet hysteresis and the basal sliding parameter appears to be the most significant parameter in our ensemble. High values for the basal sliding parameter lead to a reduced ice sheet thickness and ice volume. In our simulations the transition between a continental sized ice sheet with a high rate of basal sliding (10 mm $yr^{-1}$ $Pa^{-1}$; Marshall, 2002; Gregoire et al., 2012) and an ice sheet with no basal sliding could generate $\sim$25 m of sea level change due to an increase in the ice sheet thickness. There is some evidence for the transition from a mobile wet-based ice sheet to a static cold-based ice sheet in the proxy records during the Miocene (Lewis et al., 2008; Passchier et al., 2011; Hauptvogel and Passchier, 2012). However, it is unclear how representative these records are of the whole EAIS, or that these basal sliding rates are plausible.

Given the strong hysteresis in our simulations and the relatively low concentrations of atmospheric $CO_2$ suggested by proxies for the Oligocene, Miocene and Pliocene (Figure 5.9), there remains the question as to what generated the fluctuations in ice volume and sea level during these periods. It is both the strong hysteresis and the abrupt threshold response in our simulations which is problematic. In our simulations once this threshold is crossed a full ice sheet forms and there is then very little fluctuation in ice volume.

The middle Miocene Climatic Optimum (MMCO; 17-15 Ma) is a warming event which has been linked with retreat of the Antarctic ice sheet (Flower and Kennett, 1994). A recent study (Foster et al., 2012) suggested that atmospheric $CO_2$ peaked at 1.4 $\pm0.3\times$ PIC during this event. This is comparable to other proxy records which suggest atmospheric $CO_2$ was $\sim$1.8$\times$ PIC during the MCO (Kürschner, 2008). This is below the East Antarctic deglacial threshold of any of our simulations. Another interesting feature of the study of Foster et al. (2012) was that the proxy estimates of atmospheric $CO_2$ coupled with a record of ice volume change showed very limited hysteresis during the warming and cooling stages of the MMCO. This led the authors to suggest that, if the strong hysteresis of previous Antarctic ISM studies was correct, the change in ice volume across the MMCO could be caused by Northern Hemisphere glaciation.

In contrast to the EAIS, the WAIS and the Northern Hemisphere ice sheets are characterised by low hysteresis (Rohling et al., 2009; Pollard and DeConto, 2009). The HMB feedback for
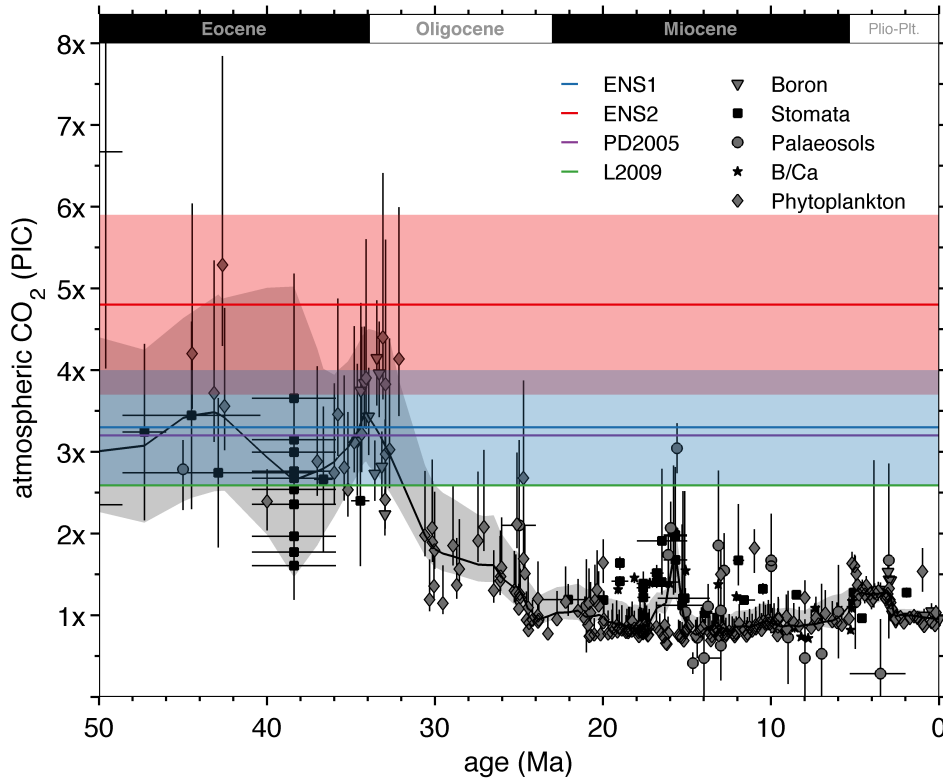
Figure 5.9: *Atmospheric CO$_2$ data compilation reproduced from Beerling and Royer (2011) with deglacial thresholds from ensemble simulations in this chapter. ENS1 - ensemble including basal sliding, ENS2 - ensemble without basal sliding, PD2005 is deglacial threshold from Pollard and DeConto (2005) and L2009 is the deglacial threshold from Langebroek et al. (2009) for their experiments including astronomical forcing.*

the EAIS is enhanced by the constraints of the continent, which generate the steep flanks at the ice sheet edge. For the Northern Hemisphere ice sheets (excluding the Greenland ice sheet) the southern extent is constrained by climate (Oerlemans, 1981) and for the WAIS instability is generated by sub-ice shelf melting (Pollard and DeConto, 2009). Indeed, our Northern Hemisphere simulations presented in Chapter 3 showed limited hysteresis. Although the onset of Northern Hemisphere glaciation is generally thought to have occurred in the Plio-Pleistocene there is limited direct evidence for partial glaciation earlier than the Plio-Pleistocene (Winkler et al., 2002; Moran et al., 2006; Eldrett et al., 2007). Additionally, the relatively low atmospheric CO$_2$ threshold ($\sim$1$\times$ PIC) for Northern Hemisphere glaciation suggested by modelling (DeConto et al., 2008), may have been crossed prior to the MMCO (Foster et al., 2012; Kürschner, 2008). Given the strong hysteresis in our results, it is possible therefore that

Northern Hemisphere glaciation, in addition to changes in the WAIS and thickening of the EAIS due to changes in basal sliding could have produced the sea level fluctuations in the period after the EOT.

## 5.5  Summary

Despite performing a wide variety of hysteresis experiments and a parametric ensemble It is difficult to reconcile the results of our GCM-ISM simulations of the EAIS with ice volume and sea level fluctuation in the Oligocene, Miocene and Pliocene and the low atmospheric $CO_2$ suggested by proxy records. There are various explanations as to why this is the case, which we summarise as:

- There was greater polar amplification than suggested by the GCM, which would result in a reduction in the deglacial atmospheric $CO_2$ threshold (Langebroek et al., 2009). This would also lower the glacial $CO_2$ threshold, which would perhaps help explain why there was not a continental scale glaciation earlier than the EOT, despite atmospheric $CO_2$ being close to the glacial threshold (see Chapter 4).

- The positive degree-day method that we have used for our surface mass-balance scheme, underestimates surface ablation due to insolation changes from astronomical forcing (van de Berg et al., 2011).

- Current proxy records underestimate atmospheric $CO_2$ concentrations during the Oligocene, Miocene and Pliocene (Foster et al., 2012)

- There was partial glaciation of the Northern Hemisphere earlier than the Plio-Pleistocene, which coupled with glaciation / deglaciation of the WAIS generated sea level fluctuations after the EOT.

- Changes in EAIS basal sliding led to changes in the volume of the EAIS even if there was not significant retreat of the ice sheet.

- The EAIS was subject to marine instability, in particular around the Wilkes and Aurora subglacial basins (Williams et al., 2010; Pierce et al., 2011), which we cannot simulate with the ISM used here.

- Proxies of sea level change are recording non glacio-eustatic sea level change and fluctuations in the $\delta^{18}$O records are caused by changes in deep-sea temperature.

It is clearly possible that some combination of these explanations is required to reconcile the GCM-ISM simulations with the proxy records. We have performed a parametric ensemble which has shown that the ice sheet hysteresis is sensitive to certain parameters. This was possible because of the computationally efficient method we developed for forcing the ISM in Chapter 3.

## Chapter 6

# The past relationship between temperature, atmospheric $CO_2$ and sea level – from modelling

## 6.1 Introduction

There has been a growing interest in what the paleo-record can tell us about the past relationship between recorders of climate (e.g. deep-sea temperature and atmospheric $CO_2$) and sea level (Archer, 2007; Rohling et al., 2009; Siddall et al., 2010a; Gasson et al., 2012; Foster and Rohling, 2013). In particular these studies have focused on what, if any, significance this has for projected future warming over long (>100 years) timescales (Archer, 2007; Rohling et al., 2009; Foster and Rohling, 2013). In this chapter we compare the results from our GCM-ISM simulations with the temperature / sea level data synthesis from Chapter 2. In addition we compare the results of our simulations with the recent atmospheric $CO_2$ / sea level data synthesis of Foster and Rohling (2013). Broadly, the largest contributor to sea level change in past warmer worlds has been from changes in the volume of the East Antarctic ice sheet. In contrast, the main contributor to sea level change in past cooler worlds has been from changes in the volume of the Northern Hemisphere ice sheets (de Boer et al., 2010). We shall therefore include the results from our previous simulations of the Northern Hemisphere ice sheets during the last glacial cycle to address sea level change for temperatures cooler than present, and our simulations of the EAIS across the EOT to address sea level change for temperatures warmer than present.

### 6.1.1 Temperature records

As discussed in Chapter 1, there are currently no globally representative proxy temperature records available covering the past 50 Ma. For example across the EOT, the temperature proxies that are available include deep-sea temperature (DST) records (Lear et al., 2000; Billups and Schrag, 2003) and sea-surface temperature records from the high latitudes (Lear et al., 2008) and low latitudes (Liu et al., 2009). In addition there are various terrestrial records available (Zanazzi et al., 2007). Because we are interested in long duration temperature change, we focused on the DST records in Chapter 1, due to the large volume and slow mixing of the deep ocean, which helps to remove regional and seasonal variations (Lear et al., 2000). However, there is uncertainty as to how representative changes in DST are of changes in global mean surface air temperature (MAT; see Chapter 1 for discussion). There are various scalings between DST and surface temperatures in the literature. For example de Boer et al. (2010) used a scaling from Northern Hemisphere surface temperature to DST of 0.20. This would suggest that temperature change would be greater at the surface than the deep sea. However, if the DST record is more representative of regions of deep-water formation, which are predominantly in the high latitudes

(Zachos et al., 2001a), it might be expected that DST change could be greater than global MAT changes due to polar amplification (Siddall et al., 2010a). In addition to this uncertainty about scaling linearly between DST and global MAT, there are other events throughout the Cenozoic, such as the opening of the Drake Passage, which could have generated a nonlinear response between global MAT and DST. For example some modelling studies suggest that the opening of the Drake Passage could have generated cooling of the deep sea and the Southern Hemisphere surface high latitudes but a warming of the surface Northern Hemisphere and low latitudes (Nong et al., 2000; Najjar, 2002). We therefore urge caution in directly comparing the DST records with surface temperature changes, although the DST record is the most globally representative record available to us.

We use the temperature output from the GCM to present our simulations as global MAT and surface temperatures at high- and low-latitudes, for comparison with the proxy records. The temperatures from the GCM simulations are presented as anomalies relative to a modern control simulation. Because we have used the GENESIS GCM with a slab ocean for the EOT simulations, we do not have DSTs from these simulations. We therefore cannot directly compare the temperature output from the GCM with the DST records. Because DSTs are arguably the most globally representative temperature record available to us (Lear et al., 2000), albeit with the caveats discussed above, we indirectly compare the DST records with the global MAT anomaly from our simulations.

In addition to the DST data, we used surface temperature data from the high latitude Southern Hemisphere and the low latitudes to create temperature-sea level cross-plots in Chapter 2. The Southern Hemisphere high latitude temperature data was composed of the sea surface temperature (SST) data of Liu et al. (2009) for the EOT and the surface air temperature (SAT) data used by Rohling et al. (2009) for the last 500 ka. The Liu et al. (2009) SST data came from ODP (Ocean Drilling Programme) sites 277 (palaeo-latitude: 59.0°S), 511 (52.5°S) and 1090 (47.5°S). The SAT data used by Rohling et al. (2009) in their temperature / sea level synthesis came from the Dome C core site in East Antarctica (75.1°S; Augustin et al., 2004). To compare our GCM simulations directly with these data, we average the SST output from the GCM simulations for 59°S (the average latitude of the 4 core sites), and calculate temperature anomalies using a control simulation. For the simulations from the last glacial cycle we calculate a SAT anomaly for the Dome C core site in East Antarctica.

For the low-latitude temperature / sea level synthesis, we used the SST data of Lear et al.

(2008) and Herbert et al. (2010). The EOT SST data of Lear et al. (2008) came from the Tanzania Drilling Project (9.2°S; Nicholas et al., 2006). The low-latitude SST data of Herbert et al. (2010), came from ODP sites 662 (1.2°S), 722 (16.4°N), 806 (0.2°N), 846 (3.6°S) and 1146 (19.3°N). We calculate low latitude temperature anomalies from the GCM simulations by averaging the SST output at 4°N (the average latitude of the 6 core sites). This enables us to compare the GCM simulations directly with the low-latitude temperature records.

## 6.2 Temperature / sea level relationship

We convert ice volumes from the GCM-ISM simulations to sea level by first accounting for the change in volume from change of state from ice (918 kg m$^{-3}$) to seawater (1028 kg m$^{-3}$) (Bamber et al., 2009), and then dividing by the ocean surface area. The ocean surface area for the EOT (372.9 $\times 10^6$ km$^2$) is based on an ocean fraction of 0.731, consistent with the palaeo-geography used in the GCM (DeConto et al., 2008). Sea levels are presented as an anomaly relative to present assuming ice-free sea level is 64 m above present (Lemke et al., 2007). For the Northern Hemisphere simulations, we assume any ice growth greater than the volume of the present day Greenland ice sheet (2.85 $\times 10^6$ km$^3$; Lemke et al., 2007) results in a sea level fall, with ice volume converted to sea level based on the modern ocean area (361.1 $\times 10^6$ km$^2$).

In Figure 6.1 the GCM-ISM simulations for the Northern Hemisphere ice sheets and EAIS are plotted as temperature / sea level cross-plots. In all of the following figures for temperatures cooler than present, sea level change is due to changes in the volume of the Northern Hemisphere ice sheets from simulations of the last glacial cycle. These simulations are the 128 member BBC_ALL ensemble from Chapter 3. The Northern Hemisphere ISM simulations use the climate from the BBC_ALL suite of HadCM3 GCM simulations, which includes evolving ice sheet boundary conditions based on ICE-5G (Singarayer and Valdes, 2010). Therefore we expect better agreement between the Northern Hemisphere simulations and the data than the EAIS simulations, which have freely evolving ice sheet boundary conditions based on the GCM matrix method. For temperatures warmer than present, sea level change is due to changes in the EAIS under Eocene/Oligocene boundary conditions. These simulations are the 25 member ensemble from Chapter 5. The EAIS simulations use the climate from the GENESIS GCM, and include astronomical forcing and albedo feedback but have no basal sliding. The EAIS simulations shown are all for a reduction in atmospheric $CO_2$ for consistency with the predominant cooling of the Cenozoic data. Simulations for an increase in atmospheric $CO_2$ are shown later to
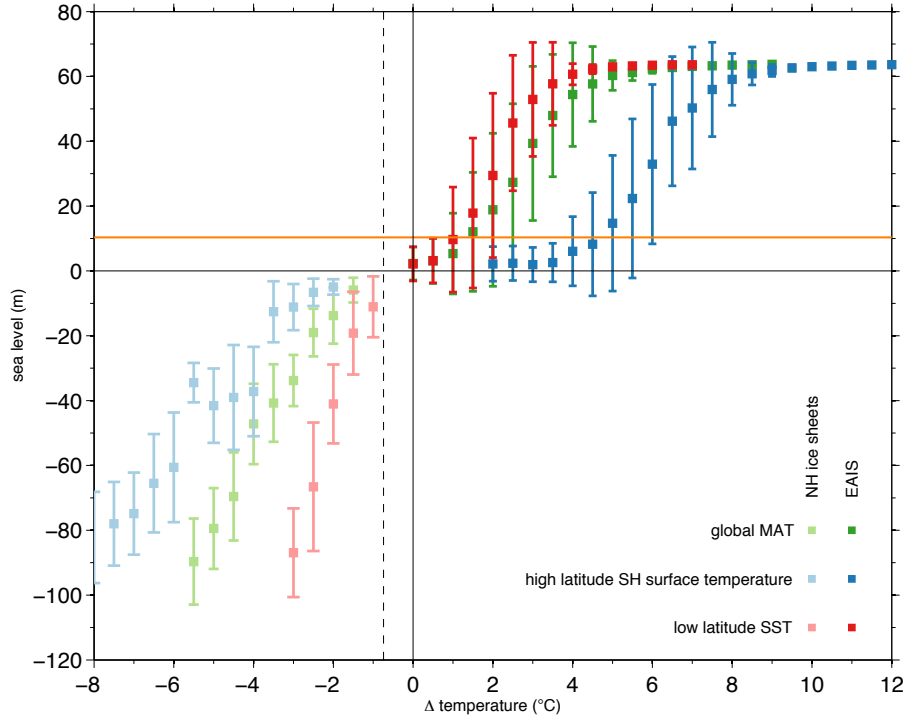
Figure 6.1: *Temperature / sea level relationship from GCM-ISM simulations. For temperatures warmer than present, the EOT simulations of the EAIS are shown, for temperatures cooler than present, the last glacial cycle simulations of the Northern Hemisphere ice sheets are shown. The Greenland ice sheet is not represented for temperatures warmer than present and the West Antarctic ice sheet is not represented at all due to the limitations of the ISM. The total sea level equivalence of the Greenland and West Antarctic ice sheets is shown as a horizontal orange line. Temperatures are shown as global mean SATs, low latitude SSTs and high latitude Southern Hemisphere surface temperatures, too enable comparison with the temperature / sea level synthesis from Chapter 3. For clarity the GCM-ISM sea level output are binned at regular 0.5 °C intervals, with error bars of 1 standard deviations of the temperatures ±0.25 °C of each bin, the raw data are included in Appendix F. Temperature anomalies are relative to modern, the vertical dashed line is pre-industrial global mean SAT.*

investigate potential hysteresis. The horizontal orange line on Figure 6.2-6.7 is sea level rise resulting from the loss of the Greenland ice sheet and the WAIS, which we do not simulate due to limitations of the ISM.

Polar amplification is clearly evident in Figure 6.1 from the difference between the low latitude and high latitude temperature plots. At equivalent sea levels, the high latitude Southern Hemisphere temperatures are typically double the global MATs. The low latitude temperatures show the smallest temperature anomalies, consistent with the data synthesis of Chapter 2. The relationship between temperature and sea level in our GCM-ISM simulations is nonlinear, with the steps caused by the formation of a continental sized EAIS, with the ice sheet then bound by the limits of the continent, prior to glaciation in the Northern Hemisphere with further cooling. This is similar to the result of de Boer et al. (2010) using a very different method. Although the transition from unglaciated conditions to a glaciated EAIS appears smooth in these plots, this is partially due to the ensemble of simulations used. Each individual simulation has an abrupt transition across the glacial threshold (see Chapter 5 and Appendix F).

The temperature / sea level output from the GCM-ISM simulations is next compared with the temperature / sea level data which we synthesised in Chapter 2. Firstly in Figure 6.2.A, DST data (Lear et al., 2000; Siddall et al., 2010a) is plotted against sea level data (Kominz et al., 2008; Siddall et al., 2010a). As mentioned previously, we do not have DST output from the GCM-ISM simulations for the EAIS. We therefore cannot directly compare the GCM-ISM simulations with the DST data. As DSTs have been regarded as representative of global change (Lear et al., 2000), we have plotted these in a separate subplot in Figure 6.2 and compare the forms of the relationship, rather than absolute temperatures.

There are some similarities between the GCM-ISM output and the DST/sea level data. There is a step in the GCM-ISM output at the onset of EAIS glaciation at a global MAT of $\sim 2-5$ °C. This is also seen in the the DST/sea level data as the step in sea level at a DST of $\sim 6$ °C, caused by the onset of EAIS glaciation at the EOT. We speculated that the first step in the DST/sea level synthesis at $\sim 8$ °C could be due to the growth of small ice sheets in the Antarctic mountain regions during the Eocene (Miller et al., 2005a, 2008a). The alternative explanation was that this could be due to changes in the volumes of the ocean basins (Müller et al., 2008; Cramer et al., 2011). This multiple stepped glaciation is not seen in our GCM-ISM simulations, with the onset of EAIS glaciation occurring in one step as the glacial threshold is crossed.
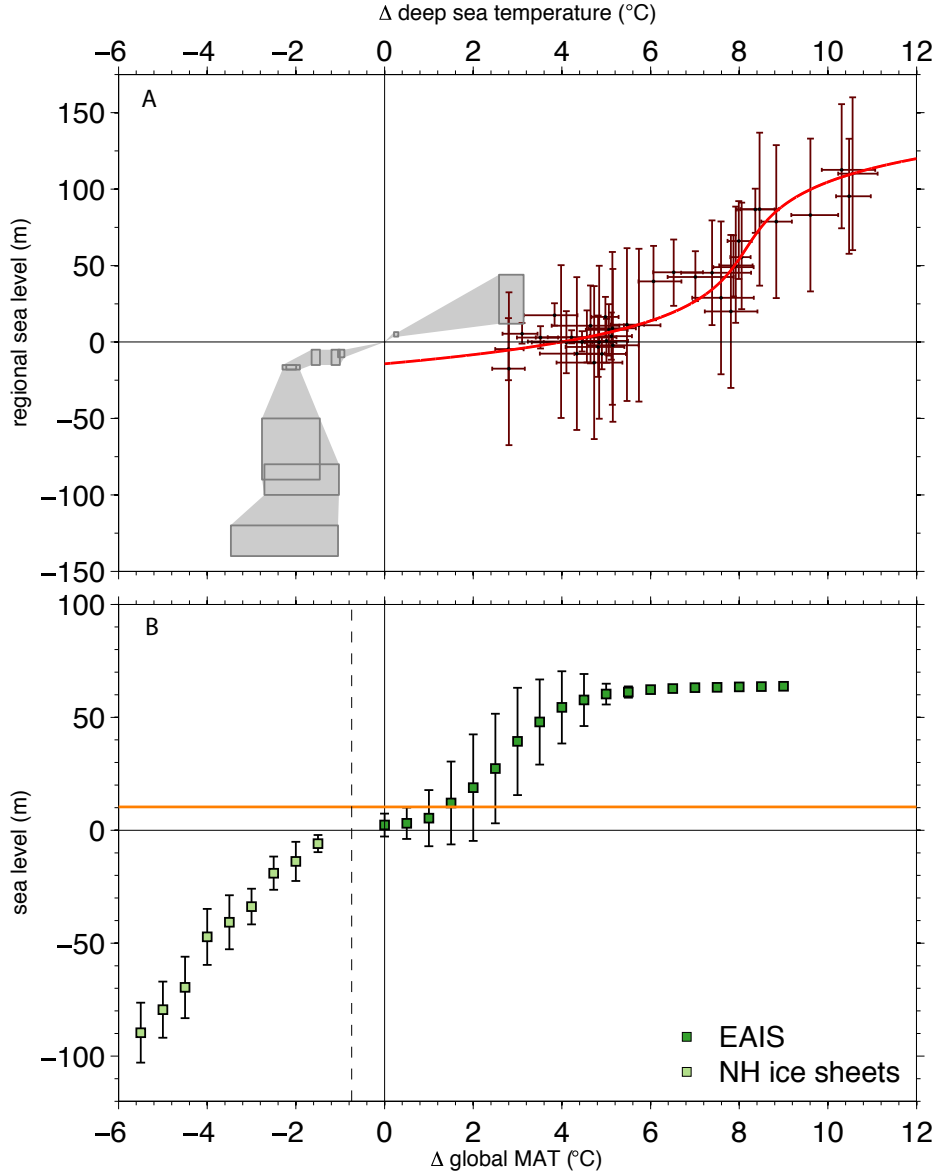
Figure 6.2: *Global mean SAT / DST versus sea level from proxy records and GCM-ISM modelling. A)*
*The DST and sea level data are as Figure 2.1. The grey data are Plio-Pleistocene data from Siddall*
*et al. (2010a), the dark red data are from 50-10 Ma using the sea level data of Kominz et al. (2008) and*
*DST data of Lear et al. (2000). B) GCM-ISM simulations are shown for global MAT. The simulations*
*are from the BBC_ALL ensemble of Northern Hemisphere ice sheets for temperatures cooler than present*
*and an ensemble of EAIS simulations for temperatures warmer than present. The GCM-ISM output is*
*binned at regular $0.5 \pm 0.25°C$ intervals, the error bars are 1 standard deviation. The Greenland ice sheet*
*is not represented for temperatures warmer than present and the WAIS is not represented at all, the total*
*sea level rise from the loss of these ice sheets is shown as a horizontal orange line. The vertical dashed*
*line is pre-industrial global MAT*

It is important to reiterate the uncertainties in the Mg/Ca DST temperature, especially the absolute temperature values, which may be affected by a lack of constraint on the past seawater composition of Mg/Ca (see Chapter 1 for discussion; Billups and Schrag, 2003; Lear, 2007; Evans and Müller, 2012). However there is broad agreement between the DST anomaly and the global MAT anomaly from the GCM-ISM simulations. For temperatures cooler than present, the GCM-ISM simulations broadly correlate with the DST and sea level data. The lowstand in the data, which is at the last glacial maximum (LGM), is at a slightly lower sea level than for our GCM-ISM simulations. These simulations do not include the growth of the Antarctic ice sheets for temperatures cooler than present, which explains part of this discrepancy. The advance of the Antarctic ice sheets at the LGM is thought to have contributed $\sim 8 - 14$ m to the sea level lowstand (Denton and Hughes, 2002; Pollard and DeConto, 2009; Mackintosh et al., 2011; de Boer et al., 2012b).

The DST data show a nonlinear response as DSTs approach the freezing point for seawater (Siddall et al., 2010a). This is clearly not evident in the global MAT output from the GCM-ISM. As the GCM-ISM output is for the global MAT, it is affected by changes in surface elevation as the ice sheets grow vertically, due to the atmospheric lapse rate. As the lapse rate is applied linearly in our simulations, it might be expected that there would be a linear response between global MAT and sea level. This effect will be most evident in the Northern Hemisphere simulations, due to the greater surface area of the North American and Eurasian ice sheets compared with the EAIS. Indeed, for the Northern Hemisphere, the response between global MAT and sea level is close to linear, in contrast to the relationship between DST and sea level.

In Figure 6.3 the GCM-ISM simulations are plotted against the high latitude Southern Hemisphere surface temperature data. In the SST data of Liu et al. (2009), the EOT and associated sea level fall occurs at temperatures $\sim 10 - 16$ °C warmer than present. In the GCM-ISM simulations the sea level fall due to the growth of a large EAIS occurs at high latitude Southern Hemisphere SSTs $\sim 5 - 8$ °C warmer than present. The cooling and sea level fall for temperatures cooler than present is similar in the GCM-ISM modelling and the data used by Rohling et al. (2009). The data suggests a slightly greater polar amplification than is shown in our GCM-ISM simulations because the range of temperature change in the data is greater than for our simulations. However, the broad form of the relationship is similar for both the data and the GCM-ISM simulations. The reduced polar amplification in our simulations under Eocene / Oligocene boundary conditions compared with the data is a known problem which also evident in other GCMs (Huber and Caballero, 2011; Lunt et al., 2012).
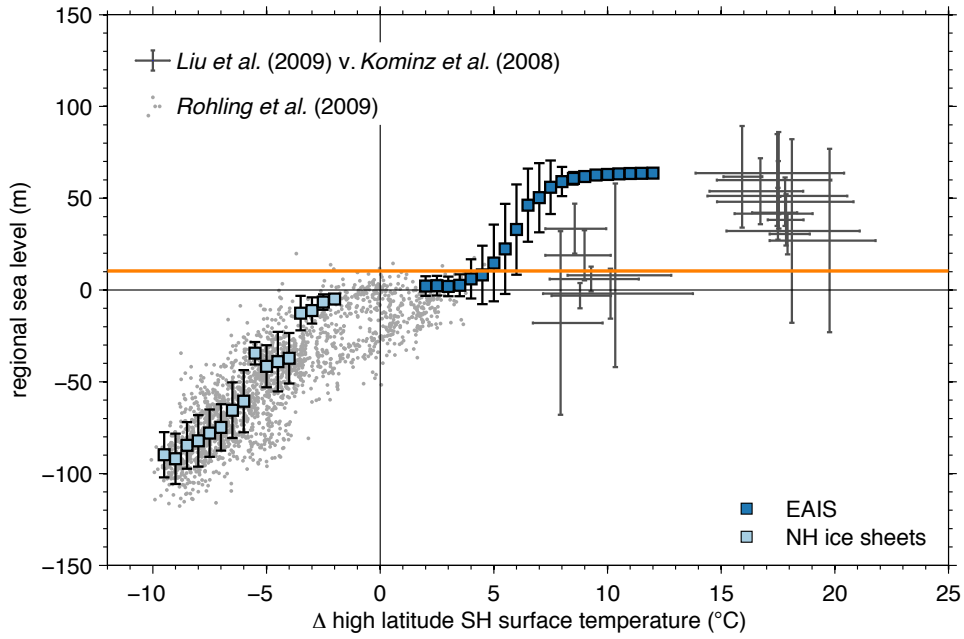
Figure 6.3: *High latitude Southern Hemisphere surface temperature versus sea level from proxy records and GCM-ISM modelling. The surface temperature and sea level data shown in grey is as Figure 2.2 (see text). The GCM-ISM simulations are shown as high latitude Southern Hemisphere SST for temperatures warmer than present, and as SAT at the core site location of Dome C, to enable comparison with the data. The GCM-ISM output is binned at regular 0.5 ±0.25 °C intervals, the error bars are 1 standard deviation. The Greenland ice sheet is not represented for temperatures warmer than present and the WAIS is not represented at all, the total sea level rise from the loss of these ice sheets is shown as a horizontal orange line.*

Finally, in Figure 6.4 we plot the GCM-ISM simulations against the low latitude SST data. Because of the reduced magnitude of the temperature response at low latitudes, and the significant errors and scatter in the data, it is difficult to determine a form to the low latitude SST to sea level relationship (if there is any). The GCM-ISM simulations show some agreement with the low latitude temperature data, however, it is difficult to determine any form to this relationship due to the limited temperature change at the low latitudes. In our simulations, ice-free conditions occur at low-latitude temperatures ~4 °C warmer than present, which is comparable to the temperature data. There is good agreement between the GCM-ISM simulations and the data for temperatures cooler than present.

One thing which is evident from the temperature / sea level plots, and is especially evident in the raw output (see Appendix F), is that multiple sea level stands can exist for a given
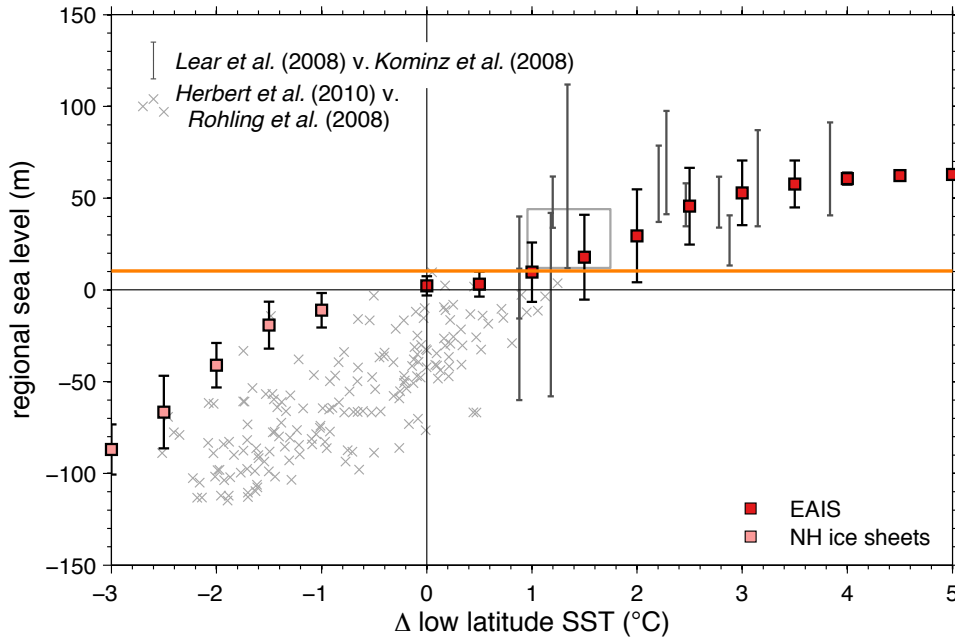
Figure 6.4: *Low latitude SSTs versus sea level from proxy records and GCM-ISM modelling. The SST and sea level data shown in grey is as Figure 2.3 (see text). The GCM-ISM simulations are shown for low latitude SST, the GCM-ISM output is binned at regular 0.5 ±0.25 °C intervals, the error bars are 1 standard deviation. The Greenland ice sheet is not represented for temperatures warmer than present and the WAIS is not represented at all, the total sea level rise from the loss of these ice sheets is shown as a horizontal orange line.*

temperature. Part of this is due to scatter due to data uncertainties and model parameter uncertainty. However, some of this response may be a result of changes in the distribution of incoming solar radiation due to changes in the astronomical forcing. This means that for a given global MAT, multiple sea level stands could have existed in the past. This clearly limits the usefulness of determining the future sea level response to a temperature forcing on centennial timescales based on the past temperature / sea level relationship on astronomical timescales.

## 6.3 Atmospheric $CO_2$ / sea level relationship

Foster and Rohling (2013) recently published an atmospheric $CO_2$ / sea level synthesis covering various time intervals over the last 40 Ma using some of the data compiled for this thesis, we reproduce this in Figure 6.5. The use of atmospheric $CO_2$ to address the long term relationship between climate and sea level has a number of advantages over using temperature proxies. As
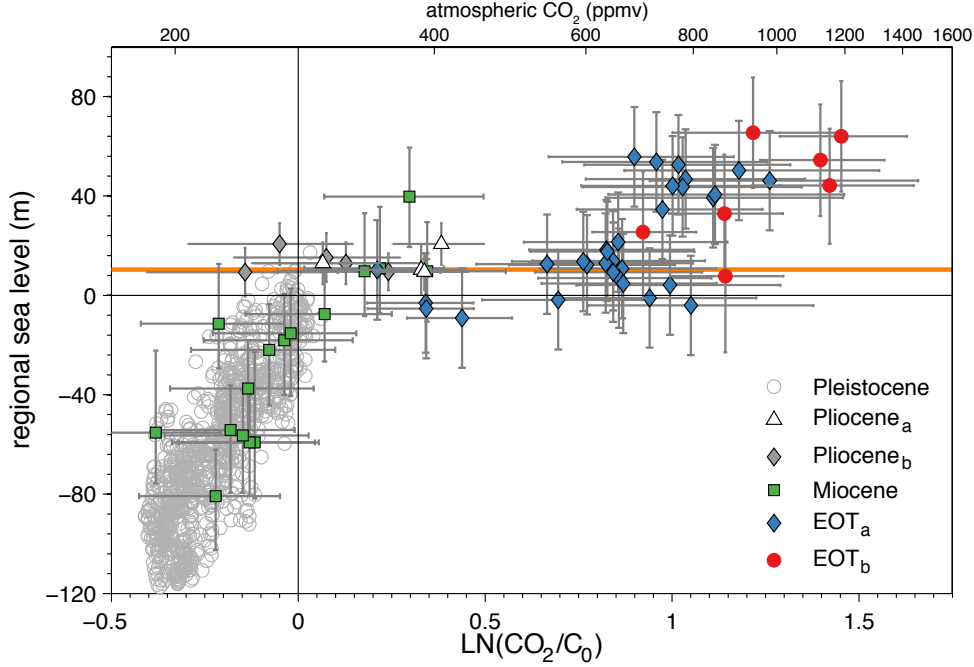
Figure 6.5: *Proxy records of atmospheric $CO_2$ against sea level, reproduced from Foster and Rohling (2013). Pleistocene data are the Red Sea sea level record of Siddall et al. (2003) and Rohling et al. (2009), plotted against $CO_2$ data from Antarctic ice cores (Petit et al., 1999; Monnin et al., 2001; Siegenthaler et al., 2005; Lüthi et al., 2008). Pliocene data are the sea level compilation of Miller et al. (2012) with boron based atmospheric $CO_2$ data for Pliocene$_a$ from Seki et al. (2010) and for Pliocene$_b$ from Bartoli et al. (2011). Miocene data are sea level from benthic foraminiferal $\delta^{18}O$ (Lear et al., 2010; Foster and Rohling, 2013) and boron isotope based $CO_2$ data from Foster et al. (2012). $EOT_a$ are sequence stratigraphy sea level data from Cramer et al. (2011) and alkenone $\delta^{13}C$ based $CO_2$ data of Pagani et al. (2011). $EOT_b$ are sea level from planktic foraminiferal $\delta^{18}O$ and boron isotope based $CO_2$ (Pearson et al., 2009). See Foster and Rohling (2013) for a full description of the data. The x-axis scale is as Foster and Rohling (2013) to take into account the logarithmic forcing of climate by atmospheric $CO_2$, $C_0$ is pre-industrial $CO_2$ (278 ppmv). The horizontal orange line is the sea level equivalence of the Greenland ice sheet and the WAIS.*

we have previously discussed, there are difficulties in interpreting surface temperature changes from DST records. Additionally, there is uncertainty as to whether isolated surface temperature records are indicative of regional change, rather than global change. Although there are significant uncertainties associated with atmospheric $CO_2$ proxies (Beerling and Royer, 2011), it is arguably a more reliable recorder of global climate changes than the presently available temperature proxies (Foster and Rohling, 2013).

Similar to the temperature / sea level synthesis from Chapter 2, Foster and Rohling (2013) noted a sigmoidal relationship between atmospheric $CO_2$ and sea level, with relatively stable sea level between $-10$ and $+20$ m above present, when atmospheric $CO_2$ was between $\sim 400$ and $\sim 650$ ppmv. Of particular interest in Figure 6.5 is the low atmospheric $CO_2$ and sea level for periods during the Miocene, which may be indicative of Northern Hemisphere glaciation (Foster et al., 2012; Foster and Rohling, 2013). However there is presently limited independent sea level data for the Miocene which could test this hypothesis; the sea level record of Kominz et al. (2008) has limited data coverage during the Miocene (John et al., 2011).

Consistent with our temperature / sea level synthesis, the majority of the data on Figure 6.5 is for a broad reduction in atmospheric $CO_2$ and associated cooling throughout the Cenozoic, with shorter intervals of increasing atmospheric $CO_2$. It is possible that the atmospheric $CO_2$ and sea level relationship would be different for a broad increase in atmospheric $CO_2$, due to hysteresis. However, the records which do cover a period of both increasing and decreasing atmospheric $CO_2$, namely the Pleistocene and the Miocene, show limited hysteresis. As discussed in the previous chapter, this could be a result of Northern Hemisphere glaciation, which is characterised by low hysteresis (Foster et al., 2012). Foster and Rohling (2013) suggested that there is possible evidence for hysteresis in their EOT data, evident in a short period of increasing atmospheric $CO_2$ after the main reduction in atmospheric $CO_2$ which led to the onset of Antarctic glaciation.

In Figure 6.6 we have plotted the output from our GCM-ISM simulations against the atmospheric $CO_2$ / sea level synthesis of Foster and Rohling (2013). Consistent with the previous figures, the EAIS simulations are for a reduction in $CO_2$. There is a very good agreement between the data synthesis of Foster and Rohling (2013) and the GCM-ISM simulations. Although the onset of Antarctic glaciation appears to be a smooth transition between $\sim 400 - 800$ ppmv, this is largely a result of parametric uncertainty in the ensemble. The individual ensemble members show a more abrupt onset to Antarctic glaciation (see Appendix F). The relatively
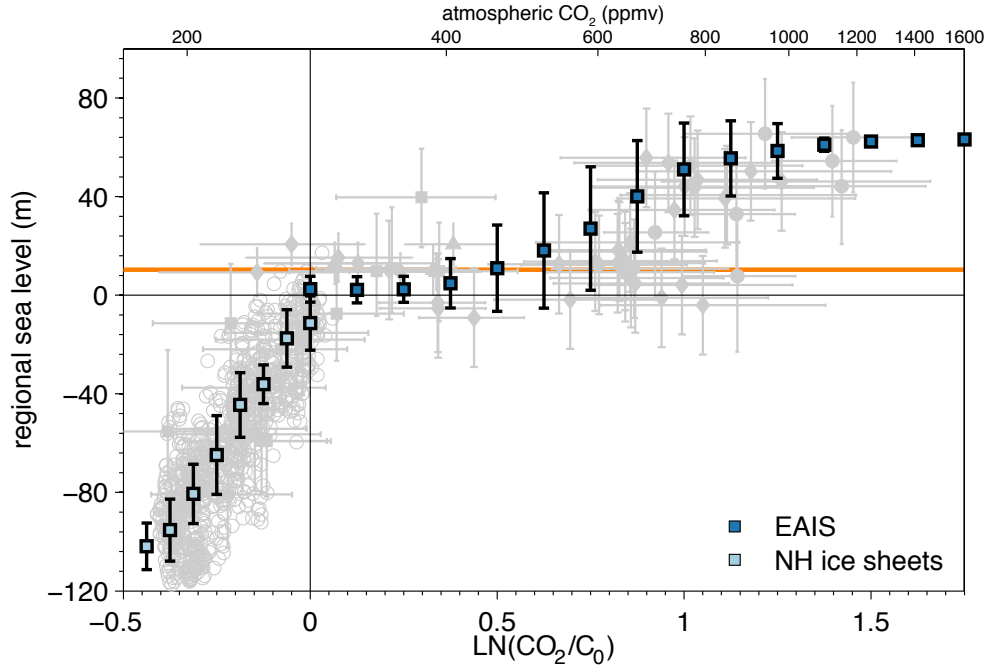
Figure 6.6: *Atmospheric $CO_2$ against sea level from data and GCM-ISM simulations. The data in grey are as Figure 6.5. For atmospheric $CO_2$ higher than pre-industrial the EAIS ensemble simulations under Eocene/Oligocene boundary conditions are shown, for a simulation with decreasing $CO_2$. For atmospheric $CO_2$ lower than pre-industrial, the Northern Hemisphere ensemble simulations for the last glacial cycle are shown. The GCM-ISM output are binned at regular intervals for clarity. The horizontal orange line is the sea level equivalence of the Greenland ice sheet and the WAIS.*

stable period after the EAIS has formed, which is evident in the data, is also clearly shown in our GCM-ISM simulations. There is good agreement between the Northern Hemisphere simulations and the data. Although as previously mentioned, the Northern Hemisphere simulations are partially constrained by the ICE-5G reconstruction.

## 6.4 Hysteresis

The previous figures have shown EAIS simulations for a reduction in atmospheric $CO_2$, consistent with the broad reduction in atmospheric $CO_2$ across the Cenozoic (Pearson and Palmer, 2000; Pearson et al., 2009; Pagani et al., 2011). In Figure 6.7 we include the equivalent simulations for an increase in atmospheric $CO_2$. Again this is based on an ensemble of GCM-ISM simulations. We have also separated the Northern Hemisphere simulations based on whether atmospheric $CO_2$ is increasing or decreasing. There is very little hysteresis evident for the
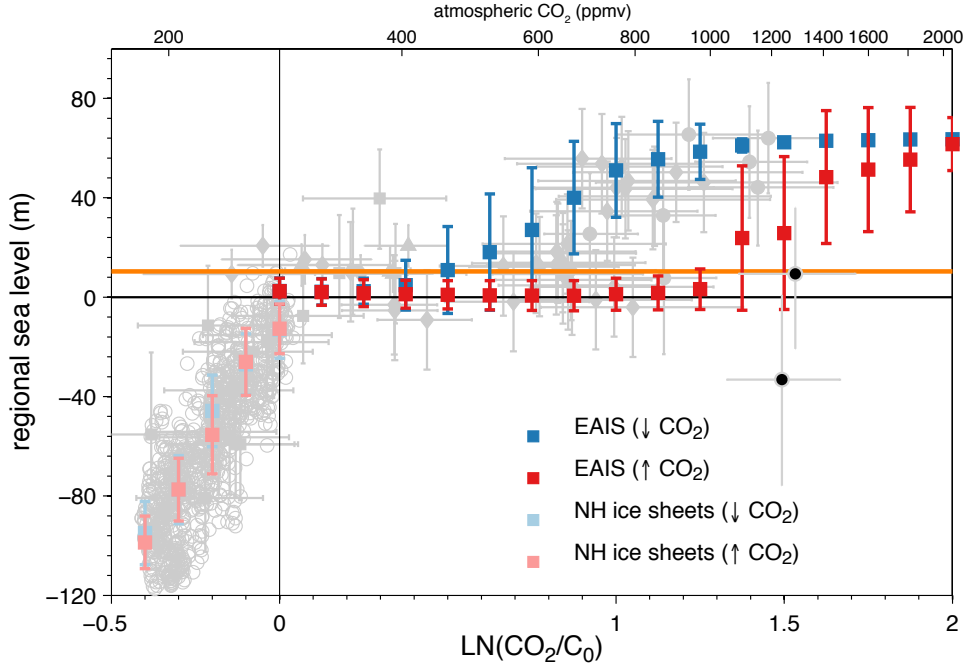
Figure 6.7: *Hysteresis in GCM-ISM simulations shown as atmospheric $CO_2$ against sea level. The EAIS ensemble simulations are shown for both a reduction in atmospheric $CO_2$ (as Figure 6.6) and also an increase in atmospheric $CO_2$. The Northern Hemisphere last glacial cycle simulations are separated depending on whether atmospheric $CO_2$ is increasing or decreasing. The data in grey are as Figure 6.5, with 2 additional data points in black from the EOT for increasing atmospheric $CO_2$ (Foster and Rohling, 2013, supplementary information), showing possible hysteresis in the data.*

Northern Hemisphere simulations in Figure 6.7, however there is a strong hysteresis for the EAIS simulations. The deglaciation of the EAIS in these simulations begins at $\sim$ 1000 ppmv and there is very little variability until this threshold is reached. Foster and Rohling (2013) included 2 additional data points in supplementary information for an increase in atmospheric $CO_2$ just after the EOT, which is potentially in agreement with this threshold, although more data is needed. If the EAIS does indeed exhibit such a strong hysteresis, which is potentially incompatible with various other sources of data (see Chapter 6 for discussion), it limits the usefulness of such syntheses in determining the long-term response of the ice sheets to projected warming in the future.

The hysteresis is also evident in our GCM-ISM simulations in plots of global MAT against sea level (Figure 6.8). A pronounced hysteresis is evident for the Antarctic ice sheet and there is potentially a small hysteresis for the Northern Hemisphere ice sheets during the last glacial cycle. For the EAIS, the glacial threshold is crossed at global MAT $\sim 2 - 5$ °C warmer than

181
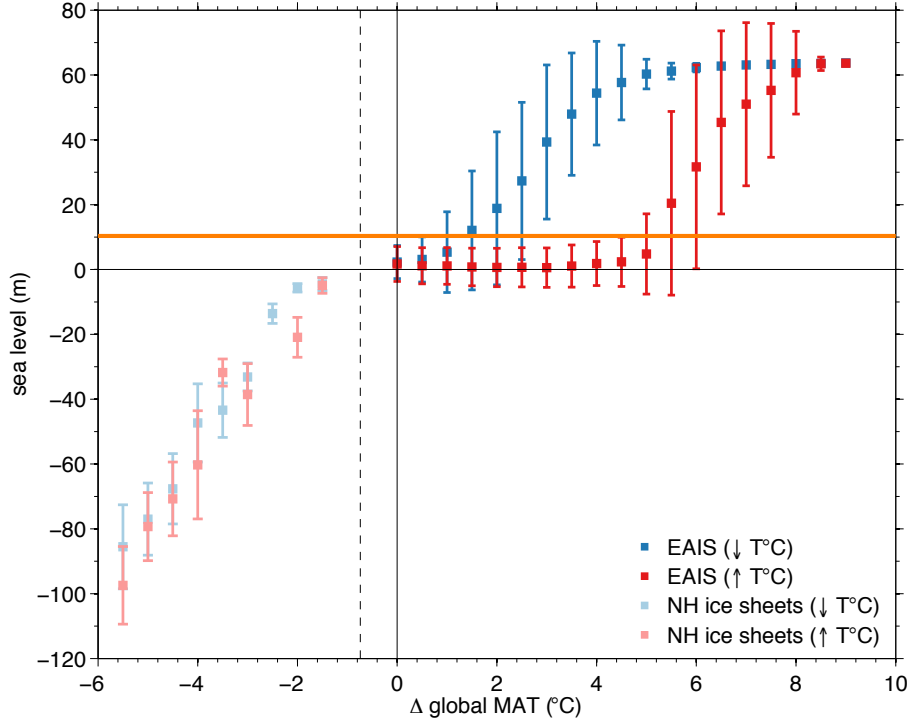
Figure 6.8: *Hysteresis in GCM-ISM simulations shown as global MAT against sea level. The EAIS ensemble simulations are shown for both a reduction in global MAT (as Figure 6.2) and also an increase in global MAT. The Northern Hemisphere last glacial cycle simulations are separated depending on whether global MAT is increasing or decreasing. Temperatures are anomalies relative to modern, the vertical dashed line shows pre-industrial global MAT.*

present, whereas the deglacial threshold is crossed at $\sim 5 - 8$ °C warmer than present. This suggests that for the EAIS, the width of the hysteresis is $\sim 3$ °C, for these simulations including astronomical forcing. Note that our GCM-ISM simulations do not include the Greenland ice sheet or WAIS for temperatures warmer than present, which are the ice sheets that are most vulnerable to future warming (Mercer, 1978; Lemke et al., 2007; Pollard and DeConto, 2009).

## 6.5   Summary

In this chapter we have attempted to bring together all of the results from the previous chapters. The data synthesis from Chapter 2 identified some interesting relationships between temperature and sea level data from the Cenozoic, some of which showed consistencies with existing

modelling studies (Huybrechts, 1993; DeConto and Pollard, 2003a; de Boer et al., 2010). We then developed a GCM-ISM modelling strategy based on that proposed by Pollard (2010), which we tested using simulations of the Northern Hemisphere ice sheets during the last glacial cycle (Singarayer and Valdes, 2010). This was then applied to long duration simulations of the EAIS under Eocene-Oligocene boundary conditions. Some of the results from these chapters are summarised here in the temperature versus sea level and atmospheric $CO_2$ versus sea level plots.

The nonlinear relationship between temperature and sea level which we identified in Chapter 2 is evident in some of the GCM-ISM simulations shown here. There is disagreement between some of our simulations and the data, in particular for high latitude Southern Hemisphere temperatures, which we suggest could be due to a reduced polar amplification in our simulations compared with the data. A nonlinear relationship was identified in a recent atmospheric $CO_2$ and sea level data synthesis (Foster and Rohling, 2013). There is very good agreement between our GCM-ISM simulations and these $CO_2$ and sea level data. The majority of these $CO_2$ data are for a broad reduction in atmospheric concentrations across the Cenozoic. The EAIS simulations we showed in Figure 6.6 were also for decreasing atmospheric $CO_2$. The equivalent EAIS simulations for increasing atmospheric $CO_2$ suggest that the EAIS exhibits a strong hysteresis. This hysteresis is not as evident in simulations of the Northern Hemisphere ice sheets during the last glacial cycle.

The strong EAIS hysteresis is potentially incompatible with sea level and atmospheric $CO_2$ records from the Oligocene, Miocene and Pliocene, unless the onset of Northern Hemisphere glaciation was much earlier than the Plio-Pleistocene. Because of this potentially strong EAIS hysteresis, we question how useful such climate / sea level plots are for predicting the response of the ice sheets to projected warming on centennial timescales (Archer, 2007; Rohling et al., 2009; Foster and Rohling, 2013). This strong hysteresis evident in our GCM-ISM simulations implies that the EAIS has been stable since the continental sized EAIS formed at the EOT. The alternative is that the strong hysteresis in our GCM-ISM simulations is incorrect, in which case the EAIS may have been surprisingly dynamic for modest atmospheric $CO_2$ concentrations, similar concentrations which are projected in the coming century due to anthropogenic emissions.

# Chapter 7

# Conclusions

## 7.1　Main findings

The aim of this thesis was to investigate the past relationship between temperature, atmospheric $CO_2$ and sea level. We approached this by first reviewing the existing long duration records of temperature and sea level, covering periods when sea level was lower than present, and also much further back in time to predominantly ice-free periods when sea level was higher than present. This analysis motivated new simulations of the large ice sheets (the Eurasian, North American and East Antarctic ice sheets) over key intervals. The previous chapter covered the main conclusions of this thesis and was intended to draw the thesis together. Here the main findings from each chapter are summarised, followed by suggested directions for future work:

### Chapter 1 - main findings

In this chapter the existing long duration records of sea level, deep-sea temperature and surface temperature for the Cenozoic were reviewed. We focused on the main sources of uncertainty in these records. For the DST records based on the Mg/Ca ratio of benthic foraminifera, a large source of potential error is uncertainties in the past Mg/Ca ratio of seawater, especially for records >1 Ma in duration (Lear et al., 2000; Billups and Schrag, 2003). This problem is complicated by uncertainties in the nature of the relationship between the Mg/Ca ratio of foraminiferal calcite and the Mg/Ca ratio of seawater (Evans and Müller, 2012). Additionally, changes in the calcite saturation state of the ocean could have affected the Mg/Ca palaeo-thermometer (Martin et al., 2002). For example, across the EOT changes in the calcite compensation depth could have masked deep-sea cooling in some records (Lear et al., 2004). The $TEX_{86}$ and $U^{k'}_{37}$ proxies for SST were also discussed.

Continuous records of past sea level on long timescales ($10^7$ years) are currently limited to records from sequence stratigraphy. We reviewed the record from the New Jersey margin, one of the most continuous records presently available (Miller et al., 2005a; Kominz et al., 2008). There are key uncertainties with such sea level records which complicates their use as a past record of glacioeustasy, for example: a lack of data during lowstands, potential instabilities of continental margins which could be misinterpreted as being a glacioeustatic signal (Müller et al., 2008; Petersen et al., 2010) and additional signals from changes in the ocean basin volume.

We then discussed the deep-sea oxygen isotope record, which is a mixed climate recorder of DST and terrestrial ice volume (Zachos et al., 2001a, 2008), and methods which attempt to

separate these two signals using ice sheet modelling (de Boer et al., 2010). Finally, we discussed asynchronously coupled climate-ice sheet modelling of the East Antarctic ice sheet (DeConto and Pollard, 2003a).

## Chapter 2 - main findings

Using the data we discussed in the previous chapter, we investigated possible forms for the relationship between temperature (both DST and SST) and sea level in the Cenozoic. This was approached by testing possible forms from previous publications which suggest various linear or nonlinear forms for this relationship (DeConto and Pollard, 2003a; Archer, 2007; de Boer et al., 2010). The nonlinear forms can be subdivided into 1) as seen in some modelling studies where a small reduction in temperature across the glacial threshold results in the growth a large ice sheet due to feedback mechanisms (Huybrechts, 1993; Pollard and DeConto, 2005; Langebroek et al., 2009) and 2) caused by the different glacial thresholds for Northern Hemisphere and Southern Hemisphere glaciation and the ice sheet carrying capacity of the Antarctic continent (de Boer et al., 2010). Although this first type of nonlinearity may be evident in the DST / sea level plots, it is likely that this is due to a lack of cooling in the DST record across the EOT. We suggested that the second nonlinear form was most evident in the data used. A linear form for this past relationship is unlikely, although when using the low latitude SST record the reduced temperature signal makes determining any form difficult.

## Chapter 3 - main findings

Here we described and tested a method for performing long duration simulations of the ice sheets, the GCM matrix method. The method was based on that described by Pollard (2010) and allows for forcing of the ice sheets from changes in the atmospheric concentration of $CO_2$, changes in the astronomical configuration and an approximation of feedbacks from the growth of an ice sheet on the climate system. This method was tested by conducting control simulations of the North American and Eurasian ice sheets through the last glacial cycle, for each of these ice sheet forcings. These tests suggested that we are able to reproduce the ice sheet response to $CO_2$ and astronomical forcing reasonably well using a limited number of climate model simulations. The largest source of error was in the approximation of ice sheet feedbacks on the climate system. We were unable to simulate a complete deglaciation of the North American and Eurasian ice sheets at the end of the last glacial cycle.

## Chapter 4 - main findings

In this chapter we investigated the atmospheric $CO_2$ thresholds for the glaciation of the East Antarctic ice sheet with the aim of ascertaining whether there could have been small ice sheets during the warmth of the Eocene. Existing climate simulations from 5 different GCMs (DeConto et al., 2008; Heinemann et al., 2009; Roberts et al., 2009; Lunt et al., 2010b; Huber and Knutti, 2011) were used to perform offline ISM simulations. In addition to using different GCMs these climate simulations also had slightly different boundary conditions, such as different palaeo-geographies.

The ISM results showed a wide disagreement between these different climate simulations. In particular the simulations using HadCM3L showed a high seasonality, which significantly limited the growth of ice even at low ($1\times$ PIC) atmospheric $CO_2$ concentrations. However 3 of the other GCM simulations provided some evidence that small ice sheets could have existed in the Eocene, based on current proxy estimates of atmospheric $CO_2$. We showed that the simulations are particularly sensitive to the choice of ISM bedrock topography and the lapse rate parameter. We discussed other mechanisms which could have prevented the growth of the ice sheets if the Eocene was ice-free.

## Chapter 5 - main findings

Here we performed long duration simulations of the glaciation and deglaciation of the East Antarctic ice sheet under Eocene / Oligocene boundary conditions to investigate ice sheet hysteresis. Because of the computationally efficient GCM matrix method described and tested in Chapter 3, we were able to perform many sensitivity simulations.

All of our simulations showed a hysteresis response and the deglacial atmospheric $CO_2$ threshold was always above the glacial threshold. The hysteresis was reduced with the inclusion of astronomical variability and increased with the inclusion of albedo feedbacks. Basal sliding had a large impact on the ice sheet hysteresis, with a high rate of basal sliding resulting in a reduced hysteresis. However, due to uncertainties about the past basal environment of the Antarctic these experiments were perhaps oversimplified. It remains difficult to reconcile the strong hysteresis and the threshold response seen in our ISM simulations with sea level records, which show significant fluctuations in ice volume in the Oligocene and Miocene, and the relatively low atmospheric $CO_2$ shown by current proxy records. We suggested a number of reasons as to why this disagreement may exist.

**Chapter 6 - main findings**

Here the results from our ice sheet modelling simulations were presented as temperature versus sea level and atmospheric $CO_2$ versus sea level plots in order to compare with the data synthesis from the first 2 chapters and the recent review of Foster and Rohling (2013). Our ice sheet simulations showed close agreement with the atmospheric $CO_2$ versus sea level data in particular. However, the strong hysteresis shown in our simulations and the use of data from the Cenozoic, which is broadly a period of long-term cooling, limits the use of these relationships to make inferences about the future response of the ice sheets to projected anthropogenic warming, in the absence of a better understanding of ice sheet hysteresis.

## 7.2   Future work

Each chapter of this thesis has identified some key areas where further work is required. In the early chapters we attempted to bring together different palaeo-proxies and modelling studies. We identified some interesting relationships in the existing data, and also highlighted significant areas for future work. However, we were limited in our ability to define better the DST and SST to sea level relationships on this long timescale given the qualitative and quantitative uncertainties in the sea level and temperature data used and incomplete durations of the data. It is evident that future improvements in DST, SST and sea level records will enable an improved understanding of this relationship.

Improvements in the individual proxy records means that syntheses, such as that of Archer (2007) and that shown in this thesis, quickly become outdated. Since the publication of the Lear et al. (2000) long-duration, low-resolution DST data set used in this thesis, improvements to the Mg/Ca temperature proxy and its application have been made, and newer, shorter-duration, higher-resolution data sets have been produced (e.g., Lear et al., 2010; Pusz et al., 2011). However, further refinement of this proxy is needed, leading to the production of a long-duration, high-resolution data set (Cramer et al., 2011). In particular issues relating to corrections for the past seawater Mg/Ca ratio need to be resolved (Evans and Müller, 2012). This is in addition to the continued development of other temperature proxies such as $TEX_{86}$ and $U^{k'}_{37}$ (Liu et al., 2009). The potential regional effects in the NJ sequence stratigraphy record mean that additional well-dated records from other regions are needed to determine to what extent this record is representative of global eustatic sea level (Cramer et al., 2011; Raymo

et al., 2011). This is in combination with work on the tectonic history of the NJ margin during the Cenozoic (Müller et al., 2008; Petersen et al., 2010). More work is needed on reconstructing past ocean circulation changes in order to determine how representative the DST record and multi-basinal compilations are of surface climate changes (Cramer et al., 2009).

The later chapters in this thesis focused on long duration ice sheet modelling. A problem when conducting such long duration simulations is that current computational limitations mean that complex climate models cannot currently be directly coupled to ice sheet models. This has led to various attempts at indirect coupling and the use of reduced complexity climate models (DeConto and Pollard, 2003a; Ganopolski et al., 2010; Pollard, 2010). The GCM matrix method we developed and tested was only partially successful in simulating the last glacial cycle. There are a number of areas where we could improve our ice sheet modelling approach.

The ice sheet model we used has no treatment of ice shelves (Rutt et al., 2009), meaning that we needed to lower the marine margin in order to simulate the formation of the Northern Hemisphere ice sheets across shallow seas (Gregoire et al., 2012). There are parameterisations now used in other ice sheet models which allow the simulation of ice transfer from grounded terrestrial ice to floating ice shelves (Schoof, 2007; Pollard and DeConto, 2009), we could use such an ISM. This would also allow us to simulate the West Antarctic ice sheet. Alternatively, we could use an ice sheet model which explicitly simulates the transfer of mass across the grounding line, such ice sheet models currently exist although are computationally expensive (Morlighem et al., 2010; Seddik et al., 2012). The surface mass balance scheme used also has limitations, especially when the astronomical configuration is changed (van de Berg et al., 2011). However, adopting a more complex energy balance method requires additional climate inputs from the climate model, some of which may be parameterised if a reduced complexity model is used (Ganopolski et al., 2010). All of these improvements will add computational expense, which could mean that we are no longer able to conduct very long duration simulations (Pollard, 2010).

There are ongoing improvements to climate models and their application. We have not used the most up-to-date versions of the climate models in this thesis. Improvements in computing power will allow the use of more sophisticated climate models for palaeo-climate applications. Novel methods of climate forcing, such as the use of climate emulators, should also be explored (Crucifix, 2012). We have mostly focused on the temporal mismatch between the climate and the ice sheets, however there is also a spatial mismatch (Pollard, 2010). Atmospheric processes

which operate on a smaller scale than GCM grids may be important for ice sheet simulation, especially at the ice sheet edge. Regional climate models could be used to help overcome this spatial mismatch, although these models are also computationally expensive (Pollard, 2010).

We have not been able to reconcile our ice sheet model simulations with proxy records from the Oligocene and Miocene (e.g. Pagani et al., 2005; Kominz et al., 2008; Foster et al., 2012; Gallagher et al., 2012), due to the strong threshold response and hysteresis in our simulations, meaning that the East Antarctic ice sheet is very stable once it forms. Broadly, there are two narratives for the past stability of the East Antarctic ice sheet. The first is that the East Antarctic was stable once it formed and did not contribute to sea level fluctuations in the Oligocene and Miocene (Pollard and DeConto, 2005). The second narrative is that the East Antarctic was dynamic during this period, under relatively modest atmospheric $CO_2$ concentrations (Foster et al., 2012; Gallagher et al., 2012). Clearly the second narrative is the more concerning when considering projected anthropogenic warming. Our study highlights that much more work is needed from both proxy records and modelling to determine which of these narratives is correct.

# Appendix A

# Large parameter ensemble

| member | $\alpha_s$ (mm d$^{-1}$ °C $^{-1}$) | $\alpha_i$ (mm d$^{-1}$ °C $^{-1}$) | $f$ | $G$ ($mWm^{-2}$) | $\gamma$ (°C km$^{-1}$) |
|---|---|---|---|---|---|
| 1 | 5.183 | 17.170 | 2.222 | -53.220 | 8.437 |
| 2 | 3.147 | 18.080 | 7.645 | -55.860 | 6.342 |
| 3 | 7.314 | 11.480 | 6.041 | -56.550 | 5.025 |
| 4 | 3.215 | 15.810 | 4.341 | -58.480 | 6.094 |
| 5 | 5.342 | 18.620 | 8.244 | -51.030 | 8.441 |
| 6 | 5.930 | 16.220 | 1.199 | -35.520 | 5.868 |
| 7 | 6.404 | 14.630 | 1.660 | -52.580 | 8.072 |
| 8 | 5.370 | 18.490 | 9.301 | -37.130 | 7.070 |
| 9 | 3.409 | 16.700 | 4.288 | -61.500 | 5.498 |
| 10 | 4.080 | 9.086 | 5.414 | -39.100 | 6.940 |
| 11 | 3.311 | 14.390 | 8.838 | -42.710 | 5.921 |
| 12 | 7.246 | 8.137 | 3.829 | -40.570 | 7.769 |
| 13 | 4.607 | 13.670 | 6.352 | -45.870 | 7.912 |
| 14 | 6.695 | 18.950 | 6.968 | -62.450 | 6.627 |
| 15 | 5.582 | 8.469 | 3.144 | -51.390 | 5.530 |
| 16 | 4.906 | 19.450 | 5.623 | -45.500 | 5.383 |
| 17 | 4.310 | 9.973 | 4.682 | -63.260 | 5.772 |
| 18 | 3.570 | 12.360 | 5.978 | -64.200 | 7.390 |
| 19 | 4.809 | 10.360 | 5.570 | -56.640 | 8.081 |
| 20 | 4.857 | 8.901 | 5.043 | -38.580 | 7.547 |
| 21 | 5.603 | 13.530 | 3.606 | -49.610 | 5.994 |

| | | | | | |
|---|---|---|---|---|---|
| 22 | 7.408 | 11.050 | 8.694 | -40.000 | 5.462 |
| 23 | 6.896 | 8.983 | 9.104 | -53.450 | 5.738 |
| 24 | 7.508 | 14.130 | 7.960 | -39.640 | 7.656 |
| 25 | 5.834 | 10.740 | 9.528 | -48.620 | 5.265 |
| 26 | 7.620 | 11.850 | 5.165 | -39.430 | 6.884 |
| 27 | 5.528 | 15.570 | 2.027 | -62.900 | 8.855 |
| 28 | 3.923 | 15.360 | 6.164 | -58.770 | 8.655 |
| 29 | 6.530 | 13.240 | 2.794 | -43.420 | 7.174 |
| 30 | 6.075 | 12.800 | 8.417 | -53.620 | 7.970 |
| 31 | 5.896 | 12.690 | 9.271 | -64.860 | 7.928 |
| 32 | 4.973 | 11.260 | 1.921 | -52.890 | 7.710 |
| 33 | 5.221 | 9.912 | 3.622 | -55.500 | 7.587 |
| 34 | 3.735 | 9.715 | 7.906 | -52.200 | 5.917 |
| 35 | 4.137 | 8.084 | 4.540 | -60.340 | 7.209 |
| 36 | 3.076 | 17.330 | 4.859 | -59.280 | 7.250 |
| 37 | 7.831 | 14.570 | 1.115 | -46.970 | 8.190 |
| 38 | 6.400 | 17.040 | 5.789 | -46.590 | 5.094 |
| 39 | 7.689 | 17.700 | 5.702 | -60.610 | 5.677 |
| 40 | 5.279 | 10.770 | 7.211 | -38.090 | 8.888 |
| 41 | 5.047 | 10.120 | 1.387 | -63.980 | 8.242 |
| 42 | 5.994 | 8.628 | 7.662 | -59.570 | 7.324 |
| 43 | 6.304 | 13.380 | 2.815 | -49.820 | 7.608 |
| 44 | 5.705 | 16.910 | 5.268 | -42.460 | 8.121 |
| 45 | 6.206 | 19.770 | 8.966 | -62.250 | 5.833 |
| 46 | 3.697 | 15.450 | 9.960 | -38.610 | 7.448 |
| 47 | 7.367 | 8.282 | 9.770 | -51.840 | 5.149 |
| 48 | 6.640 | 16.090 | 3.703 | -63.790 | 7.131 |
| 49 | 4.660 | 11.150 | 7.460 | -44.670 | 7.004 |
| 50 | 4.282 | 15.300 | 3.067 | -58.050 | 8.535 |
| 51 | 4.047 | 13.830 | 8.480 | -42.110 | 5.576 |
| 52 | 3.762 | 9.334 | 6.290 | -36.080 | 8.769 |
| 53 | 4.471 | 12.680 | 1.734 | -43.870 | 8.821 |
| 54 | 7.479 | 17.770 | 5.920 | -50.230 | 6.157 |

| 55 | 3.833 | 19.190 | 9.423 | -62.990 | 7.308 |
| 56 | 3.284 | 16.850 | 8.355 | -57.010 | 6.975 |
| 57 | 5.657 | 19.750 | 7.330 | -48.390 | 6.691 |
| 58 | 3.618 | 9.628 | 6.775 | -64.400 | 6.255 |
| 59 | 5.125 | 16.610 | 3.190 | -57.630 | 6.182 |
| 60 | 3.541 | 12.930 | 1.345 | -47.200 | 5.303 |
| 61 | 7.157 | 15.770 | 4.752 | -60.870 | 6.470 |
| 62 | 4.597 | 10.170 | 2.141 | -61.360 | 5.705 |
| 63 | 6.113 | 13.100 | 2.610 | -44.480 | 6.865 |
| 64 | 6.760 | 11.510 | 4.431 | -47.440 | 7.737 |
| 65 | 6.719 | 12.080 | 6.543 | -47.690 | 5.414 |
| 66 | 7.016 | 12.440 | 9.634 | -35.700 | 8.322 |
| 67 | 4.239 | 9.210 | 3.497 | -45.760 | 8.725 |
| 68 | 3.474 | 14.330 | 5.379 | -55.150 | 8.383 |
| 69 | 6.586 | 18.230 | 9.049 | -49.330 | 6.780 |
| 70 | 3.997 | 11.670 | 2.630 | -40.220 | 7.427 |
| 71 | 7.734 | 14.070 | 7.798 | -35.080 | 6.644 |
| 72 | 4.164 | 9.519 | 1.850 | -40.970 | 6.534 |
| 73 | 7.129 | 15.920 | 8.813 | -54.670 | 5.197 |
| 74 | 4.369 | 14.810 | 5.065 | -43.000 | 8.717 |
| 75 | 4.793 | 12.080 | 9.658 | -37.990 | 5.215 |
| 76 | 6.257 | 18.800 | 7.505 | -45.050 | 6.733 |
| 77 | 7.769 | 11.760 | 6.862 | -50.350 | 6.372 |
| 78 | 3.869 | 13.900 | 1.008 | -57.450 | 7.080 |
| 79 | 7.987 | 10.580 | 2.975 | -46.300 | 8.947 |
| 80 | 7.259 | 17.880 | 3.299 | -54.850 | 8.623 |
| 81 | 3.049 | 10.940 | 1.495 | -36.550 | 5.072 |
| 82 | 7.567 | 14.930 | 7.044 | -51.540 | 8.008 |
| 83 | 6.931 | 15.110 | 8.025 | -36.470 | 6.810 |
| 84 | 6.040 | 18.910 | 3.907 | -44.290 | 6.411 |
| 85 | 4.504 | 19.390 | 2.311 | -43.390 | 8.293 |
| 86 | 4.409 | 8.515 | 6.479 | -37.040 | 8.561 |
| 87 | 3.388 | 19.930 | 8.178 | -37.500 | 8.984 |

| | | | | | |
|---|---|---|---|---|---|
| 88 | 5.465 | 16.510 | 6.594 | -41.120 | 5.625 |
| 89 | 6.824 | 8.807 | 2.456 | -61.930 | 8.488 |
| 90 | 6.158 | 10.400 | 4.176 | -41.680 | 6.073 |
| 91 | 5.098 | 12.280 | 6.671 | -50.790 | 6.507 |
| 92 | 7.858 | 13.510 | 4.951 | -56.220 | 8.232 |
| 93 | 4.701 | 17.540 | 9.865 | -48.830 | 6.305 |
| 94 | 7.924 | 19.060 | 3.425 | -41.580 | 6.570 |
| 95 | 3.172 | 16.360 | 8.649 | -48.090 | 5.321 |
| 96 | 5.407 | 19.550 | 4.131 | -58.110 | 7.504 |
| 97 | 6.998 | 17.370 | 2.390 | -53.920 | 7.804 |
| 98 | 7.083 | 15.080 | 1.610 | -59.990 | 6.009 |
| 99 | 5.785 | 18.430 | 7.146 | -54.310 | 6.213 |
| 100 | 6.494 | 18.120 | 4.009 | -59.760 | 7.842 |

Table A.1: *Ensemble parameter values for simulations in Chapter 3*

# Appendix B

# Ice volume in BBC_ALL simulations of Singarayer and Valdes (2010)
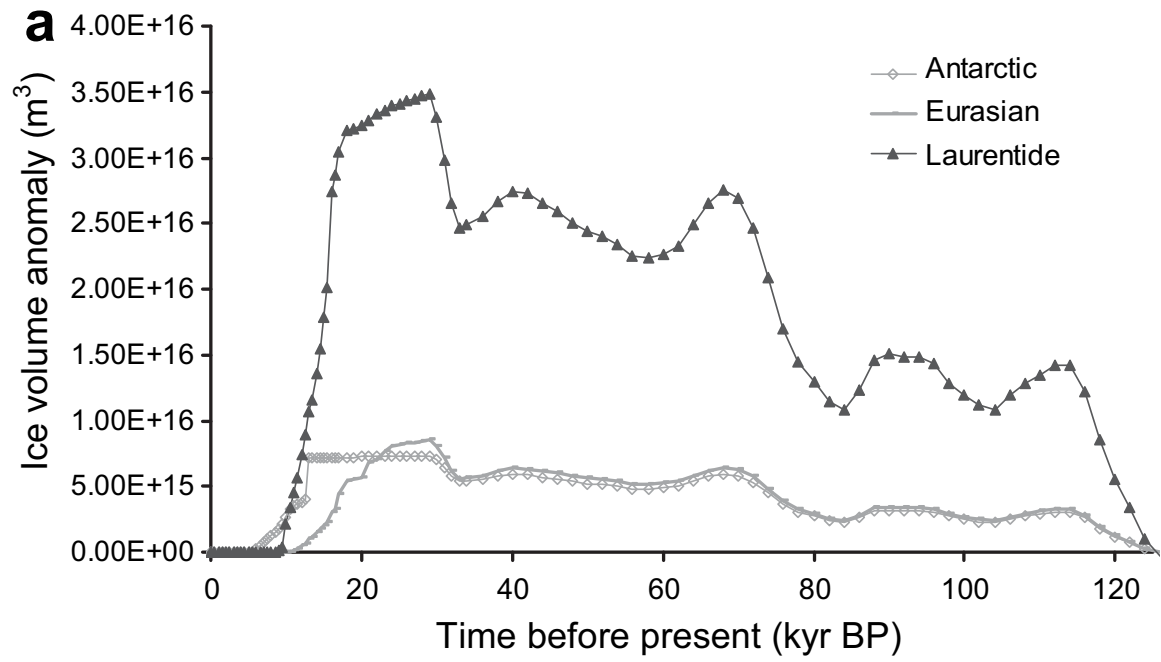
Figure B.1: *Ice volume in BBC_ALL simulations of Singarayer and Valdes (2010), used as boundary conditions in GCM simulations by scaling the ICE-5G ice sheet reconstruction to the SPECMAP $\delta^{18}O$ record of ice volume.*

# Appendix C

# Possible 'saddle-collapse' of the North American ice sheets
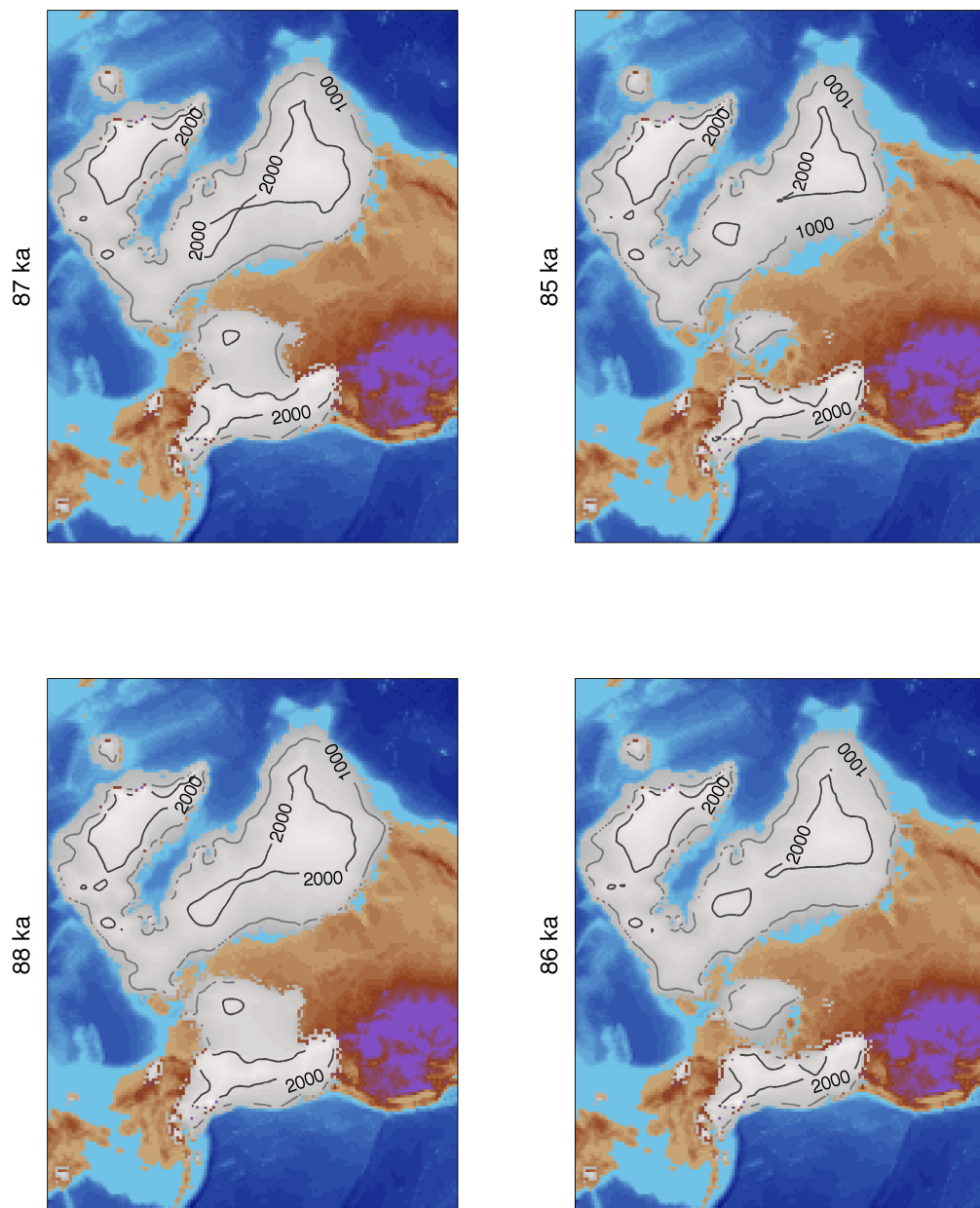
Figure C.1: *Possible 'saddle-collapse' during last glacial cycle for the North American ice sheets between 88-85 ka.*
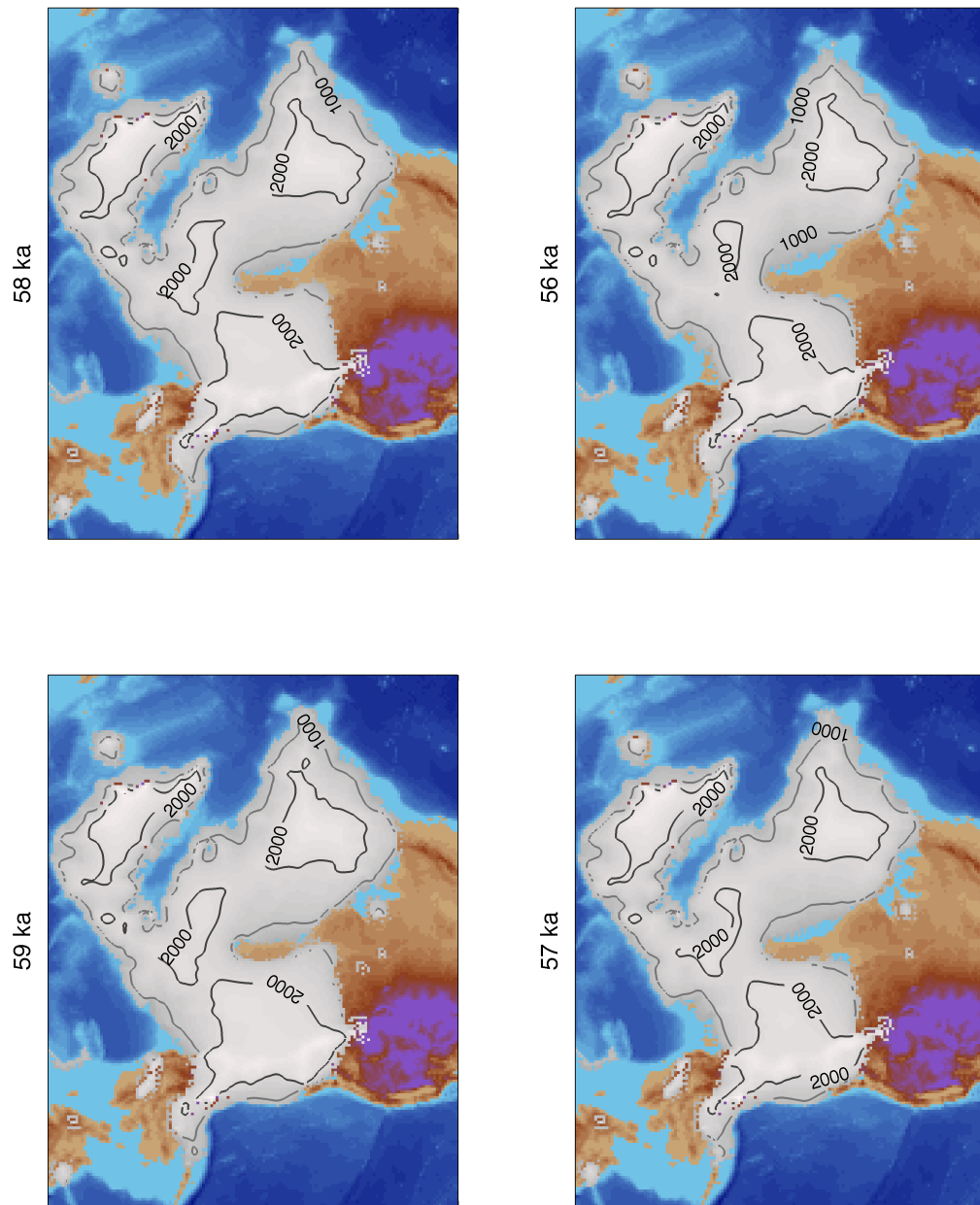
Figure C.2: *Possible 'saddle-collapse' during last glacial cycle for the North American ice sheets between 59-56 ka.*
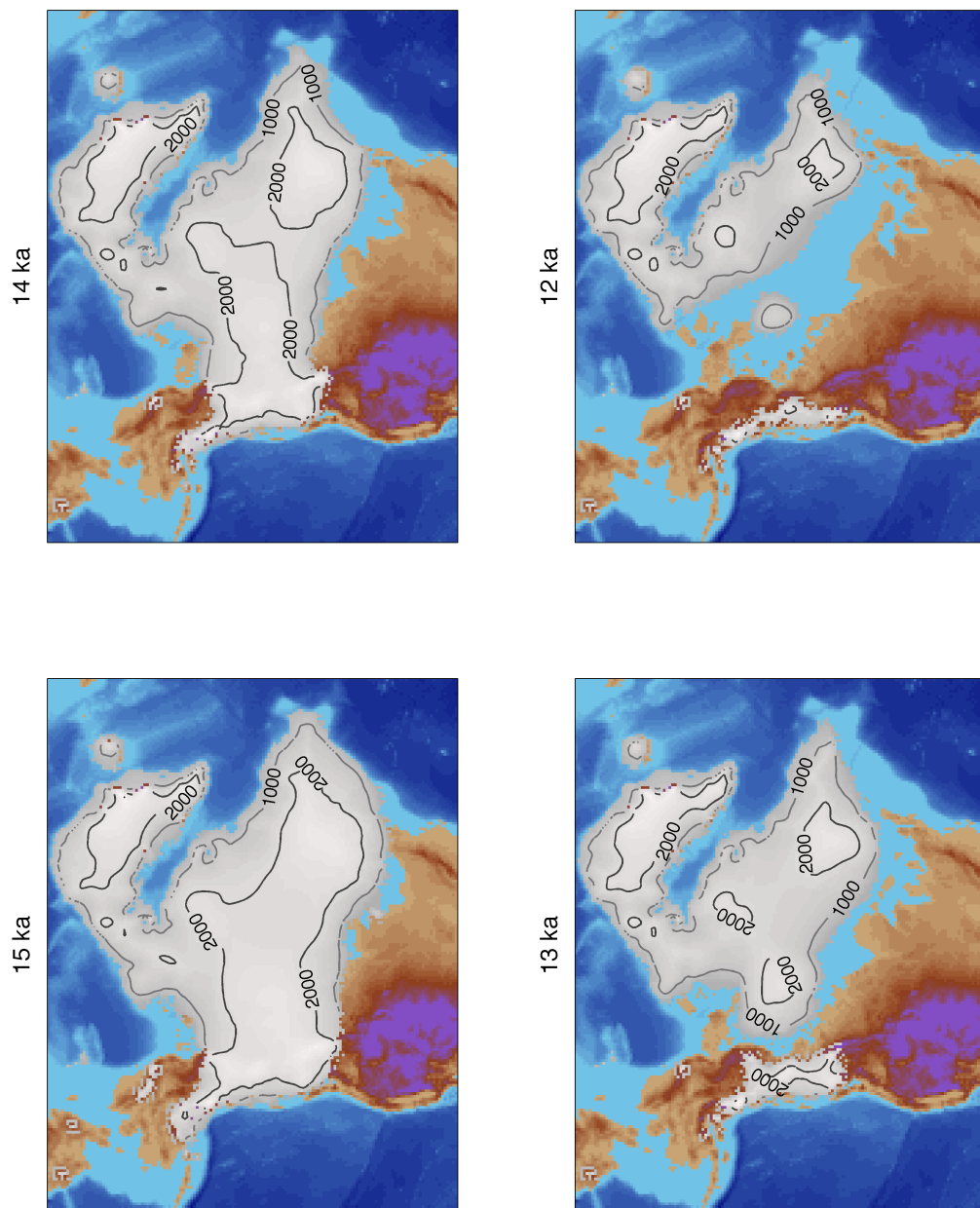
Figure C.3: *'Saddle-collapse' during last termination for the North American ice sheets between 15-12 ka, similar to Gregoire et al. (2012).*

Figure C.4: *'Saddle-collapse' during last termination for the North American ice sheets between 10-7 ka.*

# Appendix D

# EoMIP simulations
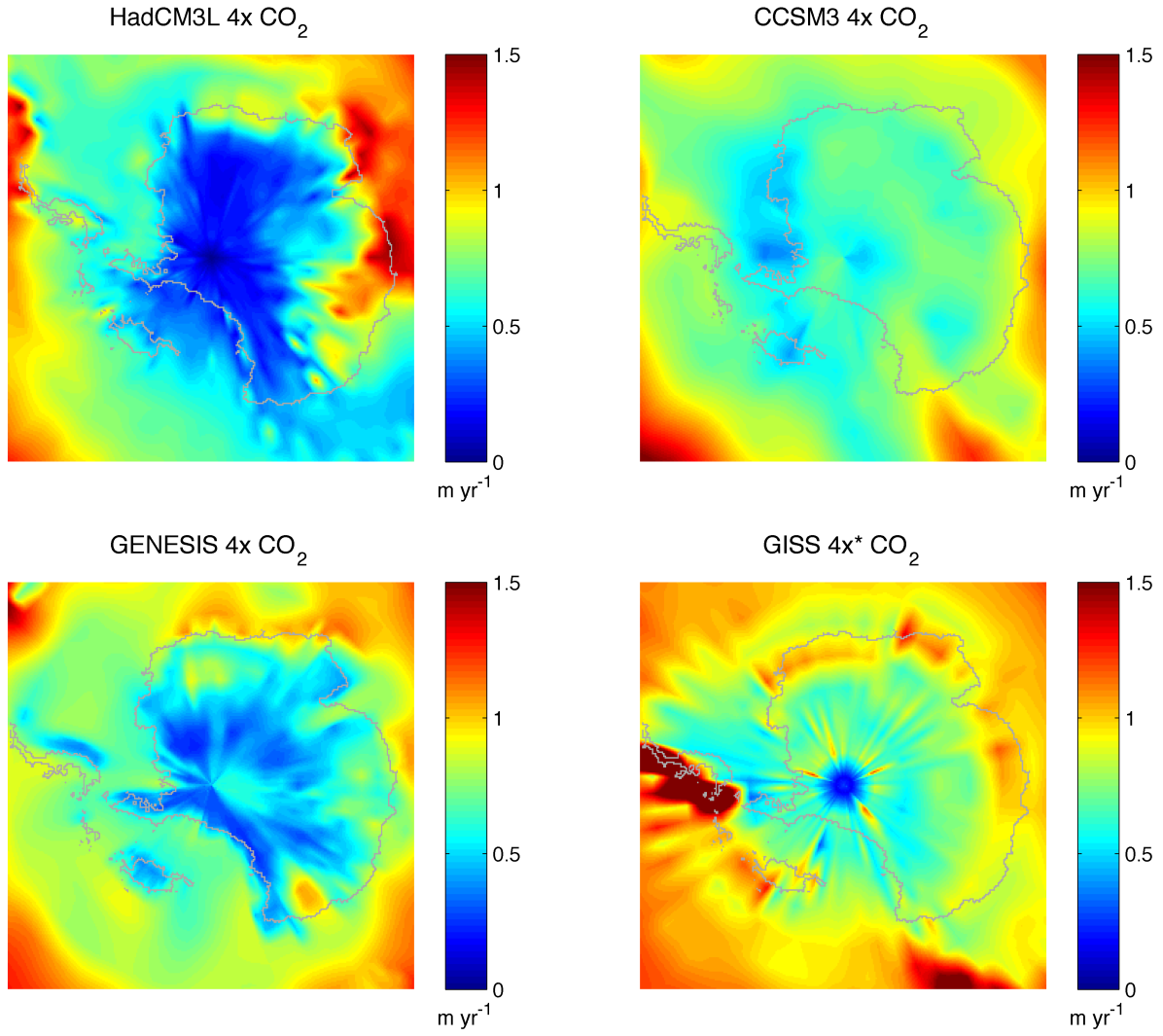
Figure D.1: *Total annual precipitation from EoMIP GCM simulations at 4× PIC. Note that the GISS simulation includes elevated CH$_4$ and is approximately equivalent to a 4.3 × PIC simulation (Roberts et al., 2009).*
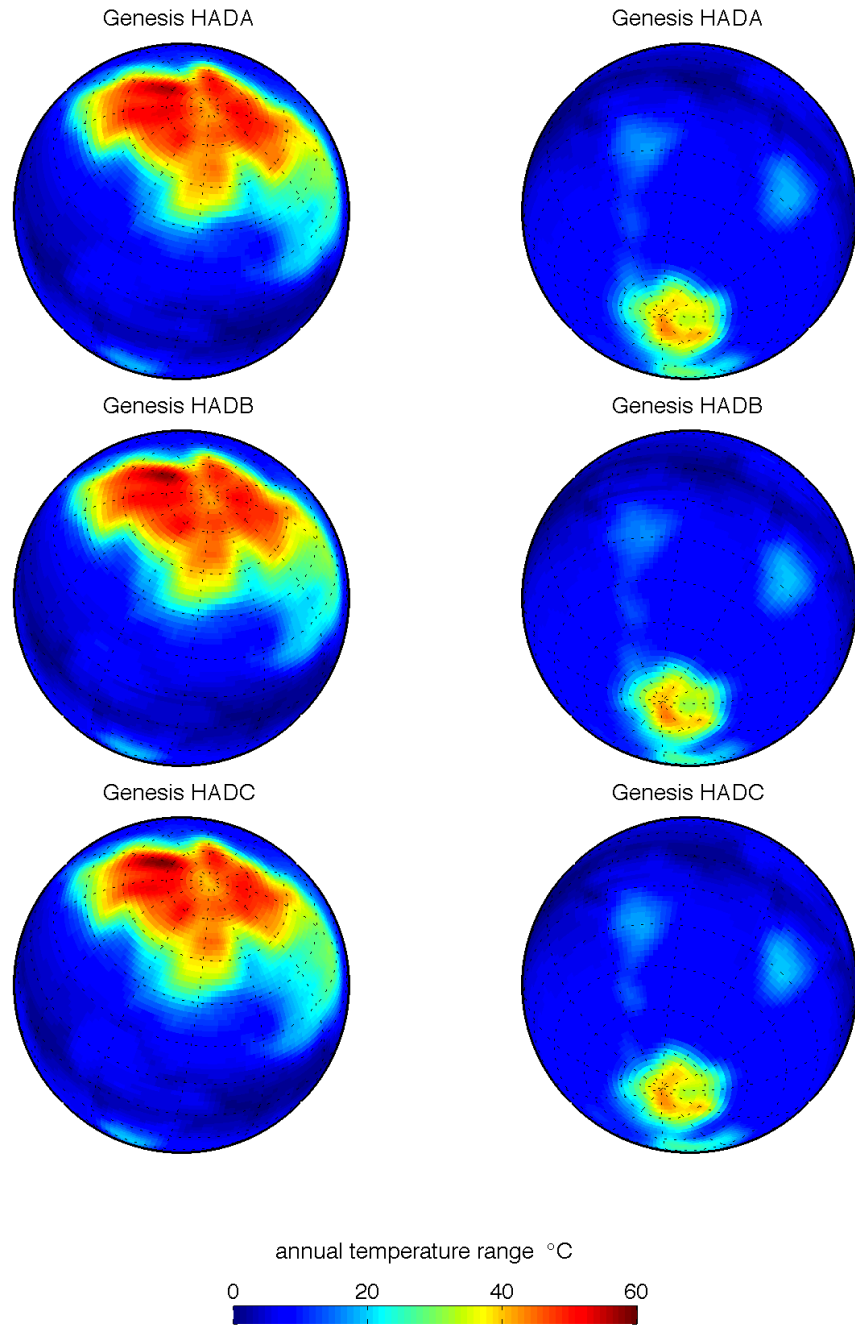
Figure D.2: *Seasonality for GENESIS simulations using the GTECH paleogeography used by Lunt et al. (2010), simulations were performed with an atmospheric $CO_2$ concentration of 314 ppm (Pollard 2012, personal communication).*

HadCML 2x CO$_2$ Moses 2.1    HadCML 2x CO$_2$ Moses 2.1

HadCML 2x CO$_2$ TRIFFID    HadCML 2x CO$_2$ TRIFFID

HadCML 4x CO$_2$ Moses 2.1    HadCML 4x CO$_2$ Moses 2.1

HadCML 4x CO$_2$ TRIFFID    HadCML 4x CO$_2$ TRIFFID

annual temperature range °C

0    20    40    60
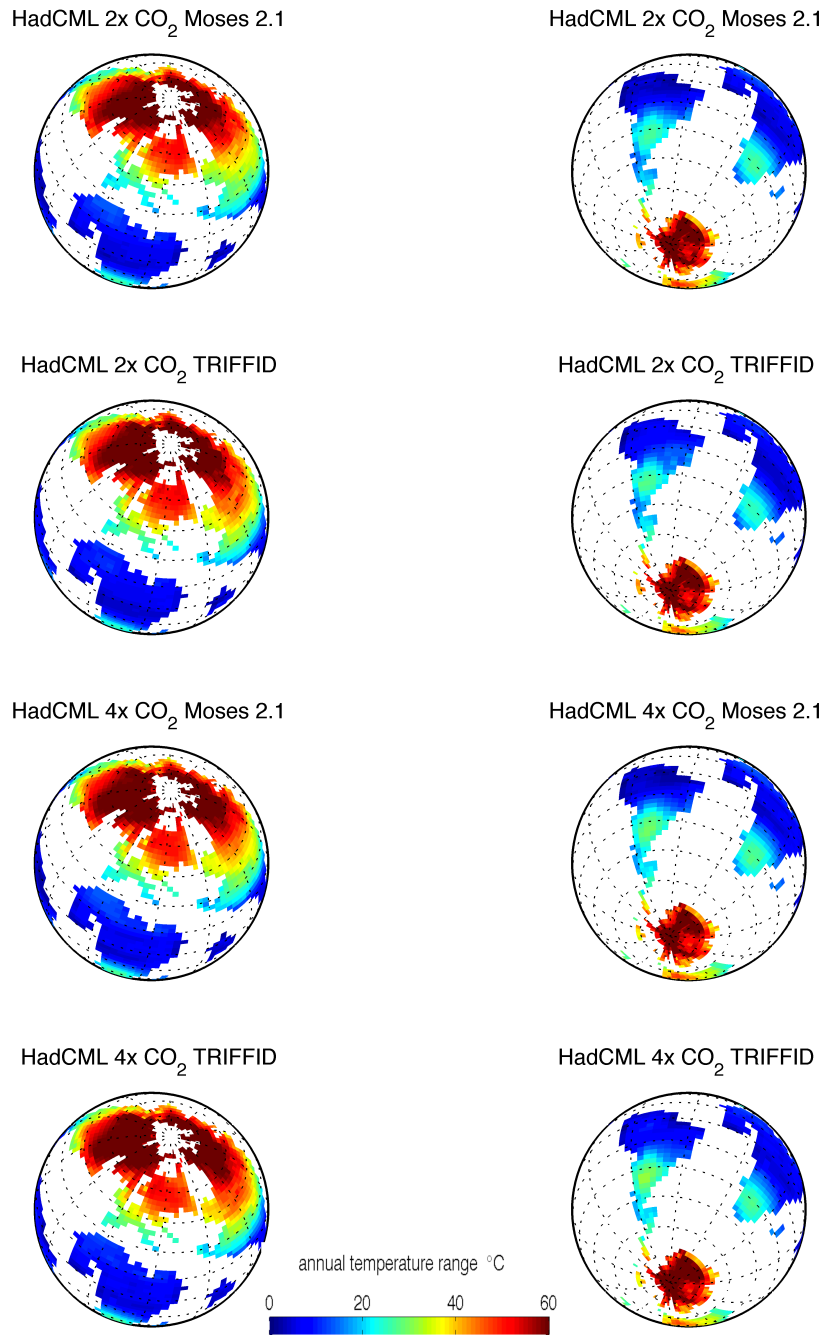
Figure D.3: *Impact of using dynamic vegetation model on seasonality of HadCM3L early Eocene simulations (Lopston 2012, personal communication).*
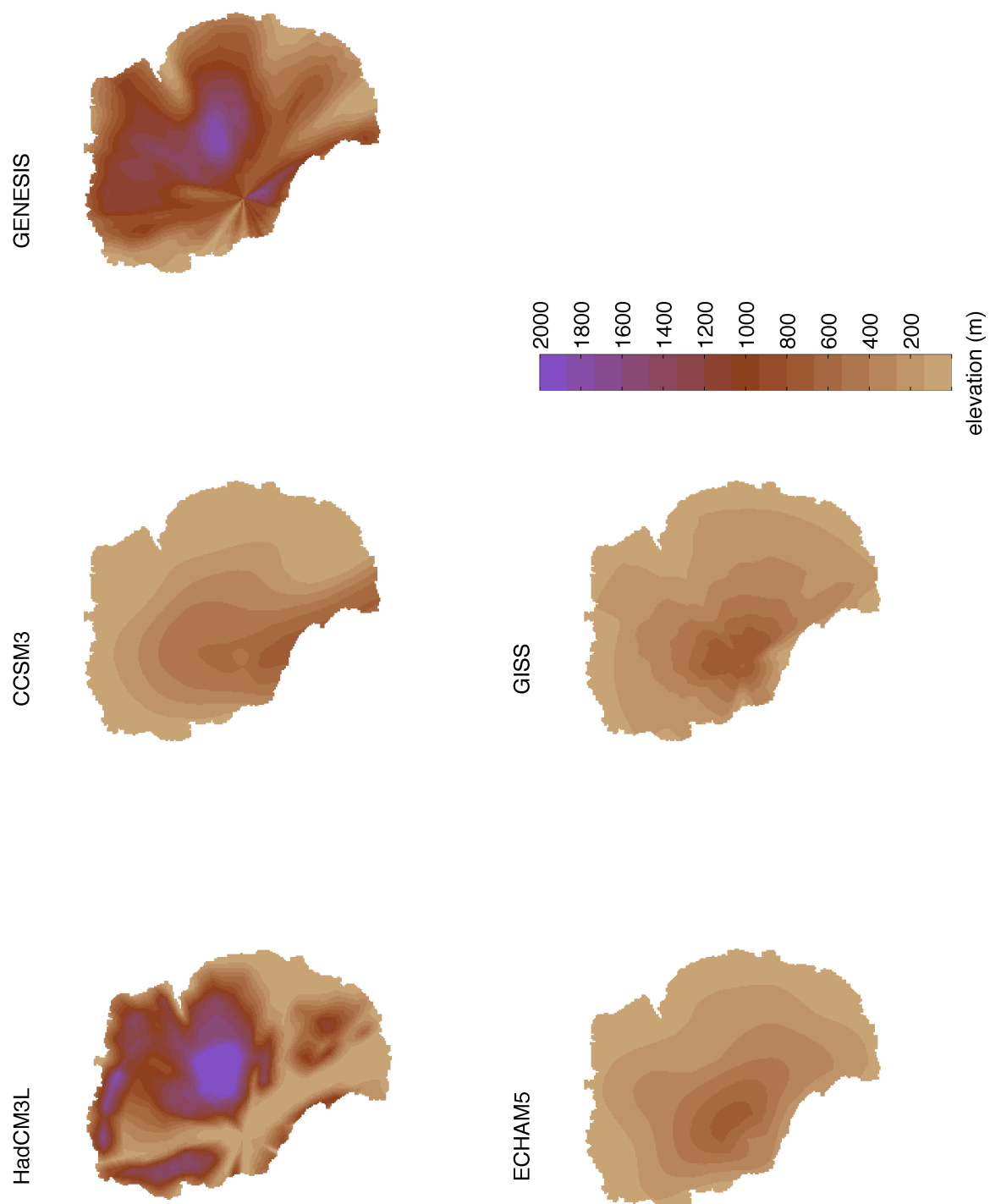
Figure D.4: *Different GCM Antarctic bedrock topographies for EoMIP simulations*

# Appendix E

# Small parameter ensemble

| member | $\alpha_s$ (mm d$^{-1}$ °C$^{-1}$) | $\alpha_i$ (mm d$^{-1}$ °C$^{-1}$) | $f$ | $B_s$ (mm yr$^{-1}$ Pa$^{-1}$) | $\gamma$ (°C km$^{-1}$) |
|---|---|---|---|---|---|
| 1 | 5.861 | 17.810 | 4.536 | 3.759 | 5.879 |
| 2 | 6.388 | 16.750 | 6.958 | 2.090 | 8.185 |
| 3 | 3.427 | 12.490 | 6.692 | 2.759 | 6.447 |
| 4 | 6.442 | 14.960 | 2.206 | 7.427 | 6.933 |
| 5 | 4.847 | 10.040 | 1.144 | 5.356 | 5.978 |
| 6 | 3.286 | 16.100 | 5.228 | 3.926 | 7.367 |
| 7 | 4.083 | 8.041 | 9.848 | 9.021 | 6.290 |
| 8 | 4.626 | 11.040 | 4.863 | 7.048 | 7.456 |
| 9 | 7.319 | 9.377 | 6.224 | 6.131 | 7.654 |
| 10 | 7.617 | 9.739 | 2.484 | 9.251 | 7.855 |
| 11 | 3.815 | 19.170 | 7.541 | 2.920 | 6.870 |
| 12 | 7.946 | 15.380 | 3.607 | 8.198 | 5.343 |
| 13 | 7.196 | 11.550 | 5.545 | 7.790 | 6.135 |
| 14 | 4.556 | 19.750 | 7.290 | 4.546 | 8.601 |
| 15 | 5.786 | 8.917 | 8.777 | 6.402 | 5.678 |
| 16 | 3.771 | 13.110 | 9.568 | 1.469 | 8.395 |
| 17 | 4.298 | 12.290 | 5.855 | 0.980 | 7.151 |
| 18 | 6.639 | 18.210 | 1.425 | 5.606 | 8.913 |
| 19 | 5.437 | 18.700 | 1.929 | 8.750 | 5.183 |
| 20 | 7.423 | 10.420 | 4.224 | 9.710 | 6.672 |
| 21 | 5.034 | 13.940 | 8.240 | 1.835 | 5.544 |

| 22 | 3.174 | 13.420 | 3.484 | 6.817 | 8.829 |
| 23 | 6.129 | 14.610 | 7.995 | 4.752 | 5.128 |
| 24 | 6.862 | 16.300 | 3.125 | 0.599 | 7.950 |
| 25 | 5.309 | 17.560 | 9.035 | 3.313 | 8.265 |

Table E.1: *Ensemble parameter values for simulations in Chapter 5*
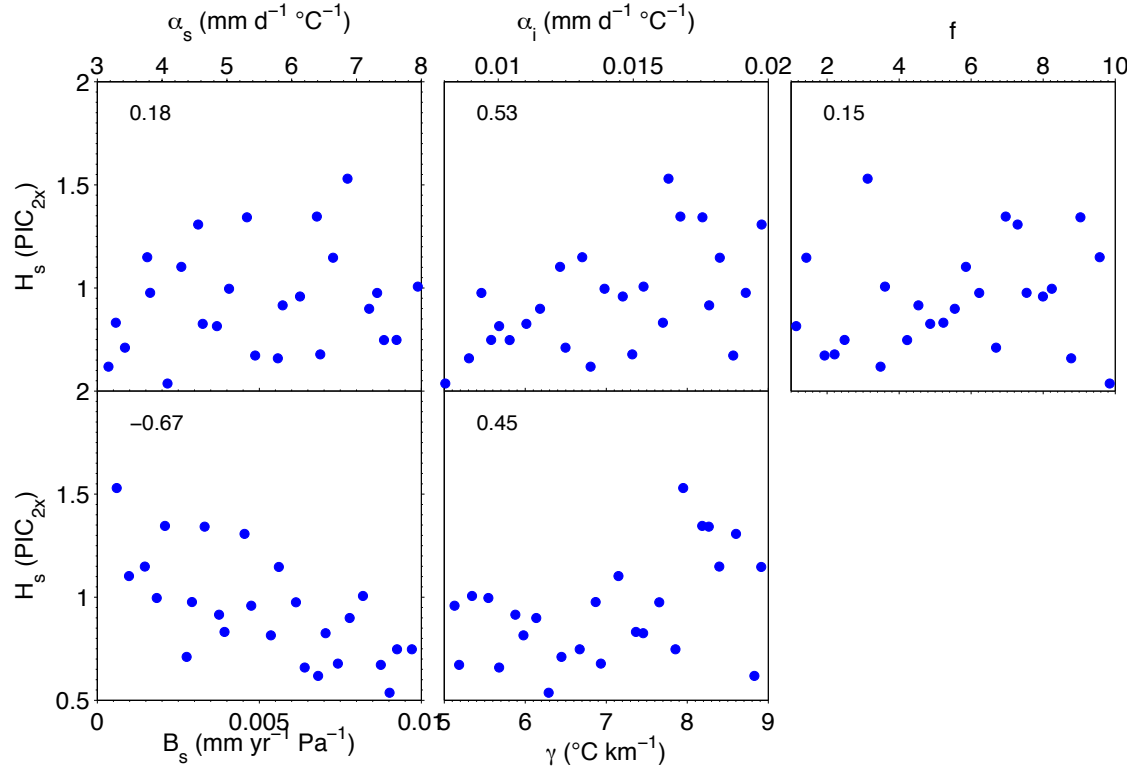
Figure E.1: *Correlation between parameter values and ice sheet hysteresis for small parameter ensemble and hysteresis experiments in Chapter 5 which include basal sliding, correlation coefficients are shown on the figures.*

# Appendix F

# Raw climate / sea level model output
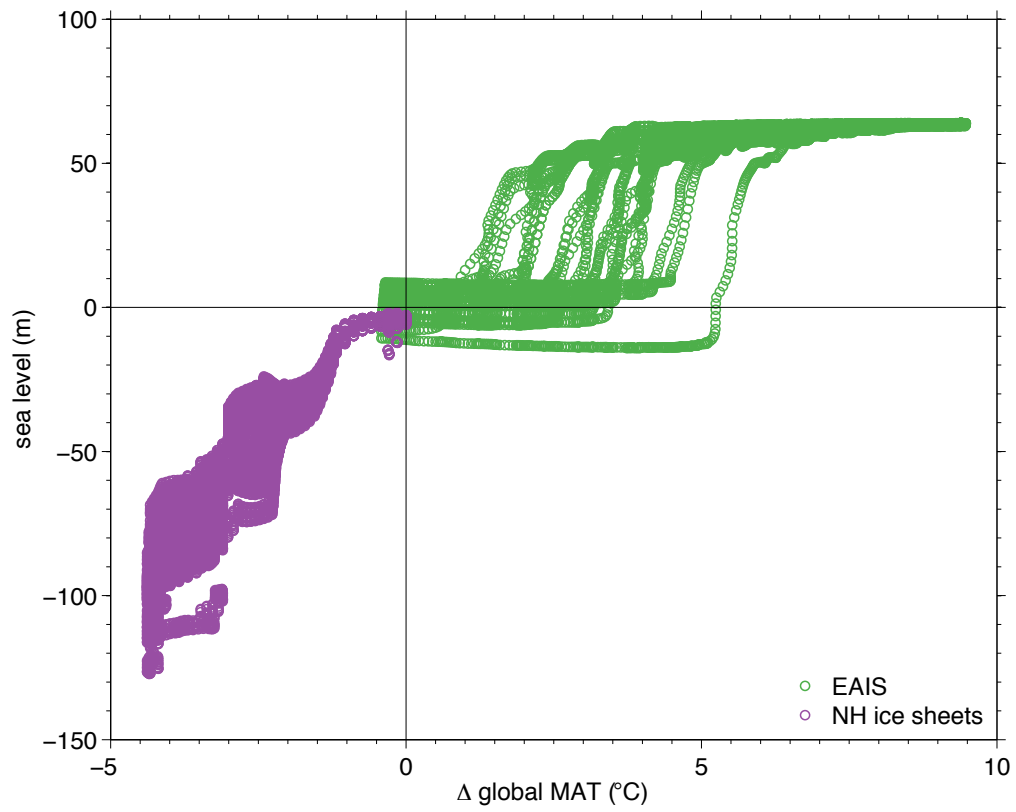
Figure F.1: *Global MAT against sea level for GCM-ISM simulations for a reduction in temperature. Showing raw ensemble output, which are binned in main thesis.*
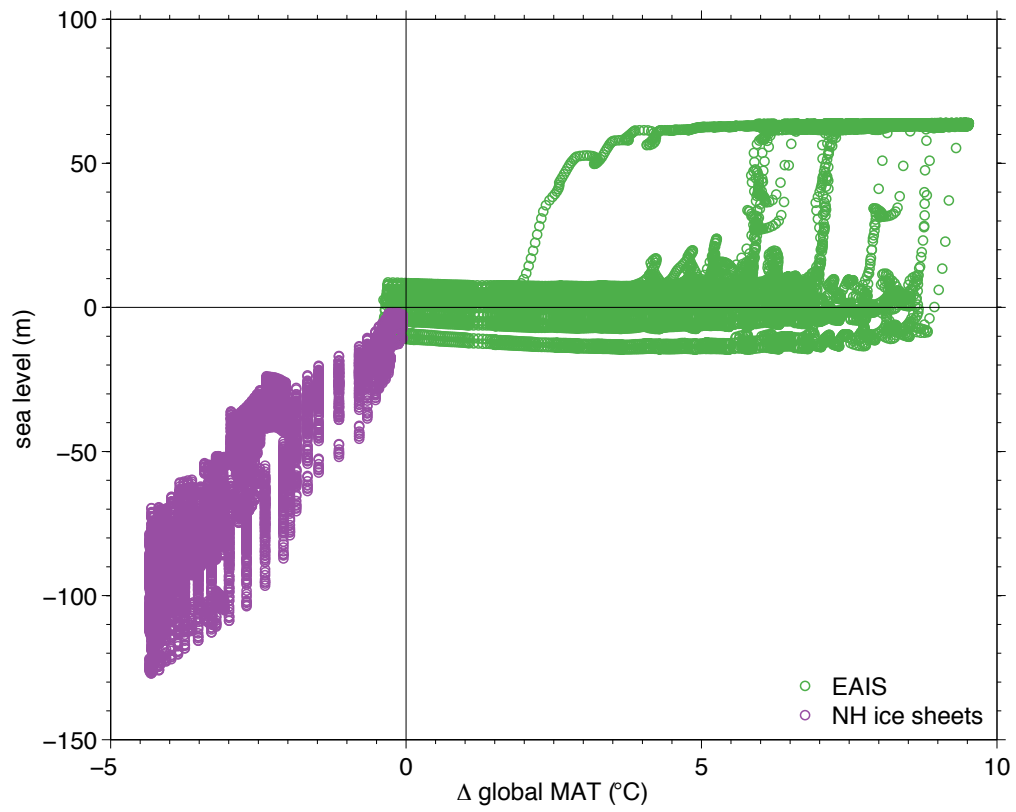
Figure F.2: *Global MAT against sea level for GCM-ISM simulations for an increase in temperature. Showing raw ensemble output, which are binned in main thesis.*
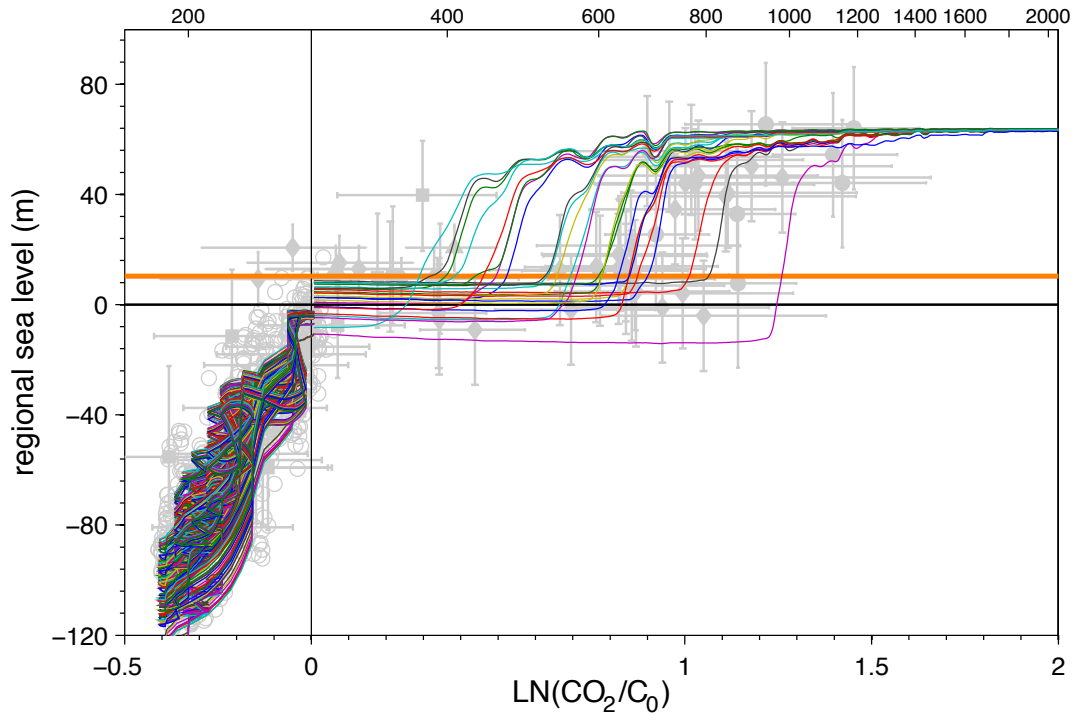
Figure F.3: *Atmospheric $CO_2$ against sea level for GCM-ISM simulations for EAIS simulations showing and reduction in atmospheric $CO_2$ and NH ice sheet simulations of the last glacial cycle. Showing raw ensemble output, which are binned in main thesis. The data shown in grey are from Foster and Rohling (2013), see main text for description*
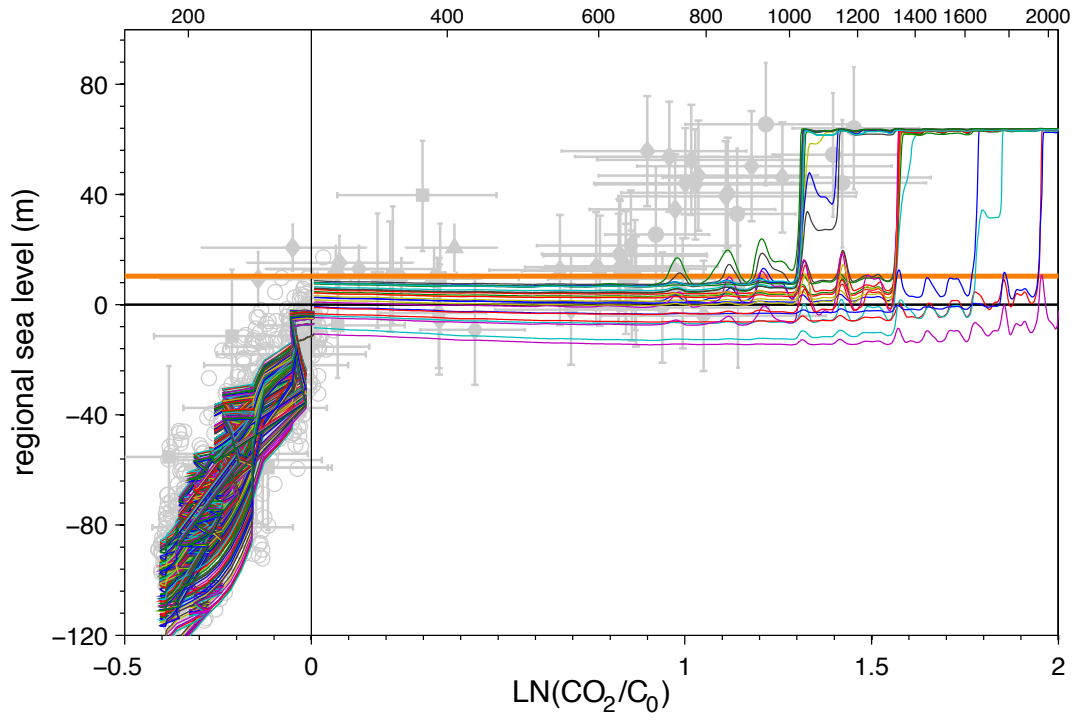
Figure F.4: *Atmospheric $CO_2$ against sea level for GCM-ISM simulations for EAIS simulations and NH ice sheet simulations showing an increase atmospheric $CO_2$. Showing raw ensemble output, which are binned in main thesis. The data shown in grey are from Foster and Rohling (2013), see main text for description*

# References

Abe-Ouchi, A. and Blatter, H. (1993). On the initiation of ice sheets. *Annals of Glaciology*, 18:203–207.

Abe-Ouchi, A., Segawa, T., and Saito, F. (2007). Climatic conditions for modelling the Northern Hemisphere ice sheets throughout the ice age cycle. *Climate of the Past*, 3(3):423–438.

Adkins, J. F., McIntyre, K., and Schrag, D. P. (2002). The salinity, temperature, and $\delta 18O$ of the glacial deep ocean. *Science*, 298(5599):1769–73.

Alley, R. B., Clark, P. U., Huybrechts, P., and Joughin, I. (2005). Ice-sheet and sea-level changes. *Science*, 310(5747):456–60.

Allison, I., Alley, R., Fricker, H., Thomas, R., and Warner, R. (2009). Ice sheet mass balance and sea level. *Antarctic Science*, 21(05):413.

Anand, P., Elderfield, H., and Conte, M. (2003). Calibration of Mg/Ca thermometry in planktonic foraminifera from a sediment trap time series. *Paleoceanography*, 18(2).

Anderson, J. B., Shipp, S. S., Lowe, A. L., Wellner, J. S., and Mosola, A. B. (2002). The Antarctic ice sheet during the Last Glacial Maximum and its subsequent retreat history: a review. *Quaternary Science Reviews*, 21(1-3):49–70.

Anderson, R., Ali, S., and Bradtmiller, L. (2009). Wind-driven upwelling in the Southern Ocean and the deglacial rise in atmospheric CO2. *Science*, 323:1443–1448.

Applegate, P. J., Kirchner, N., Stone, E. J., Keller, K., and Greve, R. (2012). An assessment of key model parametric uncertainties in projections of Greenland ice sheet behavior. *The Cryosphere*, 6(3):589–606.

Archer, D. (2007). *Global Warming: Understanding the Forecast*. Blackwell Publishing, Malden, MA.

Archer, D. and Brovkin, V. (2008). The millennial atmospheric lifetime of anthropogenic CO2. *Climatic Change*, 90(3):283–297.

Augustin, L., Barbante, C., Barnes, P. R. F., Barnola, J. M., Bigler, M., Castellano, E., Cattani, O., Chappellaz, J., Dahl-Jensen, D., Delmonte, B., Dreyfus, G., Durand, G., Falourd, S., Fischer, H.,

Flückiger, J., Hansson, M. E., Huybrechts, P., Jugie, G., Johnsen, S. J., Jouzel, J., Kaufmann, P., Kipfstuhl, J., Lambert, F., Lipenkov, V. Y., Littot, G. C., Longinelli, A., Lorrain, R., Maggi, V., Masson-Delmotte, V., Miller, H., Mulvaney, R., Oerlemans, J., Oerter, H., Orombelli, G., Parrenin, F., Peel, D. A., Petit, J.-R., Raynaud, D., Ritz, C., Ruth, U., Schwander, J., Siegenthaler, U., Souchez, R., Stauffer, B., Steffensen, J. P., Stenni, B., Stocker, T. F., Tabacco, I. E., Udisti, R., Van De Wal, R. S. W., Van Den Broeke, M., Weiss, J., Wilhelms, F., Winther, J.-G., Wolff, E. W., and Zucchelli, M. (2004). Eight glacial cycles from an Antarctic ice core. *Nature*, 429(6992):623–8.

Bamber, J. L., Ekholm, S., and Krabill, W. B. (2001). A new, high-resolution digital elevation model of Greenland fully validated with airborne laser altimeter data. *Journal of Geophysical Research*, 106(B4):6733–6745.

Bamber, J. L., Riva, R. E. M., Vermeersen, B. L. A., and LeBrocq, A. M. (2009). Reassessment of the potential sea-level rise from a collapse of the West Antarctic ice sheet. *Science*, 324(5929):901–3.

Bartoli, G., Hönisch, B., and Zeebe, R. E. (2011). Atmospheric CO2 decline during the Pliocene intensification of Northern Hemisphere glaciations. *Paleoceanography*, 26(4):PA4213.

Beerling, D. J. and Royer, D. L. (2011). Convergent Cenozoic CO2 history. *Nature Geoscience*, 4(7):418–420.

Bijl, P. K., Houben, A. J. P., Schouten, S., Bohaty, S. M., Sluijs, A., Reichart, G.-J., Sinninghe Damsté, J. S., and Brinkhuis, H. (2010). Transient Middle Eocene atmospheric CO2 and temperature variations. *Science*, 330(6005):819–21.

Bijl, P. K., Schouten, S., Sluijs, A., Reichart, G.-J., Zachos, J. C., and Brinkhuis, H. (2009). Early Palaeogene temperature evolution of the southwest Pacific Ocean. *Nature*, 461(7265):776–9.

Billups, K. and Schrag, D. (2003). Application of benthic foraminiferal Mg/Ca ratios to questions of Cenozoic climate change. *Earth and Planetary Science Letters*, 209(1-2):181–195.

Bintanja, R. and van De Wal, R. (2008). North American ice-sheet dynamics and the onset of 100,000-year glacial cycles. *Nature*, 454:869–872.

Bintanja, R., van De Wal, R., and Oerlemans, J. (2005a). Modelled atmospheric temperatures and global sea levels over the past million years. *Nature*, 437:125–128.

Bintanja, R., Wal, R. S. W. V. D., and Oerlemans, J. (2005b). A new method to estimate ice age temperatures. *Climate Dynamics*, 24(2-3):197–211.

Birchfield, G., Weertman, J., and Lunde, A. (1982). A model study of the role of high-latitude topography in the climatic response to orbital insolation anomalies. *Journal of The Atmospheric Sciences*.

Blatter, H., Greve, R., and Abe-Ouchi, A. (2011). Present state and prospects of ice sheet and glacier modelling. *Surveys in Geophysics*, 32(4-5):555–583.

Bohaty, S. M., Zachos, J. C., Florindo, F., and Delaney, M. L. (2009). Coupled greenhouse warming and deep-sea acidification in the middle Eocene. *Paleoceanography*, 24(2):1–16.

Boon, J., der Meer, F. V., Schuyl, J., de Leeuw, J., and Schenck, P. (1978). Organic geochemical analyses of core samples from Site 362, Walvis Ridge, DSDP Leg 40. *Initial Rep. Deep Sea Drill. Proj*, pages 627–637.

Bougamont, M., Bamber, J. L., and Greuell, W. (2005). A surface mass balance model for the Greenland ice sheet. *Journal of Geophysical Research*, 110(F4):F04018.

Bougamont, M., Bamber, J. L., Ridley, J. K., Gladstone, R. M., Greuell, W., Hanna, E., Payne, A. J., and Rutt, I. (2007). Impact of model physics on estimating the surface mass balance of the Greenland ice sheet. *Geophysical Research Letters*, 34(17):L17501.

Braithwaite, R. (1995). Positive degree-day factors for ablation on the Greenland ice sheet studied by energy-balance modelling. *Journal of Glaciology*, 41(137):153–160.

Brassell, S., Eglinton, G., Marlowe, I., Pflaumann, U., and Sarnthein, M. (1986). Molecular stratigraphy: a new tool for climatic assessment. *Nature*, 320:129–133.

Brochier-Armanet, C., Boussau, B., Gribaldo, S., and Forterre, P. (2008). Mesophilic Crenarchaeota: proposal for a third archaeal phylum, the Thaumarchaeota. *Nature reviews. Microbiology*, 6(3):245–52.

Brooks, C. (1949). *Climate through the ages*. Ernest Benn, London.

Brown, S. J. and Elderfield, H. (1996). Variations in Mg/Ca and Sr/Ca ratios of planktonic foraminifera caused by postdepositional dissolution: Evidence of shallow Mg-dependent dissolution. *Paleoceanography*, 11(5):543.

Browning, J., Miller, K., and Pak, D. (1996). Global implications of lower to middle Eocene sequence boundaries on the New Jersey coastal plain: The icehouse cometh. *Geology*, 24(7):639.

Browning, J. V., Miller, K. G., Sugarman, P. J., Kominz, M. a., McLaughlin, P. P., Kulpecz, A. A., and Feigenson, M. D. (2008). 100 Myr record of sequences, sedimentary facies and sea level change from Ocean Drilling Program onshore coreholes, US Mid-Atlantic coastal plain. *Basin Research*, 20(2):227–248.

Bueler, E. and Brown, J. (2009). Shallow shelf approximation as a sliding law in a thermomechanically coupled ice sheet model. *Journal of Geophysical Research*, 114(F3):1–21.

Calov, R. and Ganopolski, A. (2005). Multistability and hysteresis in the climate-cryosphere system under orbital forcing. *Geophysical Research Letters*, 32(21):4–7.

Camoin, G., Droxler, A., Miller, K. G., and Fulthorpe, C. S. (2009). Quaternary sea-level changes: Records and processes. *Global and Planetary Change*, 66(1-2):v–vii.

Charbit, S., Ritz, C., and Philippon, G. (2007). Numerical reconstructions of the Northern Hemisphere ice sheets through the last glacial-interglacial cycle. *Climate of the Past*, pages 15–37.

Christie-Blick, N., Grotzinger, J., and Von der Borch, C. (1988). Sequence stratigraphy in Proterozoic successions. *Geology*, 16(2):100–104.

Clark, P. U., Alley, R., and Pollard, D. (1999). Northern Hemisphere ice-sheet influences on global climate change. *Science*, 286(5442):1104–1111.

Clark, P. U., Dyke, A. S., Shakun, J. D., Carlson, A. E., Clark, J., Wohlfarth, B., Mitrovica, J. X., Hostetler, S. W., and McCabe, A. M. (2009). The Last Glacial Maximum. *Science*, 325(5941):710–4.

Coggon, R. M., Teagle, D. A. H., Smith-Duque, C. E., Alt, J. C., and Cooper, M. J. (2010). Reconstructing past seawater Mg/Ca and Sr/Ca from mid-ocean ridge flank calcium carbonate veins. *Science*, 327(5969):1114–7.

Connolley, W. M. and Bracegirdle, T. J. (2007). An Antarctic assessment of IPCC AR4 coupled models. *Geophysical Research Letters*, 34(22):L22505.

Conrad, C. P., Lithgow-Bertelloni, C., and Louden, K. E. (2004). Iceland, the Farallon slab, and dynamic topography of the North Atlantic. *Geology*, 32(3):177.

Conte, M. H., Thompson, A., Lesley, D., and Harris, R. P. (1998). Genetic and Physiological Influences on the Alkenone/Alkenoate Versus Growth Temperature Relationship in Emiliania huxleyi and Gephyrocapsa Oceanica. *Geochimica et Cosmochimica Acta*, 62(1):51–68.

Cornford, S. L., Martin, D. F., Graves, D. T., Ranken, D. F., Le Brocq, A. M., Gladstone, R. M., Payne, A. J., Ng, E. G., and Lipscomb, W. H. (2013). Adaptive mesh, finite volume modeling of marine ice sheets. *Journal of Computational Physics*, 232(1):529–549.

Covey, C., Sloan, L. C., and Hoffert, M. I. (1996). Paleoclimate data constraints on climate sensitivity: The paleocalibration method. *Climatic Change*, 32(2):165–184.

Cox, S. E., Thomson, S. N., Reiners, P. W., Hemming, S. R., and van de Flierdt, T. (2010). Extremely low long-term erosion rates around the Gamburtsev Mountains in interior East Antarctica. *Geophysical Research Letters*, 37(22).

Coxall, H. and Pearson, P. (2007). The Eocene-Oligocene transition. In Williams, M., editor, *Deep Time perspectives of Climate Change: Marrying the Signal From Computer Models and Biological Proxies*, pages 351–387. Geological Society, Bath, UK.

Coxall, H. K., Wilson, P. A., Palike, H., Lear, C. H., and Backman, J. (2005). Rapid stepwise onset of Antarctic glaciation and deeper calcite compensation in the Pacific Ocean. *Nature*, 433:53–57.

Cramer, B. S., Miller, K. G., Barrett, P. J., and Wright, J. D. (2011). Late Cretaceous/Neogene trends in deep ocean temperature and continental ice volume: Reconciling records of benthic foraminiferal geochemistry ($\delta$18O and Mg/Ca) with sea level history. *Journal of Geophysical Research*, 116(C12):1–23.

Cramer, B. S., Toggweiler, J. R., Wright, J. D., Katz, M. E., and Miller, K. G. (2009). Ocean overturning since the Late Cretaceous: Inferences from a new benthic foraminiferal isotope compilation. *Paleoceanography*, 24(4):1–14.

Creech, J., Baker, J., and Hollis, C. (2010). Eocene sea temperatures for the mid-latitude southwest Pacific from Mg/Ca ratios in planktonic and benthic foraminifera. *Earth and Planetary Science Letters*, 299(3-4):483–495.

Crowley, T. (1990). Are there any satisfactory geologic analogs for a future greenhouse warming? *Journal of Climate*, 3(11):1282–1292.

Crowley, T., Yip, K., and Baum, S. (1994). Snowline instability in a general circulation model: application to Carboniferous glaciation. *Climate Dynamics*, pages 363–376.

Crucifix, M. (2012). Traditional and novel approaches to palaeoclimate modelling. *Quaternary Science Reviews*, 57:1–16.

Dansgaard, W. (1964). Stable isotopes in precipitation. *Tellus*, 16(4):436–468.

Dawber, C. F. and Tripati, A. K. (2011). Constraints on glaciation in the middle Eocene (46 - 37 Ma) from Ocean Drilling Program (ODP) Site 1209 in the tropical Pacific Ocean. *Paleoceanography*, 26(2):1–17.

Dawber, C. F., Tripati, A. K., Gale, A. S., MacNiocaill, C., and Hesselbo, S. P. (2011). Glacioeustasy during the middle Eocene? Insights from the stratigraphy of the Hampshire Basin, UK. *Palaeogeography, Palaeoclimatology, Palaeoecology*, 300(1-4):84–100.

De Angelis, H. and Skvarca, P. (2003). Glacier surge after ice shelf collapse. *Science*, 299(5612):1560–2.

de Boer, B., van de Wal, R., Bintanja, R., Lourens, L., and Tuenter, E. (2010). Cenozoic global ice-volume and temperature simulations with 1-D ice-sheet models forced by benthic $\delta$18O records. *Annals of Glaciology*, 51(55):23–33.

de Boer, B., van de Wal, R. S., Lourens, L. J., and Bintanja, R. (2012a). Transient nature of the Earth's climate and the implications for the interpretation of benthic records. *Palaeogeography, Palaeoclimatology, Palaeoecology*, 335-336:4–11.

de Boer, B., Wal, R. S. W., Lourens, L. J., Bintanja, R., and Reerink, T. J. (2012b). A continuous simulation of global ice volume over the past 1 million years with 3-D ice-sheet models. *Climate Dynamics*.

DeConto, R., Lear, C., Pagani, M., Pollard, D., Wilson, P., and Palike, H. (2008). Thresholds for Cenozoic bipolar glaciation. *Nature*, 455:652–657.

DeConto, R. and Pollard, D. (2003a). Rapid Cenozoic glaciation of Antarctica induced by declining atmospheric CO2. *Nature*, 421:245–249.

DeConto, R., Pollard, D., and Harwood, D. (2007). Sea ice feedback and Cenozoic evolution of Antarctic climate and ice sheets. *Paleoceanography*, 22(3):1–18.

DeConto, R. M. and Pollard, D. (2003b). A coupled climate ice sheet modeling approach to the Early Cenozoic history of the Antarctic ice sheet. *Palaeogeography, Palaeoclimatology, Palaeoecology*, 198.

Denton, G. H. and Hughes, T. J. (2002). Reconstructing the Antarctic ice sheet at the Last Glacial Maximum. *Quaternary Science Reviews*, 21(1-3):193–202.

Dickson, J. A. D. (2002). Fossil echinoderms as monitor of the Mg/Ca ratio of Phanerozoic oceans. *Science*, 298:1222–1224.

Dolan, A., Haywood, A., and Hill, D. (2011). Sensitivity of Pliocene ice sheets to orbital forcing. *Palaeogeography, Palaeoclimatology, Palaeoecology*, 309(1-2):98–110.

Dolan, A. M., Koenig, S. J., Hill, D. J., Haywood, A. M., and DeConto, R. M. (2012). Pliocene Ice Sheet Modelling Intercomparison Project (PLISMIP) experimental design. *Geoscientific Model Development*, 5(4):963–974.

Domack, E., Duran, D., Leventer, A., Ishman, S., Doane, S., McCallum, S., Amblas, D., Ring, J., Gilbert, R., and Prentice, M. (2005). Stability of the Larsen B ice shelf on the Antarctic Peninsula during the Holocene epoch. *Nature*, 436(7051):681–5.

Dowsett, H. J. and Cronin, T. M. (1990). High eustatic sea level during the middle Pliocene: Evidence from the southeastern U.S. Atlantic Coastal Plain. *Geology*, 18:435–438.

Dowsett, H. J., Thompson, R., Barron, J., Cronin, T., Fleming, F., Ishman, S., Poore, R., Willard, D., and Holtz, T. (1994). Joint investigations of the Middle Pliocene climate I: PRISM paleoenvironmental reconstructions. *Global and Planetary Change*, 9(3-4):169–195.

Dupont-Nivet, G., Krijgsman, W., Langereis, C. G., Abels, H. A., Dai, S., and Fang, X. (2007). Tibetan plateau aridification linked to global cooling at the Eocene-Oligocene transition. *Nature*, 445(7128):635–8.

Dutton, A., Lohmann, K., and Leckie, R. (2005). Insights from the Paleogene tropical Pacific: Foraminiferal stable isotope and elemental results from Site 1209, Shatsky Rise. *Paleoceanography*, 20(3):PA3004.

Dyke, A. (2002). The Laurentide and Innuitian ice sheets during the Last Glacial Maximum. *Quaternary Science Reviews*, 21(1-3):9–31.

Dyke, A. (2004). An outline of North American deglaciation with emphasis on central and northern Canada. *Developments in Quaternary Sciences*.

Eisenman, I. and Wettlaufer, J. S. (2009). Nonlinear threshold behavior during the loss of Arctic sea ice. *PNAS*, 106(1):28–32.

El Fadli, K. I., Cerveny, R. S., Burt, C. C., Eden, P., Parker, D., Brunet, M., Peterson, T. C., Mordacchini, G., Pelino, V., Bessemoulin, P., Stella, J. L., Driouech, F., Wahab, M. A., and Pace, M. B. (2012). World Meteorological Organization Assessment of the purported World record 58C temperature extreme at El Azizia, Libya (13 September 1922). *Bulletin of the American Meteorological Society*.

Elderfield, H., Ferretti, P., Greaves, M., Crowhurst, S., McCave, I., Hodell, D., and Piotrowski, A. (2012). Evolution of ocean temperature and ice volume through the Mid-Pleistocene climate transition. *Science*, 337:704–709.

Elderfield, H., Greaves, M., Barker, S., Hall, I., Tripati, A., Ferretti, P., Crowhurst, S., Booth, L., and Daunt, C. (2010). A record of bottom water temperature and seawater $\delta18O$ for the Southern Ocean over the past 440kyr based on Mg/Ca of benthic foraminiferal Uvigerina spp. *Quaternary Science Reviews*, 29(1-2):160–169.

Eldrett, J. S., Greenwood, D. R., Harding, I. C., and Huber, M. (2009). Increased seasonality through the Eocene to Oligocene transition in northern high latitudes. *Nature*, 459(7249):969–73.

Eldrett, J. S., Harding, I. C., Wilson, P. A., Butler, E., and Roberts, A. P. (2007). Continental ice in Greenland during the Eocene and Oligocene. *Nature*, 446(7132):176–9.

European Commission (2007). Limiting global climate change to 2 degrees Celsius - the way ahead for 2020 and beyond. (last accessed: 19/02/13) http://eur-lex.europa.eu/LexUriServ/LexUriServ.do?uri=COM:2007:0002:FIN:EN:PDF.

Evans, D. and Müller, W. (2012). Deep time foraminifera Mg/Ca paleothermometry: Nonlinear correction for secular change in seawater Mg/Ca. *Paleoceanography*, 27(4):PA4205.

Fairbanks, R. (1989). A 17,000-year glacio-eustatic sea level record: influence of glacial melting rates on the Younger Dryas event and deep-ocean circulation. *Nature*, 343:637–642.

Fitzgerald, P. (2002). Landscape evolution of the Antarctic plate since the breakup of Gondwana, with an emphasis on the West Antarctic Rift System and the Transantarctic Mountains. *Royal Society of New Zealand Bulletin*, pages 453–469.

Flower, B. and Kennett, J. (1994). The middle Miocene climatic transition: East Antarctic ice sheet development, deep ocean circulation and global carbon cycling. *Palaeogeography, Palaeoclimatology, Palaeoecology*, 108.

Foster, G. L., Lear, C. H., and Rae, J. W. (2012). The evolution of pCO2, ice volume and climate during the middle Miocene. *Earth and Planetary Science Letters*, 341-344:243–254.

Foster, G. L. and Rohling, E. J. (2013). Relationship between sea level and climate forcing by CO2 on geological timescales. *PNAS*, 110(4).

Fretwell, P., Pritchard, H. D., Vaughan, D. G., Bamber, J. L., Barrand, N. E., Bell, R., Bianchi, C., Bingham, R. G., Blankenship, D. D., Casassa, G., Catania, G., Callens, D., Conway, H., Cook, a. J., Corr, H. F. J., Damaske, D., Damm, V., Ferraccioli, F., Forsberg, R., Fujita, S., Gim, Y., Gogineni, P., Griggs, J. a., Hindmarsh, R. C. a., Holmlund, P., Holt, J. W., Jacobel, R. W., Jenkins, a., Jokat, W., Jordan, T., King, E. C., Kohler, J., Krabill, W., Riger-Kusk, M., Langley, K. a., Leitchenkov, G., Leuschen, C., Luyendyk, B. P., Matsuoka, K., Mouginot, J., Nitsche, F. O., Nogi, Y., Nost, O. a., Popov, S. V., Rignot, E., Rippin, D. M., Rivera, a., Roberts, J., Ross, N., Siegert, M. J., Smith, a. M., Steinhage, D., Studinger, M., Sun, B., Tinto, B. K., Welch, B. C., Wilson, D., Young, D. a., Xiangbin, C., and Zirizzotti, a. (2013). Bedmap2: improved ice bed, surface and thickness datasets for Antarctica. *The Cryosphere*, 7(1):375–393.

Gallagher, S. J., Villa, G., Drysdale, R., Wade, B., Scher, H., Li, Q., Wallace, M. W., and Holdgate, G. (2012). A near field sea level record of East Antarctic Ice Sheet instability from 32 to 27 million years ago. *Paleoceanography*, 28:1–13.

Ganopolski, A., Calov, R., and Claussen, M. (2010). Simulation of the last glacial cycle with a coupled climate ice-sheet model of intermediate complexity. *Climate of the Past*, 6:229–244.

Gasson, E., Siddall, M., Lunt, D., Rackham, O. J. L., Lear, C. H., and Pollard, D. (2012). Exploring uncertainties in the relationship between temperature, ice volume, and sea level over the past 50 million years. *Reviews of Geophysics*, 50(RG1005):1–35.

Gebbie, G. and Huybers, P. (2011). How is the ocean filled? *Geophysical Research Letters*, 38(6):L06604.

Goldner, A., Huber, M., and Caballero, R. (2012). Does Antarctic glaciation cool the world? *Climate of the Past Discussions*, 8(4):2645–2693.

Gordon, C., Cooper, C., and Senior, C. (2000). The simulation of SST, sea ice extents and ocean heat transports in a version of the Hadley Centre coupled model without flux adjustments. *Climate Dynamics*.

Grassl, H. (2011). Climate change challenges. *Surveys in Geophysics*, 32(4-5):319–328.

Gregoire, L. J. (2010). *Modelling the Northern Hemisphere climate and ice sheets during the last deglaciation*. PhD thesis, University of Bristol.

Gregoire, L. J., Payne, A. J., and Valdes, P. J. (2012). Deglacial rapid sea level rises caused by ice-sheet saddle collapses. *Nature*, 487(7406):219–222.

Grinsted, A., Moore, J. C., and Jevrejeva, S. (2008). Reconstructing sea level from paleo and projected temperatures 200 to 2100. *Climate Dynamics*.

Gulledge, J., Victor, D., and Hefner, R. (2008). Climate change risks in the context of scientific uncertainty. In *The Global Politics of Energy*, pages 114–132. The Aspen Institute.

Gulsen, M., Smith, A. E., and Tate, D. M. (1995). A genetic algorithm approach to curve fitting. *International Journal of Production Research*, 33(7):1911–1923.

Haq, B. U., Hardenbol, J., and Vail, P. R. (1987). Chronology of fluctuating sea levels since the triassic. *Science*, 235(4793):1156–67.

Hasiuk, F. J. and Lohmann, K. C. (2010). Application of calcite Mg partitioning functions to the reconstruction of paleocean Mg/Ca. *Geochimica et Cosmochimica Acta*, 74(23):6751–6763.

Hauptvogel, D. W. and Passchier, S. (2012). Early Middle Miocene (17 to 14Ma) Antarctic ice dynamics reconstructed from the heavy mineral provenance in the AND-2A drill core, Ross Sea, Antarctica. *Global and Planetary Change*, 82-83:38–50.

Hays, J. D., Imbrie, J., and Shackleton, N. J. (1976). Variations in the Earth's orbit: pacemaker of the ice ages. *Science*, 194(4270):1121–32.

Haywood, A., Lunt, D., and Valdes, P. (2010). HadCM3L predictions of ocean temperature response to the growth of the Antarctic ice sheet during the Early Oligocene. In *EGU General Assembly 2010*, volume 12, page 4347.

Haywood, A. M., Ridgwell, A., Lunt, D. J., Hill, D. J., Pound, M. J., Dowsett, H. J., Dolan, A. M., Francis, J. E., and Williams, M. (2011). Are there pre-Quaternary geological analogues for a future greenhouse warming? *Philosophical Transactions of the Royal Society A: Mathematical, Physical and Engineering Sciences*, 369(1938):933–956.

Hebeler, F., Purves, R., and Jamieson, S. (2008). The impact of parametric uncertainty and topographic error in ice-sheet modelling. *Journal of Glaciology*, 44(188).

Heinemann, M., Jungclaus, J., and Marotzke, J. (2009). Warm Paleocene/Eocene climate as simulated in ECHAM5/MPI-OM. *Climate of the Past*, 5(1987):785–802.

Herbert, T. (2003). Alkenone paleotemperature determinations. In Holland, H. and Turekian, K., editors, *Treatise on geochemistry*, volume 6, pages 391–432. Elsevier.

Herbert, T., Peterson, L., Lawrence, K., and Liu, Z. (2010). Tropical ocean temperatures over the past 3.5 million years. *Science*, 328(5985):1530.

Hill, D., Haywood, A., Hindmarsh, R., and Valdes, P. (2007). Characterising ice sheets during the mid Pliocene: evidence from data and models. In Williams, M., Haywood, A., Gregory, F., and Schmidt, D., editors, *Deep time perspectives on climate change: marrying the signal from computer models and biological proxies*, pages 517–538. Geological Scoiety of London, London.

Hill, D., Haywood, A., Lunt, D., Otto-Bliesner, B., Harrison, S., and Braconnot, P. (2012). Paleoclimate modeling: an integrated component of climate change science. *PAGES news*, 20(2):103.

Hill, D., Haywood, A., Valdes, P., Francis, J., Lunt, D., Wade, B., and Bowman, V. (2013). Paleogeographic controls on the onset of the Antarctic Circumpolar Current. *Journal of Geophysical Research (in review)*.

Hock, R. (2003). Temperature index melt modelling in mountain areas. *Journal of Hydrology*, 282(1-4):104–115.

Hofer, D., Raible, C. C., Dehnert, A., and Kuhlemann, J. (2012). The impact of different glacial boundary conditions on atmospheric dynamics and precipitation in the North Atlantic region. *Climate of the Past*, 8(3):935–949.

Holland, P. R., Jenkins, A., and Holland, D. M. (2008). The response of ice shelf basal melting to variations in ocean temperature. *Journal of Climate*, 21(11):2558–2572.

Hollis, C., Handley, L., Crouch, E. M., Morgans, H. E., Baker, J. A., Creech, J. B., Gibbs, S., Huber, M., Schouten, S., Zachos, J. C., and Pancost, R. D. (2009). Tropical sea temperatures in the high-latitude South Pacific during the Eocene. *Geology*, 37(2):99.

Houben, A. J., van Mourik, C. A., Montanari, A., Coccioni, R., and Brinkhuis, H. (2012). The Eocene-Oligocene transition: changes in sea level, temperature or both? *Palaeogeography, Palaeoclimatology, Palaeoecology*, 335-336:75–83.

Huber, M. (2008). A hotter greenhouse? *Science*, 321(5887):353.

Huber, M., Brinkhuis, H., and Stickley, C. E. (2004). Eocene circulation of the Southern Ocean: Was Antarctica kept warm by subtropical waters? *Paleoceanography*, 19(4):1–12.

X

Huber, M. and Caballero, R. (2011). The early Eocene equable climate problem revisited. *Climate of the Past*, 7(2):603–633.

Huber, M. and Knutti, R. (2011). Anthropogenic and natural warming inferred from changes in Earth's energy balance. *Nature Geoscience*, 5(1):31–36.

Huber, M. and Nof, D. (2006). The ocean circulation in the southern hemisphere and its climatic impacts in the Eocene. *Palaeogeography, Palaeoclimatology, Palaeoecology*, 231(1-2):9–28.

Huguet, C., Cartes, J., Sinninghe Damsté, J. S., and Schouten, S. (2006). Marine crenarchaeotal membrane lipids in decapods: Implications for the TEX86 paleothermometer. *Geochemistry Geophysics Geosystems*, 7(11).

Huguet, C., Kim, J., de Lange, G., Sinninghe Damsté, J., and Schouten, S. (2009). Effects of long term oxic degradation on the Uk'37, TEX86 and BIT organic proxies. *Organic Geochemistry*, 40(12):1188–1194.

Huguet, C., Schimmelmann, A., Thunell, R., Lourens, L., Damsté, J., and Schouten, S. (2007). A study of the TEX86 paleothermometer in the water column and sediments of the Santa Barbara Basin, California. *Paleoceanography*, 22(3):PA3203.

Hulme, M. (2012). On the 'two degrees' climate policy target. In Edenhofer, O., Wallacher, J., Lotze-Campen, H., Reder, M., Knopf, B., and Müller, J., editors, *Climate Change, Justice and Sustainability: Linking Climate and Development Policy*, pages 122–125. Springer Netherlands, Dordrecht.

Hutter, K. (1983). *Theoretical glaciology - material science of ice and the mechanics of glaciers and ice sheets*. D. Reidel Publishing Company, Dordrecht.

Huybrechts, P. (1993). Glaciological modelling of the late Cenozoic East Antarctic ice sheet: stability or dynamism? *Geografiska Annaler. Series A, Physical Geography*, 75(4):221.

Huybrechts, P. (2002). Sea-level changes at the LGM from ice-dynamic reconstructions of the Greenland and Antarctic ice sheets during the glacial cycles. *Quaternary Science Reviews*, 21(1-3):203–231.

Huybrechts, P. and de Wolde, J. (1999). The dynamic response of the Greenland and Antarctic ice sheets to multiple-century climatic warming. *Journal of Climate*, pages 2169–2188.

Iman, R. and Helton, J. (1985). A comparison of uncertainty and sensitivity analysis techniques for computer models. Technical report, Sandia National Laboratories, Albuquerque NM.

Jaeger, C., Schellnhuber, H., and Brovkin, V. (2008). Stern's review and Adam's fallacy. *Climatic Change*.

Jamieson, S. S., Sugden, D. E., and Hulton, N. R. (2010). The evolution of the subglacial landscape of Antarctica. *Earth and Planetary Science Letters*, 293(1-2):1–27.

John, C., Karner, G., Browning, E., Leckie, R., Mateo, Z., Carson, B., and Lowery, C. (2011). Timing and magnitude of Miocene eustasy derived from the mixed siliciclastic-carbonate stratigraphic record of the northeastern Australian margin. *Earth and Planetary Science Letters*, 304(3-4):455–467.

Joughin, I. and Alley, R. B. (2011). Stability of the West Antarctic ice sheet in a warming world. *Nature Geoscience*, 4(8):506–513.

Jouzel, J., Masson-Delmotte, V., Cattani, O., Dreyfus, G., Falourd, S., Hoffmann, G., Minster, B., Nouet, J., Barnola, J. M., Chappellaz, J., Fischer, H., Gallet, J. C., Johnsen, S., Leuenberger, M., Loulergue, L., Luethi, D., Oerter, H., Parrenin, F., Raisbeck, G., Raynaud, D., Schilt, A., Schwander, J., Selmo, E., Souchez, R., Spahni, R., Stauffer, B., Steffensen, J. P., Stenni, B., Stocker, T. F., Tison, J. L., Werner, M., and Wolff, E. W. (2007). Orbital and millennial Antarctic climate variability over the past 800,000 years. *Science*, 317(5839):793–6.

Karner, M. B., DeLong, E. F., and Karl, D. M. (2001). Archaeal dominance in the mesopelagic zone of the Pacific Ocean. *Nature*, 409(6819):507–10.

Katz, M. E., Cramer, B. S., Toggweiler, J. R., Esmay, G., Liu, C., Miller, K. G., Rosenthal, Y., Wade, B. S., and Wright, J. D. (2011). Impact of Antarctic circumpolar current development on late Paleogene ocean structure. *Science*, 332(6033):1076–1079.

Katz, M. E., Miller, K. G., Wright, J. D., Wade, B. S., Browning, J. V., Cramer, B. S., and Rosenthal, Y. (2008). Stepwise transition from the Eocene greenhouse to the Oligocene icehouse. *Nature Geoscience*, 1(5):329–334.

Kaufman, D. and Brigham-Grette, J. (1993). Aminostratigraphic correlations and paleotemperature implications, Pliocene-Pleistocene high-sea-level deposits, northwestern Alaska. *Quaternary Science Reviews*, 12:21–33.

Keating-Bitonti, C., Ivany, L., Affek, H., Douglas, P., and Samson, S. (2011). Warm, not super-hot, temperatures in the early Eocene subtropics. *Geology*, 39(8):771–774.

Kennett, J. (1977). Cenozoic evolution of Antarctic glaciation, the circum-Antarctic Ocean, and their impact on global paleoceanography. *Journal of geophysical research*, 82(27):3843–3860.

Kim, J., Schouten, S., Hopmans, E., Donner, B., and Sinninghe Damsté, J. (2008). Global sediment core-top calibration of the TEX86 paleothermometer in the ocean. *Geochimica et Cosmochimica Acta*, 72(4):1154–1173.

Kim, J.-H., van der Meer, J., Schouten, S., Helmke, P., Willmott, V., Sangiorgi, F., Koç, N., Hopmans, E. C., and Damsté, J. S. S. (2010). New indices and calibrations derived from the distribution of crenarchaeal isoprenoid tetraether lipids: Implications for past sea surface temperature reconstructions. *Geochimica et Cosmochimica Acta*, 74(16):4639–4654.

Koenig, S. J., DeConto, R. M., and Pollard, D. (2012). Pliocene Model Intercomparison Project Experiment 1: implementation strategy and mid-Pliocene global climatology using GENESIS v3.0 GCM. *Geoscientific Model Development*, 5(1):73–85.

Kominz, M. A., Browning, J. V., Miller, K. G., Sugarman, P. J., Mizintseva, S., and Scotese, C. R. (2008). Late Cretaceous to Miocene sea-level estimates from the New Jersey and Delaware coastal plain coreholes: an error analysis. *Basin Research*, 20(2):211–226.

Kominz, M. A. and Pekar, S. F. (2001). Geological Society of America Bulletin. *Geological Society Of America Bulletin*.

Krinner, G. and Genthon, C. (1999). Altitude dependence of the ice sheet surface climate. *Geophysical Research Letters*, 26(15):2227–2230.

Krystek, M. and Anton, M. (2007). A weighted total least-squares algorithm for fitting a straight line. *Measurement Science and Technology*, 18(11):3438–3442.

Kürschner, W. (2008). The impact of Miocene atmospheric carbon dioxide fluctuations on climate and the evolution of terrestrial ecosystems. *PNAS*, 105(2).

Lakse, G. and Masters, G. (1997). A global digital map of sediment thickness. *EOS Trans, AGU*, 78(F483).

Lambeck, K. (1996). Limits on the areal extent of the Barents Sea ice sheet in Late Weichselian time. *Global and Planetary Change*, 12:41–51.

Lambeck, K. and Nakiboglu, S. (1980). Seamount loading and stress in the ocean lithosphere. *J. geophys. Res*, 85(80):6403–6418.

Langebroek, P. M., Paul, A., and Schulz, M. (2009). Antarctic ice-sheet response to atmospheric CO2 and insolation in the Middle Miocene. *Climate of the Past*, 5(4):633–646.

Larson, R. (1991). Geological consequences of superplumes. *Geology*, 19:963–966.

Laskar, J., Robutel, P., Joutel, F., Gastineau, M., Correia, A. C. M., and Levrard, B. (2004). A long-term numerical solution for the insolation quantities of the Earth. *Astronomy & Astrophysics*, 285:261–285.

Lea, D., Mashiotta, T., and Spero, H. (1999). Controls on magnesium and strontium uptake in planktonic foraminifera determined by live culturing. *Geochimica et Cosmochimica Acta*, 63(16):2369–2379.

Lear, C. (2007). Mg/Ca palaeothermometry: a new window into Cenozoic climate change. In Williams, M., Haywood, A., Gregory, F., and Schmidt, D., editors, *Deep Time perspectives of Climate Change: Marrying the Signal From Computer Models and Biological Proxies*, pages 1–25. Geological Society of London, London.

Lear, C., Elderfield, H., and Wilson, P. (2000). Cenozoic deep-sea temperatures and global ice volumes from Mg/Ca in benthic foraminiferal calcite. *Science*, 287:269–272.

Lear, C. H., Bailey, T. R., Pearson, P. N., Coxall, H. K., and Rosenthal, Y. (2008). Cooling and ice growth across the Eocene-Oligocene transition. *Geology*, 36(3):251.

Lear, C. H., Mawbey, E. M., and Rosenthal, Y. (2010). Cenozoic benthic foraminiferal Mg/Ca and Li/Ca records: Toward unlocking temperatures and saturation states. *Paleoceanography*, 25(4):1–11.

Lear, C. H., Rosenthal, Y., Coxall, H., and Wilson, P. (2004). Late Eocene to early Miocene ice sheet dynamics and the global carbon cycle. *Paleoceanography*, 19(4):1–11.

Lee, W. (1970). On the global variations of terrestrial heat-flow. *Physics of the Earth and Planetary Interiors*, 2:332–341.

Lemke, P., Ren, J., Alley, R., Allison, I., Carrasco, J., Flato, G., Fujii, Y., Kaser, G., Mote, P., Thomas, R., and Zhang, T. (2007). Observations: Changes in snow, ice and frozen ground. In Solomon, S., Qin, D., Manning, M., Chen, Z., Marquis, M., Averyt, K., Tignor, M., and Miller, H., editors, *Climate Change 2007: The Physical Science Basis. Contribution of Working Group I to the Fourth Assessment Report of the Intergovernmental Panel on Climate Change*. Cambridge University Press, Cambridge, UK.

Lewis, A. R., Marchant, D. R., Ashworth, A. C., Hedenäs, L., Hemming, S. R., Johnson, J. V., Leng, M. J., Machlus, M. L., Newton, A. E., Raine, J. I., Willenbring, J. K., Williams, M., and Wolfe, A. P. (2008). Mid-Miocene cooling and the extinction of tundra in continental Antarctica. *PNAS*, 105(31):10676–80.

Liebrand, D., Lourens, L. J., Hodell, D. A., de Boer, B., van de Wal, R. S. W., and Pälike, H. (2011). Antarctic ice sheet and oceanographic response to eccentricity forcing during the early Miocene. *Climate of the Past*, 7(3):869–880.

Lisiecki, L. and Raymo, M. (2005). A Pliocene-Pleistocene stack of 57 globally distributed benthic $\delta18O$ records. *Paleoceanography*, 20:1–17.

Liu, Z., Pagani, M., Zinniker, D., Deconto, R., Huber, M., Brinkhuis, H., Shah, S. R., Leckie, R. M., and Pearson, A. (2009). Global cooling during the Eocene-Oligocene climate transition. *Science*, 323(5918):1187–90.

Livermore, R., Nankivell, A., Eagles, G., and Morris, P. (2005). Paleogene opening of Drake Passage. *Earth and Planetary Science Letters*, 236(1-2):459–470.

Lowenstein, T. K., Timofeeff, M. N., Brennan, S. T., Hardie, L. A., and Demicco, R. V. (2001). Oscillations in Phanerozoic seawater chemistry: evidence from fluid inclusions. *Science*, 294(5544):1086–8.

Lunt, D., Foster, G., Haywood, A., and Stone, E. (2008). Late Pliocene Greenland glaciation controlled by a decline in atmospheric CO2 levels. *Nature*, 454:1102–1106.

Lunt, D., Haywood, A., Schmidt, G., Salzmann, U., Valdes, P., and Dowsett, H. (2010a). Earth system sensitivity inferred from Pliocene modelling and data. *Nature Geoscience*, 3:60–64.

Lunt, D. J., Dunkley Jones, T., Heinemann, M., Huber, M., LeGrande, A., Winguth, A., Loptson, C., Marotzke, J., Roberts, C. D., Tindall, J., Valdes, P., and Winguth, C. (2012). A model-data comparison for a multi-model ensemble of early Eocene atmosphere-ocean simulations: EoMIP. *Climate of the Past*, 8(5):1717–1736.

Lunt, D. J., Ridgwell, A., Sluijs, A., Zachos, J., Hunter, S., and Haywood, A. (2011). A model for orbital pacing of methane hydrate destabilization during the Palaeogene. *Nature Geoscience*, 4(11):775–778.

Lunt, D. J., Ross, I., Hopley, P. J., and Valdes, P. J. (2007). Modelling Late Oligocene C4 grasses and climate. *Palaeogeography, Palaeoclimatology, Palaeoecology*, 251(2):239–253.

Lunt, D. J., Valdes, P. J., Jones, T. D., Ridgwell, A., Haywood, A. M., Schmidt, D. N., Marsh, R., and Maslin, M. (2010b). CO2-driven ocean circulation changes as an amplifier of Paleocene-Eocene thermal maximum hydrate destabilization. *Geology*, 38(10):875–878.

Lüthi, D., Le Floch, M., Bereiter, B., Blunier, T., Barnola, J.-M., Siegenthaler, U., Raynaud, D., Jouzel, J., Fischer, H., Kawamura, K., and Stocker, T. F. (2008). High-resolution carbon dioxide concentration record 650,000-800,000 years before present. *Nature*, 453(7193):379–82.

Lythe, M. and Vaughan, D. (2001). BEDMAP: A new ice thickness and subglacial topographic model of Antarctica. *Journal of Geophysical Research*, 106(B6):11335–11351.

Mackintosh, A., Golledge, N., Domack, E., Dunbar, R., Leventer, A., White, D., Pollard, D., DeConto, R., Fink, D., Zwartz, D., Gore, D., and Lavoie, C. (2011). Retreat of the East Antarctic ice sheet during the last glacial termination. *Nature Geoscience*, 4(3):195–202.

Markwick, P. (1998). Fossil crocodilians as indicators of Late Cretaceous and Cenozoic climates: implications for using palaeontological data in reconstructing palaeoclimate. *Palaeogeography, Palaeoclimatology, Palaeoecology*, 137(3-4):205–271.

Marlowe, I. (1984). *Lipids as paleoclimatic indicators*. Phd, University of Bristol.

Marlowe, I., Brassell, S., Eglinton, G., and Green, J. (1990). Long-chain alkenones and alkyl alkenoates and the fossil coccolith record of marine sediments. *Chemical Geology*, 88(3-4):349–375.

Marshall, S. J. (2002). Basal temperature evolution of North American ice sheets and implications for the 100-kyr cycle. *Geophysical Research Letters*, 29(24):2214.

Marshall, S. J., James, T. S., and Clarke, G. K. (2002). North American ice sheet reconstructions at the Last Glacial Maximum. *Quaternary Science Reviews*, 21(1-3):175–192.

Martin, P. A., Lea, D. W., Rosenthal, Y., Shackleton, N. J., Sarnthein, M., and Papenfuss, T. (2002). Quaternary deep sea temperature histories derived from benthic foraminiferal Mg/Ca. *Earth and Planetary Science Letters*, 198(1-2):193–209.

Martinson, D., Pisias, N., and Hays, J. (1987). Age dating and the orbital theory of the ice ages: Development of a high-resolution 0 to 300,000-year chronostratigraphy. *Quaternary Research*, 29:1–29.

Matthews, R. and Poore, R. (1980). Tertiary $\delta$18O record and glacio-eustatic sea-level fluctuations. *Geology*, 8:501–504.

McGranahan, G., Balk, D., and Anderson, B. (2007). The rising tide: assessing the risks of climate change and human settlements in low elevation coastal zones. *Environment and Urbanization*, 19(1):17–37.

McGuffie, K. and Henderson-Sellers, A. (2005). *A Climate Modelling Primer*. Wiley, Chichester, 3rd edition.

McKay, M., Beckman, R., and Conover, W. (1979). A comparison of three methods for selecting values of input variables in the analysis of output from a computer code. *Technometrics*, 21(2):239–245.

Medina-Elizalde, M. and Lea, D. (2005). The mid-Pleistocene transition in the Tropical Pacific. *Science*, 310(5750):1009.

Mengel, J., Short, D., and North, G. (1988). Seasonal snowline instability in an energy balance climate model. *Climate Dynamics*, 1:127–131.

Mercer, J. (1978). West Antarctic ice sheet and CO2 greenhouse effect: a threat of disaster. *Nature*, 271(26):321–325.

Merlis, T. M. and Khatiwala, S. (2008). Fast dynamical spin-up of ocean general circulation models using Newton-Krylov methods. *Ocean Modelling*, 21(3-4):97–105.

Miall, A. (1992). Exxon global cycle chart: An event for every occasion? *Geology*, 20(9):787.

Micheels, A., Bruch, A. A., Uhl, D., Utescher, T., and Mosbrugger, V. (2007). A Late Miocene climate model simulation with ECHAM4/ML and its quantitative validation with terrestrial proxy data. *Palaeogeography, Palaeoclimatology, Palaeoecology*, 253(1-2):251–270.

Miller, K., Fairbanks, R., and Mountain, G. (1987). Tertiary oxygen isotope synthesis, sea level history, and continental margin erosion. *Paleoceanography*, 2(1):1–19.

Miller, K., Kominz, M., and Browning, J. (2005a). The Phanerozoic record of global sea-level change. *Science*, 310(1293).

Miller, K., Mountain, G., Browning, J., Kominz, M., Sugarman, P., Christie-Blick, N., Katz, M., and Wright, J. (1998). Cenozoic global sea level, sequences, and the New Jersey transect: results from coastal plain and continental slope drilling. *Reviews of Geophysics*, 36(4):569–601.

Miller, K., Wright, J., and Browning, J. (2005b). Visions of ice sheets in a greenhouse world. *Marine Geology*, 217(3-4):215–231.

Miller, K., Wright, J., and Fairbanks, R. (1991). Unlocking the ice house: Oligocene-Miocene oxygen isotopes, eustasy, and margin erosion. *Journal of Geophysical Research*, 96:6829–6848.

Miller, K., Wright, J., Katz, M., Browning, J., Cramer, B., Wade, B., and Mizintseva, S. (2008a). A view of Antarctic ice-sheet evolution from sea-level and deep-sea isotope changes during the Late Cretaceous-Cenozoic. In *Antarctica: A Keystone in a Changing World-Proceedings of the 10th International Symposium on Antarctic Earth Sciences*, pages 55–70.

Miller, K. G., Browning, J. V., Aubry, M.-P., Wade, B. S., Katz, M. E., Kulpecz, A. A., and Wright, J. D. (2008b). Eocene-Oligocene global climate and sea-level changes: St. Stephens Quarry, Alabama. *Geological Society of America Bulletin*, 120(1):34.

Miller, K. G., Sugarman, P. J., Browning, J. V., Horton, B. P., Stanley, A., Kahn, A., Uptegrove, J., and Aucott, M. (2009a). Sea-level rise in New Jersey over the past 5000 years: Implications to anthropogenic changes. *Global and Planetary Change*, 66(1-2):10–18.

Miller, K. G., Wright, J. D., Browning, J. V., Kulpecz, A., Kominz, M., Naish, T. R., Cramer, B. S., Rosenthal, Y., Peltier, W. R., and Sosdian, S. (2012). High tide of the warm Pliocene: Implications of global sea level for Antarctic deglaciation. *Geology*, G32869:1–4.

Miller, K. G., Wright, J. D., Katz, M. E., Wade, B. S., Browning, J. V., Cramer, B. S., and Rosenthal, Y. (2009b). Climate threshold at the Eocene-Oligocene transition: Antarctic ice sheet influence on ocean circulation. In Koeberl, C. and Montanari, A., editors, *SPE452: The Late Eocene EarthHothouse, Icehouse, and Impacts*, volume 80301, pages 169–178. Geological Society of America.

Mitrovica, J. X., Gomez, N., and Clark, P. U. (2009). The sea-level fingerprint of West Antarctic collapse. *Science*, 323(5915):753.

Mitrovica, J. X., Tamisiea, M. E., Davis, J. L., and Milne, G. A. (2001). Recent mass balance of polar ice sheets inferred from patterns of global sea-level change. *Nature*, 409(6823):1026–9.

Monnin, E., Indermühle, A., Dällenbach, A., Flückiger, J., Stauffer, B., Stocker, T. F., Raynaud, D., and Barnola, J. M. (2001). Atmospheric CO2 concentrations over the last glacial termination. *Science*, 291(5501):112–4.

Moran, K., Backman, J., Brinkhuis, H., Clemens, S. C., Cronin, T., Dickens, G. R., Eynaud, F., Gattacceca, J., Jakobsson, M., Jordan, R. W., Kaminski, M., King, J., Koc, N., Krylov, A., Martinez, N., Matthiessen, J., McInroy, D., Moore, T. C., Onodera, J., O'Regan, M., Pälike, H., Rea, B., Rio, D., Sakamoto, T., Smith, D. C., Stein, R., St John, K., Suto, I., Suzuki, N., Takahashi, K., Watanabe, M., Yamamoto, M., Farrell, J., Frank, M., Kubik, P., Jokat, W., and Kristoffersen, Y. (2006). The Cenozoic palaeoenvironment of the Arctic Ocean. *Nature*, 441(7093):601–5.

Morlighem, M., Rignot, E., Seroussi, H., Larour, E., Ben Dhia, H., and Aubry, D. (2010). Spatial patterns of basal drag inferred using control methods from a full-Stokes and simpler models for Pine Island Glacier, West Antarctica. *Geophysical Research Letters*, 37(14):1–6.

Muller, P., Kirst, G., Ruhland, G., Von Storch, I., and Rosell-Melé, A. (1998). Calibration of the alkenone paleotemperature index Uk37' based on core-tops from the eastern South Atlantic and the global ocean (60 N-60 S). *Geochimica et Cosmochimica Acta*, 62(10):1757–1772.

Müller, R., Sdrolias, M., and Gaina, C. (2008). Long-term sea-level fluctuations driven by ocean basin dynamics. *Science*, 319(1357).

Naish, T. R. and Wilson, G. S. (2009). Constraints on the amplitude of Mid-Pliocene (3.6 - 2.4 Ma) eustatic sea-level fluctuations from the New Zealand shallow-marine sediment record. *Philosophical transactions. Series A, Mathematical, physical, and engineering sciences*, 367(1886):169–87.

Najjar, R. G. (2002). Modeling geographic impacts on early Eocene ocean temperature. *Geophysical Research Letters*, 29(15):2–5.

Nicholas, C. J., Pearson, P. N., Bown, P. R., Dunkley, T., Huber, B. T., Karega, A., Lees, J. A., Mcmillan, I. K., Halloran, A. O., Singano, J. M., and Wade, B. S. (2006). Stratigraphy and sedimentology of the Upper Cretaceous to Paleogene Kilwa Group, southern coastal Tanzania. *Journal of African Earth Sciences*, 45:431–466.

Nong, G. T., Najjar, R. G., Seidov, D., and Peterson, W. H. (2000). Simulation of ocean temperature change due to the opening of Drake Passage. *Geophysical Research Letters*, 27(17):2689.

Nordhaus, W. (1979). Strategies for the control of carbon dioxide. In *The efficient use of energy resources*. Yale University Press, New Haven.

North, G. (1975). Theory of energy balance climate models. *Journal of the Atmospheric Sciences*, 32(11):2033–2043.

North, G. (1984). The small ice cap instability in diffusive climate models. *Journal of the Atmospheric Sciences*, 41(23):3390–3395.

Notz, D. (2009). The future of ice sheets and sea ice: Between reversible retreat and unstoppable loss. *PNAS*, 106(49):20590–20595.

Nurnberg, D., Bijma, J., and Hemleben, C. (1996). Assessing the reliability of magnesium in foraminiferal calcite as a proxy for water mass temperatures. *Geochimica et Cosmochimica Acta*, 60(5):803–814.

Oerlemans, J. (1981). Some basic experiments with a vertically-integrated ice sheet model. *Tellus*, 33:1–11.

Oerlemans, J. (1982). Glacial cycles and ice-sheet modelling. *Climatic Change*, 4(4):353–374.

Oerlemans, J. (2002). On glacial inception and orography. *Quaternary International*, 95:5–10.

Oerlemans, J. (2004). Correcting the Cenozoic $\delta18O$ deep-sea temperature record for Antarctic ice volume. *Palaeogeography, Palaeoclimatology, Palaeoecology*, 208(3):195–205.

Orlić, M. and Pasarić, Z. (2013). Semi-empirical versus process-based sea-level projections for the twenty-first century. *Nature Climate Change*, (April):1–4.

Pagani, M., Huber, M., Liu, Z., Bohaty, S. M., Henderiks, J., Sijp, W., Krishnan, S., and Deconto, R. M. (2011). The role of carbon dioxide during the onset of Antarctic glaciation. *Science*, 334:1261–1264.

Pagani, M., Liu, Z., Lariviere, J., and Ravelo, A. C. (2009). High Earth-system climate sensitivity determined from Pliocene carbon dioxide concentrations. *Science*, 3:27–30.

Pagani, M., Zachos, J. C., Freeman, K. H., Tipple, B., and Bohaty, S. (2005). Marked decline in atmospheric carbon dioxide concentrations during the Paleogene. *Science*, 309(5734):600–3.

Paillard, D. (1998). The timing of Pleistocene glaciations from a simple multiple-state climate model. *Nature*, 391:916–918.

Pälike, H., Norris, R. D., Herrle, J. O., Wilson, P. A., Coxall, H. K., Lear, C. H., Shackleton, N. J., Tripati, A. K., and Wade, B. S. (2006). The heartbeat of the Oligocene climate system. *Science*, 314:1894–8.

Passchier, S., Browne, G., Field, B., Fielding, C. R., Krissek, L. A., Panter, K., and Pekar, S. F. (2011). Early and middle Miocene Antarctic glacial history from the sedimentary facies distribution in the AND-2A drill hole, Ross Sea, Antarctica. *Geological Society of America Bulletin*, 123(11-12):2352–2365.

Pattyn, F., Schoof, C., Perichon, L., Hindmarsh, R. C. A., Bueler, E., de Fleurian, B., Durand, G., Gagliardini, O., Gladstone, R., Goldberg, D., Gudmundsson, G. H., Huybrechts, P., Lee, V., Nick, F. M., Payne, A. J., Pollard, D., Rybak, O., Saito, F., and Vieli, A. (2012). Results of the Marine Ice Sheet Model Intercomparison Project, MISMIP. *The Cryosphere*, 6(3):573–588.

Payne, A. (1995). Limit cycles in the basal thermal regime of ice sheets. *Journal of Geophysical Research*, 100(B3):4249–4263.

Pearson, P., Van Dongen, B., Nicholas, C., Pancost, R., Schouten, S., Singano, J., and Wade, B. (2007). Stable warm tropical climate through the Eocene Epoch. *Geology*, 35(3):211.

Pearson, P. N., Foster, G. L., and Wade, B. S. (2009). Atmospheric carbon dioxide through the Eocene-Oligocene climate transition. *Nature*, 461(7267):1110–3.

Pearson, P. N., McMillan, I. K., Wade, B. S., Jones, T. D., Coxall, H. K., Bown, P. R., and Lear, C. H. (2008). Extinction and environmental change across the Eocene-Oligocene boundary in Tanzania. *Geology*, 36(2):179.

Pearson, P. N. and Palmer, M. R. (2000). Atmospheric carbon dioxide concentrations over the past 60 million years. *Nature*, 406(6797):695–9.

Peck, V. L., Yu, J., Kender, S., and Riesselman, C. R. (2010). Shifting ocean carbonate chemistry during the Eocene-Oligocene climate transition: Implications for deep-ocean Mg/Ca paleothermometry. *Paleoceanography*, 25(4):1–9.

Pekar, S. F., Christie-blick, N., Kominz, M. A., and Miller, K. G. (2002). Calibration between eustatic estimates from backstripping and oxygen isotopic records for the Oligocene. *Geology*, 30(10):903–906.

Pekar, S. F. and DeConto, R. M. (2006). High-resolution ice-volume estimates for the early Miocene: Evidence for a dynamic ice sheet in Antarctica. *Palaeogeography, Palaeoclimatology, Palaeoecology*, 231(1-2):101–109.

Pekar, S. F., Hucks, A., Fuller, M., and Li, S. (2005). Glacioeustatic changes in the early and middle Eocene (51 - 42 Ma): Shallow - water stratigraphy from ODP Leg 189 Site 1171 (South Tasman Rise) and deep-sea $\delta$18O records. *Geological Society of America Bulletin*, 117(7):1081.

Peltier, W. (2004). Global glacial isostasy and the surface of the ice - age Earth: The ICE - 5G (VM2) model and GRACE. *Annual Review of Earth and Planetary Sciences*, 32(1):111–149.

Peltier, W. R. (1974). The impulse response of a Maxwell Earth. *Reviews of Geophysics*, 12(4):649.

Peters, S. E., Carlson, A. E., Kelly, D. C., and Gingerich, P. D. (2010). Large-scale glaciation and deglaciation of Antarctica during the Late Eocene. *Geology*, 38(8):723–726.

Petersen, K. D., Nielsen, S. B., Clausen, O. R., Stephenson, R., and Gerya, T. (2010). Small-scale mantle convection produces stratigraphic sequences in sedimentary basins. *Science*, 329(5993):827–830.

Petit, J., Jouzel, J., Raynaud, D., Barkov, N., Barnola, J., Basile, I., Bender, M., Chappellaz, J., Davis, M., Delaygue, G., Delmotte, M., Kotlyakov, V., Legrand, M., Lipenkov, V., Lorius, C., Pepin, L., Ritz, C., Saltzman, E., and Stievenard, M. (1999). Climate and atmospheric history of the past 420,000 years from the Vostok ice core, Antarctica. *Nature*, 399:429–436.

Pierce, E. L., Williams, T., van de Flierdt, T., Hemming, S. R., Goldstein, S. L., and Brachfeld, S. a. (2011). Characterizing the sediment provenance of East Antarctica's weak underbelly: The Aurora and Wilkes sub-glacial basins. *Paleoceanography*, 26(4):n/a–n/a.

Pollard, D. (1982). A simple ice sheet model yields realistic 100 kyr glacial cycles. *Nature*, 296(5855):334–338.

Pollard, D. (2010). A retrospective look at coupled ice sheet-climate modeling. *Climatic Change*, 100(1):173–194.

Pollard, D. and DeConto, R. (2005). Hysteresis in Cenozoic Antarctic ice-sheet variations. *Global and Planetary Change*, 45(1-3):9–21.

Pollard, D. and DeConto, R. (2009). Modelling West Antarctic ice sheet growth and collapse through the past five million years. *Nature*, 458:329–332.

Pollard, D. and DeConto, R. M. (2003). Antarctic ice and sediment flux in the Oligocene simulated by a climate ice sheet sediment model. *Palaeogeography, Palaeoclimatology, Palaeoecology*, 198:53–67.

Pollard, D. and DeConto, R. M. (2012a). A simple inverse method for the distribution of basal sliding coefficients under ice sheets, applied to Antarctica. *The Cryosphere*, 6(5):953–971.

Pollard, D. and DeConto, R. M. (2012b). Description of a hybrid ice sheet-shelf model, and application to Antarctica. *Geoscientific Model Development Discussions*, 5(2):1077–1134.

Pollard, D., DeConto, R. M., and Nyblade, A. A. (2005). Sensitivity of Cenozoic Antarctic ice sheet variations to geothermal heat flux. *Global and Planetary Change*, 49(1-2):63–74.

Pollard, D. and Thompson, S. L. (1997). Driving a high-resolution dynamic ice-sheet model with GCM climate: ice-sheet initiation at 116 000 BP. *Annals of Glaciology*, 25:296–304.

Pope, V., Brown, S., Clark, R., Collins, M., Collins, W., Dearden, C., Gunson, J., Harris, G., Jones, C., Keen, a., Lowe, J., Ringer, M., Senior, C., Sitch, S., Webb, M., and Woodward, S. (2007). The Met Office Hadley Centre climate modelling capability: the competing requirements for improved resolution, complexity and dealing with uncertainty. *Philosophical transactions. Series A, Mathematical, physical, and engineering sciences*, 365(1860):2635–57.

Pope, V., Gallani, M., Rowntree, P., and Stratton, R. (2000). The impact of new physical parametrizations in the Hadley Centre climate model: HadAM3. *Climate Dynamics*, 16:123–146.

Pope, V. D. and Stratton, R. A. (2002). The processes governing horizontal resolution sensitivity in a climate model. *Climate Dynamics*, 19(3-4):211–236.

Prahl, F., Collier, R., Dymond, J., Lyle, M., and Sparrow, M. (1993). A biomarker perspective on prymnesiophyte productivity in the northeast Pacific Ocean. *Deep Sea Research Part I: Oceanographic Research Papers*, 40(10):2061–2076.

Prahl, F., Pilskaln, C., and Sparrow, M. (2001). Seasonal record for alkenones in sedimentary particles from the Gulf of Maine. *Deep Sea Research Part I: Oceanographic Research Papers*, 48(2):515–528.

Prahl, F. and Wakeham, S. (1987). Calibration of unsaturation patterns in long-chain ketone compositions for palaeotemperature assessment. *Nature*, 330:367–369.

Prahl, F. G., Wolfe, G. V., and Sparrow, M. A. (2003). Physiological impacts on alkenone paleothermometry. *Paleoceanography*, 18(2):1025.

Pusz, A. E., Thunell, R. C., and Miller, K. G. (2011). Deep water temperature, carbonate ion, and ice volume changes across the Eocene-Oligocene climate transition. *Paleoceanography*, 26(2):1–15.

Rahmstorf, S. (2007). A semi-empirical approach to projecting future sea-level rise. *Science*, 315(5810):368.

Rahmstorf, S., Perrette, M., and Vermeer, M. (2011). Testing the robustness of semi-empirical sea level projections. *Climate Dynamics*, 39(3-4):861–875.

Raymo, M., Hearty, P., DeConto, R., O'Leary, M., Dowsett, H. J., Robinson, M. M., and Mitrovica, J. (2009). PLIOMAX: Pliocene maximum sea level project. *PAGES news*, 17(2):4–5.

Raymo, M., Lisiecki, L., and Nisancioglu, K. (2006). Plio-Pleistocene ice volume, Antarctic Climate, and the Global $\delta$18O Record. *Science*, 313(July):492–495.

Raymo, M. E., Mitrovica, J. X., OLeary, M. J., DeConto, R. M., and Hearty, P. J. (2011). Departures from eustasy in Pliocene sea-level records. *Nature Geoscience*, 4(5):328–332.

Reeh, N. (1991). Parameterization of melt rate and surface temperature on the Greenland ice sheet. *Polarforschung*, 5913:113–128.

Ridley, J., Huybrechts, P., Gregory, J., and Lowe, J. (2005). Elimination of the Greenland ice sheet in a high CO2 climate. *Journal of Climate*, 18:3409–3427.

Rignot, E. (2004). Accelerated ice discharge from the Antarctic Peninsula following the collapse of Larsen B ice shelf. *Geophysical Research Letters*, 31(18):2–5.

Ritz, C., Fabre, A., and Letréguilly, A. (1997). Sensitivity of a Greenland ice sheet model to ice flow and ablation parameters: consequences for the evolution through the last climatic cycle. *Climate Dynamics*, 13:11–24.

Roberts, C. D., LeGrande, A. N., and Tripati, A. K. (2009). Climate sensitivity to Arctic seaway restriction during the early Paleogene. *Earth and Planetary Science Letters*, 286(3-4):576–585.

Rogozhina, I., Hagedoorn, J. M., Martinec, Z., Fleming, K., Soucek, O., Greve, R., and Thomas, M. (2012). Effects of uncertainties in the geothermal heat flux distribution on the Greenland Ice Sheet: An assessment of existing heat flow models. *Journal of Geophysical Research*, 117(F2):1–16.

Rohling, E. and Cooke, S. (1999). Stable oxygen and carbon isotope ratios in foraminiferal carbonate. In Sen Gupta, B., editor, *Modern Foraminifera*, chapter 14, pages 239–258. Kluwer Acad, Dordrecht, Netherlands.

Rohling, E., Grant, K., Bolshaw, M., Roberts, A., Siddall, M., Hemleben, C., and Kucera, M. (2009). Antarctic temperature and global sea level closely coupled over the past five glacial cycles. *Nature Geoscience*, 2:500–504.

Rohling, E. J., Medina-Elizalde, M., Shepherd, J. G., Siddall, M., and Stanford, J. D. (2012). Sea surface and high-latitude temperature sensitivity to radiative forcing of climate over several glacial cycles. *Journal of Climate*, 25(5):1635–1656.

Rosenthal, Y., Boyle, E., and Slowey, N. (1997). Temperature control on the incorporation of magnesium, strontium, fluorine, and cadmium into benthic foraminiferal shells from Little Bahama Bank: Prospects for thermocline paleoceanography. *Geochimica et Cosmochimica Acta*, 61(17):3633–3643.

Rosenthal, Y. and Lohmann, G. P. (2002). Accurate estimation of sea surface temperatures using dissolution-corrected calibrations for Mg/Ca paleothermometry. *Paleoceanography*, 17(3):1–6.

Rosenthal, Y., Lohmann, G. P., Lohmann, K. C., and Sherrell, R. M. (2000). Incorporation and preservation of Mg in Globigerinoides sacculifer: implications for reconstructing the temperature and 18 O/ 16 O of seawater. *Paleoceanography*, 15(1):135.

Rowlands, D. J., Frame, D. J., Ackerley, D., Aina, T., Booth, B. B. B., Christensen, C., Collins, M., Faull, N., Forest, C. E., Grandey, B. S., Gryspeerdt, E., Highwood, E. J., Ingram, W. J., Knight, S., Lopez, A., Massey, N., McNamara, F., Meinshausen, N., Piani, C., Rosier, S. M., Sanderson, B. M., Smith, L. A., Stone, D. A., Thurston, M., Yamazaki, K., Hiro Yamazaki, Y., and Allen, M. R. (2012). Broad range of 2050 warming from an observationally constrained large climate model ensemble. *Nature Geoscience*, 5(4):256–260.

Rowley, D. B. (2002). Rate of plate creation and destruction: 180 Ma to present. *Geological Society of America Bulletin*, 114(8):927–933.

Rutt, I. C., Hagdorn, M., Hulton, N. R. J., and Payne, A. J. (2009). The Glimmer community ice sheet model. *Journal of Geophysical Research*, 114(F2):1–22.

Sahagian, D. and Jones, M. (1993). Quantified Middle Jurassic to Paleocene eustatic variations based on Russian Platform stratigraphy: Stage level resolution. *Bulletin of the Geological Society of America*, 105(8):1109.

Savin, S. M. and Douglas, R. G. (1973). Stable isotope and magnesium geochemistry of recent planktonic foraminifera from the South Pacific. *Geological Society Of America Bulletin*, 84:2327–2342.

Scher, H. D. and Martin, E. E. (2009). Timing and climatic consequences of the opening of Drake Passage. *Science*, 312(5772):428–30.

Scherer, R. P. (1998). Pleistocene Collapse of the West Antarctic Ice Sheet. *Science*, 281(5373):82–85.

Schmidt, G. and Archer, D. (2009). Too much of a bad thing. *Nature*, 458:1117–1118.

Schneider von Deimling, T., Ganopolski, A., Held, H., and Rahmstorf, S. (2006). How cold was the Last Glacial Maximum? *Geophysical Research Letters*, 33(14):1–5.

Schoof, C. (2007). Marine ice-sheet dynamics. Part 1. The case of rapid sliding. *Journal of Fluid Mechanics*, 573:27–55.

Schouten, S., Hopmans, E., Schefuß, E., and Sinninghe Damsté, J. S. (2002). Distributional variations in marine crenarchaeotal membrane lipids: a new tool for reconstructing ancient sea water temperatures? *Earth and Planetary Science Letters*, 204(1-2):265–274.

Schubert, R., Schellnhuber, H., Buchmann, N., Epiney, A., Griesshammer, R., Kulessa, M., Messner, D., Rahmstorf, S., and Schmid, J. (2006). The future oceans-warming up, rising high, turning sour. Technical report, German Advisory Council on Global Change (WBGU), Berlin.

Seddik, H., Greve, R., Zwinger, T., Gillet-Chaulet, F., and Gagliardini, O. (2012). Simulations of the Greenland ice sheet 100 years into the future with the full Stokes model Elmer/Ice. *Journal of Glaciology*, 58(209):427–440.

Seki, O., Foster, G. L., Schmidt, D. N., Mackensen, A., Kawamura, K., and Pancost, R. D. (2010). Alkenone and boron-based Pliocene pCO2 records. *Earth and Planetary Science Letters*, 292(1-2):201–211.

Sewall, J. O., Sloan, L. C., Huber, M., and Wing, S. (2000). Climate sensitivity to changes in land surface characteristics. *Global and Planetary Change*, 26(4):445–465.

Sexton, P. F., Wilson, P. A., and Pearson, P. N. (2006). Microstructural and geochemical perspectives on planktic foraminiferal preservation: 'Glassy' versus 'Frosty'. *Geochemistry Geophysics Geosystems*, 7(12).

Shackleton, N. (1967). Oxygen isotope analyses and Pleistocene temperatures re-assessed. *Nature*, 215(5096):15–17.

Shackleton, N. and Kennett, J. (1975). Paleotemperature history of the Cenozoic and the initiation of Antarctic glaciation: oxygen and carbon isotope analyses in DSDP Sites 277, 279, and 281. *Initial Rep. Deep Sea Drill. Proj*, 29:743–755.

Shakun, J., Clark, P., He, F., Marcott, S., and Mix, A. (2012). Global warming preceded by increasing carbon dioxide concentrations during the last deglaciation. *Nature*, 484(7392):49–54.

Shevenell, A. E., Kennett, J. P., and Lea, D. W. (2008). Middle Miocene ice sheet dynamics, deep-sea temperatures, and carbon cycling: A Southern Ocean perspective. *Geochemistry Geophysics Geosystems*, 9(2).

Siddall, M., Hönisch, B., Waelbroeck, C., and Huybers, P. (2010a). Changes in deep Pacific temperature during the mid-Pleistocene transition and Quaternary. *Quaternary Science Reviews*, 29:170–181.

Siddall, M., Kaplan, M. R., Schaefer, J. M., Putnam, A., Kelly, M. A., and Goehring, B. (2010b). Changing influence of Antarctic and Greenlandic temperature records on sea-level over the last glacial cycle. *Quaternary Science Reviews*, 29:410–423.

Siddall, M., Rohling, E., Almogi-labin, A., Hemleben, C., Meischner, D., Schmeltzer, I., and Smeed, D. A. (2003). Sea-level fluctuations during the last glacial cycle. *Nature*, 423:19–24.

Siegenthaler, U., Stocker, T. F., Monnin, E., Lüthi, D., Schwander, J., Stauffer, B., Raynaud, D., Barnola, J.-M., Fischer, H., Masson-Delmotte, V., and Jouzel, J. (2005). Stable carbon cycle-climate relationship during the Late Pleistocene. *Science*, 310(5752):1313–7.

Siegert, M., Dowdeswell, J., Hald, M., and Svendsen, J. (2001). Modelling the Eurasian ice sheet through a full (Weichselian) glacial cycle. *Global and Planetary Change*, 31:367–385.

Sijp, W. P., England, M. H., and Huber, M. (2011). Effect of the deepening of the Tasman Gateway on the global ocean. *Paleoceanography*, 26(4):1–18.

Sijp, W. P., England, M. H., and Toggweiler, J. R. (2009). Effect of Ocean Gateway Changes under Greenhouse Warmth. *Journal of Climate*, 22(24):6639–6652.

Sikes, E., Farrington, J., and Keigwin, L. (1991). Use of the alkenone unsaturation ratio Uk'37 to determine past sea surface temperatures: core-top SST calibrations and methodology considerations. *Earth and Planetary Science Letters*, 104:36–47.

Sikes, E., Howard, W., Samson, C., Mahan, T., Robertson, L., and Volkman, J. (2009). Southern Ocean seasonal temperature and Subtropical Front movement on the South Tasman Rise in the late Quaternary. *Paleoceanography*, 24(2):PA2201.

Sikes, E., Volkman, J., Robertson, L., and Pichon, J. (1997). Alkenones and alkenes in surface waters and sediments of the Southern Ocean: Implications for paleotemperature estimation in polar regions. *Geochimica et Cosmochimica Acta*, 61(7):1495–1505.

Singarayer, J. S. and Valdes, P. J. (2010). High-latitude climate sensitivity to ice-sheet forcing over the last 120kyr. *Quaternary Science Reviews*, 29(1-2):43–55.

Sinninghe Damsté, J. S., Schouten, S., Hopmans, E. C., Duin, A. C. T. V., and Geenevasen, J. A. J. (2002). Crenarchaeol: the characteristic core glycerol dibiphytanyl glycerol tetraether membrane lipid of cosmopolitan pelagic crenarchaeota. *Journal Of Lipid Research*, 43:1641–1651.

Smith, R., Gregory, J., and Osprey, A. (2008). A description of the FAMOUS (version XDBUA) climate model and control run. *Geoscientific Model Development*, 1:53–68.

Solgaard, A. M. and Langen, P. L. (2012). Multistability of the Greenland ice sheet and the effects of an adaptive mass balance formulation. *Climate Dynamics*.

Solomon, S., Qin, D., Manning, Z., Marquis, M., Averyt, K., Tignor, M., and Miller, H. (2007). A report of Working Group 1 of the Intergovernmental Panel on Climate Change. In *Climate Change 2007: The Physical Science Basis*, chapter Summary fo. Cambridge University Press, Cambridge, UK.

Sosdian, S. and Rosenthal, Y. (2009). Deep-sea temperature and ice volume changes across the Pliocene-Pleistocene climate transitions. *Science*, 325(5938):306–10.

Spasojević, S., Liu, L., Gurnis, M., and Müller, R. D. (2008). The case for dynamic subsidence of the U.S. east coast since the Eocene. *Geophysical Research Letters*, 35(8):1–6.

Sprengel, C., Baumann, K.-H., and Neuer, S. (2000). Seasonal and interannual variation of coccolithophore fluxes and species composition in sediment traps north of Gran Canaria (29N 15W). *Marine Micropaleontology*, 39(1-4):157–178.

Steffen, W., Burbidge, A., Hughes, L., Kitching, R., Lindenmayer, D., Musgrave, W., Stafford-Smith, M., and Werner, P. (2009). *Australia's biodiversity and climate change: a strategic assessment of the vulnerability of Australia's biodiversity to climate change.* CSIRO Publising.

Stone, E. J., Lunt, D. J., Rutt, I. C., and Hanna, E. (2010). Investigating the sensitivity of numerical model simulations of the modern state of the Greenland ice-sheet and its future response to climate change. *The Cryosphere*, 4(3):397–417.

Sun, D., Pinker, R. T., and Kafatos, M. (2006). Diurnal temperature range over the United States: A satellite view. *Geophysical Research Letters*, 33(5):L05705.

Sundal, A. V., Shepherd, A., Nienow, P., Hanna, E., Palmer, S., and Huybrechts, P. (2011). Melt-induced speed-up of Greenland ice sheet offset by efficient subglacial drainage. *Nature*, 469(7331):521–4.

Svendsen, J. (2004). Late Quaternary ice sheet history of northern Eurasia. *Quaternary Science Reviews*, 23(11-13):1229–1271.

Tarasov, L. and Peltier, W. (1999). Impact of thermomechanical ice sheet coupling on a model of the 100 kyr ice age cycle. *Journal of Geophysical Research*, 104(D8):9517–9545.

Tarasov, L. and Peltier, W. (2004). A geophysically constrained large ensemble analysis of the deglacial history of the North American ice-sheet complex. *Quaternary Science Reviews*, 23(3-4):359–388.

Taylor, L. L., Banwart, S. A., Valdes, P. J., Leake, J. R., and Beerling, D. J. (2012). Evaluating the effects of terrestrial ecosystems, climate and carbon dioxide on weathering over geological time: a global-scale process-based approach. *Philosophical transactions of the Royal Society of London. Series B, Biological sciences*, 367(1588):565–82.

ten Brink, U. S., Hackney, R. I., Bannister, S., Stern, T. A., and Makovsky, Y. (1997). Uplift of the Transantarctic Mountains and the bedrock beneath the East Antarctic ice sheet. *Journal of Geophysical Research*, 102(B12):27603–27621.

Ternois, Y., Sicre, M.-A., Boireau, A., Beaufort, L., Miquel, J., and Jeandel, C. (1998). Hydrocarbons, sterols and alkenones in sinking particles in the Indian Ocean sector of the Southern Ocean. *Organic Geochemistry*, 28(7-8):489–501.

Thompson, S. L. and Pollard, D. (1997). Ice-sheet mass balance at the Last Glacial Maximum from the GENESIS version 2 global climate model. *Annals of Glaciology*, 25:250–258.

Thomsen, C., Schulz-Bull, D., Petrick, G., and Duinker, J. (1998). Seasonal variability of the long chain alkenone flux and the effect on the Uk'37 index in the Norwegian Sea. *Organic Geochemistry*, 28(5):311–323.

Toggweiler, J. R. and Bjornsson, H. (2000). Drake Passage and palaeoclimate. *Journal of Quaternary Science*, 15(4):319–328.

Tripati, A., Backman, J., Elderfield, H., and Ferretti, P. (2005). Eocene bipolar glaciation associated with global carbon cycle changes. *Nature*, 436(7049):341–6.

Turner, J., Connolley, W. M., Lachlan-Cope, T. A., and Marshall, G. J. (2006). The performance of the Hadley Centre Climate Model (HadCM3) in high southern latitudes. *International Journal of Climatology*, 26(1):91–112.

UNFCCC (2009). Draft decision - / CP . 15. (last accessed: 19/02/13). http://unfccc.int/resource/docs/2009/cop15/eng/l07.pdf.

Urey, H. (1947). The thermodynamic properties of isotopic substances. *Journal of the Chemistry Society*, pages 562–581.

Utescher, T., Böhme, M., and Mosbrugger, V. (2011). The Neogene of Eurasia: Spatial gradients and temporal trends The second synthesis of NECLIME. *Palaeogeography, Palaeoclimatology, Palaeoecology*, 304(3-4):196–201.

Utescher, T., Erdei, B., François, L., and Mosbrugger, V. (2007). Tree diversity in the Miocene forests of Western Eurasia. *Palaeogeography, Palaeoclimatology, Palaeoecology*, 253(1-2):226–250.

Utescher, T., Mosbrugger, V., Ivanov, D., and Dilcher, D. L. (2009). Present-day climatic equivalents of European Cenozoic climates. *Earth and Planetary Science Letters*, 284(3-4):544–552.

Vail, P., Mitchum, R., Todd, R., Widmier, J., Thompon, S., Sangree, J., Bubb, J., and Hatlelid, W. (1977). Seismic stratigraphy and global changes of sea level. In Payton, C., editor, *Seismic Stratigraphy - Applications to Hydrocarbon Exploration*, pages 49–212. AAPG.

van de Berg, W. J., van den Broeke, M., Ettema, J., van Meijgaard, E., and Kaspar, F. (2011). Significant contribution of insolation to Eemian melting of the Greenland ice sheet. *Nature Geoscience*, 4(10):679–683.

Van der Veen, C. (1999). *Fundamentals of Glacier Dynamics*. AA Balkema.

Vermeer, M. and Rahmstorf, S. (2009). Global sea level linked to global temperature. *PNAS*, 106(51):21527–21532.

Volkman, J., Eglinton, G., Corner, E., and Forsberg, T. (1980). Long-chain alkenes and alkenones in the marine coccolithophorid Emiliania Huxleyi. *Phytochemistry*, 19:1–4.

von der Heydt, A. and Dijkstra, H. A. (2008). The effect of gateways on ocean circulation patterns in the Cenozoic. *Global and Planetary Change*, 62(1-2):132–146.

Wade, B. S. and Palike, H. (2004). Oligocene climate dynamics. *Paleoceanography*, 19(4):PA4019.

Waelbroeck, C., Labeyrie, L., Michel, E., Duplessy, J., McManus, J., Lambeck, K., Balbon, E., and Labracherie, M. (2002). Sea-level and deep water temperature changes derived from benthic foraminifera isotopic records. *Quaternary Science Reviews*, 21(1-3):295–305.

Wardlaw, B. and Quinn, T. (1991). The record of Pliocene sea-level change at Enewetak atoll. *Quaternary Science Reviews*, 10:247–258.

Weaver, P., Chapman, M., Eglinton, G., Zhao, M., Rutledge, D., and Read, G. (1999). Combined coccolith, foraminiferal, and biomarker reconstruction of paleoceanographic. *Paleoceanography*, 14(3):336–349.

Weertman, J. (1961). Stability of ice-age ice sheets. *Journal of Geophysical Research*, 66(11):3783–3792.

Weertman, J. (1976). Milankovitch solar radiation variations and ice age ice sheet sizes. *Nature*, 261:17–20.

Weijers, J., Schouten, S., Spaargaren, O., and Sinninghe Damsté, J. (2006). Occurrence and distribution of tetraether membrane lipids in soils: Implications for the use of the TEX86 proxy and the BIT index. *Organic geochemistry*, 37(12):1680–1693.

Wilkinson, B. and Algeo, T. (1989). Sedimentary carbonate record of calcium - magnesium cycling. *American Journal of Science*, 289(10):1158.

Williams, T., van de Flierdt, T., Hemming, S. R., Chung, E., Roy, M., and Goldstein, S. L. (2010). Evidence for iceberg armadas from East Antarctica in the Southern Ocean during the late Miocene and early Pliocene. *Earth and Planetary Science Letters*, 290(3-4):351–361.

Wilschut, F., Bintanja, R., and van de Wal, R. (2006). Ice-sheet modelling characteristics in sea-level-based temperature reconstructions over the last glacial cycle. *Journal of Glaciology*, 52(176):149–158.

Wilson, D. and Luyendyk, B. (2009). West Antarctic paleotopography estimated at the Eocene-Oligocene climate transition. *Geophysical Research Letters*, 36:10–13.

Wilson, D. S., Jamieson, S. S., Barrett, P. J., Leitchenkov, G., Gohl, K., and Larter, R. D. (2011). Antarctic topography at the EoceneOligocene boundary. *Palaeogeography, Palaeoclimatology, Palaeoecology*.

Wilson, G. (1995). The Neogene East Antarctic ice sheet: A dynamic or stable feature? *Quaternary Science Reviews*, pages 101–123.

Winguth, A., Shellito, C., Shields, C., and Winguth, C. (2010). Climate Response at the PaleoceneEocene Thermal Maximum to Greenhouse Gas ForcingA Model Study with CCSM3. *Journal of Climate*, 23(10):2562–2584.

Winkler, A., Wolf-Welling, T., Stattegger, K., and Thiede, J. (2002). Clay mineral sedimentation in high northern latitude deep-sea basins since the Middle Miocene (ODP Leg 151, NAAG). *International Journal of Earth Sciences*, 91(1):133–148.

Winsborrow, M. C., Andreassen, K., Corner, G. D., and Laberg, J. S. (2010). Deglaciation of a marine-based ice sheet: Late Weichselian palaeo-ice dynamics and retreat in the southern Barents Sea reconstructed from onshore and offshore glacial geomorphology. *Quaternary Science Reviews*, 29(3-4):424–442.

Winton, M. (2006). Does the Arctic sea ice have a tipping point? *Geophysical Research Letters*, 33(23):L23504.

WMO (2012). Global Weather and Climate Extremes. (last accessed: 19/02/13). http://wmo.asu.edu/.

Wright, J. D., Sheridan, R. E., Miller, K. G., Uptegrove, J., Cramer, B. S., and Browning, J. V. (2009). Late Pleistocene Sea level on the New Jersey Margin: Implications to eustasy and deep-sea temperature. *Global and Planetary Change*, 66(1-2):93–99.

Wuchter, C., Schouten, S., Coolen, Marco, J., L., and Damste, J. S. S. (2004). Temperature-dependent variation in the distribution of tetraether membrane lipids of marine Crenarchaeota: Implications for TEX86 paleothermometry. *Paleoceanography*, 19(4):1–10.

Wuchter, C., Schouten, S., Wakeham, S., and Damsté, J. (2005). Temporal and spatial variation in tetraether membrane lipids of marine Crenarchaeota in particulate organic matter: Implications for TEX86 paleothermometry. *Paleoceanography*, 20(PA3013):1–11.

Wuchter, C., Schouten, S., Wakeham, S., and Damsté, J. (2006). Archaeal tetraether membrane lipid fluxes in the northeastern Pacific and the Arabian Sea: Implications for TEX86 paleothermometry. *Paleoceanography*, 21(PA4208):1–9.

Xu, X., Lithgow-Bertelloni, C., and Conrad, C. (2006). Global reconstructions of Cenozoic seafloor ages: Implications for bathymetry and sea level. *Earth and Planetary Science Letters*, 243(3-4):552–564.

Yokoyama, Y., Lambeck, K., De Deckker P, Johnston, P., and Fifield, L. (2000). Timing of the Last Glacial Maximum from observed sea-level minima. *Nature*, 406(6797):713–6.

You, Y., Huber, M., Müller, R. D., Poulsen, C. J., and Ribbe, J. (2009). Simulation of the Middle Miocene Climate Optimum. *Geophysical Research Letters*, 36(4):0–4.

Zachos, J., Pagani, M., Sloan, L., Thomas, E., and Billups, K. (2001a). Trends, rhythms, and aberrations in global climate 65 Ma to present. *Science*, 292(5517):686.

Zachos, J., Stott, L., and Lohmann, K. (1994). Evolution of early Cenozoic marine temperatures. *Paleoceanography*, 9(2):353–387.

Zachos, J. C., Dickens, G. R., and Zeebe, R. E. (2008). An early Cenozoic perspective on greenhouse warming and carbon-cycle dynamics. *Nature*, 451(7176):279–83.

Zachos, J. C., Shackleton, N. J., Revenaugh, J. S., Pälike, H., and Flower, B. P. (2001b). Climate response to orbital forcing across the Oligocene-Miocene boundary. *Science*, 292(5515):274–8.

Zanazzi, A., Kohn, M. J., MacFadden, B. J., and Terry, D. O. (2007). Large temperature drop across the Eocene-Oligocene transition in central North America. *Nature*, 445(7128):639–42.

Zweck, C. and Huybrechts, P. (2005). Modeling of the Northern Hemisphere ice sheets during the last glacial cycle and glaciological sensitivity. *Journal of Geophysical Research*, 110(D7).